The geochemical record of metamorphic fluid-rock interaction in subducted terranes

Inaugural dissertation

of the Faculty of Science

University of Bern

presented by

Thorsten A. Markmann

from Mainz, Germany

Supervisor of the doctoral thesis:

Prof. Dr. Pierre Lanari

Prof. Dr. Daniela Rubatto

Institute of Geological Sciences

University of Bern

The geochemical record of metamorphic fluid-rock interaction in subducted terranes

Inaugural dissertation

of the Faculty of Science

University of Bern

presented by

Thorsten A. Markmann

from Mainz, Germany

Supervisor of the doctoral thesis:

Prof. Dr. Pierre Lanari

Institute of Earth Sciences, University of Lausanne

Prof. Dr. Daniela Rubatto

Institute of Geological Sciences, University of Bern

Accepted by the Faculty of Science

Bern, 29.11.2024 The Dean

Prof. Dr. Jean-Louis Reymond

"WE know little of the earth's internal parts, or of the materials which compose it at any considerable depth below the surface. But upon the surface of this globe, the more inert matter is replenished with plants, and with animals and intellectual beings."

James Hutton, THEORY of the EARTH, 1788

Acknowledgements

My deepest gratitude goes to my supervisor, Pierre Lanari. The past (almost) four years of my PhD journey with you have been an incredibly exciting time, filled with joy, challenges, unexpected turns, adventures, and, most importantly, invaluable lessons for the future. I sincerely thank you for your guidance, patience, for the countless moments we shared in the pursuit of science, at conferences, and beyond.

I would also like to extend my thanks to Daniela Rubatto, my second supervisor, for always being open to discussions about geochemistry and SIMS data. I hope we can one day do the excursion to Lago di Cignana we wanted to do in the first year.

A huge thank you goes to the CPaG group: Hugo Dominguez, Jacob Forshaw, Philip Hartmeier, Jiahui Liu, Qian Zhang, and Aiyana Diwa. It has been an extraordinary journey with all of you. I will forever cherish the moments we shared at the institute, during coding camps, and at conferences. Without you, this PhD would have been far tougher and definitely less enjoyable.

A special "γεια σας, γεια σας, Καλημέρα" and "Ευχαριστώ πολύ" to my fieldwork partners on Syros, Valentin Laurent and Martin Engi. My heartfelt thanks to Catherine, Jacobos, and Justine, who always welcomed me warmly at the Alkyon and showed such interest in my work on Syros—Ευχαριστώ πολύ!

I am also deeply grateful to the entire petrology group for fostering an incredible, supportive, and motivating environment. It was a joy to work and learn in such a welcoming atmosphere. Special thanks to Jörg Hermann, Thomas Pettke, Francesca Piccoli, Renée Tamblyn, Coralie Vesin, Michelle Ulrich, Mona Lüder, Nils Gies, Luca Pacchiega, and Mahyra Tedeschi for making this experience truly enriching.

To my office mates in Room 044, Ferdi and Sandro, thank you for standing by me and offering encouragement throughout the PhD process (even though you finish before me!).

I would also like to thank everyone at the Institute of Geology in Bern for contributing to the warm and collegial atmosphere that made working there a pleasure. Special recognition to Stefan Brechbühl, Thomas Aebi, and Nadine Lötscher from the preparation lab for their

excellent work and for always making time for a chat. My gratitude also goes to the student assistants who helped prepare bulk rock analyses, Marco Bermanec and Aiyana Diwa.

To my long-time friends in Germany: Sophie, Jens, Anna, Oli, Viki, David, Isabel, Sophie (II), Bene, and Timur. Thank you for your support, even from a distance. I also want to thank the friends I made during my time in Switzerland: Alba, Corin, Silvano, Katharina, Vivi, Elisa, Natasha, Alberto, and Arianna. You all made this journey so much more meaningful.

Finally, my deepest gratitude is reserved for my family. To my parents, Sabine and Joachim, thank you for your endless love and support throughout my entire journey. To my siblings, Andreas and Katherina, as well as my grandparents, thank you for your constant encouragement and for being there, even when I missed you all during the long days and weeks away.

This project has received funding from the European Research Council (ERC) under the European Union's Horizon 2020 research and innovation program (grant 850530), from the Swiss National Science Foundation (SNSF, grants IZSEZ0_210259 and 206021_170722).

Abstract

Dehydration during metamorphism in subduction zones plays a crucial role in the redistribution of fluids within the subducting oceanic crust. This can can lead to significant fluid-rock interactions during metamorphism, which affects the mineral growth and stability, whereas fluid fluxes play a critical role in mass transfer and element recycling on Earth. This thesis investigates fluid-rock interaction and metamorphic processes in subduction zones, focusing on how fluid release, transport, and mineral growth shape geochemical signatures during prograde metamorphism. Integrating methodological advancements and applications to natural samples from high-pressure terranes, this work provides a detailed perspective on the fluid-mediated geochemical evolution of subducted rocks, particularly within the Cyclades (Greece) and the European Alps.

Chapter 2 introduces a novel routine approach for quantitative compositional mapping using LA-ICP-MS, which enables high-resolution, major to trace element analysis of compositionally zoned minerals, such as garnet. The routine stresses the usage of an accurate pixel allocation strategy of square pixels. Implemented within the open-source XMapTools software, the mapping approach addresses calibration challenges in inhomogeneous phases and demonstrates accurate calibration across diverse geological contexts, such as garnet-bearing eclogites, feldspar and biotite in migmatites, and rutile in metapelites.

Chapter 3 presents a petrochemical model that integrates mechanical and thermodynamic simulations to explore the effects of dehydration reactions on fluid release and pressure fluctuations within subducting rocks. The model results emphasize the link between metamorphic reactions and episodic brittle failure, and highlights the fluid release in pulses. This interplay has implications for transient permeability and fluid flow along shear zones in subduction environments. Applications to the Monviso ophiolite indicate that brittle failure episodes may correlate with observed compositional zoning in garnet from subducted metagabbro. Fluid pressure variations during metamorphism can potentially modify the incorporation of elements into garnet as resolved for chemically zoned garnets in bluecshists from Syros.

Chapter 4 examines fluid-rock interaction in subducted oceanic crust on Syros through

in-situ oxygen isotope analyses of garnet and phengite. Variations in $\delta^{18}O$ across different lithologies reflect hydrothermal alteration during seafloor processes and subsequent interaction with isotopically heavier fluids during high-pressure metamorphism. The isotopic data suggest that fluid infiltration was extensive in certain areas, notably Katergaki, while other sites experienced limited interaction, supporting a model of localized fluid transfer and mineral stabilization.

Chapter 5 investigates garnet growth mechanisms and their geochemical implications in blueschist samples from Syros, using 3D micro-computed tomography and 2D compositional mapping. Findings show that garnet growth was influenced by fluid infiltration and mineral breakdown, leading to trace element zoning patterns indicative of interface-controlled growth and episodic fluid pressure changes. Differences in trace element distribution between samples reveal that garnet in the locality Katergaki interacted with externally derived fluids, producing oscillatory zoning not observed in samples from the locality Achladi.

Collectively, this thesis illustrates how compositional mapping, petrochemical modelling, and isotopic analysis together provide insights into the geochemical processes at play during subduction. This work underscores the role of fluids in regulating mineral stability, mass transfer, and the overall geochemical evolution of subducted lithologies, with implications for the dynamics of element recycling and metamorphism in Earth's crust and mantle.

Contents

List of Figures

List of Tables

Chapter 1

General Introduction

1.1 Treatise of the geological perspective

Modern geology was profoundly shaped by the discovery of continental drift (Wegener, 1912) and seafloor spreading at mid-ocean ridges (Hess, 1962), which culminated in the theory of plate tectonics (McKenzie & Parker, 1967; Morgan, 1968). These groundbreaking studies laid the foundation for understanding the Earth as a versatile geodynamic system in constant motion. Today, subduction zones — where oceanic crust is subducted into the Earth's mantle — are recognized as key components of the global elemental cycle, linking the Earth's interior with the hydrosphere, atmosphere, and lithosphere (e.g., Hacker, 2008; Ito et al., 2003; Manning, 2004; Schmidt & Poli, 2003; Spandler & Pirard, 2013). Despite the fact that the total amount of water entering subduction zones over the course of a million years is roughly equivalent to the entire volume of today's oceans (e.g., Plümper et al., 2017, and references therein), Earth's oceans have not disappeared. This paradox highlights that the mechanisms controlling fluid release and migration within subducting slabs and how fluids are cycled between the Earth's interior and its surface are only partially understood.

The subduction of hydrated oceanic crust plays a critical role in Earth's geochemical cycles, as increasing temperature and pressure during prograde metamorphism trigger key mineralogical reactions. Hydrous phases — minerals containing structurally bound H_2O — decompose as oceanic lithosphere is buried deeper into the Earth, releasing aqueous fluids into the surrounding environment (see Figure 1.1 Manning, 2004; Poli & Schmidt, 2002; Schmidt & Poli, 2003; Zheng et al., 2016). This fluid release is vital to the recycling processes in subduction zones, as it exerts a first-order control on element transport, reaction kinetics, and heat transfer. Additionally, these fluids play a key role in triggering arc magmatism and seismic activity (Bebout & Penniston-Dorland, 2016; Hacker, Peacock, et al., 2003; Hermann et al., 2006; Kerrick & Connolly, 2001; Kirby et al., 1996; Kita et al., 2006; Peacock, 1996, 2009; Peacock & Wang, 1999; Schmidt & Poli, 2014; Schmidt & Poli, 1998; Shiina et al., 2013; Spandler et al., 2011; Tatsumi, 2005; Zheng, 2019).

The primary challenge in studying fluids in subduction zones lies in the fact that these processes can only be investigated indirectly, through the examination of exhumed slices of ancient subduction zones. Specifically, blueschist and eclogite metamorphic rocks serve as direct witnesses to dehydration reactions and the redistribution of aqueous fluids and elements within the crust. These rocks are preserved in a few high-pressure terranes around the world (e.g., Tsujimori et al., 2006; Warren, 2013; Whitney et al., 2020), and provide key evidence of fluid flow during subduction processes (e.g., Philippot & Selverstone, 1991; Plümper et al., 2017; Spandler & Hermann, 2006; Strating & Vissers, 1991; Taetz et al., 2018; Zack & John, 2007). To bridge the gap left by indirect natural observations, petrological, thermomechanical, and geochemical models have been developed to assess

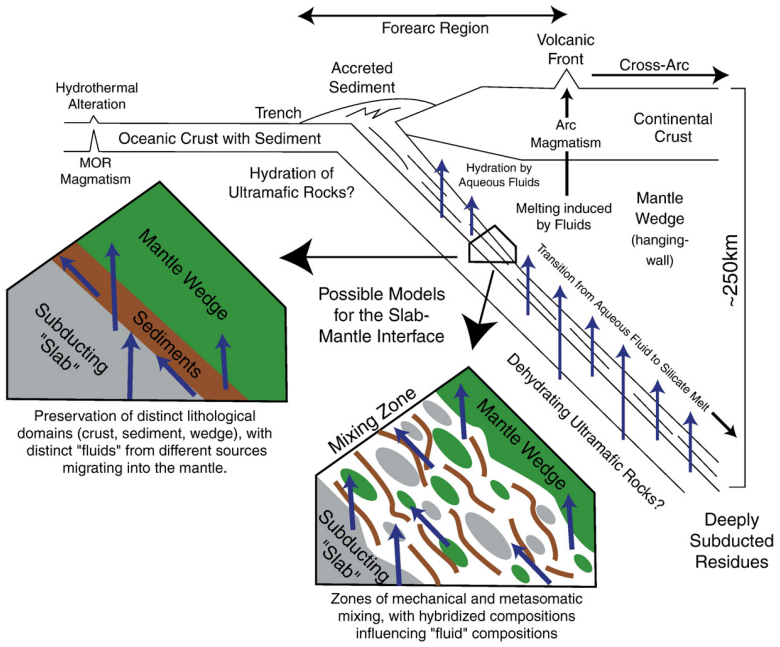

Figure 1.1: Schematic representation of an ocean-continent subduction zone, illustrating the fluid pathways within a recycled crustal section and at the slab-mantle interface from Bebout (2007).

fluid release from devolatilization reactions in subduction zones and their influence on heat transfer, element cycling, and fluid migration (e.g., Ague & Nicolescu, 2014; Baxter & Caddick, 2013; Connolly, 1997, 2010; Connolly & Podladchikov, 1998; Hacker, Abers, & Peacock, 2003; Konrad-Schmolke et al., 2011; Malvoisin et al., 2015; Morishige & van Keken, 2018; Peacock, 1996; Syracuse et al., 2010; Van Keken et al., 2002; Wilson et al., 2014). Recent advances have focused on coupling fluid production and migration with geochemical signatures in stable mineral phases, such as oxygen isotopes and trace elements (Konrad-Schmolke et al., 2011; Konrad-Schmolke et al., 2023; Vho et al., 2020), attempting to replicate natural phenomena. These models, along with cutting-edge analytical techniques, now enable the investigation of fluid-rock interactions by studying the geochemical signatures preserved in metamorphic minerals. Advances in electron microprobe analysis (EPMA), ion microprobe techniques like secondary ion mass spectrometry (SIMS), and laser ablation inductively-coupled-plasma mass-spectrometry (LA-ICP-MS) have enhanced the ability to probe microscale geochemical variations. Isotopes and trace elements, in particular, serve as valuable tracers for fluid-rock interactions.

Metamorphic minerals often exhibit compositional zoning in major, trace, and isotopic compositions, with oxygen being especially useful as it is a major component of both fluids and minerals. Variations in tracer elements or isotopes are closely linked to changes in temperature, pressure, and fluid presence (Martin et al., 2014; Page et al., 2014; Raimondo et al., 2012; Rubatto & Angiboust, 2015; Ulrich et al., 2024), while pH can also affect

tracers like boron isotopes (Vesin et al., 2024). The challenge of recording compositional zoning (Dempster, 1985; Hickmott, 1988; Hickmott & Spear, 1992; Hollister, 1966; Kretz, 1993; Schwandt et al., 1996; Tracy et al., 1976; Yang & Rivers, 2002) has been addressed through advancements in analytical techniques, allowing high-resolution geochemical mapping (Chabala et al., 1995; Lanari et al., 2019; Paton et al., 2011; Woodhead et al., 2007, 2008). However, quantifying compositions in zoned or inhomogeneous minerals remains a challenge.

Garnet is one of the most widely used proxies for isotope and trace element studies, as it is a major mineral in various metamorphic rocks and forms under a broad range of temperature and pressure conditions (Baxter & Caddick, 2013; Caddick et al., 2010; Hermann, 2003; Konrad-Schmolke et al., 2006; Yang & Rivers, 2001). The nucleation and growth of porphyroblasts, such as garnet, are critical in metamorphic petrology, capturing key stages of a rock's metamorphic history. Techniques like micro-computed tomography (µCT) allow for 3D analysis of porphyroblast distribution, providing insights into growth mechanisms (e.g., Carlson & Denison, 1992; Denison & Carlson, 1997). Garnet growth and its chemical composition, however, are intrinsically linked to fluid presence, which affects the availability of chemical components and the kinetics of mineral reactions (Carlson, 2011; Gaidies et al., 2017, 2021; George et al., 2018). Despite extensive studies in recent decades, the intricate influence of fluids on the geochemical zoning of porphyroblasts remains an active area of research.

1.2 Objectives of the Study

The primary objective of this thesis is to investigate prograde metamorphism and fluid-rock interaction processes in subduction zones through two key approaches: I) the development of new software tools, and II) the application of state-of-the-art analytical techniques, such as in-situ oxygen isotope measurements via SIMS and quantitative compositional mapping, to document fluid-rock interactions in high-pressure terranes.

The software development component consists of two main parts. Part 1 focuses on modelling fluid fluxes using petrochemical approaches, which integrate petrological modelling of mineral phase assemblages with a chemical model for oxygen isotope composition (e.g., Vho et al., 2020). As conceptualized in Figure 1.1, current petrological models predict a continuous release of fluid from rocks during subduction and ongoing dehydration (e.g., Baxter & Caddick, 2013; Gies et al., 2024; Hacker, Peacock, et al., 2003). However, natural observations suggest that fluid flux is episodic (e.g., Hoover et al., 2022; John et al., 2012; Pattison & Tinkham, 2009; Spandler & Hermann, 2006), highlighting a significant discrepancy. To address this, a mechanical model is integrated into the petro-

chemical framework, enabling a comprehensive evaluation of fluid release from rocks, its transfer, and the interactions between multiple rock types and fluids. Part 2 focuses on developing an integrated measurement routine and an optimized data reduction scheme for processing quantitative compositional data obtained from LA-ICP-MS mapping. Mapping multi-phase assemblages is a powerful method for assessing the elemental distribution in minerals on a broad scale. However, calibration remains limited to elements that are homogeneously distributed within the minerals, as well as the pixel classification process (e.g., Paul et al., 2014). Currently, no established mapping protocol takes into account optimized pixel allocation strategies to enhance data quality while addressing the complexities of multi-phase assemblages, and this work aims to fill that gap.

The developed tools are then applied to natural samples, where petrological investigations and oxygen isotope analyses at the microscale are conducted on high-pressure terranes from the European Alps and the Cyclades (Greece). By integrating these tools and methods, this thesis offers a comprehensive examination of metamorphic processes in subduction zones, contributing to a deeper understanding of how fluids and their release influence mineral growth and geochemical evolution in these dynamic geological environments.

1.3 Contributions of the Thesis

The key contributions of this thesis are:

- Theoretical Contributions: The mechanisms governing the release and migration of aqueous fluids in subducting slabs are analyzed from both mechanical and geochemical perspectives. This includes a detailed discussion of how these processes are recorded through porphyroblast growth and traced via isotope and trace element measurements at the microscale in mineral phases. Additionally, the study highlights the importance of compositional data treatment from mapping experiments and 3D data reconstruction from µCT, providing deeper insights into fluid-rock interactions and the role of fluid migration in subduction zones.

- Methodological Advances: Two significant analytical methodologies were developed: (1) an enhanced approach for LA-ICP-MS mapping, and (2) a new petrochemical modelling technique. Moreover, a multi-scale 2D and 3D workflow was introduced, enabling a comprehensive geochemical analysis of ancient subducted crust, integrating both chemical and structural data from different spatial scales.

- Practical Applications: The newly developed tools and methodological improvements were applied to case studies from the European Alps and the Cyclades. These ap-

plications included state-of-the-art 2D and 3D outcrop mapping, 3D sample recovery and analysis using µCT, along with high-resolution quantitative chemical mapping via EPMA and LA-ICP-MS. Additionally, in-situ oxygen isotope analysis of garnet and phengite provided insights into fluid-rock interaction. The novel petrochemical modelling tool, ThorPT, was also employed to evaluate fluid production, extraction, and transfer in multi-rock systems, with a particular focus on the mechanical behavior of these processes. This holistic approach allowed for a comprehensive understanding of the fluid dynamics, trace element redistribution, and mechanical influences during metamorphism in these geological settings.

1.4 Thesis Structure

This dissertation is conceptualised as four chapters written in article format. This comprises

Chapter 2: Multi-phase quantitative compositional mapping by LA-ICP-MS: analytical approach and data reduction protocol implemented in XMapTools.

This chapter is an published article in Chemical Geology. Co-authors are Pierre Lanari, Francesca Piccoli, Thomas Pettke, Renée Tamblyn, Mahyra Tedeschi, Mona Lueder, Barbara E. Kunz, Nicolas Riel, and Joshua Laughton

LA-ICP-MS is widely used in geosciences and materials science due to its versatility, high chemical resolution, and minimal sample preparation. However, advancements in data handling and quality enhancement depend on the development of specialized measurement routines tailored to the technique's capabilities and the complexity of the samples. This chapter addresses both challenges by introducing two key innovations. First, it presents a novel measurement routine for major, minor, and trace element mapping, specifically designed for samples composed of multiple materials, such as rock slices with diverse mineral phases. Second, it introduces a custom software tool that allows for the individual treatment of different mineral phases, enabling high-precision quantification of compositionally zoned materials. These developments significantly improve the accuracy and applicability of LA-ICP-MS for complex sample analysis. The developments serve as a tool in this work.

Chapter 3: Mechanical modelling in petrochemical models: implications for fluid extraction in subduction zones

This chapter is a manuscript under review in Journal of Metamorphic Geology. Pierre Lanari is a co-author.

This chapter introduces a new petrochemical modelling software designed to enable users to create detailed modelling scenarios based on field observations. The software allows for the incorporation of bulk rock compositions and other constraints to simulate the

metamorphic evolution of geological sequences. It facilitates the testing of mineral assemblage evolution, reconstructs the oxygen isotope composition of stable mineral phases, and models fluid transfer between lithologies in multi-rock scenarios along a defined pressure and temperature (P–T) path. A key advancement presented in this chapter is a new model for evaluating the mechanical integrity of the rocks being modelled, which integrates volume and pressure changes with thermodynamic principles. This mechanical integrity is critical for understanding fluid transport, release, and transfer within the Earth's crust. The software's capabilities are demonstrated using natural examples from subduction zones, illustrating its value in real-world geological applications.

Chapter 4: Isotope evidence of fluid-rock interaction processes in blueschists and eclogites on Syros (Cyclades, Greece)

This chapter consists of an article to be submitted to the Journal of Petrology. Co-authors are Pierre Lanari, Valentin Laurent, and Daniela Rubatto.

This chapter focuses on the study of fluid-rock interactions in subduction zones, with the island of Syros (Cyclades, Greece) serving as a case study due to its exceptionally well-preserved blueschist and eclogite facies rocks. The chapter explores the processes of fluid flow and metasomatism, particularly in the absence of major dehydration reactions, such as the formation of olivine, which are typically observed in subduction settings. Using a combination of techniques, including major element mapping, isotope analysis of various mineral phases, and a petrochemical model, the study reconstructs fluid transfer and interactions within a multi-rock outcrop scenario. The 3D investigation provides detailed insights into the metasomatic processes that affected the region, contributing to a deeper understanding of how fluids behave in subduction zones.

Chapter 5: Garnet porphyroblast analysis in 2D to 3D: Insights for major to trace element zoning in blueschists-facies rocks from Syros

This chapter consists of an article to be edited and submitted to the Journal of Petrology. Pierre Lanari is a co-author.

This chapter presents an in-depth analysis of garnet porphyroblasts in blueschist-facies rocks from Syros, focusing on prophyroblast shapes and their major to trace element zoning. This is achieved by using a combination of 2D and 3D techniques, including µCT and LA-ICP-MS mapping. The outcome of the study is the reconstruction of the growth history and chemical evolution of garnet porphyroblasts. The analysis reveals zoning patterns that reflect the metamorphic conditions during garnet growth, providing key insights into the pressure-temperature (P-T) evolution and fluid interactions in subduction zone environments. By integrating 3D data, the chapter highlights the complexities of garnet growth and how it can be used to trace fluid-related processes in high-pressure metamorphic rocks.

Bibliography

Ague, J. J., & Nicolescu, S. (2014). Carbon dioxide released from subduction zones by fluid-mediated reactions. *Nature Geoscience*, *7*(5), 355–360. https://doi.org/10.1038/ngeo2143

Baxter, E. F., & Caddick, M. J. (2013). Garnet growth as a proxy for progressive subduction zone dehydration. *Geology*, *41*(6), 643–646. https://doi.org/10.1130/G34004.1

Bebout, G. E. (2007). Metamorphic chemical geodynamics of subduction zones. *Earth and Planetary Science Letters*, *260*(3-4), 373–393. https://doi.org/10.1016/j.epsl.2007.05.050

Bebout, G. E., & Penniston-Dorland, S. C. (2016). Fluid and mass transfer at subduction interfaces-The field metamorphic record. *Lithos*, *240-243*, 228–258. https://doi.org/10.1016/j.lithos.2015.10.007

Caddick, M. J., Konopásek, J., & Thompson, A. B. (2010). Preservation of garnet growth zoning and the duration of prograde metamorphism. *Journal of Petrology*, *51*(11), 2327–2347. https://doi.org/10.1093/petrology/egq059

Carlson, W. D. (2011). Porphyroblast crystallization: linking processes, kinetics, and microstructures. *International Geology Review*, *53*(3-4), 406–445. https://doi.org/10.1080/00206814.2010.496184

Carlson, W. D., & Denison, C. (1992). Mechanisms of Porphyroblast Crystallization: Results from High-Resolution Computed X-ray Tomography. *Science*, *257*(5074), 1236–1239. https://doi.org/10.1126/science.257.5074.1236

Chabala, J., Soni, K., Li, J., Gavrilov, K., & Levi-Setti, R. (1995). High-resolution chemical imaging with scanning ion probe SIMS. *International Journal of Mass Spectrometry and Ion Processes*, *143*(100), 191–212. https://doi.org/10.1016/0168-1176(94)04119-R

Connolly, J. A. (1997). Devolatilization-generated fluid pressure and deformation-propagated fluid flow during prograde regional metamorphism. *Journal of Geophysical Research: Solid Earth*, *102*(B8), 18149–18173. https://doi.org/10.1029/97JB00731

Connolly, J. A. (2010). The Mechanics of Metamorphic Fluid Expulsion. *Elements*, *6*(3), 165–172. https://doi.org/10.2113/gselements.6.3.165

Connolly, J. A., & Podladchikov, Y. Y. (1998). Compaction-driven fluid flow in viscoelastic rock. *Geodinamica Acta*, *11*(2-3), 55–84. https://doi.org/10.1080/09853111.1998.11105311

Dempster, T. J. (1985). Garnet zoning and metamorphism of the Barrovian type area, Scotland. *Contributions to Mineralogy and Petrology*, *89*(1), 30–38. https://doi.org/10.1007/BF01177588

Denison, C., & Carlson, W. D. (1997). Three-dimensional quantitative textural analysis of metamorphic rocks using high-resolution computed X-ray tomography: Part II. Application to natural samples. *Journal of Metamorphic Geology*, *15*(1), 45–57. https://doi.org/10.1111/j.1525-1314.1997.00007.x

Gaidies, F., Milke, R., Heinrich, W., & Abart, R. (2017, March). Metamorphic mineral reactions: Porphyroblast, corona and symplectite growth. In *Mineral reaction kinetics: Microstructures, textures, chemical and isotopic signatures* (pp. 469–540, Vol. 16). Mineralogical Society of Great Britain & Ireland. https://doi.org/10.1180/EMU-notes.16.14

Gaidies, F., Morneau, Y. E., Petts, D. C., Jackson, S. E., Zagorevski, A., & Ryan, J. J. (2021). Major and trace element mapping of garnet: Unravelling the conditions, timing and rates of metamorphism of the Snowcap assemblage, west-central Yukon. *Journal of Metamorphic Geology*, *39*(2), 133–164. https://doi.org/10.1111/jmg.12562

George, F. R., Gaidies, F., & Boucher, B. (2018). Population-wide garnet growth zoning revealed by LA-ICP-MS mapping: implications for trace element equilibration and syn-kinematic deformation during crystallisation. *Contributions to Mineralogy and Petrology*, *173*(9), 1–22. https://doi.org/10.1007/s00410-018-1503-0

Gies, N. B., Konrad-Schmolke, M., & Hermann, J. (2024). Modeling the Global Water Cycle—The Effect of Mg-Sursassite and Phase a on Deep Slab Dehydration and the Global Subduction Zone Water Budget. *Geochemistry, Geophysics, Geosystems*, *25*(3). https://doi.org/10.1029/2024GC011507

Hacker, B. R. (2008). H2O subduction beyond arcs. *Geochemistry, Geophysics, Geosystems*, *9*(3). https://doi.org/10.1029/2007GC001707

Hacker, B. R., Abers, G. A., & Peacock, S. M. (2003). Subduction factory 1. Theoretical mineralogy, densities, seismic wave speeds, and H 2 O contents. *Journal of Geophysical Research: Solid Earth*, *108*(B1), 1–26. https://doi.org/10.1029/2001JB001127

Hacker, B. R., Peacock, S. M., Abers, G. A., & Holloway, S. D. (2003). Subduction factory 2. Are intermediate-depth earthquakes in subducting slabs linked to metamorphic dehydration reactions? *Journal of Geophysical Research: Solid Earth*, *108*(B1). https://doi.org/10.1029/2001JB001129

Hermann, J. (2003). Experimental evidence for diamond-facies metamorphism in the Dora-Maira massif. *Lithos*, *70*(3-4), 163–182. https://doi.org/10.1016/S0024-4937(03)00097-5

Hermann, J., Spandler, C., Hack, A., & Korsakov, A. V. (2006). Aqueous fluids and hydrous melts in high-pressure and ultra-high pressure rocks: Implications for element transfer in subduction zones. *Lithos*, *92*(3-4), 399–417. https://doi.org/10.1016/j.lithos.2006.03.055

Hess, H. H. (1962). History of Ocean Basins. In *Petrologic studies*. Geological Society of America. https://doi.org/10.1130/Petrologic.1962.599

Hickmott, D. (1988). Trace element zoning in garnets: implications for metamorphic petrogenesis.

Hickmott, D., & Spear, F. S. (1992). Major-and trace-element zoning in garnets from calcareous pelites in the NW shelburne falls Quadrangle, Massachusetts: Garnet growth histories in retrograded rocks. *Journal of Petrology*, *33*(5), 965–1005. https://doi.org/10.1093/petrology/33.5.965

Hollister, L. S. (1966). Garnet Zoning: An Interpretation Based on the Rayleigh Fractionation Model. *Science*, *154*(3757), 1647–1651. https://doi.org/10.1126/science.154.3757.1647

Hoover, W. F., Penniston-Dorland, S., Baumgartner, L., Bouvier, A.-S., Dragovic, B., Locatelli, M., Angiboust, S., & Agard, P. (2022). Episodic fluid flow in an eclogite-facies shear zone: Insights from Li isotope zoning in garnet. *Geology*, *50*(6), 746–750. https://doi.org/10.1130/G49737.1

Ito, E., Stern, R. J., & Douthitt, C. (2003). Insights into operation of the subduction factory from the oxygen isotopic values of the southern Izu–Bonin–Mariana Arc. *Island Arc*, *12*(4), 383–397. https://doi.org/10.1046/j.1440-1738.2003.00408.x

John, T., Gussone, N., Podladchikov, Y. Y., Bebout, G. E., Dohmen, R., Halama, R., Klemd, R., Magna, T., & Seitz, H.-M. (2012). Volcanic arcs fed by rapid pulsed fluid flow through subducting slabs. *Nature Geoscience*, *5*(7), 489–492. https://doi.org/10.1038/ngeo1482

Kerrick, D., & Connolly, J. A. (2001). Metamorphic devolatilization of subducted oceanic metabasalts: implications for seismicity, arc magmatism and volatile recycling. *Earth and Planetary Science Letters*, *189*(1-2), 19–29. https://doi.org/10.1016/S0012-821X(01)00347-8

Kirby, S. H., Stein, S., Okal, E. A., & Rubie, D. C. (1996). Metastable mantle phase transformations and deep earthquakes in subducting oceanic lithosphere. *Reviews of Geophysics*, *34*(2), 261–306. https://doi.org/10.1029/96RG01050

Kita, S., Okada, T., Nakajima, J., Matsuzawa, T., & Hasegawa, A. (2006). Existence of a seismic belt in the upper plane of the double seismic zone extending in the along-arc direction at depths of 70–100 km beneath NE Japan. *Geophysical Research Letters*, *33*(24), 1–5. https://doi.org/10.1029/2006GL028239

Konrad-Schmolke, M., Babtist, J., Handy, M. R., & O'Brien, P. J. (2006). The Physico-Chemical Properties of a Subducted Slab from Garnet Zonation Patterns (Sesia Zone, Western Alps). *Journal of Petrology*, *47*(11), 2123–2148. https://doi.org/10.1093/petrology/egl039

Konrad-Schmolke, M., Halama, R., Chew, D., Heuzé, C., De Hoog, J. C. M., & Ditterova, H. (2023). Discrimination of thermodynamic and kinetic contributions to the heavy rare earth element patterns in metamorphic garnet. *Journal of Metamorphic Geology*, *41*(4), 465–490. https://doi.org/10.1111/jmg.12703

Konrad-Schmolke, M., Zack, T., O'Brien, P. J., & Barth, M. (2011). Fluid migration above a subducted slab - Thermodynamic and trace element modelling of fluid-rock interaction in partially overprinted eclogite-facies rocks (Sesia Zone, Western Alps). *Earth and Planetary Science Letters*, *311*(3-4), 287–298. https://doi.org/10.1016/j.epsl.2011.09.025

Kretz, R. (1993). A garnet population in Yellowknife schist, Canada. *Journal of Metamorphic Geology*, *11*(1), 101–120. https://doi.org/10.1111/j.1525-1314.1993.tb00134.x

Lanari, P., Ferrero, S., Goncalves, P., & Grosch, E. G. (2019). Metamorphic geology: Progress and perspectives. *Geological Society Special Publication*, *478*(1), 1–12. https://doi.org/10.1144/SP478-2018-186

Malvoisin, B., Podladchikov, Y. Y., & Vrijmoed, J. C. (2015). Coupling changes in densities and porosity to fluid pressure variations in reactive porous fluid flow: Local thermodynamic equilibrium. *Geochemistry, Geophysics, Geosystems*, *16*(12), 4362–4387. https://doi.org/10.1002/2015GC006019

Manning, C. E. (2004). The chemistry of subduction-zone fluids. *Earth and Planetary Science Letters*, *223*(1-2), 1–16. https://doi.org/10.1016/j.epsl.2004.04.030

Martin, L. A. J., Hermann, J., Gauthiez-Putallaz, L., Whitney, D. L., Vitale Brovarone, A., Fornash, K. F., & Evans, N. J. (2014). Lawsonite geochemistry and stability – implication for trace element and water cycles in subduction zones. *Journal of Metamorphic Geology*, *32*(5), 455–478. https://doi.org/10.1111/jmg.12093

McKenzie, D. P., & Parker, R. L. (1967). The North Pacific · an Example of Tectonics on a Sphere. *Nature*, *216*, 1276–1280.

Morgan, W. J. (1968). Rises, trenches, great faults, and crustal blocks. *Journal of Geophysical Research (1896-1977)*, *73*(6), 1959–1982. https://doi.org/https://doi.org/10.1029/JB073i006p01959

Morishige, M., & van Keken, P. E. (2018). Fluid Migration in a Subducting Viscoelastic Slab. *Geochemistry, Geophysics, Geosystems*, *19*(2), 337–355. https://doi.org/10.1002/2017GC007236

Page, F. Z., Essene, E. J., Mukasa, S. B., & Valley, J. W. (2014). A garnet-zircon oxygen isotope record of subduction and exhumation fluids from the Franciscan complex, California. *Journal of Petrology*, *55*(1), 103–131. https://doi.org/10.1093/petrology/egt062

Paton, C., Hellstrom, J., Paul, B., Woodhead, J. D., & Hergt, J. (2011). Iolite: Freeware for the visualisation and processing of mass spectrometric data. *Journal of Analytical Atomic Spectrometry*, *26*(12), 2508–2518. https://doi.org/10.1039/c1ja10172b

Pattison, D. R., & Tinkham, D. K. (2009). Interplay between equilibrium and kinetics in prograde metamorphism of pelites: An example from the Nelson aureole, British Columbia. *Journal of Metamorphic Geology*, *27*(4), 249–279. https://doi.org/10.1111/j.1525-1314.2009.00816.x

Paul, B., Woodhead, J. D., Paton, C., Hergt, J. M., Hellstrom, J., & Norris, C. A. (2014). Towards a Method for Quantitative LA-ICP-MS Imaging of Multi-Phase Assemblages: Mineral Identification and Analysis Correction Procedures. *Geostandards and Geoanalytical Research*, *38*(3), 253–263. https://doi.org/10.1111/j.1751-908X.2014.00270.x

Peacock, S. M. (1996, March). Thermal and Petrologic Structure of Subduction Zones. In *Geophysical monograph series* (pp. 119–133, Vol. 96). https://doi.org/10.1029/GM096p0119

Peacock, S. M. (2009). Thermal and metamorphic environment of subduction zone episodic tremor and slip. *Journal of Geophysical Research*, *114*(8), B00A07. https://doi.org/10.1029/2008JB005978

Peacock, S. M., & Wang, K. (1999). Seismic Consequences of Warm Versus Cool Subduction Metamorphism: Examples from Southwest and Northeast Japan. *Science*, *286*(5441), 937–939. https://doi.org/10.1126/science.286.5441.937

Philippot, P., & Selverstone, J. (1991). Trace-element-rich brines in eclogitic veins: implications for fluid composition and transport during subduction. *Contributions to Mineralogy and Petrology*, *106*(4), 417–430. https://doi.org/10.1007/BF00321985

Plümper, O., John, T., Podladchikov, Y. Y., Vrijmoed, J. C., & Scambelluri, M. (2017). Fluid escape from subduction zones controlled by channel-forming reactive porosity. *Nature Geoscience*, *10*(2), 150–156. https://doi.org/10.1038/ngeo2865

Poli, S., & Schmidt, M. W. (2002). Petrology of Subducted Slabs. *Annual Review of Earth and Planetary Sciences*, *30*(1), 207–235. https://doi.org/10.1146/annurev.earth.30.091201.140550

Raimondo, T., Clark, C., Hand, M., Cliff, J., & Harris, C. (2012). High-resolution geochemical record of fluid-rock interaction in a mid-crustal shear zone: A comparative study of major element and oxygen isotope transport in garnet. *Journal of Metamorphic Geology*, *30*(3), 255–280. https://doi.org/10.1111/j.1525-1314.2011.00966.x

Rubatto, D., & Angiboust, S. (2015). Oxygen isotope record of oceanic and high-pressure metasomatism: a P–T–time–fluid path for the Monviso eclogites (Italy). *Contributions to Mineralogy and Petrology*, *170*(5-6), 44. https://doi.org/10.1007/s00410-015-1198-4

Schmidt, M. W., & Poli, S. (2014). Devolatilization During Subduction. In *Treatise on geochemistry* (2nd ed., pp. 669–701, Vol. 4). Elsevier. https://doi.org/10.1016/B978-0-08-095975-7.00321-1

Schmidt, M. W., & Poli, S. (1998). Experimentally based water budgets for dehydrating slabs and consequences for arc magma generation. *Earth and Planetary Science Letters*, *163*(1-4), 361–379. https://doi.org/10.1016/S0012-821X(98)00142-3

Schmidt, M. W., & Poli, S. (2003). Generation of Mobile Components during Subduction of Oceanic Crust. In *Treatise on geochemistry* (pp. 567–591, Vol. 3-9). Elsevier. https://doi.org/10.1016/B0-08-043751-6/03034-6

Schwandt, G. S., Papke, J. J., & Shearer, C. K. (1996). Trace element zoning in pelitic garnet of the Black Hills, South Dakota. *American Mineralogist*, *81*(9-10), 1195–1207. https://doi.org/10.2138/am-1996-9-1018

Shiina, T., Nakajima, J., & Matsuzawa, T. (2013). Seismic evidence for high pore pressures in the oceanic crust: Implications for fluid-related embrittlement. *Geophysical Research Letters*, *40*(10), 2006–2010. https://doi.org/10.1002/grl.50468

Spandler, C., & Hermann, J. (2006). High-pressure veins in eclogite from New Caledonia and their significance for fluid migration in subduction zones. *Lithos*, *89*(1-2), 135–153. https://doi.org/10.1016/j.lithos.2005.12.003

Spandler, C., Pettke, T., & Rubatto, D. (2011). Internal and external fluid sources for eclogite-facies veins in the Monviso Meta-ophiolite, Western Alps: Implications for fluid flow in subduction zones. *Journal of Petrology*, *52*(6), 1207–1236. https://doi.org/10.1093/petrology/egr025

Spandler, C., & Pirard, C. (2013). Element recycling from subducting slabs to arc crust: A review. *Lithos*, *170-171*, 208–223. https://doi.org/10.1016/j.lithos.2013.02.016

Strating, E., & Vissers, R. (1991). Dehydration-induced fracturing of eclogite-facies peridotites: Implications for the mechanical behaviour of subducting oceanic lithosphere. *Tectonophysics*, *200*(1-3), 187–198. https://doi.org/10.1016/0040-1951(91)90014-J

Syracuse, E. M., van Keken, P. E., & Abers, G. A. (2010). The global range of subduction zone thermal models. *Physics of the Earth and Planetary Interiors*, *183*(1-2), 73–90. https://doi.org/10.1016/j.pepi.2010.02.004

Taetz, S., John, T., Bröcker, M., Spandler, C., & Stracke, A. (2018). Fast intraslab fluid-flow events linked to pulses of high pore fluid pressure at the subducted plate interface. *Earth and Planetary Science Letters*, *482*, 33–43. https://doi.org/10.1016/j.epsl.2017.10.044

Tatsumi, Y. (2005). The subduction factory: How it operates in the evolving Earth. *GSA Today*, *15*(7), 4–10. https://doi.org/10.1130/1052-5173(2005)015[4:TSFHIO]2.0.CO;2

Tracy, R. J., Robinson, P., & Thompson, A. B. (1976). Garnet composition and zoning in the determination of temperature and pressure of metamorphism, central Massachusetts. *American Mineralogist*, *61*(7-8), 762–775.

Tsujimori, T., Sisson, V. B., Liou, J. G., Harlow, G. E., & Sorensen, S. S. (2006). Very-low-temperature record of the subduction process: A review of worldwide lawsonite eclogites. *Lithos*, *92*(3-4), 609–624. https://doi.org/10.1016/j.lithos.2006.03.054

Ulrich, M., Rubatto, D., Hermann, J., Markmann, T. A., Bouvier, A.-s., & Deloule, E. (2024). Olivine formation processes and fluid pathways in subducted serpentinites revealed by in-situ oxygen isotope analysis (Zermatt-Saas, Switzerland). *Chemical Geology*, *649*(November 2023), 121978. https://doi.org/10.1016/j.chemgeo.2024.121978

Van Keken, P. E., Kiefer, B., & Peacock, S. M. (2002). High-resolution models of subduction zones: Implications for mineral dehydration reactions and the transport of water into the deep mantle. *Geochemistry, Geophysics, Geosystems*, *3*(10). https://doi.org/10.1029/2001GC000256

Vesin, C., Rubatto, D., & Pettke, T. (2024). The history of serpentinisation at mid-ocean ridges: Insights from in situ trace elements coupled with oxygen and boron isotopes. *Chemical Geology*, *654*(March), 122060. https://doi.org/10.1016/j.chemgeo.2024.122060

Vho, A., Lanari, P., Rubatto, D., & Hermann, J. (2020). Tracing fluid transfers in subduction zones: an integrated thermodynamic and δ18O fractionation modelling approach. *Solid Earth*, *11*(2), 307–328. https://doi.org/10.5194/se-11-307-2020

Warren, C. J. (2013). Exhumation of (ultra-)high-pressure terranes: Concepts and mechanisms. *Solid Earth*, *4*(1), 75–92. https://doi.org/10.5194/se-4-75-2013

Wegener, A. (1912). Die Entstehung der Kontinente. *Geologische Rundschau*, *3*(4), 276–292. https://doi.org/10.1007/BF02202896

Whitney, D. L., Fornash, K. F., Kang, P., Ghent, E. D., Martin, L., Okay, A. I., & Vitale Brovarone, A. (2020). Lawsonite composition and zoning as tracers of subduction processes: A global review. *Lithos*, *370-371*, 105636. https://doi.org/10.1016/j.lithos.2020.105636

Wilson, C. R., Spiegelman, M., van Keken, P. E., & Hacker, B. R. (2014). Fluid flow in subduction zones: The role of solid rheology and compaction pressure. *Earth and Planetary Science Letters*, *401*, 261–274. https://doi.org/10.1016/j.epsl.2014.05.052

Woodhead, J. D., Hellstrom, J., Hergt, J. M., Greig, A., & Maas, R. (2007). Isotopic and Elemental Imaging of Geological Materials by Laser Ablation Inductively Coupled Plasma-Mass Spectrometry. *Geostandards and Geoanalytical Research*, *31*(4), 071117031212003–??? https://doi.org/10.1111/j.1751-908X.2007.00104.x

Woodhead, J. D., Hellstrom, J., Paton, C., Hergt, J., Greig, A., & Maas, R. (2008). A guide to depth profiling and imaging applications of ICP-MS. *Mineralogical Association of Canada short course series*, (40), 135–145.

Yang, P., & Rivers, T. (2001). Chromium and manganese zoning in pelitic garnet and kyanite: Spiral, overprint, and oscillatory (?) zoning patterns and the role of growth rate. *Journal of Metamorphic Geology*, *19*(4), 455–474. https://doi.org/10.1046/j.0263-4929.2001.00323.x

Yang, P., & Rivers, T. (2002). The origin of Mn and Y annuli in garnet and the thermal dependence of P in garnet and Y in apatite in calc-pelite and pelite, Gagnon terrane, western Labrador. *American Mineralogist*, *88*(8-9), 1398.

Zack, T., & John, T. (2007). An evaluation of reactive fluid flow and trace element mobility in subducting slabs. *239*, 199–216. https://doi.org/https://doi.org/10.1016/j.chemgeo.2006.10.020

Zheng, Y. F. (2019). Subduction zone geochemistry. *Geoscience Frontiers*, *10*(4), 1223–1254. https://doi.org/10.1016/j.gsf.2019.02.003

Zheng, Y. F., Chen, R. X., Xu, Z., & Zhang, S. B. (2016). The transport of water in subduction zones. *Science China Earth Sciences*, *59*(4), 651–682. https://doi.org/10.1007/s11430-015-5258-4

Chapter 2

Multi-phase quantitative compositional mapping by LA-ICP-MS: analytical approach and data reduction protocol implemented in XMapTools

Abstract

Mapping of trace element signatures is an expanding tool in geoscience and material sciences, which allows the study of solid materials, and processes that may not be captured by major elements. Developments in laser-ablation inductively-coupled-plasma mass-spectrometry (LA-ICP-MS) capabilities in the last decade now provide the necessary spatial resolution for in situ element mapping. The acquisition of two-dimensional, fully quantitative and geologically meaningful data with LA-ICP-MS is still a challenging task, and a particular obstacle is the calibration of inhomogeneous phases, such as chemically zoned minerals. This work presents a novel approach to data reduction and image generation for multi-element mapping employing LA-ICP- quadrupole MS (LA-ICP-QMS), implemented in the free and open-source software XMapTools. Three geological applications are presented to illustrate the benefits of the procedures. Garnet from an eclogitic sample (Latto Hills, Togo) and plagioclase, k-feldspar, biotite from a migmatite sample (El Oro Complex, Ecuador) were mapped multiple times at different spatial resolutions to test the calibration quality and chemical detection capabilities. Rutile in a metapelite sample (Val Malenco, Italian Alps) was mapped, and Zr-in-rutile thermometry shows a temperature range of 510 to 550 °C within a single grain. The accuracy of the LA-ICP-MS method was verified by comparison with zoned major and minor element maps (garnet, plagioclase) and Ti-in-biotite geothermometry maps obtained by electron probe microanalysis (EPMA). A spatial resolution of up to 5 µm is achieved with LA-ICP-QMS, which is similar to the resolution reported for LA-ICP time-of-flight mass spectrometry (LA-ICP-TOFMS), albeit at significantly lower acquisition speed. Maps with lower spatial resolution offer better chemical detection power as demonstrated by lower per-pixel limit of detection (LOD) map calculation. Moreover, such maps are also recorded faster. The pixel allocation strategy and the instrumental conditions also have a direct impact on map quality. We recommend that maps are interpolated to square pixels, where a pixel consists of multiple sweeps to gain an improved detection power. Benchmarks using an emulated LA-ICP-MS mapping show that the spot size, together with scan direction, can lead to a shift in composition depending on the feature size of chemical patterns. This is verified by mapping a thin <50 µm annulus in garnet visible in REE and such compositional shifts can have a significant impact on e.g., diffusion modelling. The new software solution provides a multi-standard and variable composition calibration of LA-ICP-MS maps with single pixel LOD filtering at 95% confidence, allowing the user to quantify inhomogeneous materials of major and trace elements simultaneously with improved accuracy.

2.1 Introduction

The use of Laser-Ablation Inductively-Coupled-Plasma Mass Spectrometry (LA-ICP-MS) mapping has increased dramatically over the past decade, especially for in situ (semi-) quantification of major, minor and trace element compositions of geological materials (Phillips et al., 2023; Raimondo et al., 2017; Rubatto et al., 2020; Ubide et al., 2015; Ulrich et al., 2009). LA-ICP-MS is commonly used for single-spot measurements where the signal is integrated over the ablation crater, which is approximately 10–30 µm deep. Spot locations can be determined using surface imaging techniques that capture the uppermost few micrometers of the sample only. The homogeneity of the sample with depth remains unknown except for transmitted light microscopy inspection for the presence of inclusions or cracks; however, the transient signal acquired in single spot mode offers information on whether sample composition is homogeneous down the ablated crater depth. An alternative strategy is to use line scanning instead of single spots to collect intensity data that can be calibrated to produce chemical maps (Paton et al., 2011; Woodhead et al., 2007, 2008). Although quantitative compositional mapping is common for other instruments such as electron probe micro-analysis (EPMA) (e.g., Lanari et al., 2019), the analytical protocol development for LA-ICP-MS mapping is much less advanced. This is due to both analytical and data reduction challenges. Developing an analytical protocol implemented in publicly available software for broader use can therefore help to advance the applicability of LA-ICP-MS mapping methods and, for example, reveal previously unseen details missed by single spot data acquisition routines.

Most LA-ICP-MS systems in geological laboratories can be used for mapping, provided an automated sample stage with µm resolution and $\leq$ 2 µm positioning accuracy is available. A simple mapping protocol can be easily implemented as it requires little sample preparation, and several analytical strategies are available (Ubide et al., 2015; Ulrich et al., 2009). The number of elements analyzed in mapping mode with a quadrupole can reach well over 30 with best detection capabilities at the sub-µg/g level within measurement times >4 hours (Lanari & Piccoli, 2020; Raimondo et al., 2017). More complex techniques have also been developed to address the limitations of the approach, particularly in terms of spatial resolution. For example, custom-designed systems have been used to resolve single-pulse signals by combining ultrafast laser cells with specific data processing algorithms to achieve sub-spot resolution (Fox et al., 2017; Plotnikov et al., 2008; Van Malderen et al., 2015). This allows the study of synchronization problems between the pulsed laser ablation and the ICP-MS signal recording processes, known as aliasing, as well as artefacts such as blurring and smearing (Gundlach-Graham & Günther, 2016; Norris et al., 2021; Pettke et al., 2000; van Elteren et al., 2019). However, such analytical setups are usually limited to a more restricted number of elements and often require longer measurement times (e.g.,

Fox et al., 2017). Quantitative compositional mapping using laser ablation time-of-flight MS (LA-ICP-TOFMS) extends the application to higher spatial resolution, faster measurement and a larger set of elements to be measured in one experiment, albeit at higher limits of detection (LOD; Rubatto et al. (2020) and Savard et al. (2023)).

Regardless of the measurement protocol chosen, a software solution is required for data reduction and processing of LA-ICP-MS maps. Several software solutions exist in the geochemical community (see Chew et al., 2021, for a review). All provide basic tools for converting the raw signal into element intensity maps in X–Y space. This step requires a background correction, followed by a drift correction using the intensity of a known reference material. The maps can be calibrated using an external and internal standardization procedure, provided that an elemental composition for a single mineral can be fixed to a spatially constant value as an internal standard and the composition of the same element in a well-characterized calibration material is known as an external standard (see Table 2.1 for definitions). However, most natural materials like minerals show compositional zoning (e.g., Tracy, 1982) or do not have an element with a constant stoichiometry (e.g., amphiboles, phyllosilicates, feldspars, spinel), necessitating a new solution for internal calibration. After calibration, the map data can be displayed in various chemical diagrams (Lanari & Piccoli, 2020; Raimondo et al., 2017). The most popular software solution for the construction and calibration of LA-ICP-MS maps is the commercial software IOLITE (Paton et al., 2011) with the add-ons CellSpace (Paul et al., 2012) and Monocle (Petrus et al., 2017). Quantitative maps generated with IOLITE can be imported into XMapTools (Lanari et al., 2014, 2019) for further transformations and data visualization (Lanari & Piccoli, 2020; Raimondo et al., 2017; Rubatto et al., 2020). To date, there is no free open source software that can create intensity maps, perform pixel classification, and offer quantification of element maps that are rigorously filtered for the LOD for each individual pixel. This contribution presents a new measurement routine for quantitative compositional mapping by LA-ICP quadrupole MS (LA-ICP-QMS). An advanced data reduction environment is provided to process and calibrate the raw data embedded in the open-source and free software solution XMapTools (Lanari et al., 2023). The procedure involves the guided generation of intensity maps from time-resolved signals using an interpolation approach. Quantified elemental data for individual pixels are obtained by using an external standardization protocol combined with variable mass fractions of the element used for internal standardization, a previously unavailable prerequisite for minerals of variable compositions. The proposed procedure includes a rigorous calculation of the LOD for individual pixels. Three examples from metamorphic rocks are used to demonstrate the potential of this method for petrological applications.

Term	Definition
Acquisition time	Total time of backgrounds and scan times for a given map.
Background	Gas blank measurement usually around 30 to 50 s. This accounts for 11 to 30% of the total acquisition time (see text).
Dwell time	Net measurement time on one analyte (in s).
External standard	Material of known composition used for measurement calibration following the IUPAC definition after Ettre (1993).
Fluence	On-sample surface energy density (in J/cm^2).
Internal standard	A known element concentration in the sample used to convert apparent element concentrations obtained from external standardization into true sample element concentrations following the IUPAC definition after Ettre (1993).
Detector settling time	The time needed by the detector to go from one mass to the next in the element list.
Mask	Selection of an area of pixels by a particular shape.
Analyte	Isotope and element of interest set to measure in an element list in the ICP-MS software corresponds to the m/z ratio of analyte = dalton.
Pixel	The spatial information of one value such as a concentration assigned in X-Y space.
Pulse	Application of the laser optical power for a duration on the sample.
Repetition rate	The number of laser pulses emitted per second (in Hz).
Region of interest (ROI)	An area of several pixels of interest sampled from the dataset.
Scan	Laser sampling in line scan mode.
Scan time	Time that laser is ablating and ICP-MS is recording.
Secondary standard	A reference material of known composition used for quality control purpose by comparison with a primary standard.
Spot	The shape of the laser beam here as a circular aperture (in µm).
Sweep	The acquisition of one full sequence of analytes in transient signal mode.
Sweep time	Total time in s required to measure all the analytes in sequence once.
Transient raw signal	The raw data output as one continuous time-resolved record of analyte signal intensities.

Table 2.1: Definition of terms used in the text.

2.2 Methods

2.2.1 Data acquisition

Time resolved analysis resolution

The sweep time of a given acquisition method, controls the time resolved analysis resolution in a transient signal of a line scan. For LA-ICP-QMS, if long element lists are needed (>20 elements), the dwell times should be as short as possible to reduce artefacts caused by non-representative sampling (e.g., Pettke et al., 2000), and long enough to detect the element of interest. For a given element (i), the LOD can be calculated following Pettke et al. (2012):

$$\mathrm{LOD}_i = \frac{3.29\sqrt{\overline{I_i^{\mathrm{Bkg}}} \cdot DT_i \cdot \left(1 + \frac{N_i}{N_{\mathrm{bkg}}}\right)} + 2.71}{N_i \cdot DT_i \cdot S_i} \tag{2.2.1}$$

where $\overline{I_i^{\mathrm{Bkg}}}$ is the mean intensity of the background (cps), DT_i the dwell time (s), N_{bkg} the number of sweeps for the background measurement, S_i the sensitivity of analyte i (in cps per μg/g of material), and N_i the number of sweeps for the measurement of the analyte in the sample. The numerical coefficients 2.71 and 3.29 relate to 5% probabilities of false positive and false negative detections as derived from a Poisson distribution (Pettke et al., 2012). The sensitivity S_i of the analyte is defined after Longerich et al. (1996):

$$S_i = \frac{I^{\mathrm{int}}_{\mathrm{unk}} \cdot C^{\mathrm{int}}_{\mathrm{std}} \cdot I^{i}_{\mathrm{std}}}{C^{i}_{\mathrm{std}} \cdot I^{\mathrm{int}}_{\mathrm{std}} \cdot C^{\mathrm{int}}_{\mathrm{unk}}} \tag{2.2.2}$$

with I as the intensity (cps) and c as the mass fraction (μg/g) of the internal standard element (int) in the external standard (std) and the unknown sample (unk). Increasing the dwell time and/or the number of sweeps of an element (i) results in a decrease of the LOD, keeping all other parameters unchanged.

Spatial resolution

The spatial resolution of the signal in X and Y directions are different and depend on the scanning direction (vertical or horizontal). Perpendicular to the scan direction, the spatial resolution is controlled by the beam diameter, while along the scan direction it is controlled by the number of overlapping pulses. This number is determined by the repetition rate, which is the product of the scan speed and the sweep time (Fig. 2.1). The scan speed v (expressed in μg/s) can be calculated as:

$$v = \frac{d}{n \cdot t_{\mathrm{acq}}} \tag{2.2.3}$$

where d is the beam diameter (in μg), t_{acq} is the sweep time (in s), and n is the number of sweeps measured over a scan distance equal to the beam diameter. The spatial resolution along the scan direction is therefore directly proportional to the number of sweeps per scan distance. Fast scan speed is obtained for $n = 1$, corresponding to a single sweep acquired during a scan distance equal to the beam diameter (Fig. 2.1a). If n is greater than 1, more than one sweep is acquired for a scan distance equal to the beam diameter (Fig. 2.1b), resulting in a higher spatial resolution along the scan direction. Spatial resolution is thus inversely proportional to scan speed, keeping all other parameters constant. At high scan speeds ($v > \frac{d}{t_{\mathrm{acq}}}$) it is also to consider that the analytes are measured sequentially, the sweep and simultaneous stage motion results in a small shift of the spatial reference between the successively analyzed analytes (Norris et al., 2021; Raimondo et al., 2017).

The compositional information of a given map is provided for each pixel individually that compose the map. The spatial resolution of the final map is defined by the pixel size.

This differs from the spatial resolution of the signal discussed above. Different strategies can be used to convert the measured signal into pixel values. The first strategy is to assign an intensity value to a pixel for each sweep between the start and end positions during the scan. Square pixels are obtained if $n = 1$ (Fig. 2.1a) and rectangular pixels if $n > 1$ (Fig. 2.1b). This strategy is simple to implement and is used in IOLITE (Paton et al., 2011). Here, for circular laser beams, the material ablated in the outside half-circle at the start and end positions of the sweep is incorrectly included in the pixel value (Fig. 2.1b-c). A similar problem would occur if a square or rectangular beam shape were used. The second strategy is to apply oversampling in one or two dimensions and, additionally, signal deconvolution to reconstruct the true pixel intensity values from all individual measurements (van Elteren et al., 2021). This method offers a more accurate spatial resolution in the map, but has the limitation that the deconvolution process can lead to an increase in the signal uncertainty and therefore affect the precision of the measurement (van Elteren et al., 2021). The third strategy — the one developed here — is to use interpolation methods to transform the intensity signal into maps of square pixels using a value of n that is greater than 1. A circular beam is used here because the energy density is more homogeneous for circular beams for laser systems relying on focusing (and not imaging) optics. In addition, the circular beam shape translates into a rectangular area when scanning in line direction (Fig. 2.1). Scanning over features that are smaller than the beam size will inevitably cause spatial resolution problems for either circular or rectangular beam shapes (see discussion).

Measurement of unknowns and standard materials

The map area of the sample is usually selected based on BSE images or composition maps obtained by EPMA. This area is scanned with horizontal or vertical lines, which are lined up touching each other. Ideally the scanning direction is perpendicular to the compositional features, offering better spatial resolution in the compositional map. A minimum resolution of 10,000 pixels (i.e., 100×100 pixels) is recommended for each map measured by LA-ICP-MS (Lanari2020). The external and secondary standards used for calibration and quality control need to be scanned frequently to properly monitor instrumental drift (e.g., Longerich et al., 1996). In the proposed protocol, calibration is performed at least every 30 minutes at the exact same instrumental and data acquisition parameters. A minimum number of 100 sweeps for one line scan on the standard material is used to ensure a statistically meaningful measurement. The length of the line scan on the standard material is determined by the scanning speed and therefore the number of analytes and their dwell times (Eq. 2.2.3). In other studies, spot measurements were used to calibrate maps (George et al., 2018).

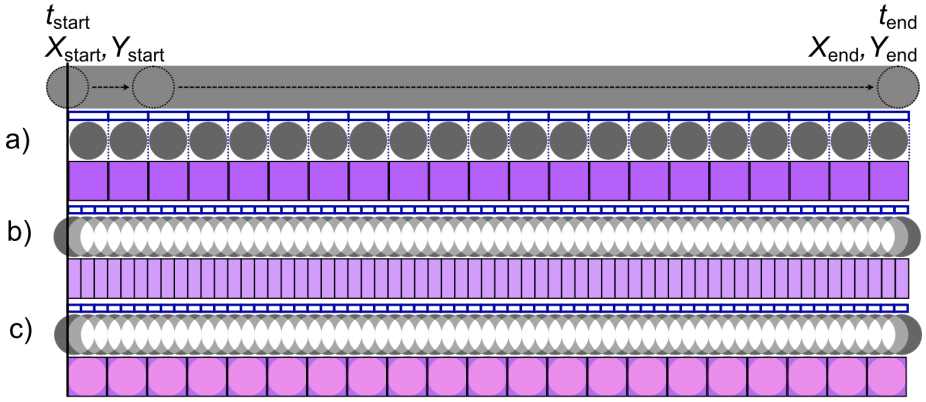

Figure 2.1: Continuous line scanning with the laser in X and Y directions and pixel mapping. Three examples are illustrated using a fixed value for the total sweep and variable scan speeds and pixel reconstruction strategies. The values of tend are different in (a) and (b) and the same in (b) and (c). The blue rectangles represent one sweep. The gray circles show the center position of the laser beam of each single sweep recording, and the purple squares show the shape and position of the pixels on the final map. (a) Fast scan speed resulting in a single sweep measurement for a scan distance equal to the beam diameter. The pixel allocation for the center position results in squared pixels of the same size as the beam diameter. (b–c) Slow scan speed resulting in three sweep cycle measurements for a scan distance equal to the beam diameter. Two pixel generation strategies are illustrated: in (b), a rectangular pixel is generated for each sweep, while in (c) squared pixels are obtained by interpolation across three sweeps for this example as implemented in this work (see text for further explanations).

2.2.2 Map generation strategy and implementation in XMapTools

The data reduction scheme was implemented in the open source software XMapTools 4.3 (Lanari et al., 2014, 2019). Two modules have been developed for LA-ICP-MS applications: a converter module (Fig. S2.4) and a calibration module (Fig. S2.5). The converter module includes signal intensity extraction, background correction, standard selection and interpolation, and intensity map generation. The calibration module is used for individual calibration of masked regions of pixels.

Converter module

Files containing the transient intensity data are imported together with a compatible laser ablation system log file. Automatic synchronization is performed by comparing the time of the first "laser on" state with the position — in time — of the first transient signal increase in the derivative of the total intensity signal. Signal intensities are then extracted from the raw transient signal by the defined time intervals for each background and line scan measurement for standards and unknowns. A background correction is first applied and the detected background sweep cycles are interpolated over the time series for each element. Four interpolation methods are available to choose from: linear, polynomial (de-

gree 2), step function, and a custom spline. The custom spline is obtained by cubic spline data interpolation of a signal. Signal integration intervals are selected automatically by excluding 10% of the total number of sweeps for the start and end of each background measurement. This value can be manually adjusted for all measurements. The start and end positions of individual background interval measurements can also be set manually. An automatic outlier rejection filter is also applied to each background measurement, rejecting any measurement that is more than 5 scaled median absolute deviation from the median value. The interpolation is then subtracted from the line measurement signal to generate background corrected intensity data, similar to procedures used in IOLITE (Paton et al., 2011) or SILLS (Guillong et al., 2008). In the next step, one or multiple external standards are selected prior to map generation. Similar to the background selection, an automatic selection is made by excluding 10% of the total number of sweeps at the start and end of each measurement. Manual adjustment of this threshold is possible, as is examination of the signal and modification of the start and end positions of each selection. The four interpolation methods described above are available for external standard data interpolation. A secondary standard is then used to verify the quality of the calibration. The selected secondary standard is automatically selected by excluding 10% of the sweep cycles at the beginning and end of each measurement. Once a primary and secondary standard have been selected, a comparison is made between the calculated (using the mean intensity value of all selected sweep cycles) and reference element mass fractions of the secondary standard by selecting an element for internal standardization (see below). Finally, for the unknowns, the start and end positions for each line scan is automatically selected to have an intensity signal that is consistent with the spatial position of the laser between scans. The map area is converted into a Cartesian grid of square pixels with a size equal to that of the beam diameter (Fig. 2.1). The grid is defined by positions corresponding to pixels. The intensity signal corresponding to each sweep is spatially referenced to the center position of the corresponding scan (Fig. 2.1). The resulting signal intensity grid has a different resolution along the scan direction when $n \neq 1$ (see Eq. 2.2.3). Intensities for the central position of each pixel on the map grid are obtained by interpolating the intensity signal grid surface using a gridded cubic interpolation of the non-zero measurements obtained via a Delaunay triangulation. This procedure is used to extract all data, the background intensity maps from the interpolated background measurements and the intensity maps for standards and unknowns.

Calibration module

Masked regions of pixels corresponding to a single class (single phases, such as a mineral, glass or metal) within the intensity maps are calibrated individually using an internal standardization approach (Longerich et al., 1996):

$$\frac{C^i_{\text{unk}}}{C^i_{\text{std}}} = \frac{I^i_{\text{unk}}}{k \cdot I^i_{\text{std}}} \tag{2.2.4}$$

c^i_{unk} is the mass fraction of element (i) in the unknown sample, c^i_{std} the mass fraction of element i in the calibration material, I^i_{unk} is the intensity (cps) of element i in the unknown sample, and I^i_{std} the intensity (cps) of element i in the calibration material. The variable k represents the internal standardization factor and forms part of the relative sensitivity factor (RSF) following Halter et al. (2002):

$$k = \frac{I^{\text{int}}_{\text{unk}} \cdot C^{\text{int}}_{\text{std}}}{I^{\text{int}}_{\text{std}} \cdot C^{\text{int}}_{\text{unk}}} \tag{2.2.5}$$

Pixels in the intensity map are calibrated using an analyte of known composition, i.e. the internal standard element (int), in a calibration material and the sample. Each calibration uses either a constant or a variable internal standard element mass fraction as selected by the user. A single value for the internal standard element mass fraction (i.e., $c^{\text{int}}_{\text{std}}$) is commonly used for calibration, but this strategy can only be applied to phases where the internal standard element mass fraction is constant across the phase in the mapped area. To calibrate inhomogeneous materials, a variable internal standard element mass fraction needs to be used. If the variation in the mass fraction of the internal standard element is known, the measured intensities in the map can be matched to the known mass fraction of the internal standard element. In both cases, constant or variable value, the composition is determined by an external technique or mineral stoichiometry, and is set as percent oxide weight which is automatically converted to µg/g element. The constant composition method applies this value to all pixels of the selected class regardless of the intensity value. The variable composition method uses a linear relationship between intensity and composition of the internal standard element. This relationship is manually defined by the user by selecting at least two regions of interest (ROI) and assigning a fixed composition value to each. This information can then be used for interpolation and calibration of materials with a variable internal standard element mass fraction. In addition, a choice of multiple external standards for individual element calibration has been implemented. While this approach is often used to calibrate LA-ICP-MS spot measurements to improve analytical accuracy, to our knowledge none of the mapping software solutions to date offer this feature. Different external standards can be selected by the user for different elements being sampled. Finally, the LOD maps are calculated using equation 2.2.1.

Additional tools

Intensity maps can be used for phase classification using the machine learning algorithms implemented in XMapTools 4.3 (Lanari2023). The quantitative compositional maps ob-

tained after calibration can be used for structural formula calculations and thermobarometry using functions from the PTtoolbox (Laughton, 2023). Advanced data interrogation is available using the sampling functions or the data visualization module of XMapTools (Lanari et al., 2014, 2019). A spider diagram module is also available and includes advanced tools for visualization and graphical representation or trace element data (Raimondo et al., 2017).

2.3 Application examples

Three case studies have been selected to examine the workflow and calibrations, as well as measurement acquisition conditions and will illustrate selected aspects and benefits of our novel approach. The first example shows a comparison between fast and slow scanning speeds for mapping eclogitic garnets and omphacite from Latto Hills in Togo (maps 1.1, 1.2, and 1.3). The second example shows two multiphase maps acquired with different spatial resolutions of a migmatite sample from the El Oro complex in Ecuador (maps 2.1 and 2.2). This example contains minerals that show strong chemical zoning across the mapped area, thus requiring the variable composition method for internal standardization. The third case study provides trace element maps of rutile from Val Malenco in the Italian Alps used for thermometry (map 3.1). Data reduction was performed entirely with XMapTools 4.3 (Lanari et al., 2023). Mineral classification was performed using the random forest algorithm. All data presented in this study, including the raw signal, the intensity and calibrated maps, are available in Supplementary Material 2 and in a Zenodo data repository (https://zenodo.org/doi/10.5281/zenodo.8340229).

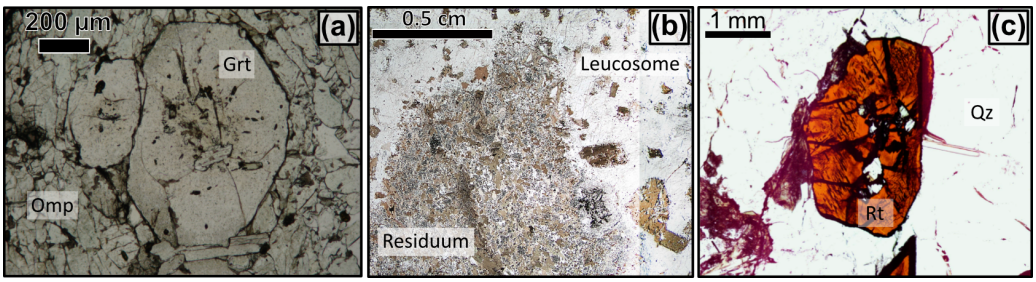

Figure 2.2: Optical images of the (a) garnet DKE-352, (b) migmatite BA1013 and (c) rutile from sample AS19–3. (a) Shows the targeted garnet grain in a matrix of pyroxene. (b) The residuum with higher biotite abundance next to the leucosome with larger biotite flakes but higher plagioclase abundance. (c) Image of the mapped rutile grain inside the matrix of quartz with visible exsolution needles of ilmenite. Mineral abbreviations are from Warr (2021)

2.3.1 Analytical conditions

LA-ICP-MS

Mapping experiments were performed at the Institute of Geological Sciences, University of Bern, using an ASI Resonetics RESOlution-SE 193nm excimer laser system with the S155 dual volume sample cell coupled to an Agilent 7900 quadrupole mass spectrometer. The ablated material was transported from the ablation cell to the plasma in an atmosphere of He at a flux of 0.7 L/min mixed with Ar (0.86-0.87 L/min) and N2 (0.003 L/min) at the exit of the ablation cell. At the beginning of each session instrument optimization included setting the ThO/Th intensity ratio to below 0.3% for low oxide production, and to ensure robust plasma conditions monitored by a U/Th sensitivity ratio of >0.97 (Günther & Hattendorf, 2005). The samples, consisting of polished thin sections (30 µm thick), were loaded into a spring holder of the S155 sample cell. The map areas were defined by a rectangular shape containing evenly spaced line scans using the GeoStar© software (Norris Scientific). A round aperture shape was chosen for all sessions to minimize variations in laser energy density across the beam area. The map size, laser beam diameter and scanning speeds for each map are given in Table 2.2. Detailed instrument conditions are given in Supplementary Material 1. Each map acquisition contains line scans measured over standard reference material and unknowns, i.e., the samples. The sample surface was pre-cleaned prior to each line scan using an aperture one size larger than the beam diameter used for the map and a scanning speed 10 times the normal scanning speed. The data were acquired in transient analysis mode in one continuous acquisition. The following three reference materials were used to evaluate data quality GSD-1G, NIST SRM 612 and NIST SRM 610 (Jochum et al., 2005). For each mapping session, at least two of the three reference materials were used, so that always one primary and one secondary standard material were included (see Supplementary Material 1). Primary and secondary standard materials were measured with at least one scan every half an hour with a minimum distance determined by equation 2.2.3 based on the scan speed in the respective experiment and acquiring a minimum of 100 sweep.

Electron probe micro-analysis

EPMA was performed using a JEOL JXA-8200 instrument at the Institute of Geological Sciences, University of Bern. Each EPMA session consisted of the measurement of spot analyses and X-ray maps. Analytical conditions for spot analyses were 15 KeV accelerating voltage, 10 nA specimen current and 40 s dwell times including 2×10 s of background measurement. Nine oxide compositions were measured using synthetic and natural standards as follow: wollastonite/orthoclase/garnet (SiO_2), orthoclase (K_2O), albite (Na_2O),

magnetite/garnet (FeO, TiO_2), anorthite (Al_2O_3, CaO), forsterite (MgO) and tephroite (MnO). Analytical conditions for mapping were 15 KeV accelerating voltage, 100 nA beam current and varying dwell times depending on the size of the map. Mapping with EPMA was performed to compare the element distribution obtained by mapping with LA-ICP-MS.

2.3.2 Sample description and map generation

Garnet DKE-352

Sample DKE-352 is a glaucophane-bearing eclogite from the Latto Hills, Togo. The observed mineral association consists of garnet (35-40 vol%), omphacite (15-20%), glaucophane (10-15%), zoisite (15-20%), paragonite (<5%), phengite (<5%), quartz (10-15%) and rutile (<5%). Accessory minerals (<2 vol%) include apatite, zircon, allanite, titanite, ilmenite and hematite. The peak metamorphic minerals in this eclogite have recorded ultra-high pressure conditions of 2.8–3.0 GPa and 620–700 °C during the formation of the West Gondwana Orogen at ~610 Ma (Ganade de Araujo et al., 2014). The garnet grain recording the widest range of chemical variability in major elements from core to rim observed in sample DKE-352 was selected for the LA-ICP-MS analysis (Fig. 2.3). Three LA-ICP-MS maps were collected on the selected garnet grain (Tab. 2.2). Map 1.1 (Fig. 2.5) was obtained with a spatial resolution of 12 µm to cover the entire grain and includes surrounding minerals such as pyroxene and mica. Map 1.2 and Map 1.3 (Fig. 2.5) were obtained one month later. Compared to map 1.1, a beam diameter of 5 µm was used to image the mantle to rim transition at a higher spatial resolution. Garnet in the three maps was calibrated using a variable composition of Ca used as the internal standard element. In each case the higher value of Ca was taken in the core area (78,617 µg/g Ca corresponding to 11.00 wt% CaO) and the lower value in the rim (42,882 µg/g Ca corresponding to 6.00 wt% CaO). These CaO contents were determined using average values for ROI in the major element maps obtained by EPMA.

Migmatite BA1013

Sample BA1013 is a migmatite from the El Oro Complex, Ecuador. The sample was collected in the pelitic domain of a metasedimentary xenolith embedded in the Marcabelli pluton (Riel et al., 2013). Two textural and mineralogical domains can be distinguished. (1) The biotite-poor (<15 vol%, grain size 0.5–1 mm) leucocratic domain accounts for ~45 vol% of the rock and is composed of K-feldspar (~35 vol%), plagioclase (~45%), biotite (<15%), quartz (<1%), ilmenite (<1%), magnetite (<1%), and apatite (<1%). This domain is interpreted as a result of partial biotite dehydration melting (Vielzeuf1988) and referred to as the leucosome. (2) The biotite-rich (>30 vol%, grain size 100–300

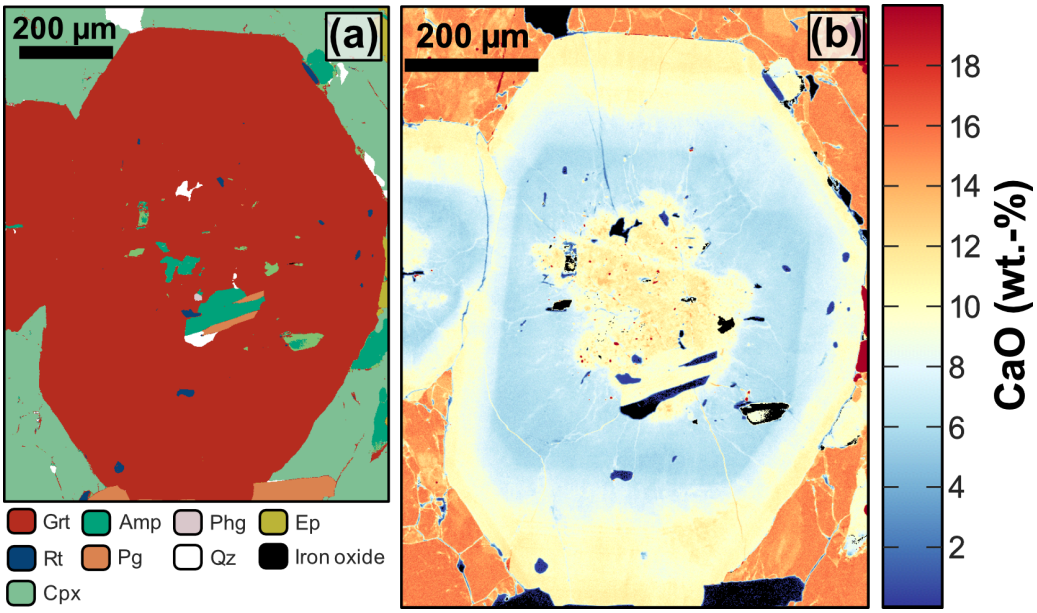

Figure 2.3: Phase assemblage map (a) and major element compositional map of CaO in wt% for all phases (b) of sample DKE-352. (a) Shows inclusions of amphibole, rutile, and epidote in the garnet. (b) Garnet shows compositional variation between ∼4 to 13 wt% CaO. All phases are calibrated separately (see text for more information). Mineral abbreviations are from Warr (2021)

µm) melanocratic domain makes up ∼55 vol% of the rock and contains biotite (>30%), plagioclase (∼55%), cordierite (∼8%), spinel (∼1%), apatite (<1%) and magnetite (<1%). This domain does not show evidence of melt and is referred to as the residuum. An area of interest was selected at the contact between the leucosome and the residuum (see Fig. 2.2 and 2.4a). The three main phases, plagioclase, biotite, and K-feldspar show major element variation. Plagioclase is strongly zoned in anorthite molar fraction from 0.1 to 1.0 (Fig. 2.3b), as reflected in major element variations (∼10 wt% in NaO; ∼20 wt% in CaO; ∼15 wt% in Al_2O_3; and ∼20 wt% in SiO_2). Biotite shows a variation of <2 wt% in SiO_2 and a higher variability of ∼5 wt% in Al_2O_3. K-feldspar varies ∼2 wt% in SiO_2, ∼3 wt% in NaO and <1 wt% in Al_2O_3. Two adjacent maps of 1x4 mm^2 were obtained within the same area of the element maps from EPMA in two separate sessions. The first part map 2.1 was obtained with a spatial resolution of 20 µm and the second part map 2.2 with 10 µm in a separate analytical session, both covering the leucosome and residuum domains. Internal standardization of plagioclase was done with variable CaO mass fraction, because plagioclase contains no major element of constant mass fraction suitable for internal standardization with a constant value. For each map part, the minimum and maximum anorthite molar fraction in plagioclase (X_{an}) domains were defined as ROI for the calibration. Map 2.1 regions are in the high X_{an} domain (131,504 µg/g Ca corresponding to 18.40 wt% CaO) and low X_{an} next to the larger biotite grain (30,732 µg/g Ca corresponding to 4.30 wt% CaO). Map 2.2 regions relate to a medium-high X_{an} patchy

domain at the contact between the two map parts (95,055 µg/g Ca corresponding to 13.30 wt% CaO) and a low X_{an} domain near the biotite flake (25,729 µg/g Ca corresponding to 3.60 wt% CaO). Calibration of biotite used Si as the internal standard element with a value of 166,861 µg/g corresponding to 35.70 wt% SiO_2. K-feldspar was calibrated using Al as the internal standard element with a value of 98,450 µg/g corresponding to 18.60 wt% of Al_2O_3. All values were determined using average values for ROIs in the major element maps obtained by EPMA.

Rutile AS19-3

The metapelite sample AS19-3 from Alpe Senevedo Superiore, Val Malenco (Italian Alps) reached high-pressure upper greenschist facies conditions of ∼1.0 ± 0.3 GPa and 475 ± 25 °C (Bissig & Hermann, 1999). The observed mineral association consists of garnet (∼10 vol%), chlorite (∼15%), amphibole (∼35%), quartz (∼20%), white mica (∼10%) and rutile (∼10%). Rutile occurs as ∼200 µm–sized grains within the matrix and can reach cm–sized grains within the quartz layer. The latter contains ilmenite dissolution needles. The mapped rutile grain originates from the quartz domain (see Figure 2.2). A map of 2.5 mm^2 size has been acquired using LA-ICP-MS covering ∼80% of the rutile grain shown in Figure 2.2c. Rutile in the map was calibrated using Ti as internal standard element (599,260 µg/g Ti corresponding to 99.96 wt% of TiO_2).

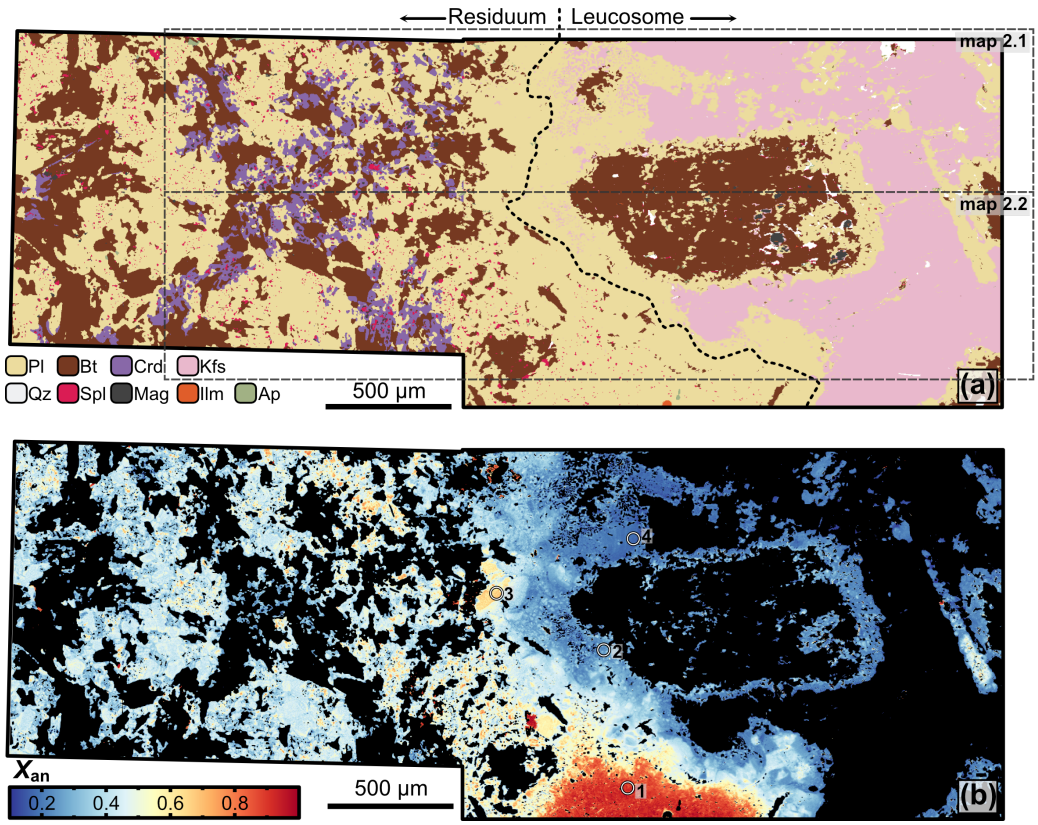

Figure 2.4: Mineral phase assemblage map (a) and map of X_{an} (b) acquired with EPMA for plagioclase of the migmatite sample BA1013. The shape of the maps results from stitching of two subsets of maps from EPMA. (a) Showing the contact between the leucosome (right) and residuum (left). Inclusion phases in plagioclase smaller than 10 µm can be identified. Gray dashed fields represent the areas of map 2.1 and 2.2. (b) Strong zoning can be seen for X_{an} from almost pure anorthite to albite with a transition along the contact between residuum and leucosome. Circles define ROIs of extracted CaO mass fraction used for calibration. ROI 1 through 4 yield CaO values of 18.40, 4.30, 13.30, and 3.60 wt%, respectively. Mineral abbreviations are from Warr (2021)

Map	Map size [mm²]	Map size X*Y [px]	Nr Pixels	Laser beam diameter [µm]	Scan speed [µm/s]	Time [hh:mm]	Surface energy [J/cm²]	Nb of elements	Total sweep time [s]	Mineral phase	Primary Standard	Fraction of background measurement [%]
Example 1 – Garnet DKE-350												
1.1	4	91x91	8281	12	7.5	03:20	5	38	0.46	Garnet	GSD-1G NIST SRM 612	17.5
1.2	0.1	46x68	3128	5	3	02:50	5	19	0.51	Garnet	GSD-1G NIST SRM 612	25.6
1.3	0.075	47x60	2820	5	3	03:00	5	19	0.51	Garnet	GSD-1G NIST SRM 612	29.4
Example 2 – Migmatite BA1013												
2.1	4	165x37	6105	20	12	04:15	5	38	0.46	Plagioclase	GSD-1G NIST SRM 612	15.0
2.2	4	330x60	19800	10	6	13:40	5	38	0.46	Plagioclase	GSD-1G NIST SRM 612	11.8
Example 3 – Rutile AS19-3												
3.1	2.5	108x89	9612	16	10	06:54	5	26	0.32	Rutile	NIST SRM 610 NIST SRM 612	17.0

Table 2.2: Summary of applied LA-ICP-MS mapping conditions for application example 1 to 3. The dwell times used for each analyte are provided in Table S1.

2.4 Results

2.4.1 Garnet DKE-352

The results of structural formula calculations for garnet are shown in Figure 2.5 and trace element maps in Figure2.6. Additional compositional maps are in the Supplementary Material 2. Major, minor, and trace element maps for pyroxene from both EPMA and LA-ICP-MS are provided in Supplementary Material 2 but not discussed here. The maps of the end-member molar fractions (X_{alm} for almandine defined as molar Fe/(Fe+Mg+Ca+Mn); X_{sps} for spessartine as Mn/(Fe+Mg+Ca+Mn); X_{prp} for pyrope as Mg/(Fe+Mg+Ca+Mn); and X_{grs} for grossular as Ca/(Fe+Mg+Ca+Mn)) obtained by LA-ICP-MS are consistent with those obtained using the EPMA (Fig. 2.5). Distinct compositional zoning is observed between core, mantle and rim for X_{sps} and X_{grs}, whereas X_{alm} and X_{prp} show patchy distribution within the mantle. The X_{alm} LA-ICP-MS maps show slightly higher contents of ∼1-3% in the patchy areas compared to EPMA data (Figs. 2.5a-d). Small veinlets connecting the outermost rim and the core of the garnet grain are observed in the X_{sps} map (Fig. 2.5e). The distribution of X_{sps} also shows an increase around the garnet core, separating core from mantle. These veinlets are still visible but not well resolved in the LA-ICP-MS maps, especially for the 12 µm resolution (Fig. 2.5f). The sharpness of the veinlets is improved in the maps obtained with 5 µm resolution (Fig. 2.5g). Faint oscillatory zoning is observed in the EPMA X_{grs} map (see arrow in Fig. 2.5m) but is not resolved in the LA-ICP-MS maps. The garnet sample DKE-352 shows strong compositional zoning for most trace elements (Supplementary Material 2). A discussion of the systematics and differences between the LA-ICP-MS maps is based on Dy, Lu, and Y (Figs.2.6a-f). An annulus is visible for Dy, Lu, and Y at the boundary between core and mantle. This feature is thin and sharp in the REE maps (e.g., Figs.2.6a-c) and is positionally consistent with the manganese enrichment around the garnet core (Figs. 2.5e-h). Similarly, the transition between mantle and rim in the REE maps is sharper than that observed for the major elements. Furthermore, the elements Dy, Lu, and Y show a similar trend of increasing content from the inner rim to the outer rim and a sharp contrast between the mantle part wrapping the annulus and progressing towards the inner rim. The three selected elements were reproduced between the three maps 1.1, 1.2 and 1.3. The average mantle composition in Dy is 19.5 µg/g for map 1.1, 17.9 µg/g for map 1.2 and map 1.3, and showing differences up to 8.5%. Values for Y decrease from mantle to inner rim from ∼116 µg/g to ∼25 µg/g in map 1.1 and from ∼119 µg/g to ∼24 µg/g in map 1.2 (similar for map 1.3), which corresponds to differences between map 1.1 and 1.2 of 2.5% and 4%, respectively. The average value of Lu in the mantle is 1.8 µg/g in map 1.1 and 1.9 to 2.0 µg/g in map 2.2 and 2.3 corresponding to a difference of 5 to 8%. A larger difference is found in Dy and Lu content of the annulus when comparing map 1.1 with map 1.2 and 1.3. Map 1.1 records

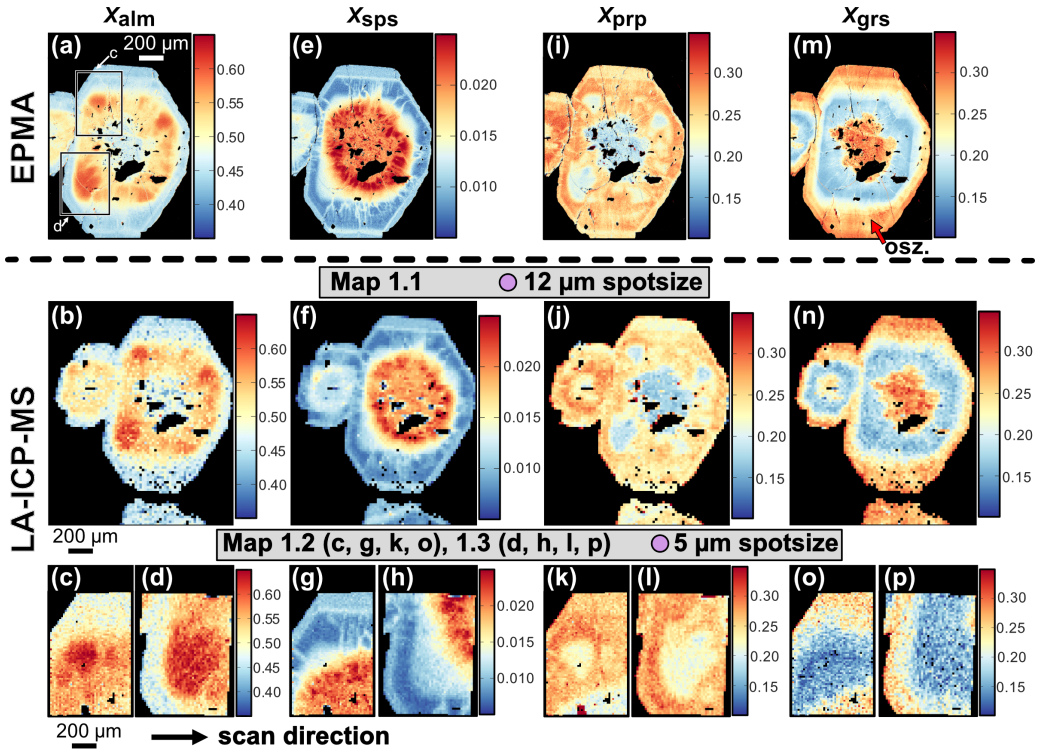

Figure 2.5: Calculated end-member maps of X_{alm} (a–d), X_{sps} (e–h), X_{prp} (i–l) and X_{grs} (m–p) in garnet (DKE-352) for EPMA (a, e, I, m) and LA-ICP-MS mapping (b–d, f–h, j–l, n–p). (b, f, j, n) The results from mapping with 12 µm spot size. (c–d, g–h, k-l, o–p) The repeated mapping with a spot size of 5 µm. (a) Map of X_{alm} showing the sections of map 1.2 and 1.3 (black squares), which are shown in panel (c) and (d). (m) Oscillatory zoning is indicated in the garnet rim marked with the red arrow and acquired with EPMA. The scale shown is representative of all maps.

generally lower values for the annulus with a maximum value of 58 µg/g whereas map 1.2 and 1.3 reach up to 75 µg/g. This is a difference of 25%. Comparing the LOD of the pixels for the three elements between the three maps shows some expected differences related to the spatial resolution. The LODs are generally higher for the maps with the smaller spot size and this is visible in the Dy and Lu maps where some pixels in the garnet mantle region are below the LOD (see Figs.2.6a-f). This is due to the fact that the mass of aerosol ablated per unit time increases with increasing pixel size (keeping all other parameters constant); hence, the LOD is inversely proportional to pixel size. The average LOD of Dy for map 1.1 is 0.9 µg/g, and for maps 1.2 and 1.3 it is 2.7 µg/g. The LOD of Lu is 0.2 µg/g for map 1.1, and 0.7 µg/g for maps 1.2 and 1.3. For Y it is 0.28 µg/g and 0.74 µg/g, respectively.

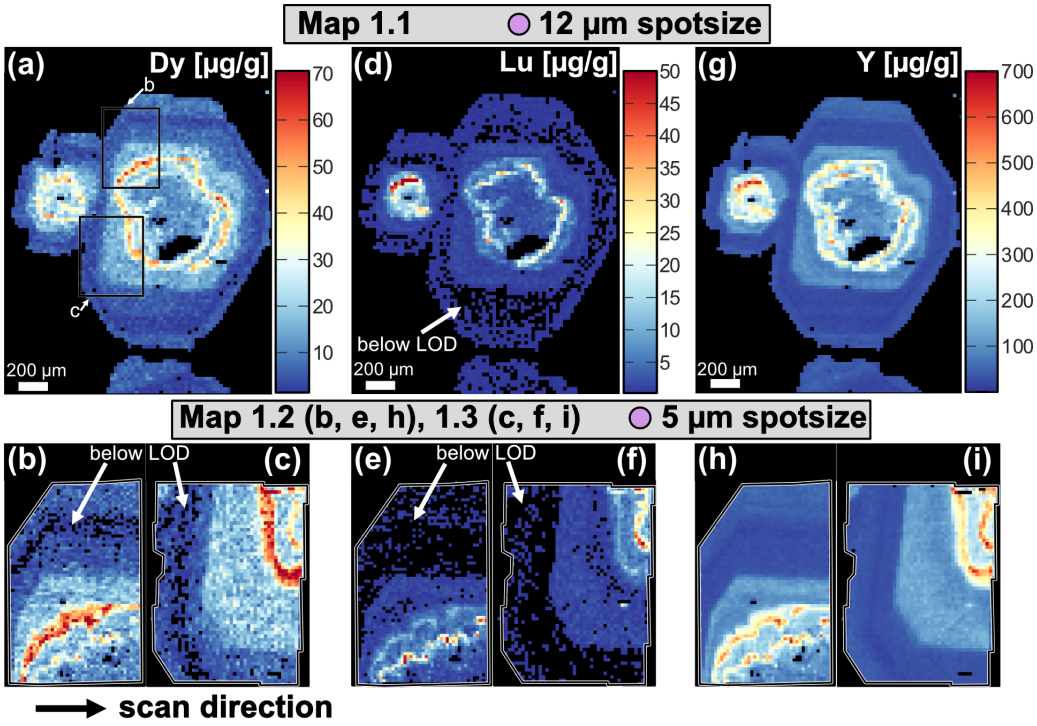

Figure 2.6: LA-ICP-MS element maps for selected trace elements Dy (a–c), Lu (d–f), and V (g–i) in garnet (DKE-352). (a, d, g) Maps acquired with 12 µm spot size. (b–c, e–f, h–i) Maps acquired with 5 µm spot size. (b–c) Annulus shows higher content for Dy and a second annulus compared to the map in (a) acquired with lower spatial resolution. (b–f) A significant part of the pixels in the rim are black, representing pixels for which the apparent element mass fraction is below the corresponding LOD per pixel calculated individually for each element (white arrows). (b–c, e–f, h–i). The white line traces the grain boundary of the garnet.

2.4.2 Migmatite BA1013

Compositional maps for biotite, K-feldspar, and plagioclase were generated using constant and variable mass fractions for the internal standard element (see above). Pixels corresponding to other phases (e.g., magnetite and cordierite) were not considered due to their mixed composition. The calibration procedure, including the generation of maps for LOD, is presented using the example of Ba for the two LA-ICP-MS maps (Fig. 2.7). The maps for major elements (CaO, Na_2O, Al_2O_3) and structural formula maps (X_{an}) for plagioclase obtained by LA-ICP-MS are then compared with EPMA data (Fig. 2.8). The comparison between EPMA and LA-ICP-MS data also includes maps of Ti-in-biotite thermometry (Fig. 2.9). Finally, results for selected trace elements are shown in Figure 2.10. Additional maps of major elements, structural formulae and trace elements of plagioclase, biotite and K-feldspar are in Supplementary Material 2. Map 2.1 was measured with 20 µm spot size and shows generally higher pixel intensities in Ba for all phases compared to map 2.2 which was measured with 10 µm spot size (Fig. 2.7b). After calibration no significant difference in major and trace element pattern is observed between maps 2.1 and 2.2 (e.g., Ba in Fig. 2.7c). Plagioclase shows a homogeneous distribution of Ba (∼300 µg/g), with the exception that lower contents (∼70 µg/g) are observed in the high X_{an} domains (Fig. 2.4b). Biotite shows patchy Ba zoning especially in the larger grain located in the leucosome domain. K-feldspar shows both patchy zoning and domain zoning in Ba with a decrease of ∼2000 µg/g between the upper and lower part of the leucosome. Note that the transition between these two K-feldspar compositions is not located at the boundary between the two maps. Calculated maps of LOD (Fig. 2.7d) show ∼50% lower values in map 2.1 (20 µm) compared to map 2.2 (10 µm), again illustrating the inverse proportionality between pixel size and LOD for a given analytical protocol. The LOD map shown in figure 2.7d displays a pattern that reflects the different minerals present in the mapped area, because the ablation rate per unit time is variable for different minerals. As a consequence, the mineral-specific sensitivities for each analyte are variable for different minerals, resulting in variable LODs for the minerals mapped (keeping all other analytical parameters constant; compare equation 2.2.1). After calibration, an excellent agreement in composition is observed between maps 2.1 and 2.2 for major, minor and trace elements (Figs. 2.7, 2.8, 2.10), and between EPMA and LA-ICP-MS quantitative maps. The CaO maps of plagioclase obtained by LA-ICP-MS and EPMA record a compositional variation of ∼20.0 wt% with a patchy zoning along the transition from residuum to leucosome (Figs. 2.8a, e). Plagioclase zoning in Na_2O shows ∼10.0 wt% variation across the area for both LA-ICP-MS and EPMA maps (Figs. 2.8b, f). Maps of LA-ICP-MS and EPMA show both illustrate the variation between almost pure anorthite and albite in the calculated map of X_{an}. Two selected ROIs show the local average value for X_{an}, one in the leucosome and one in the residuum area (see Figs. 2.8d, h). The value from EPMA results show in average 19% X_{an} (integrating 3400 pixels) and

LA-ICP-MS shows 18% X_{an} (integrating 180 pixels) in the leucosome. In the residuum, X_{an} determined by EPMA is 63% (integrating 470 pixels) while that determined by LA-ICP-MS is 61% (integrating 21 pixels) on average. The Ti-in-biotite temperature map obtained from EPMA results shown in Figure 2.9a illustrates a gradual increase from left to right in the residuum domain from 600-700 °C. The large biotite flake in the leucosome domain yields the highest temperature of between 700 and 750°C showing a slight irregular zoning pattern. LA-ICP-MS results illustrate the same gradual temperature increase in the residuum and similar zoning of the biotite in the leucosome (Fig. 2.9b). As a test, the same ROI in the EPMA and LA-ICP-MS maps return values for Ti, X_{Mg}, and temperature that are identical within analytical uncertainties (displaying a difference of 0.5%, 0.5%, and <0.2%, respectively). Plagioclase, biotite, and K-feldspar show moderate to strong zoning in several trace elements as well as sectional differences between leucosome and residuum, which is shown using Sr in K-feldspar, Sr, La, and Nd in Plagioclase and Li, Co, V, and Rb in biotite (see Fig. 2.10). All trace element maps of K-feldspar, plagioclase, and biotite show no major difference at the boundary between the two maps 2.1 and 2.2, which were measured using the presented mapping routine with LA-ICP-MS but in separate analytical sessions (see Fig. 2.10 and S2.2). Instead, the generated maps resolve spatial patterns of trace element distribution in the different mineral grains and domains (Fig. 2.10 and S2.2).

2.4.3 Rutile AS19-3

Results of trace element distribution and a temperature map calculated using a Zr-in-rutile thermometer (Tomkins et al., 2007) are shown in Figure 2.11. The element Ta is chosen as an example of observed trace element zoning in rutile. Additional trace element maps and temperature maps using additional calibrated functions are shown in Supplementary Material 2. Sharp contrasts in the trace element patterns in rutile are shown using Zr and Ta (Figs. 2.11a-b). Zirconium and Ta are partially correlated, and the highest trace element contents are visible in a curved feature on the left side of the grain with ∼70 µg/g Zr and ∼190 µg/g Ta. The temperature map follows the Zr distribution with the highest temperature of ∼550 °C in the curved feature and lower temperatures of 515-530 °C towards the rim.

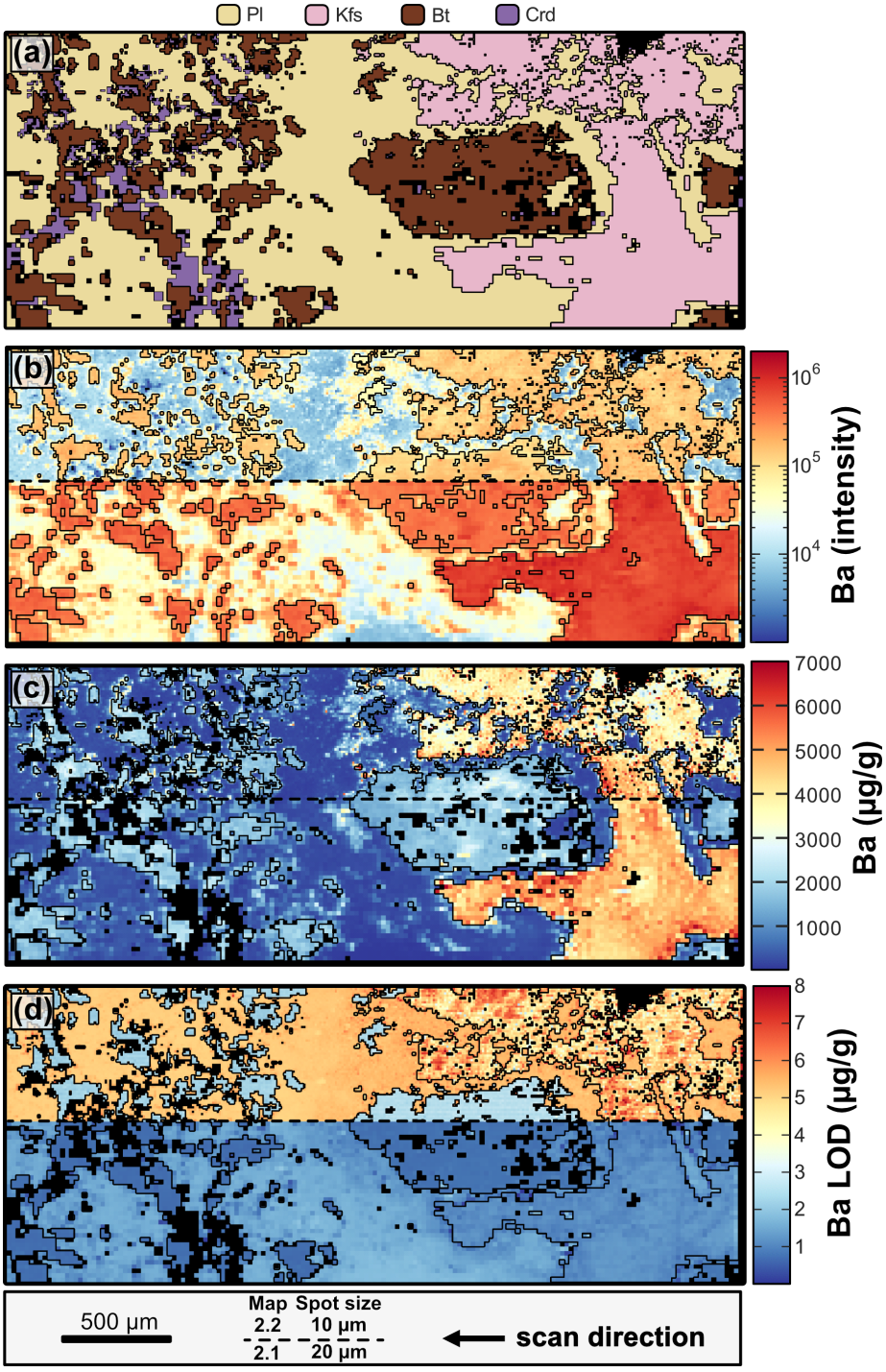

Figure 2.7: Compilation of (a) the mineral assemblage, (b) the background corrected intensity map of Ba, (c) calibrated quantitative map of Ba and (d) map of the LOD per pixel for Ba in the phases of biotite, plagioclase and K-feldspar in sample BA1013. Lower half in the map represents map 2.1 using 20 µm spot size and the upper half map 2.2 using 10 µm spot size of adjacent domains in the sample. (b) The intensities in map 2.1 are larger by at least a factor of 2 compared to map 2.2, resulting from larger aerosol masses measured per unit time per pixel for the larger spot size. (c) After calibration, the interface between the two maps shows a smooth transition. (d) The LOD per pixel in the lower half of the map is roughly half the mass fraction of that in the upper half of the map. Black outlines have been added to highlight grain boundaries in all images in this figure. Mineral abbreviations are from Warr (2021).

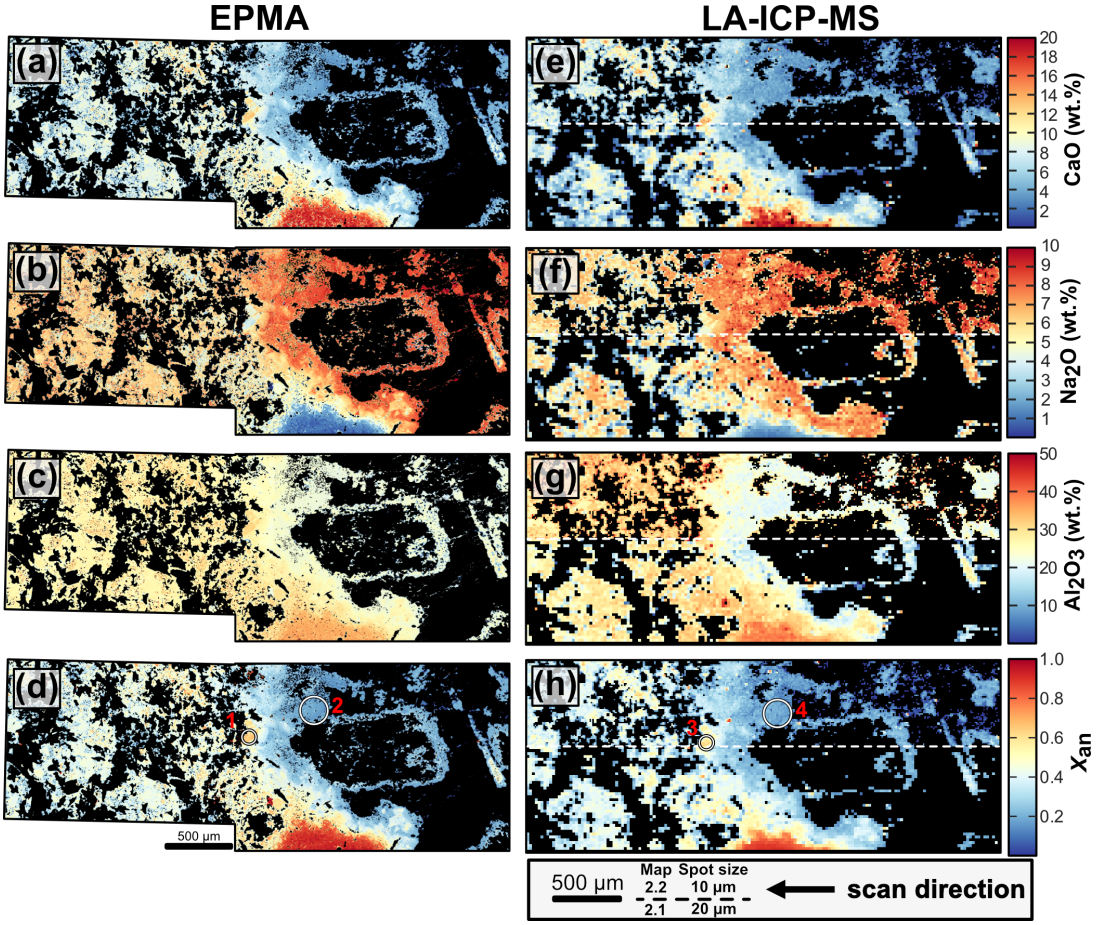

Figure 2.8: Calibrated maps for plagioclase of CaO, Na_2O, and Al_2O_3 and calculated map of X_{an} maps for EPMA and LA-ICP-MS in sample BA1013. (d, h) ROIs in the leucosome and residuum represented as circles (1–4 in red). EPMA ROI 1 yield 0.63 ($\pm$0.05) X_{an} and 0.19 ($\pm$0.03) X_{an} for ROI 2 in leucosome and residuum respectively. LA-ICP-MS yield 0.61 ($\pm$0.03) X_{an} in ROI 3 and 0.18 ($\pm$0.03) X_{an} in ROI 4 for leucosome and residuum, respectively.

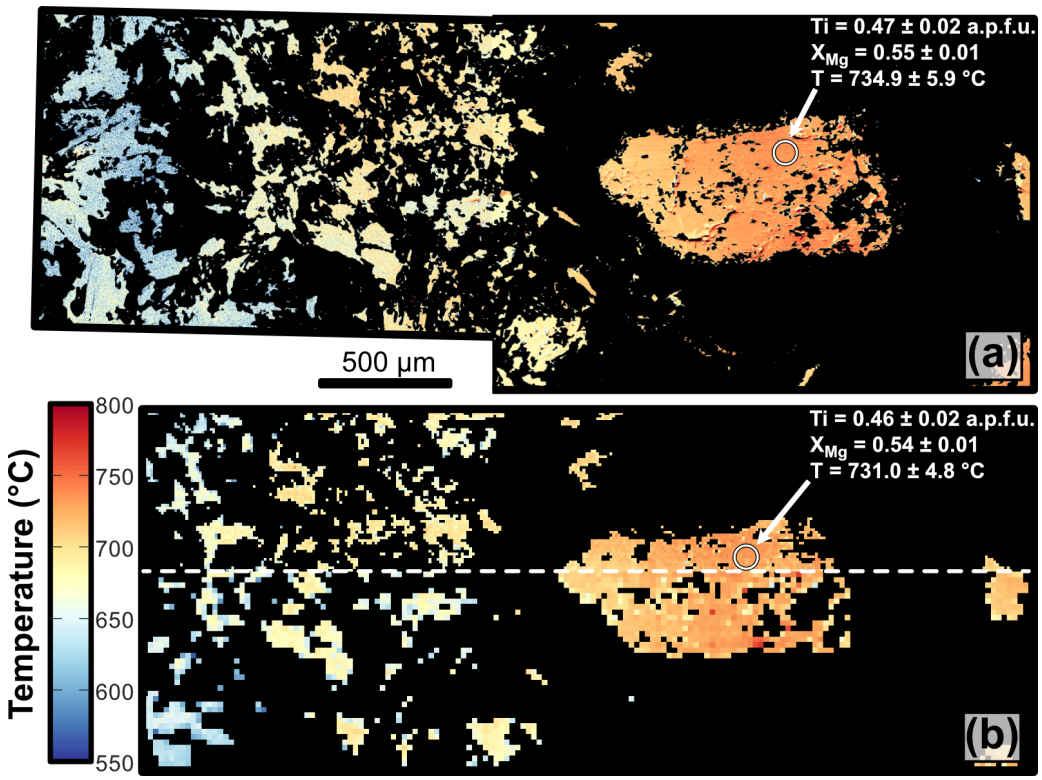

Figure 2.9: Temperature maps of biotite calculated using the Ti-in-biotite thermometer of Henry et al. (2005) obtained by (a) EPMA, (b) LA-ICP-MS in sample BA1013. The comparison of results for the same ROI (white circle) in the large crystal of the leucosome reveals that calculated temperatures are identical within uncertainties for the EPMA and LA-ICP-MS maps. Mean and standard deviation values were obtained from the pixel values within the circular ROI. The measurement precision of the LA-ICP-MS temperature determination (2σ = 0.65%) is slightly higher than that of the EPMA determination (2σ = 0.8%).

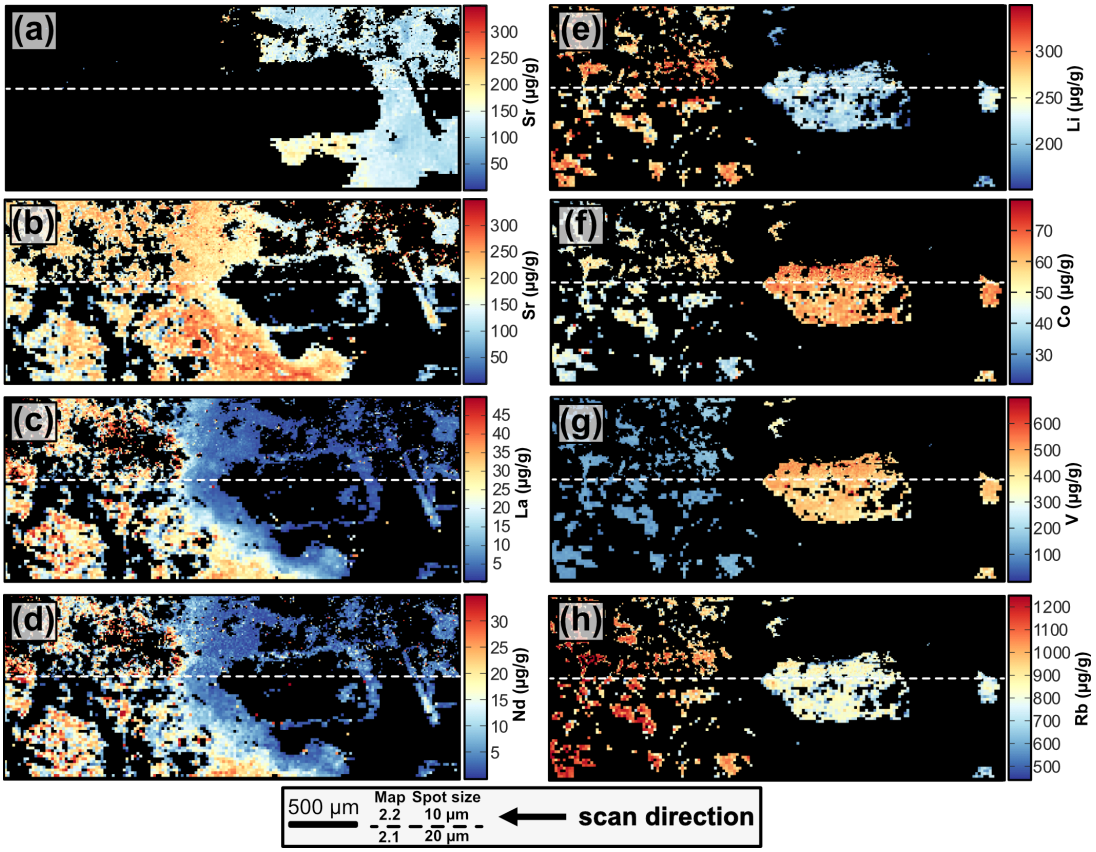

Figure 2.10: Quantitative trace element maps obtained by LA-ICP-MS (a) Sr in K-feldspar, (b–d) Sr, La, and Nd in plagioclase, and (e–f) Li, Co, V, and Rb in biotite of sample BA1013. Colour codes represent element mass fractions per pixel while black pixels in the map represent apparent element mass fractions below the respective LODs calculated individually for each element in every pixel.

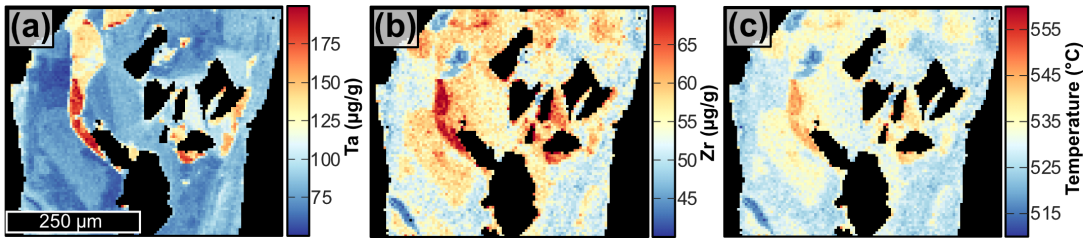

Figure 2.11: Trace element maps of Zr and Ta in rutile and temperature map of rutile calculated using the Zr-in-rutile thermometer of Tomkins et al. (2007) obtained by LA-ICP-MS. (a–b) The elements Ta and Zr show a patchy zonation with no correlation to the cracks visible in Fig. 2.2c. (c) The temperature map shows variation in the temperature of maximum ~7.5% difference, from ~510 to 550 °C. Black map domains represent other phases.

2.5 Discussion

Six datasets including 19 to 38 measured elements resulting in a total of 178 intensity maps were acquired by LA-ICP-MS from three geological samples showing various mineral phases ranging across diverse metamorphic grades. Compositional maps were calculated from the time series intensity data using our novel data reduction protocol implemented in XMapTools. The following discussion focuses on the relevant features and advantages of our new method and the tools provided by our mapping approach, the resolution of the generated maps, and the quantification of element mass fractions and associated LODs calculated for each element per pixel as well as for ROIs. LA-ICP-MS mapping was compared with EPMA maps to evaluate the calibration quality. However, EPMA maps are not required and calibration of LA-ICP-MS maps can be done by single spot analyses or any other technique that can determine the internal standard element content used in the defined ROI.

2.5.1 Mapping method

High-resolution mapping of garnet (Fig. 2.6) can be performed at the same spatial resolution and similar detection power as recent LA-ICP-TOFMS experiments (Bussweiler et al., 2020; Rubatto et al., 2020). The acquisition rates calculated in this study using the total measurement time for standards and unknowns ranges between 15 and 40 pixels/min. This is similar to Raimondo2017 and significantly slower than LA-ICP-TOFMS (∼170 to 3300 pixels/min in Rubatto et al. (2020) or ∼1500 in Savard et al. (2023)). The acquisition rate of this study could be improved by reducing the number of sweeps per pixel. For n = 1, the acquisition rate would be between 45 and 120 pixels/min. This is still lower than what was reported by Konrad-Schmolke et al. (2023). Similar figures could be obtained by reducing the duration of the background measurement, which accounts for 11 to 30% of the acquisition time in our data acquisition procedure and depends on the scan duration of a single line (Tables 2.1 and 2.2) and the duration of the washout (1.4 to 7.9%). The duration of the background measurement could be reduced; however, this results in higher LODs, if all other parameters are kept constant (see Eq. 2.2.1 and Fig. S2.6). Each mapping experiment requires ascertaining the balance between spatial resolution and compositional detection capability. Maps can be collected faster by increasing the spot size. In the example of the migmatite sample BA1013, the beam diameter of map 2.1 is twice that of map 2.2, allowing mapping to be performed 3 times faster. The loss in spatial resolution is moderate because similar zoning patterns could be resolved in the composition for minerals, especially for large grains at least 20 times the diameter of the laser beam. However, this depends on the size of compositional zoning features and thus also on the grain size of the target area. For example, a 500 µm biotite grain and its internal chemical

zoning are reasonably well resolved when imaged with a 20 µm beam diameter (Fig. 2.10). Grains smaller than 400 µm are better resolved in the 10 µm spatial resolution map as only then can similar features be resolved as in EPMA maps (Fig. 2.8). Spatial resolution of maps is inversely proportional to LOD of the analytes per pixel. Larger beam diameters (= poorer spatial resolution) result in a significant gain in detection power as illustrated by the LOD value (Fig. 2.7d). As a result, more pixels are generally below LOD when a higher spatial resolution — i.e. a smaller spot size — is used (Fig. 2.6), and analyte mass fractions near the respective LODs are measured less precisely. Increasing the resolution by a factor of 2 (e.g., from 20 µm to 10 µm) will increase the measurement time by 3 to 4 times and double the respective LODs.

Precision and accuracy

The maps of samples DKE-352 and BA1013 are useful to evaluate the precision and accuracy of our mapping approach. Accuracy was assessed for major and minor elements by comparing LA-ICP-MS maps to EPMA maps (see Figs. 2.5 and 2.8). We recall that a well-calibrated QMS instrument is necessary for the testing process, notably the calibration of the pulse to analog detector signal conversion factor. The three maps of sample DKE-352 and the two maps of sample BA1013 were acquired with different measurement conditions (on different days; Table 2.1). Quality tests on secondary standards (GSD-1G, NIST SRM 610 and NIST SRM 612) returned mass fraction data in the maps that are generally within 10% of preferred values (see Supplementary Material 1), demonstrating accuracy of our mapped element mass fraction data. Moreover, our maps also document excellent external reproducibility, as merged compositional maps do not reveal measurement day dependent content jumps or other differences in patterns. The LA-ICP-MS major element maps reproduce the maps obtained by EPMA, illustrated by identical zoning patterns and element mass fraction data that differ by less than 10%, mostly identical to within a few percent. The accuracy of LA-ICP-MS mapping was tested by structural formula calculations for sample BA1013 using CaO mass fractions for internal standardization of the LA-ICP-MS maps. The EPMA structural formula calculations are known to have a precision of ∼1%. The X_{an} of plagioclase is within 3 to 5.5% between EPMA and LA-ICP-MS data (Fig. 2.8). Part of the differences can be explained by the lower spatial resolution of the LA-ICP-MS maps. This is the case for the ∼100 µm wide albite-rich plagioclase domain surrounding the large biotite grain in the leucosome. Map 2.1, obtained with a spot size of 20 µm, shows a close agreement with the EPMA results, with only a few percent difference compared to the EPMA data, and the higher spatial resolution map 2.2 shows even better agreement with the EPMA data, with a difference of <5% in X_{an}. The larger difference in the low spatial resolution map can be explained by the presence of pixels representing a mixed composition between plagioclase, biotite and K-feldspar. For samples DKE-352, the end-member

fractions of garnet obtained by EPMA and LA-ICP-MS mostly agree to within 5%. Zoning domains that are smaller than 200 µm can show slightly higher difference below 10%. This differences can also be explained by the larger beam diameter of the LA-ICP-MS, between 5 and 14 times larger than the 1 µm beam size used for EPMA mapping. Another test was performed using the Ti-in-biotite thermometer of Henry et al. (2005) for the migmatite sample BA1013. The reference material GSD-1G was used as the external standard and Si as the internal standard element, resulting in a biotite temperature of 731.0 ± 4.8 °C (Ti = 0.46 ± 0.02 apfu; X_{Mg} = 0.54 ± 0.01) with LA-ICP-MS extracted from the circular ROI. The average temperature of the selected ROI shows a difference of ∼4 °C compared to EPMA results. This is well within the respective measurement uncertainties of EPMA and LA-ICP-MS and smaller than the uncertainty inherent in the calibration of the Ti-in-biotite thermometer by Henry et al. (2005). In contrast to the eclogite sample DKE-352, which is externally standardized to NIST SRM 612, the X_{Mg} of biotite is more reliably determined using GSD-1G as an the external standard because the calibration for Mg and Fe is better when high-Mg-Fe standards are used. Moreover, the map of sample BA1013 calibrated using NIST SRM 612 as the external standard results in an average biotite temperature of 775.2 ± 4.3 °C for the ROI shown in Figure 2.9 (Ti = 0.49 ± 0.02 apfu; X_{Mg} = 0.69 ± 0.01), 44 °C higher than that obtained by external standardization on GSD-1G. These differences illustrate well the limited reliability of NIST SRM 612 external standardization for Fe, Mg, Ti, and, by implication, for other major/minor elements that are present in NIST SRM 612 at ca. 40 µg/g mass fraction only. This is why we use GSD-1G for external calibration, which has a basaltic major and minor element composition. Importantly, it also emphasizes the benefit of using different external standards for different elements as implemented in XMapTools, to improve the accuracy of LA-ICP-MS map calibration for compositionally diverse minerals covering a wide range of element contents. The accuracy of the LA-ICP-MS map calibration for trace elements presented in this study compares favorably to the accuracy obtained for single-spot measurements using the same reference material for external standardization and employing the same element mass fraction for internal standardization. In sample DKE-352, the trace element mass fractions obtained for all maps are consistent within ±3% for Yb, Er, Y, <10% for Sc, V, Cr, Dy, Ho, Lu and <15% for Tm. Similarly to major elements, compositional zoning patterns smaller than 100–150 µm are visible and show more extreme differences (e.g., maps 1.2 and 1.3 in Fig2.6) due to the spatial resolution effect discussed above. An interesting feature is the REE-rich annulus where two key differences can be seen in the trace element maps (Fig. 2.6). First, the maps 1.2 and 1.3, which represent a higher spatial resolution, consistently show higher contents when compared to map 1.1, which was obtained with a lower resolution. For example, measured Dy content increases from 58 to 75 µg/g corresponding to a 25% increase with increasing annulus thickness. The second ring of the annulus is

almost absent in map 1.1 due to the lower spatial resolution. The second difference is best observed in map 1.2, where Dy reaches values of 50 µg/g when the annulus is oriented perpendicular to the scanning direction and 58 µg/g (corresponding to a difference of 14%) when oriented parallel to the scanning direction. Clearly, mapping at lower spatial resolution was insufficient to fully resolve the narrow high-content zone, as further evaluated in the next section.

Pixel allocation and direction of scanning

The ultimate aim of 2D mapping is the spatial presentation of element content data via the assignment of pixels on a two-dimensional grid. The approach proposed in this study involves generating square pixels from a line scan using an interpolation method, as opposed to the rectangular pixels commonly employed in other software (Chew et al., 2021, and references therein). The interpolation method allows to minimize the number of incorrectly assigned laser pulses to each pixel (see van Elteren et al., 2019)(Fig. 2.1). Figure 2.12 illustrates different results of converting the intensity signal of one single scan into an intensity map. The intensity measurement for each sweep (black dashed line) can be averaged or interpolated to obtain square pixels. Alternatively, averaging of sweeps is used, for example, in the CellSpace software solution (Paul et al., 2012). In the case of an annulus or any other type of narrow feature that generates a high-intensity signal measured by a single sweep, the interpolation method is much more precise than the averaging method (Fig. 2.12). However, the gridded cubic interpolation via the Delaunay triangulation method was used in this work due to better performance in the numerous 2D maps generated during this study. Importantly, we recommend to use three sweeps for each squared pixel (n = 3 in Fig 2.1a). If three sweeps are integrated into a squared pixel, a sufficiently slow scanning speed is required to obtain the resolution of chemical features for the given spatial resolution. This approach cannot resolve features smaller than the spot size, as other studies have also noted (Jollands, 2020; van Elteren et al., 2021). Importantly, interpolation methods allow for representative recording of fast transient signals, thus avoiding potential problems with aliasing, as previously reported for other strategies (Norris et al., 2021; Van Malderen et al., 2018). Moreover, including multiple sweeps in a single square pixel also reduces the element LODs per pixel, thus significantly improving element detectability for our LA-ICP-MS mapping protocol. The data reduction method implemented in XMapTools has the flexibility of using any value of n, the number of sweeps per square pixel, which is determined by the user's LA-ICP-MS setup as detailed above. The interpolation is performed on a rectangular Cartesian grid with a pixel size equal to the beam diameter. In practice, the scanning speed and the number of sweeps integrated into one squared pixel can be calculated by utilizing equation 2.2.3.

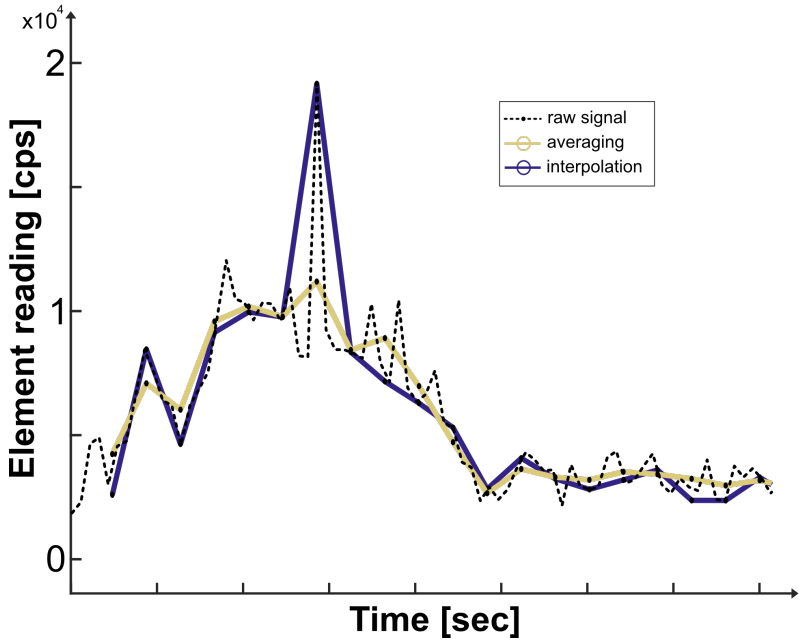

Figure 2.12: Transformation of the raw intensity signal to intensities used for maps, based on a single-scan example. The method of the commonly used average (yellow line) and interpolation method presented in this work (blue line) are shown for comparison. Both interpolation and averaging take three raw signal measurements into account before transforming them to one value.

We developed a virtual mapping example to further illustrate and quantify the potential artefacts of the interpolation approach. A "real intensity map" is created with an ultra-high resolution (1×10-2 µm). This program measures the intensity acquired for a given beam size and scan speed by averaging a shape corresponding to the scanned surface of each sweep. It simulates the results of a measurement from a LA-ICP-MS system, and the data extracted from the simulation underwent the same interpolation approach as implemented in XMapTools. In Figure 2.13, a band of 10 µm width oriented perpendicular to the scanning direction is shown, which has a pixel value of 34 µg/g. Each experiment has a fixed value of 3 sweeps per pixel (n=3). If the beam size is twice the width of the band, the maximum intensity is reduced by ∼33% and the distance of a mixed signal intensity into the pixel is roughly 3 times the width of the band. When the beam size is similar to the width of the band the true feature size is measured whereas the maximum intensity is still reduced by ∼5%. The slight increase in the measured intensity before the annulus also shows a possible smearing effect which still occurs with similar spot size to the feature. Our finding is consistent with the results on analytical convolution artefacts presented by Jollands (2020). As shown in the maps of sample DKE-352, the true composition of any feature can be resolved for cases where the feature size corresponds to at least two times the beam size. For pure scanning perpendicular to mineralogical or chemical features, the use of rectangular beam shapes can help in their spatial resolution (e.g. Jollands, 2020).

In theory, the presented interpolation method can spatially resolve the true composition of features as small as the beam diameter, but with a subordinate smoothing effect (Fig. 2.13c).

Determination of element-specific LOD per pixel in LA-ICP-MS maps

Quantified element maps are effective at showing regions of similar composition and relative differences such as zoning patterns as shown in several published studies (Ahmed et al., 2020; Bovay et al., 2022; Bussweiler et al., 2020; Drost et al., 2018; Fox et al., 2017; Gaidies & George, 2021; George et al., 2018; Gundlach-Graham et al., 2018; Hagen-Peter et al., 2021; McCarron et al., 2014; Paul et al., 2014; Petrus et al., 2017; Piccoli et al., 2022; Raimondo et al., 2017; Rittner & Müller, 2012; Savard et al., 2023; Tamblyn et al., 2021; Tamblyn et al., 2020; Tual et al., 2022; Ubide et al., 2015; Ulrich et al., 2009; Woodhead et al., 2016). However, none of the cited studies compute LOD maps and only a few filter the quantified maps to assess which pixel values were detected at statistically defined confidence. To date, only Gundlach-Graham et al. (2018) have calculated the LOD per pixel using a single laser pulse and filtering resulting maps. Rubatto et al. (2020) developed an approach to determine the LOD per pixel based on the mass removed per pixel in the sample. Additionally, Rittner and Müller (2012) discard pixels with values below an average LOD. Other studies have only defined regions within the mapped areas, extracted the data, and calculated the LOD or limit of quantification (LOQ) from such ROIs (Petrus et al., 2017; Raimondo et al., 2017; Zhu et al., 2016). Conversely, the LOD calculation presented in our work is based on equation 2.2.1 proposed by Pettke et al. (2012) and provides the LOD for each pixel at 95% confidence in a classified and calibrated phase. The magnitude of the LOD is dependent on the number of sweeps in each pixel and the sensitivity during measurement, and the user can influence this by selecting appropriate map measurement settings. The software XMapTools allows the user to view each LOD map calculated for each element individually, and the final maps can then be filtered for LOD by user selection. Mapping experiments in this study included up to 38 analytes in the element list and no measurement artefacts are detected in the generated maps. Low abundance elements in the mapped phases may go undetected (as they are below the LOD) depending on the sampling parameters (Fig. 2.6 and Supplementary Material 2). Maps of Ba in sample BA1013 show that the sampling parameters influence the LOD, as expected (Fig. 2.7d). The 20 µm spot map has an LOD of ~3 µg/g for Ba and is half the LOD calculated for the 10 µm spot size map. Variations in the LOD values are the result of the sensitivity factor and therefore the pixel intensities recorded (see Eq. 1). The Lu maps in garnet from sample DKE-352 provide an example of when the LOD is reached for domains of relatively low Lu abundance (Figs.2.6d-f). In the case where no filter is applied for the pixels, Lu appears to be detected in low abundance domains and may even

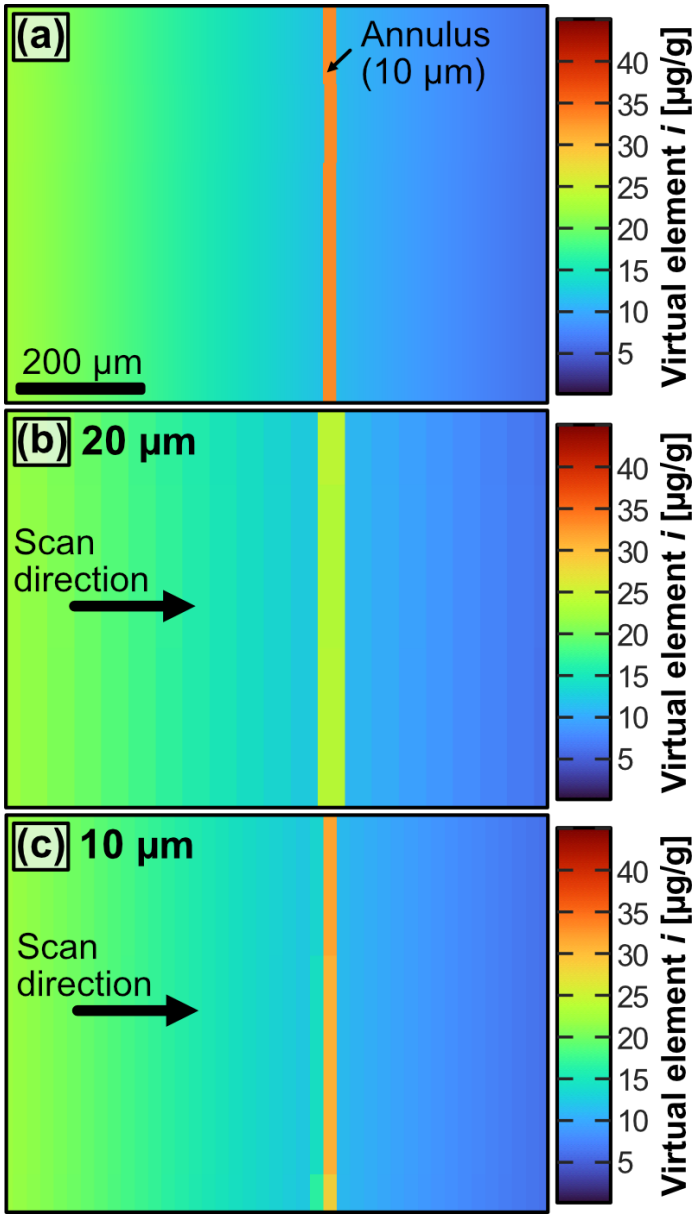

Figure 2.13: Virtual mapping of an annulus of higher content with different spot sizes. (a) The virtual distribution of element i in a phase is shown with a band width of 10 µm and a composition of 34 µg/g. (b) Virtual results from scanning with LA-ICP-MS using a spot size of 20 µm. (c) Virtual results from scanning with LA-ICP-MS using a spot size of 10 µm. (b-c) Direction of scanning is from left to right in the images (black arrow).

resolve a zoning pattern, although the average LOD for Lu is 0.2 µg/g for the map 1.1 and 0.7 µg/g for map 1.2 and 1.3. Similarly, Raimondo et al. (2017) present continuous zoned maps of Lu in garnet that reach low values of Lu with values below 1 µg/g. Filtering the image for pixels that are below the calculated LOD identifies ∼6% of the REE pixel data as non-significant in map 1.1 (Fig. 2.6d) and ∼35% in maps 1.2 and 1.3 (Figs.2.6e-f), all displayed as black pixels. Maps are intended to guide the eye to read chemical information; therefore, we consider filtering pixels for LOD to be mandatory for removing potentially misleading information. An LOD filter represents a prerequisite for preventing data below the LOD from being interpreted (see examples in Figs. 2.14 & 2.15).

2.5.2 Application examples

Major and trace element mapping is essential to resolve, recognize, and interpret spatial variations in geochemical patterns, to eventually better understand petrogenetic processes. With the three application examples presented we now showcase the potential of multi-mineral mapping for the investigation of metamorphic processes.

Garnet DKE-352

Spatial correlation of chemical signatures in garnet has the potential to reveal mechanisms of crystal growth, recrystallization and resorption, element diffusion, elemental (re)distribution and open-system processes during metamorphism (George & Gaidies, 2017; Raimondo et al., 2017; Rubatto et al., 2020). For example, major and trace element maps show that the garnet in sample DKE-352 contains concentric zoning (Figs. 2.5 &2.6). The garnet core major element zonation patterns (Ca, Mn) correlate with enrichments in V and Cr (and to a lesser extent Ti and Zr; Supp. Fig. S1) and low Lu, Dy, and Y contents (Figs. 2.5 &2.6). The enrichment in the slow-diffusing elements V, Cr, Ti, and Zr are related to the presence of former minerals which were located in the garnet core prior to garnet growth (Angiboust et al., 2014; Moore et al., 2013; Spandler et al., 2011). Mapping also shows that the core is encircled by an increase in Mn and a sharp increase in the REE content, forming a double annulus. This double annulus is best seen at the highest spatial resolution used for mapping, which is a spot size of 5 µm. The formation of an annulus in garnet, especially in Y+REE, as seen for Dy and Lu (Fig. 2.6) and Y+HREE (Fig. 2.14 and Supplementary Material 2), is often associated with the breakdown of major and/or accessory phases, for example allanite (Boston et al., 2017; Gieré et al., 2011; Pyle & Spear, 2003), but no enrichment in Ca or Sr is detected. The REE pattern also shows an increase in MREE from core to mantle (Fig. 2.14), which may be related to allanite and/or lawsonite breakdown (Spandler et al., 2003). The rim again shows an increase in HREE and a decrease in MREE, a zonation which is also visible on the major element

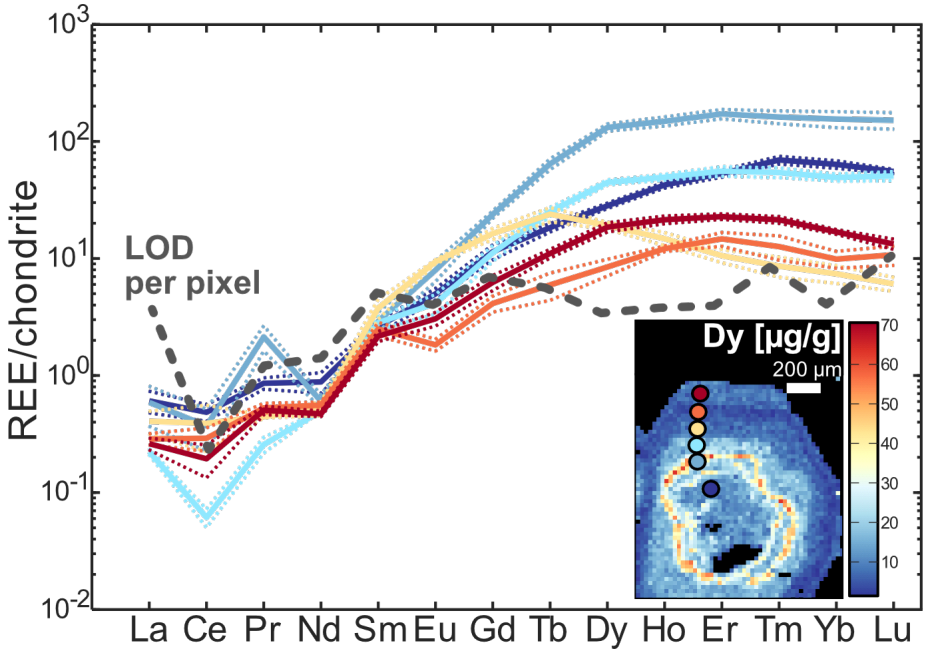

Figure 2.14: Chondrite-normalized REE patterns for six circular ROIs from core to rim (blue to red) in the garnet grain of sample DKE-352. The annulus (gray-blue curve) shows enrichment in HREE, while the mantle region (yellow curve) shows enrichment in MREE and depletion in HREE. The rim region again shows a depletion in MREE and enrichment in HREE. Data is extracted using the Spider module of XMapTools. The gray dashed line represents the average LOD per pixel for the REE. Colored dashed lines represent the 1 SE of the integrated value of the ROI. Normalization follows Taylor and McLennan (1985).

maps and that can be related to changes in bulk and REE composition. Radial veinlets in X_{sps} are not visible in trace elements, but may be the result of a selective replacement process (Rubatto et al., 2020).

Migmatite BA1013

In the migmatitic sample, we demonstrate effective mapping of a large area of two genetically distinct domains (the leucosome, or melt domain, and the residuum) that contain relatively small-scale features. Biotite is enriched in the transition metals Sc, Ti, V, Cr, Mn, Fe, Co, Zn, Zr, and depleted in Li and Rb in the leucosome compared to the residuum (Figs. 2.10e-h and Supplementary Material 2). In biotite, patchy zoning is observed for Ba and Cr with comparatively higher contents preserved in the large grain within the leucosome. Interestingly, the transition metals are preserved in peritectic biotite at the melting temperature of 750 °C (Icenhower & London, 1995; Kunz et al., 2022), whereas Li and Rb were mobilized by the melt and enriched in the leucosome (Icenhower & London, 1996). Similarly, Sr contents in plagioclase and K-feldspar show a continuous decrease towards the residuum (Figs. 2.10a-b). REE maps also show La and Nd enriched sites in plagioclase located in the residuum which correlate with the highest anorthite compo-

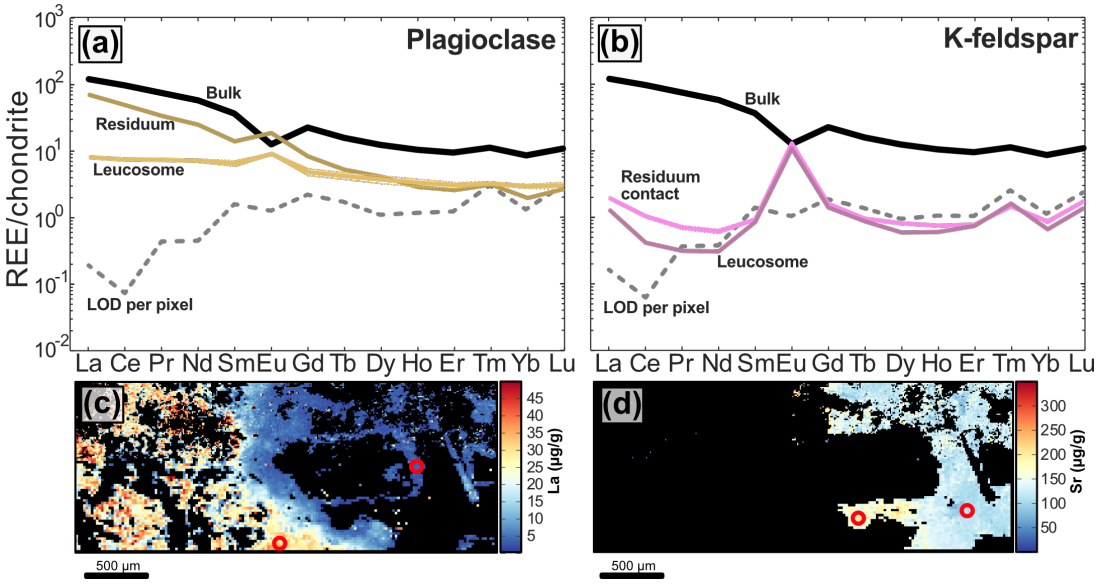

Figure 2.15: Chondrite-normalized REE patterns for circular ROIs in sample BA1013. (a) Plagioclase REE patterns from two ROIs, one in the leucosome and one in the residuum. (b) K-feldspar REE patterns from two ROIs, one in the leucosome and one at the contact to the residuum. (c-d) Map of La in plagioclase and Sr in K-feldspar guide the selection of the ROIs (red circles). (a–b) REE pattern of the local bulk composition by integrating biotite, plagioclase and K-feldspar (black solid line). Gray dashed line represents the averaged LOD per pixel of REE in plagioclase and K-feldspar respectively. Normalization follows Taylor and McLennan (1985).

sition (Figs. 2.10c-d and Fig. 2.8). The spatial relationships can be selected for closer examination of REE patterns using ROIs plotted in a chondrite-normalized trace element distribution diagram (Fig. 2.15). The leucosome domain shows systematic depletion in LREE for plagioclase and K-feldspar compared to the residuum.

Rutile AS19-3

The combination of trace element patterns and a thermometer or barometer can allow for linking element behaviour and metamorphic conditions, e.g., the connection between fluid pulses and thermal conditions in subduction zones Meinhold (2010). Rutile can provide temperature information from Zr-in-rutile thermometry (Cherniak et al., 2007; Tomkins et al., 2007; Zack et al., 2004) and is able to incorporate a variety of trace elements. Mapping of rutile from sample AS19-3 reveals strong compositional zoning, for example, zoning of Zr in at least five different domains with a range of ∼30 µg/g. Temperatures calculated from the Zr-in-rutile thermometer according to equation 8 in Tomkins et al. (2007) reveal a significant temperature variation of ∼40 °C, ranging from 510 to 550 °C (see Fig. 2.11). To the contrast, a series of single spot analysis could potentially yield a similar temperature range, and most likely would be interpreted to be homogeneous due to the uncertainty of

the method. Visualization of the sharp Zr zoning pattern could not be reconstructed by traditional single spot analysis, but can assist in interpreting the formation of the rutile grain. In addition, similar zoning patterns can be observed in other trace elements (e.g., Ta 70 to 180 µg/g, Fig. 2.11). This might support that zoning domains are the result of multiple growth episodes, as Zr incorporation in rutile is expected to be temperature dependent when the system is in equilibrium and the assemblage is zircon buffered Tomkins et al. (e.g. 2007) and Zack et al. (2004). Furthermore, the sharp zoning of trace elements now visible in the maps indicates that diffusion did not play a major role in the post-crystallization history of this rutile grain, as is commonly assumed for grains larger than 200 µm at temperatures of around 500 °C (Cherniak et al., 2007).

2.6 Conclusion

The detailed comparison between EPMA and LA-ICP-MS data shows that for well calibrated instruments compositional mapping by LA-ICP-MS is robust not only for trace elements but also for major and minor elements. Structural formula and end-member fraction maps can be calculated from LA-ICP-MS data with a quality similar to EPMA mapping. In addition, thermobarometry is more precise than EPMA even when based on major elements (e.g., X_{Mg}) and minor elements (Ti-in-biotite). However, achieving such a high level of accuracy requires calibration over a variable composition for the internal standard element in cases where the phases of interest are chemically variable. In addition, the use of multiple external standards offers the possibility of improving the accuracy of the trace element mass fraction, especially for specific element contents that may not be precisely known in a given external standard material. Moreover, our procedures provide the calculation of LODs for each pixel individually with 95% confidence, thus preventing the interpretation of non-significant data on maps. These novel features are incorporated into the calibration procedure and implemented in XMapTools. Increasing the spatial resolution by decreasing the spot size results in an improved resolution of geochemical features in relatively small mineral grains, but at the expense of chemical detection power, i.e., increasing LODs as shown on LOD maps. Moreover, while a larger spot size provides better chemical detection power, a low spatial resolution can result in a mixing composition for grains and other chemical features. We also found that directional scanning and lower spatial resolution can lead to a deviation in the true value of a geochemical feature. Using the proposed squared pixel interpolation method and virtual mapping test, we show that the true composition can be resolved when the beam diameter is equal to, or smaller than, the feature size, but may contain a smoothing effect. Finding a way to minimize the smoothing and mixing effect is desirable as it can affect the application of e.g., trace element diffusion modelling in garnet based on quantitative data from maps. Regardless, the novel procedure

described in this paper improves the analysis, calibration and open-source software tools available to understand major and trace elements in LA-ICP-MS maps.

Bibliography

Ahmed, A. D., Hood, S. B., Cooke, D. R., & Belousov, I. (2020). Unsupervised clustering of LA-ICP-MS raster map data for geological interpretation: A case study using epidote from the Yerington district, Nevada. *Applied Computing and Geosciences*, *8*, 100036. https://doi.org/10.1016/j.acags.2020.100036

Angiboust, S., Pettke, T., De Hoog, J. C. M., Caron, B., & Oncken, O. (2014). Channelized Fluid Flow and Eclogite-facies Metasomatism along the Subduction Shear Zone. *Journal of Petrology*, *55*(5), 883–916. https://doi.org/10.1093/petrology/egu010

Bissig, T., & Hermann, J. (1999). From pre-Alpine extension to Alpine convergence: The example of the southwestern margin of the Margna nappe (Val Malenco, N-Italy). *Schweizerische Mineralogische und Petrographische Mitteilungen*, *79*(3), 363–380.

Boston, K. R., Rubatto, D., Hermann, J., Engi, M., & Amelin, Y. (2017). Geochronology of accessory allanite and monazite in the Barrovian metamorphic sequence of the Central Alps, Switzerland. *Lithos*, *286-287*, 502–518. https://doi.org/10.1016/j.lithos.2017.06.025

Bovay, T., Lanari, P., Rubatto, D., Smit, M., & Piccoli, F. (2022). Pressure–temperature–time evolution of subducted crust revealed by complex garnet zoning (Theodul Glacier Unit, Switzerland). *Journal of Metamorphic Geology*, *40*(2), 175–206. https://doi.org/10.1111/jmg.12623

Bussweiler, Y., Gervasoni, F., Rittner, M., Berndt, J., & Klemme, S. (2020). Trace element mapping of high-pressure, high-temperature experimental samples with laser ablation ICP time-of-flight mass spectrometry – Illuminating melt-rock reactions in the lithospheric mantle. *Lithos*, *352-353*, 105282. https://doi.org/10.1016/j.lithos.2019.105282

Cherniak, D. J., Manchester, J., & Watson, E. B. (2007). Zr and Hf diffusion in rutile. *Earth and Planetary Science Letters*, *261*(1-2), 267–279. https://doi.org/10.1016/j.epsl.2007.06.027

Chew, D., Drost, K., Marsh, J. H., & Petrus, J. A. (2021). LA-ICP-MS imaging in the geosciences and its applications to geochronology. https://doi.org/10.1016/j.chemgeo.2020.119917

Drost, K., Chew, D., Petrus, J. A., Scholze, F., Woodhead, J. D., Schneider, J. W., & Harper, D. A. T. (2018). An Image Mapping Approach to U-Pb LA-ICP-MS Carbonate Dating and Applications to Direct Dating of Carbonate Sedimentation. *Geochemistry, Geophysics, Geosystems*, *19*(12), 4631–4648. https://doi.org/10.1029/2018GC007850

Fox, M., Tripathy-Lang, A., & Shuster, D. L. (2017). Improved spatial resolution of elemental maps through inversion of LA-ICP-MS data. *Chemical Geology*, *467*(July), 30–41. https://doi.org/10.1016/j.chemgeo.2017.07.001

Gaidies, F., & George, F. R. (2021). The interfacial energy penalty to crystal growth close to equilibrium. *Geology*, *49*(8), 988–992. https://doi.org/https://doi.org/10.1130/G48715.1

Ganade de Araujo, C. E., Weinberg, R. F., & Cordani, U. G. (2014). Extruding the Borborema Province (NE-Brazil): a two-stage Neoproterozoic collision process. *Terra Nova*, *26*(2), 157–168. https://doi.org/10.1111/ter.12084

George, F. R., & Gaidies, F. (2017). Characterisation of a garnet population from the Sikkim Himalaya: insights into the rates and mechanisms of porphyroblast crystallisation. *Contributions to Mineralogy and Petrology*, *172*(7). https://doi.org/10.1007/s00410-017-1372-y

George, F. R., Gaidies, F., & Boucher, B. (2018). Population-wide garnet growth zoning revealed by LA-ICP-MS mapping: implications for trace element equilibration and syn-kinematic deformation during crystallisation. *Contributions to Mineralogy and Petrology*, *173*(9), 1–22. https://doi.org/10.1007/s00410-018-1503-0

Gieré, R., Rumble, D., Günther, D., Connolly, J. A., & Caddick, M. J. (2011). Correlation of growth and breakdown of major and accessory minerals in metapelites from Campolungo, Central Alps. *Journal of Petrology*, *52*(12), 2293–2334. https://doi.org/10.1093/petrology/egr043

Guillong, M., Meier, D. L., Allan, M. M., Heinrich, C. A., & Yardley, B. W. D. (2008). SILLS: A Matlab-Based Program for the Reduction of Laser Ablation ICP–MS Data of Homogeneous Materials and Inclusions. *Mineralogical Association of Canada Short Course*, *40*, 328–333.

Gundlach-Graham, A., Garofalo, P. S., Schwarz, G., Redi, D., & Günther, D. (2018). High-resolution, Quantitative Element Imaging of an Upper Crust, Low-angle Cataclasite (Zuccale Fault, Northern Apennines) by Laser Ablation ICP Time-of-Flight Mass Spectrometry. *Geostandards and Geoanalytical Research*, *42*(4), 559–574. https://doi.org/10.1111/ggr.12233

Gundlach-Graham, A., & Günther, D. (2016). Toward faster and higher resolution LA-ICPMS imaging: On the co-evolution of la cell design and ICPMS instrumentation Young Investigators in Analytical and Bioanalytical Science. *Analytical and Bioanalytical Chemistry*, *408*(11), 2687–2695. https://doi.org/10.1007/s00216-015-9251-8

Günther, D., & Hattendorf, B. (2005). Solid sample analysis using laser ablation inductively coupled plasma mass spectrometry. *TrAC Trends in Analytical Chemistry*, *24*(3), 255–265. https://doi.org/10.1016/j.trac.2004.11.017

Hagen-Peter, G., Wang, Y., Hints, O., Prave, A. R., & Lepland, A. (2021). Late diagenetic evolution of Ordovician limestones in the Baltoscandian basin revealed through trace-element mapping and in situ U–Pb dating of calcite. *Chemical Geology*, *585*(September), 120563. https://doi.org/10.1016/j.chemgeo.2021.120563

Halter, W. E., Pettke, T., Heinrich, C. A., & Rothen-Rutishauser, B. (2002). Major to trace element analysis of melt inclusions by laser-ablation ICP-MS: Methods of quantification. *Chemical Geology*, *183*(1-4), 63–86. https://doi.org/10.1016/S0009-2541(01)00372-2

Henry, D. J., Guidotti, C. V., & Thomson, J. A. (2005). The Ti-saturation surface for low-to-medium pressure metapelitic biotites: Implications for geothermometry and Ti-substitution mechanisms. *American Mineralogist*, *90*(2-3), 316–328. https://doi.org/10.2138/am.2005.1498

Icenhower, J., & London, D. (1995). An experimental study of element partitioning among biotite, muscovite, and coexisting peraluminous silicic melt at 200 MPa (H2 O). *American Mineralogist*, *80*(11-12), 1229–1251. https://doi.org/10.2138/am-1995-11-1213

Icenhower, J., & London, D. (1996). Experimental partitioning of Rb, Cs, Sr, and Ba between alkali feldspar and peraluminous melt. *American Mineralogist*, *81*(5-6), 719–734. https://doi.org/10.2138/am-1996-5-619

Jochum, K. P., Willbold, M., Raczek, I., Stoll, B., & Herwig, K. (2005). Chemical Characterisation of the USGS Reference Glasses GSA-1G, GSC-1G, GSD-1G, GSE-1G, BCR-2G, BHVO-2G and BIR-1G Using EPMA, ID-TIMS, ID-ICP-MS and LA-ICP-MS. *Geostandards and Geoanalytical Research*, *29*(3), 285–302. https://doi.org/10.1111/j.1751-908X.2005.tb00901.x

Jollands, M. C. (2020). Assessing analytical convolution effects in diffusion studies: Applications to experimental and natural diffusion profiles (M. Lepidi, Ed.). *PLOS ONE*, *15*(11), e0241788. https://doi.org/10.1371/journal.pone.0241788

Konrad-Schmolke, M., Halama, R., Chew, D., Heuzé, C., De Hoog, J. C. M., & Ditterova, H. (2023). Discrimination of thermodynamic and kinetic contributions to the heavy rare earth element patterns in metamorphic garnet. *Journal of Metamorphic Geology*, *41*(4), 465–490. https://doi.org/10.1111/jmg.12703

Kunz, B. E., Warren, C. J., Jenner, F. E., Harris, N. B., & Argles, T. W. (2022). Critical metal enrichment in crustal melts: The role of metamorphic mica. *Geology*, *50*(11), 1219–1223. https://doi.org/10.1130/G50284.1

Lanari, P., & Piccoli, F. (2020). New horizons in quantitative compositional mapping – Analytical conditions and data reduction using XMapTools. *IOP Conference Series: Materials Science and Engineering*, *891*(1), 012016. https://doi.org/10.1088/1757-899X/891/1/012016

Lanari, P., Markmann, T., Laughton, J., & Tedeschi, M. (2023). xmaptools/XMapTools_Public: XMapTools 4.2. https://doi.org/10.5281/zenodo.7656957

Lanari, P., Vho, A., Bovay, T., Airaghi, L., & Centrella, S. (2019). Quantitative compositional mapping of mineral phases by electron probe micro-analyser. *Geological Society, London, Special Publications*, *478*(1), 39–63. https://doi.org/10.1144/SP478.4

Lanari, P., Vidal, O., De Andrade, V., Dubacq, B., Lewin, E., Grosch, E. G., & Schwartz, S. (2014). XMapTools: A MATLAB©-based program for electron microprobe X-ray image processing and geothermobarometry. *Computers and Geosciences*, *62*, 227–240. https://doi.org/10.1016/j.cageo.2013.08.010

Laughton, J. (2023). PTtoolbox. https://doi.org/10.5281/zenodo.10040860

Longerich, H. P., Jackson, S. E., & Günther, D. (1996). Laser ablation inductively coupled plasma mass spectrometric transient signal data acquisition and analyte concentration calculation. *Journal of Analytical Atomic Spectrometry*, *11*(9), 899–904. https://doi.org/10.1039/JA9961100899

McCarron, T., Gaidies, F., McFarlane, C. R. M., Easton, R. M., & Jones, P. (2014). Coupling thermodynamic modeling and high-resolution in situ LA-ICP-MS monazite geochronology: evidence for Barrovian metamorphism late in the Grenvillian history of southeastern Ontario. *Mineralogy and Petrology*, *108*(6), 741–758. https://doi.org/10.1007/s00710-014-0343-5

Meinhold, G. (2010). Rutile and its applications in earth sciences. *Earth-Science Reviews*, *102*(1), 1–28. https://doi.org/https://doi.org/10.1016/j.earscirev.2010.06.001

Moore, S. J., Carlson, W. D., & Hesse, M. A. (2013). Origins of yttrium and rare earth element distributions in metamorphic garnet. *Journal of Metamorphic Geology*, *31*(6), 663–689. https://doi.org/10.1111/jmg.12039

Norris, C. A., Danyushevsky, L., Olin, P., & West, N. R. (2021). Elimination of aliasing in LA-ICP-MS by alignment of laser and mass spectrometer. *Journal of Analytical Atomic Spectrometry*, *36*(4), 733–739. https://doi.org/10.1039/d0ja00488j

Paton, C., Hellstrom, J., Paul, B., Woodhead, J. D., & Hergt, J. (2011). Iolite: Freeware for the visualisation and processing of mass spectrometric data. *Journal of Analytical Atomic Spectrometry*, *26*(12), 2508–2518. https://doi.org/10.1039/c1ja10172b

Paul, B., Paton, C., Norris, A., Woodhead, J. D., Hellstrom, J., Hergt, J., & Greig, A. (2012). CellSpace: A module for creating spatially registered laser ablation images within the Iolite freeware environment. *Journal of Analytical Atomic Spectrometry*, *27*(4), 700. https://doi.org/10.1039/c2ja10383d

Paul, B., Woodhead, J. D., Paton, C., Hergt, J. M., Hellstrom, J., & Norris, C. A. (2014). Towards a Method for Quantitative LA-ICP-MS Imaging of Multi-Phase Assemblages: Mineral Identification and Analysis Correction Procedures. *Geostandards*

and Geoanalytical Research, *38*(3), 253–263. https://doi.org/10.1111/j.1751-908X.2014.00270.x

Petrus, J. A., Chew, D. M., Leybourne, M. I., & Kamber, B. S. (2017). A new approach to laser-ablation inductively-coupled-plasma mass-spectrometry (LA-ICP-MS) using the flexible map interrogation tool 'Monocle'. *Chemical Geology*, *463*(May), 76–93. https://doi.org/10.1016/j.chemgeo.2017.04.027

Pettke, T., Heinrich, C. A., Ciocan, A. C., & Günther, D. (2000). Quadrupole mass spectrometry and optical emission spectroscopy: detection capabilities and representative sampling of short transient signals from laser-ablation. *J. Anal. At. Spectrom.*, *15*(9), 1149–1155. https://doi.org/10.1039/B001910K

Pettke, T., Oberli, F., Audétat, A., Guillong, M., Simon, A. C., Hanley, J. J., & Klemm, L. M. (2012). Recent developments in element concentration and isotope ratio analysis of individual fluid inclusions by laser ablation single and multiple collector ICP-MS. *Ore Geology Reviews*, *44*, 10–38. https://doi.org/10.1016/j.oregeorev.2011.11.001

Phillips, S. E., Argles, T. W., Warren, C. J., Harris, N. B. W., & Kunz, B. E. (2023). Kyanite petrogenesis in migmatites: resolving melting and metamorphic signatures. *Contributions to Mineralogy and Petrology*, *178*(2), 10. https://doi.org/10.1007/s00410-022-01991-w

Piccoli, F., Lanari, P., Hermann, J., & Pettke, T. (2022). Deep subduction, melting, and fast cooling of metapelites from the Cima Lunga Unit, Central Alps. *Journal of Metamorphic Geology*, *40*(1), 121–143. https://doi.org/10.1111/jmg.12621

Plotnikov, A., Vogt, C., Wetzig, K., & Kyriakopoulos, A. (2008). A theoretical approach to the interpretation of the transient data in scanning laser ablation inductively coupled plasma mass spectrometry: Consideration of the geometry of the scanning area. *Spectrochimica Acta Part B: Atomic Spectroscopy*, *63*(4), 474–483. https://doi.org/10.1016/j.sab.2007.12.012

Pyle, J. M., & Spear, F. S. (2003). Yttrium zoning in garnet: Coupling of major and accessory phases during metamorphic reactions. *American Mineralogist*, *88*(4), 708.

Raimondo, T., Payne, J., Wade, B., Lanari, P., Clark, C., & Hand, M. (2017). Trace element mapping by LA-ICP-MS: assessing geochemical mobility in garnet. *Contributions to Mineralogy and Petrology*, *172*(4), 17. https://doi.org/10.1007/s00410-017-1339-z

Riel, N., Guillot, S., Jaillard, E., Martelat, J.-E., Paquette, J.-L., Schwartz, S., Goncalves, P., Duclaux, G., Thebaud, N., Lanari, P., Janots, E., & Yuquilema, J. (2013). Metamorphic and geochronogical study of the Triassic El Oro metamorphic complex, Ecuador: Implications for high-temperature metamorphism in a forearc zone. *Lithos*, *156-159*, 41–68. https://doi.org/10.1016/j.lithos.2012.10.005

Rittner, M., & Müller, W. (2012). 2D mapping of LA-ICPMS trace element distributions using R. *Computers and Geosciences*, *42*, 152–161. https://doi.org/10.1016/j.cageo.2011.07.016

Rubatto, D., Burger, M., Lanari, P., Hattendorf, B., Schwarz, G., Neff, C., Keresztes Schmidt, P., Hermann, J., Vho, A., & Günther, D. (2020). Identification of growth mechanisms in metamorphic garnet by high-resolution trace element mapping with LA-ICP-TOFMS. *Contributions to Mineralogy and Petrology*, *175*(7), 61. https://doi.org/10.1007/s00410-020-01700-5

Savard, D., Dare, S., Bédard, L. P., & Barnes, S.-j. (2023). A New Mapping Protocol for Laser Ablation (with Fast-Funnel) Coupled to a Time-of-Flight Mass Spectrometer (LA-FF-ICP-ToF-MS) for the Rapid, Simultaneous Quantification of Multiple Minerals. *Geostandards and Geoanalytical Research*, 1–23. https://doi.org/10.1111/ggr.12482

Spandler, C., Hermann, J., Arculus, R., & Mavrogenes, J. (2003). Redistribution of trace elements during prograde metamorphism from lawsonite blueschist to eclogite facies; implications for deep subduction-zone processes. *Contributions to Mineralogy and Petrology*, *146*(2), 205–222. https://doi.org/10.1007/s00410-003-0495-5

Spandler, C., Pettke, T., & Rubatto, D. (2011). Internal and external fluid sources for eclogite-facies veins in the Monviso Meta-ophiolite, Western Alps: Implications for fluid flow in subduction zones. *Journal of Petrology*, *52*(6), 1207–1236. https://doi.org/10.1093/petrology/egr025

Tamblyn, R., Brown, D., Hand, M., Morrissey, L., Clark, C., & Anczkiewicz, R. (2021). The 2 Ga eclogites of Central Tanzania: Directly linking age and metamorphism. *Lithos*, *380-381*, 105890. https://doi.org/10.1016/j.lithos.2020.105890

Tamblyn, R., Hand, M., Kelsey, D., Anczkiewicz, R., & Och, D. (2020). Subduction and accumulation of lawsonite eclogite and garnet blueschist in eastern Australia. *Journal of Metamorphic Geology*, *38*(2), 157–182. https://doi.org/10.1111/jmg.12516

Taylor, S. R., & McLennan, S. M. (1985). *The Continental Crust: Its Composition and Evolution*. Blackwell, Oxford.

Tomkins, H. S., Powell, R., & Ellis, D. J. (2007). The pressure dependence of the zirconium-in-rutile thermometer. *Journal of Metamorphic Geology*, *25*(6), 703–713. https://doi.org/10.1111/j.1525-1314.2007.00724.x

Tracy, R. J. (1982, December). Chapter 9. COMPOSITIONAL ZONING and INCLUSIONS in METAMORPHIC MINERALS. In *Characterization of metamorphism through mineral equilibria* (pp. 354–398, Vol. 501). De Gruyter. https://doi.org/10.1515/9781501508172-013

Tual, L., Smit, M. A., Cutts, J., Kooijman, E., Kielman-Schmitt, M., Majka, J., & Foulds, I. (2022). Rapid, paced metamorphism of blueschists (Syros, Greece) from laser-based

zoned Lu-Hf garnet chronology and LA-ICPMS trace element mapping. *Chemical Geology*, *607*(January), 121003. https://doi.org/10.1016/j.chemgeo.2022.121003

Ubide, T., McKenna, C. A., Chew, D. M., & Kamber, B. S. (2015). High-resolution LA-ICP-MS trace element mapping of igneous minerals: In search of magma histories. *Chemical Geology*, *409*, 157–168. https://doi.org/10.1016/j.chemgeo.2015.05.020

Ulrich, T., Kamber, B. S., Jugo, P. J., & Tinkham, D. K. (2009). Imaging element- distribution patterns in minerals by Laser Ablation–Inductively Coupled Plasma–Mass Spectrometry (LA–ICP–MS). *The Canadian Mineralogist*, *47*(5), 1001–1012. https://doi.org/10.3749/canmin.47.5.1001

Van Malderen, S. J., Van Elteren, J. T., & Vanhaecke, F. (2015). Development of a fast laser ablation-inductively coupled plasma-mass spectrometry cell for sub-μm scanning of layered materials. *Journal of Analytical Atomic Spectrometry*, *30*(1), 119–125. https://doi.org/10.1039/c4ja00137k

Van Malderen, S. J., van Elteren, J. T., Šelih, V. S., & Vanhaecke, F. (2018). Considerations on data acquisition in laser ablation-inductively coupled plasma-mass spectrometry with low-dispersion interfaces. *Spectrochimica Acta - Part B Atomic Spectroscopy*, *140*, 29–34. https://doi.org/10.1016/j.sab.2017.11.007

van Elteren, J. T., Šala, M., & Metarapi, D. (2021). Comparison of single pulse, multiple dosage, and 2D oversampling / deconvolution LA-ICPMS strategies for mapping of (ultra)low-concentration samples. *Talanta*, *235*(August), 122785. https://doi.org/10.1016/j.talanta.2021.122785

van Elteren, J. T., Šelih, V. S., & Šala, M. (2019). Insights into the selection of 2D LA-ICP-MS (multi)elemental mapping conditions. *Journal of Analytical Atomic Spectrometry*, *34*(9), 1919–1931. https://doi.org/10.1039/C9JA00166B

Warr, L. N. (2021). IMA–CNMNC approved mineral symbols. *Mineralogical Magazine*, *85*(3), 291–320. https://doi.org/10.1180/mgm.2021.43

Woodhead, J. D., Hellstrom, J., Hergt, J. M., Greig, A., & Maas, R. (2007). Isotopic and Elemental Imaging of Geological Materials by Laser Ablation Inductively Coupled Plasma-Mass Spectrometry. *Geostandards and Geoanalytical Research*, *31*(4), 071117031212003–??? https://doi.org/10.1111/j.1751-908X.2007.00104.x

Woodhead, J. D., Hellstrom, J., Paton, C., Hergt, J., Greig, A., & Maas, R. (2008). A guide to depth profiling and imaging applications of ICP-MS. *Mineralogical Association of Canada short course series*, (40), 135–145.

Woodhead, J. D., Horstwood, M. S., & Cottle, J. M. (2016). Advances in isotope ratio determination by LA-ICP-MS. *Elements*, *12*(5), 317–322. https://doi.org/10.2113/gselements.12.5.317

Zack, T., Moraes, R., & Kronz, A. (2004). Temperature dependence of Zr in rutile: Empirical calibration of a rutile thermometer. *Contributions to Mineralogy and Petrology*, *148*(4), 471–488. https://doi.org/10.1007/s00410-004-0617-8

Zhu, Z.-Y., Cook, N., Yang, T., Ciobanu, C., Zhao, K.-D., & Jiang, S.-Y. (2016). Mapping of Sulfur Isotopes and Trace Elements in Sulfides by LA-(MC)-ICP-MS: Potential Analytical Problems, Improvements and Implications. *Minerals*, *6*(4), 110. https://doi.org/10.3390/min6040110

Chapter 3

Mechanical modelling in petrochemical models: implications for fluid extraction in subduction zones

Abstract

The dissolution of hydrous minerals during prograde metamorphism in subduction zones can result in an increase in fluid pressure due to volume changes associated with the reaction. The local changes in fluid pressure are evaluated through the integration of mechanical and petrological modelling. This approach combines a mechanical model based on Mohr-Coulomb theory with thermodynamic modelling using Gibbs energy minimisation, calculated by Theriak-Domino, and an oxygen isotope fractionation model. This combination enables the prediction of brittle failure based on thermodynamic calculations and considering volume changes, fluctuations in fluid pressure, and differential stress. The model demonstrates that metamorphic dehydration reactions are a principal factor in the mechanical integrity of the system. The limitation of fluid extraction to brittle failure events serves to emphasise the episodic extraction of fluids that occurs during metamorphism in subduction zones. The model is able to account for the formation of up to 4 vol% of fluid-filled porosity in the absence of brittle failure, which is in accordance with the findings of a number of geophysical studies. In serpentinites, the calculated time-averaged permeability values demonstrate episodes of high permeability (10^{-20} to 10^{-19} m^2), which can be linked to olivine formation in cm-sized veins, as well as in shear bands, and/or shear zones. The garnet from a metagabbro in the Monviso ophiolite complex in the Western Alps, shows a good correlation between the predicted frequency of brittle failure episodes and the oscillatory compositional zoning in Mn. The presence of veins, fractures, and shear zones within the crust effectively facilitates fluid flow. The episodic extraction of accumulated fluid can intensify the degree of fluid-rock interaction processes in subduction zones, which can subsequently affect mass transfer.

3.1 Introduction

There are several metamorphic reactions occurring in the Earth's crust and mantle that consume or produce aqueous fluids consisting of H_2O with small amounts of CO_2, CH_4 and other aqueous species. In subduction zones these fluids contribute largely to arc magmatism, mass transfer, and seismicity (Bebout & Penniston-Dorland, 2016; Etheridge et al., 2021; Hacker, Peacock, et al., 2003; Kerrick & Connolly, 2001; Kirby et al., 1996; Padrón-Navarta et al., 2010; Peacock, 2009; Saffer & Tobin, 2011; Sibson, 2013). During prograde metamorphism, the H_2O bounded in minerals is released as the minerals dissolve, contributing to the production of aqueous fluids. Released fluids can migrate vertically upward within rock grain boundaries or fractures, as they are less dense and volatile, and flow along grain boundaries, fractures, and other structural patterns (Ague & Nicolescu, 2014; Malvoisin et al., 2015). Brittle deformation in the crust has often been associated with fluid production during metamorphic reactions and fluid migration away from the production site (Cox, 2010; Etheridge, 1983; Giuntoli et al., 2024; Gold & Soter, 1984; Hacker, Abers, & Peacock, 2003). The movement of a fluid along grain boundaries is referred to as pervasive flow whereas a high conductive transfer is described as channelized flow (Ague & Nicolescu, 2014; Zack & John, 2007). There is evidence that dehydration can lead to both fluid channeling and pervasive fluid migration (Bovay et al., 2021; Huber et al., 2022; Stewart & Ague, 2020).

Two main approaches have been used in previous studies to gain a better understanding of fluid production and fluid flow in the crust.

- Global fluid fluxes have been investigated using petrological and/or petrochemical models based on equilibrium thermodynamics assuming that the fluid is instantaneously extracted from the rock system during a metamorphic reaction. Such models can predict the conditions under which a particular reaction will occur, estimate the magnitude of fluid fluxes and/or calculate the isotopic composition of the fluid. For example, garnet growth—often associated with a dehydration reaction—can be linked to water production during progressive burial in subduction zone (Baxter & Caddick, 2013). Models of reacting rock systems can also include calculation of the trace element budgets and partitioning between the fluid and rock (Konrad-Schmolke et al., 2011). These models have been used to study fluid-rock interaction processes, for example to explain the fluid-induced trace element patterns commonly observed in high-pressure minerals. In addition, the oxygen isotopic composition of the stable mineral and fluid phases can be simulated with such models for closed and open system conditions (Vho et al., 2020). Multi-layer models can simulate fluid production in specific lithologies such as serpentinites, and its infiltration into other lithologies such as mafic or metasedimentary layers and calculate the corresponding change in

the isotopic signature of the bulk and mineral phases. Similar simulations can be applied for the water transfer from the slab that is infiltrating the forearc mantle wedge, which causes serpentinization (Vho et al., 2020). Applying fluid transfer models to large-scale scenarios such as subduction zones can quantify not only the fluid fluxes associated to dehydration reactions, but also the amount of deeply subducted water that is recycled to the deep mantle (Gies et al., 2024). However, these models do not take into account the possible mechanical mechanisms that control fluid extraction, which is either instantaneous or occurring when the amount of fluid exceed a threshold value (Wilson et al., 2014).

- The second approach is to use thermomechanical models that can simulate fluid movement in porous media. These two-phase flow models involve porous compaction and viscous-plastic deformation of the solid matrix, mass and momentum conservation coupled with Darcy flow for the fluid (Connolly, 1997; Malvoisin et al., 2015; Mckenzie, 1984; Morishige & van Keken, 2018; Wang et al., 2019). Mass, momentum, and energy conservative equations are solved to describe the fluid or melt movement by compaction. Different matrixes and geological problems can be tested by using such an approach and exemplarily the transport velocity of major and trace elements in melt could be estimated (Mckenzie, 1984). A similar approach can also be applied to rocks that undergo devolatilisation reactions, which results in an aqueous fluid pressure gradient. The reaction front propagation can be described as a creep of porosity waves and imply the temporal focus of a fluid flux was identified couple to metamorphic dehydration (Connolly, 1997). The fluid pathways in a dehydrating subducting slab have been simulated using this approach, confirming the possibility of trenchward or arcward fluid movements (Morishige & van Keken, 2018; Wang et al., 2019). Typically, such 2D or 3D simulations are designed for km-scale models and rarely consider mineral reactions as predicted by thermodynamic models. Models that include deformation mechanisms rely on permeability and fluid viscosity, parameters that are still poorly constrained (Mckenzie, 1984; Morishige & van Keken, 2018; Wilson et al., 2014). Coupling of thermodynamic data with such models often comes with a trade-off. Either it has to neglect deformation or needs assumptions of fluid flow (buoyancy-driven) and/or requires simplified thermodynamic data for acceptable performance such as using precomputed look-up tables (Malvoisin et al., 2015). In addition, mineralogical and chemical reactions can affect viscous flow and estimated fluid release in subduction zone models, which in turn modify permeability and fluid migration (Beinlich et al., 2020; Bras et al., 2023; Plümper et al., 2012). Plümper et al. (2017) also showed that the fluid flow in dehydrating rocks does not necessarily follow a Darcy behaviour. Dehydration reactions are associated with the nucleation and growth of minerals and can often be described by a reaction front

propagating in a network.

None of the above approaches can explain increase in the P-to-S velocity ratio obtained from geophysical studies, which are interpreted to reflect zones of high fluid-filled porosity of up to 4 vol% (Abers et al., 2009; Audet et al., 2009; Egbert et al., 2022; Gosselin et al., 2020; Kodaira et al., 2004; Peacock, 2009; Peacock et al., 2011; Shiina et al., 2013). Controversially, the presence of free fluid in the crust is also often associated with extensional hydraulic fracturing or shear failure (Bukała et al., 2020; Cox, 2010; Cox et al., 1987; Etheridge, 1983; Etheridge et al., 1983; Jung et al., 2004; Niu et al., 2003; Secor, 1965; Sibson, 2017; Sippl et al., 2018). To date, there is no model that links metamorphic reactions and fluid production with a mechanical model that responses to the occurring volume changes of the system. Such a thermodynamically evolving system might link to the mechanical failure of rocks undergoing subduction zone metamorphism responsible for seismic activity. A preliminary attempt was proposed for melts, but is restricted to isobaric conditions (Etheridge et al., 2021).

In this study, we propose a framework for petrochemical modelling that combines chemical equilibrium calculations and isotope fractionation with a mechanical model of brittle rock failure. The implementation in Python® is distributed as an open-source modelling package ThorPT available at https://github.com/neoscalc/ThorPT. The thermodynamic calculations are performed using Theriak-Domino (de Capitani & Brown, 1987; de Capitani & Petrakakis, 2010) and combined with an oxygen isotope composition model (Vho et al., 2020). Fluid extraction from the considered system is associated with volume changes controlled by metamorphic reactions and is assumed to take place when brittle failure occurs. Mechanical failure is predicted using a mechanical model based on the Mohr-Coulomb theory. This integrated model is applied to different rock types to re-evaluate fluid extraction during the subduction of altered oceanic crust and to investigate possible triggers.

3.2 Mechanical model for rock failure and fluid extraction

3.2.1 Failure criteria

The occurrence and mechanisms of brittle deformation in rocks buried below the brittle-ductile transition is a standing debate in geology (e.g., Yamato et al., 2019). From the perspective of classical rock mechanics, brittle rock failure is described semi-quantitatively as a function of material properties (internal friction, tensile strength, and cohesion) and the differential stress (Jaeger, 1979; Sibson, 2013, and references therein). The failure envelope in normal stress versus shear stress space is defined as

$$\tau = C + (\sigma_n - P_f) \cdot \mu \tag{3.2.1}$$

where τ is the shear stress (in MPa), σn is the normal stress, and Pf is the fluid pressure with the material properties C for the rock cohesion (MPa) and μ the internal friction coefficient (see Figure 3.1). In this space, the stress state of the rock is represented by a circle, with a diameter equal to the differential stress. The differential stress can be obtained from the maximum and minimum normal stress

$$\Delta\sigma = \sigma_1 - \sigma_3 \tag{3.2.2}$$

The Griffith failure criterion is an extension of the Mohr-Coulomb failure criterion describing the complete failure envelope in shear stress against normal stress

$$\tau^2 = 4S^2 + 4S(\sigma_n - P_f) \tag{3.2.3}$$

where S is the tensile strength of the rock (MPa) and follows the empirical observation with the cohesion $C \approx 2S$ (see Figure 3.1; Griffits (1921), Jaeger (1979), Secor (1965), and Sibson (2000)).

In a rock without fluid, failure can only occur due to changes in the material properties (μ, C, or S; see Figure 3.1c) or by an increase in the shear stress on the system (Figure 3.1d). In a rock system including fluid, the fluid pressure applies a mechanical effect and acts as an additional tensile stress on the rock system (Figure 3.1e). The normal stress is reduced by the amount of the fluid pressure to an effective stress σ' defined as:

$$\sigma_1' = \sigma_1 - P_f, \quad \sigma_3' = \sigma_3 - P_f, \quad \text{and} \quad \sigma_n' = \sigma_n - P_f \tag{3.2.4}$$

This rock mechanics framework allows the failure of a rock to be evaluated in three different ways (Figure 3.1a). (1) Pure extensional failure as the brittle extensional failure, also known as hydraulic fracturing or mode 1 cracks, requires low differential stress expressed by the condition $\sigma < 4S$ and the minimum effective normal stress to overcome the tensile strength of the rock. The critical fluid pressure is defined as:

$$P_f^{\text{crit}} = \sigma_3 + S \tag{3.2.5}$$

(2) Extensional-shear failure, applies for intermediate differential stress values with the condition $\sigma < 4S < 5.66S$. The critical fluid pressure is defined as (Cox, 2010):

$$P_f^{\text{crit}} = \frac{8S(\sigma_1 + \sigma_3) - (\sigma_1 - \sigma_3)^2}{16S} \tag{3.2.6}$$

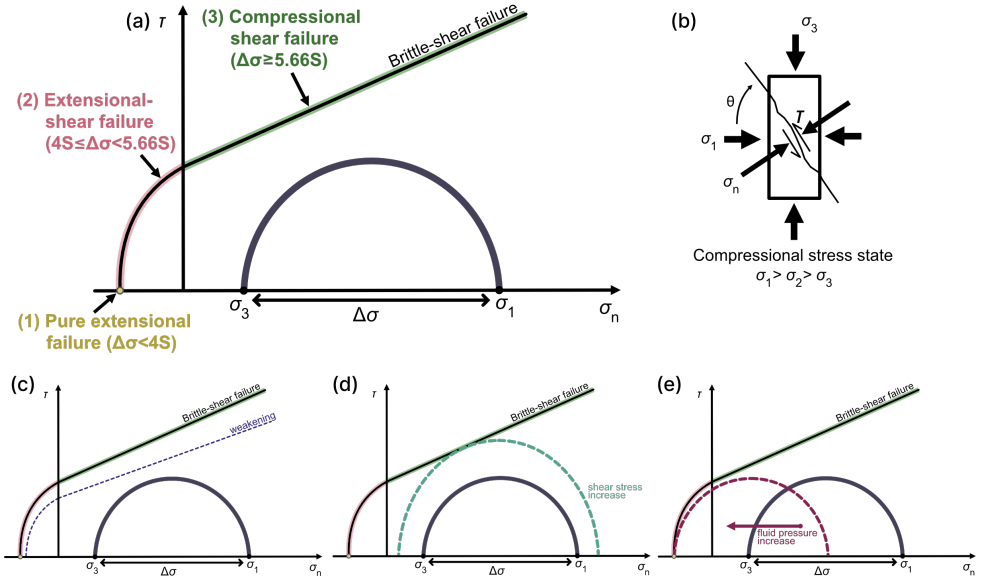

Figure 3.1: Mohr-Coulomb failure mode diagram in compressive stress state. (a) Representation of the rock as a circle in the shear stress-normal stress space and the failure envelope. The diameter of the circle is defined by the differential stress (see Equation 3.2.3). Failure modes can be (1) pure extension failure (yellow), (2) extension-shear failure (red), and (3) compression-shear failure (green). (b) Compression stress state of the rock system showing maximum, minimum and normal stress and the angle of misorientation of the failure plane. (c) Weakening of the rock by changing S and μ results in a displacement of the failure envelope (modified after Yamato et al., 2019). (d) Increasing the shear stress changes the differential stress and therefore the circle diameter. (e) An increase in fluid pressure drives the circle toward a lower normal stress.

(3) Compressional shear failure occurs for high differential stress values with $\sigma \geq 5.66S$ resulting in a critical fluid pressure defined as:

$$P_f^{\text{crit}} = \frac{C}{\mu} + \frac{\sigma_1 + \sigma_3}{2} - \frac{\sigma_1 - \sigma_3}{2}\cos(2\theta) - \frac{\sigma_1 - \sigma_3}{2\mu}\sin(2\theta) \tag{3.2.7}$$

with Θ as the misorientation angle corresponding to the angle between a fault and the maximum normal stress σ_1 (Cox, 2010).

3.2.2 Coupling thermodynamic modelling with failure mechanics

Thermodynamic models can be used to simulate the evolution of a rock system along a pressure temperature path (Baxter & Caddick, 2013; Hernández-Uribe & Palin, 2019; Lanari & Duesterhoeft, 2019). These petrological models assume a closed system at thermodynamic equilibrium as predicted by Gibbs free energy minimisation and can be combined into petrochemical models by integrating the calculation of oxygen isotope fractionation or trace element fractionation for the stable mineral assemblage (Konrad-Schmolke et al., 2011; Vho et al., 2020). Coupling these petrochemical models with failure mechanics re-

quires to link the thermodynamic pressure with the differential stress, fluid pressure, and volume changes from mineral reactions.

In classic equilibrium thermodynamics, a closed system at fixed pressure (P) and temperature (T) conditions evolves towards equilibrium by minimizing its Gibbs free energy (e.g., Connolly, 2005; de Capitani & Brown, 1987; de Capitani & Petrakakis, 2010). The system can be composed of solid mineral phases and fluid phases (Figure 3.2). For simplicity, only an aqueous fluid is considered as the dominant fluid phase in the following. The thermodynamic pressure of such a closed system is generally assumed to be the same for all mineral phases and for the fluid. At equilibrium, i.e. when the Gibbs free energy is minimized, the system has relaxed to any differential stress and represents a static system under thermodynamic pressure (Moulas et al., 2019; Nordstrom & Munoz, 1994). Moulas et al. (2019) demonstrated that the mean stress of a system is close to the lithostatic pressure P_{lith} on large timescales (>10 kyr) including volumetric deformation and differential stress values lower than 100 MPa. In this case, the lithostatic pressure P_{lith} can be used as the thermodynamic pressure P for modelling. For a system with a fluid-filled porosity, the fluid pressure is close to the lithostatic pressure, which represents the mean stress (see Figure 3.2; Connolly & Podladchikov, 2004; Etheridge et al., 2021; Hobbs & Ord, 2018; Saffer & Tobin, 2011; Sibson, 2013).

The fluid pressure is equal to the thermodynamic pressure for a system in thermodynamic equilibrium. For the case where P and T are changed, the system reacts to reach a new equilibrium state. Phase reactions occur to reach chemical equilibrium at the new P–T conditions. The volume change related to the reaction cause a pressure change (ΔP) which can be calculated as (Duesterhoeft et al., 2014):

$$\Delta P = \frac{\sigma_n \left(V_{\text{Sys1}} + \Delta V\right)}{V_{\text{Sys1}}} - \sigma_n \tag{3.2.8}$$

with V_{Sys2} the initial volume of the rock before reaction (system 2) and with ΔV defined as

$$\Delta V = V_{\text{Sys2}} - V_{\text{Sys1}} = V_{\text{Solid2}} + V_{\text{Fluid2}} - V_{\text{Solid1}} - V_{\text{Fluid1}} \tag{3.2.9}$$

where V_{Sys2} is the volume of the new reacted system at chemical equilibrium. The fluid pressure is then the mean stress plus the pressure changes due to volume changes using Equation 3.2.8, which becomes

$$P_f = \sigma_n + \Delta P = \frac{\sigma_n \left(V_{\text{Sys1}} + \Delta V\right)}{V_{\text{Sys1}}} \tag{3.2.10}$$

with the magnitude of ΔP depending on the type of reaction such as the mineral

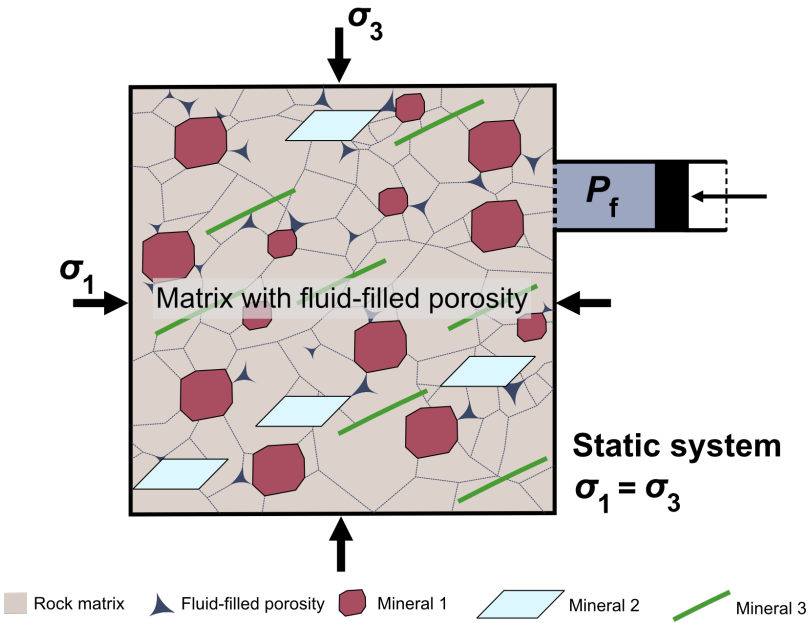

Figure 3.2: Section through a rock system consisting of minerals porphyroblasts in a mineral matrix and a fluid-filled porosity which is connected in 3D. The system is assumed to be closed and at thermodynamic equilibrium therefore there is no differential stress ($\sigma_1 = \sigma_3$). The fluid pressure can be modified from the surrounding and is represented by a valve mechanism (modified after Hobbs & Ord, 2018). When the system receives pressure changes from internal work (volumetric changes) and/or surrounding (increasing vertical load or shear stress) the fluid pressure will adapt to the new condition by moving the valve mechanism. The variables σ_1 and σ_3 represent the maximum and minimum normal stress, respectively, and P_f is the fluid pressure.

or fluid phases involved. In a fluid-filled porous system, the fluid will accommodate the pressure changes from volume changes of the solids and additionally the differential stress (Mazzucchelli et al., 2024). The fluid pressure can increase or decrease depending on a mineral reaction. This pressure change is represented by a valve mechanism in Figure 3.2.

In a petrological modelling framework, the Gibbs free energy can be minimised after each P and T increment and the fluid pressure calculated using Equation 3.2.10 (Figure 3.3). The following description is based on prograde metamorphism with production of a fluid phase by dehydration reaction and at a fixed differential stress, but it can be applied to other conditions such as retrograde metamorphism. In step 1, the system is in chemical and mechanical equilibrium at given P and T conditions (Fig 3.3a-b). Stage 2 represents the system after a small change in P and T in the absence of mechanical failure. After the reaction, the stable phases predicted by Gibbs free energy minimisation at P_2–T_2 include a fluid phase (Figure 3.3c). At this stage, the associated volume changes cause an increase in fluid pressure that is insufficient to cause mechanical failure (Figure 3.3d). The differential stress is also not large enough to cause failure. Step 3 represents the system following a new small increment in P and T. In this case, the associated volume change causes a further increase in the fluid pressure triggering mechanical failure (Figure 3.3f) causing the fluid to be extracted from the system (Figure 3.3e). The mechanical failure in this example occurs by extensional failure, but other modes are possible (see Figure 3.1). Step 4 represents the system after fluid extraction when it has chemically and mechanically equilibrated to P_3 and T_3 conditions (Figures 3.3g-h).

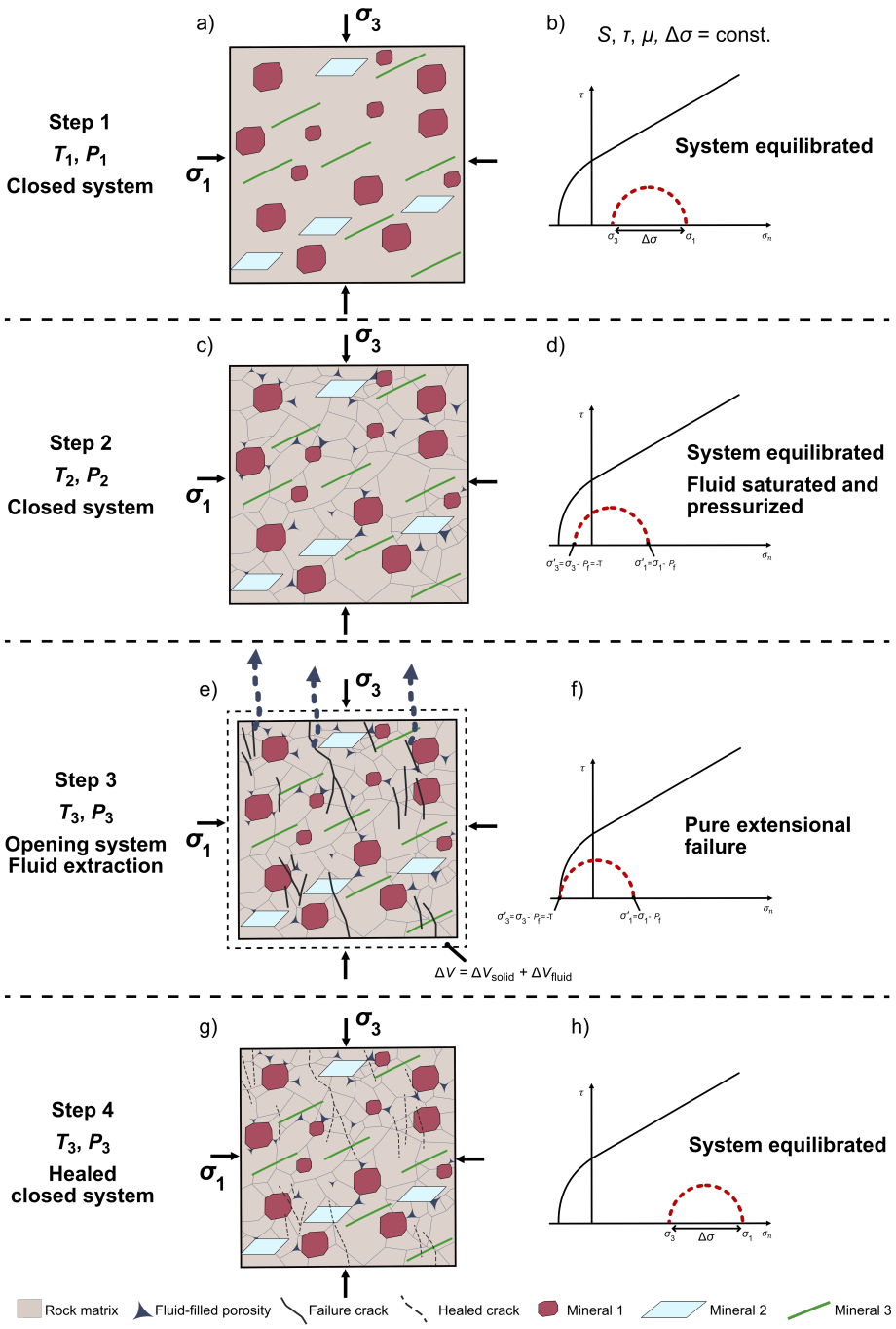

Figure 3.3: Failure criterion test in a system under stress and changing its solid and fluid volume during metamorphic reaction for given conditions for variables S, τ, μ, and $\Delta\sigma$. (a) Equilibrated rock system with no free fluid phase at T_1 and P_1. (b) Mohr-Coulomb diagram for the intact system. (c) Equilibrated and fluid saturated rock system at T_1 and P_1. (d) Mohr-Coulomb diagram for the intact system with fluid-filled porosity. (e) Volume change of the reacting system at the new conditions of T_2 and P_2. The system experiences a negative volume change and the fluid pressure is affecting the mechanical stability of the system (see panel d). Positive volume change is similar calculated following Equation 3.2.8. (f) Mohr circle is moving to the left due to the change in effective stress caused by the fluid pressure and hits the failure envelope. Here, $P_f > \sigma_3$ and $\sigma'_3 \geq -S$ so that pure extensional failure is predicted. (g) After extraction the system is healing and is in thermodynamic and mechanical equilibrium. (h) Mohr-Coulomb diagram of the healed and intact system at the new equilibrated P and T condition.

3.3 Petrochemical model calculator ThorPT

The petrochemical modelling was performed using a free and open source software package written in Python® called ThorPT available at https://github.com/neoscalc/ThorPT. The thermodynamic modelling software Theriak-Domino (de Capitani & Brown, 1987; de Capitani & Petrakakis, 2010) was used to perform the Gibbs energy minimisations for a given bulk system composition during its evolution along a P–T path. For each iteration step on the predefined P–T path, the starting rock is modelled using Gibbs free energy minimisation giving predicted stable phase assemblages. Mineral phase fractionation is possible as this effect can significantly affect the predictions of the thermodynamic model (Lanari et al., 2017). Here the produced garnet is fractionated at each step and a new reactive bulk composition is calculated. Additionally, spherical diffusion for garnet major elements can be applied to account for any diffusional transport by using the Julia package "DiffusionGarnet" (Dominguez, 2024). The oxygen isotope composition $\delta^{18}O$ for the predicted stable phases is modelled based on oxygen isotope fractionation similar to Vho et al. (2020) using an internally consistent oxygen isotope fractionation database (Vho et al., 2019). Additionally, fluid extraction is implemented as fractionation and can modify the reactive bulk composition for both the amount of H_2O and ^{18}O. The fluid fractionation is regulated by the implemented mechanical model and fluid are only extracted when brittle failure is predicted (see above). The failure criteria and fluid fractionation are tested for every P–T increment when a free fluid phase is predicted to be stable is the calculated phase assemblage.

In the ThorPT software, the user can set the following model parameters (see Table 3.1): (1) the P–T path, (2) Disable/Enable the fluid transmission and interaction, (3) the thermodynamic database used for Gibbs free energy minimisation, (4) the bulk rock composition (in wt%), (5) the number of moles of hydrogen, extra oxygen for Fe speciation and/or carbon, (6) the initial $\delta^{18}O$ value of the bulk rock, and (7) the mechanical properties of the system including the tensile strength, differential stress, and internal friction parameter. In addition, the fluid fractionation scheme can be set as: (1) no fractionation, (2) continuous fractionation where fractionation is performed at each increment when a free fluid is present, or, (3) discontinuous fractionation occurring when brittle failure is predicted by the mechanical failure model.

3.3.1 *P–T* path definition using the Pathfinder module

The P–T trajectory can be defined using the built-in Pathfinder module. This module can generate P–T–t trajectories for burial or exhumation by entering a velocity and angle of movement. An existing P–T path, for example from a publication, can be interactively

	Example rock
Description	**Value and comment**
Type	Metabasalt (Unaltered basalt after Gale et al. (2013)
Path increments	500 MPa and 10 °C
Model scenario	Isolated mode (optional: transmitting)
Thermodynamic parameters	
Database	tc55 (revised version of Holland and Powell (1998), and following to Vho et al. (2020))
Solution models	Holland and Powell (2003) for calcite–dolomite–magnesite. Holland and Powell (1998) for garnet, white mica and talc. Holland and Powell (1996) for omphacite. Holland, Baker, and Powell (1998) for chlorite. Diener et al. (2007) for amphibole.
Equation of state for fluid	CORK equations from Holland and Powell (1991).
Oxide wt.%	SiO_2 | TiO_2 | Al_2O_3 | FeO | Fe_2O_3 | MnO | MgO | CaO | Na_2O | K_2O
	50.47 | 1.68 | 14.7 | FeO 10.43 | 0 | 0 | 7.58 | 11.39 | 2.79 | 0.16
Moles of hydrogen	0.6
Moles of excess carbon	0
Geochemical parameters	
Oxygen isotope fractionation factors	DBOXYGEN 2.0.3 (Vho et al., 2019)
Starting bulk $\delta^{18}O$	5.7 ‰
Fluid & Mechanical parameters	
Fluid phase fractionated	water.fluid (named as in the thermodynamic database)
Fluid fractionation mechanism	Mechanical Model (optional: No extraction / Continuous)
Fluid fraction leaving the system	100% when present as a free fluid phase
Fluid pressure	Mean stress
Tensile strength	20 MPa
Differential stress	50 MPa

Table 3.1: Overview of model set-up parameters. Selected settings represent the model used for the metabasalt benchmark.

digitised from an image. The following scenario "subduction zone" is used by default to assign a time and depth to each step from the burial rate. The top of the model is buried beneath a two-layer structure representing the overlying crust (density 2800 kg/m^3) and mantle (density 3300 kg/m^3). The generated P–T path represents the value of P and T at each step for the top layer in the model. The layering structure in the Pathfinder package can be defined by an input text file to adapt it to different scenarios. For the default two layer model the lithostatic pressure at depth is related to the layer thicknesses by

$$P_{\text{litho}} = (\delta_{\text{layer 1}} \cdot h_{\text{layer 1}} + \delta_{\text{layer 2}} \cdot h_{\text{layer 2}}) \cdot g \tag{3.3.1}$$

with g the gravitational acceleration m/s^2, δ (kg/m^3) the density of layer 1 and 2 and h (m) the thickness of the layers. During subduction the second layer, which is overlaying directly the slab is increasing in thickness and so is the total thickness of the two-layer model. The depth related to a lithostatic pressure is then given by the sum of h1 and h2, which is linked to the assumed burial rate given by convergence speed of the subducting plate and the angle of dip of the slab:

$$h_{\text{total}} = h_{\text{layer 1}} + h_{\text{layer 2}} = v \cdot t \cdot \sin(\varphi) \tag{3.3.2}$$

with the subducting angle (in °), v the horizontal convergence rate (in m/s) and t the

time (in s).

The pressure and temperature within the model column itself may differ from the top conditions given by the input P–T trajectory. The pressure of each "rock" layer is also influenced by the layers above it. For each rock layer in the model, the pressure is calculated as:

$$P_{\text{rock layer } i} = P_{\text{litho}} + (\delta_{\text{rock layer 1}} \cdot h_{\text{rock layer 1}} + \cdots + \delta_{\text{rock layer } i-1} \cdot h_{\text{rock layer } i-1}) \cdot g \quad (3.3.3)$$

The temperature in the model column is modelled using an error function to describe the temperature increase with increasing thickness, which is commonly implemented in large scale numerical models (Gerya et al., 2002; Gies et al., 2024; Van Keken et al., 2002). For smaller scale models this can be simplified by assuming an identical temperature at the top and bottom of the model. The temperature profile is given by

$$T_{\text{Column}} = T_{\text{Top}} + (T_{\text{Bottom}} - T_{\text{Top}}) \cdot \text{erf}\left(\frac{2x}{d}\right) \quad (3.3.4)$$

with T_{Top} as the temperature at the top of the model column as defined by the value of the P–T step , T_{Bottom} as the temperature assumed at the bottom of the model (e.g., 100 °C warmer than the top), x as the position within the model, and d the complete thickness of the whole model. In the case of a subducting slab, this profile represents a close to linear increase of the temperature at the top and a more homogeneous temperature profile at the bottom.

The path increment values in P and T represent the step size between two minimisations (Table 3.1). These values are adjustable and represent the conditions under which the reactive part of the system reaches a new equilibrium state. Between two steps, the mineral assemblage and the fluid are held metastable without any reaction. Larger increment values may represent a delay in the reactivity of the system and can be seen as an analogue of reaction overstepping (Pattison et al., 2011; Yamato et al., 2022). In the following, we have used increment values of 500 MPa for ΔP and 10 °C for ΔT. Once at least one of these conditions is satisfied along the predefined P–T path, a new Gibbs free energy minimisation is performed.

3.3.2 Mechanical properties

The implemented mechanical model framework depends on three parameters, the coefficient of internal friction (μ) and tensile strength (S) of the bulk rock material and the differential stress ($\Delta\sigma$) of the surrounding rock. The internal friction coefficient is set to 0.75 as

a representative value for most lithologies of the crust at greater depth (Byerlee, 1978; Jaeger, 1979; Sibson, 2000).

Typical tensile strength values reported for different rock types are shown in Figure 3.4a (Lockner, 1995; Sibson, 2017; Strating & Vissers, 1991). Sedimentary or low competence rocks have tensile strength values in the range of 1 to 10 MPa, whereas higher competence crystalline rocks have higher values around 20 MPa and possibly higher (Figure 3.4a). Estimates based on outcrop studies and petrological observations suggest that mafic and ultramafic rocks under eclogite facies conditions have higher values up to 38 MPa for metagabbro and 47 MPa for peridotite, whereas estimates for serpentinised mantle are much lower at ∼12 MPa (Figure 3.4). However, the observations of fractures in regionally metamorphosed rocks suggests tensile strengths values of 20 MPa or less (Etheridge, 1983). The values of 3 MPa for serpentinites, 10 MPa for sedimentary rocks and 20 MPa for basalts have been chosen here to represent an increase from low competence to high competence lithologies while being compatible with the common observation of fractures in all lithologies.

Typical values for differential stress are summarised in Figure 3.4b, compiled from the geological record, geophysical studies and laboratory experiments (e.g., Bird, 1978; Byerlee, 1978; Condit & French, 2022; Hanks, 1977; Hosokawa & Hashimoto, 2022; Kato et al., 2010; Lockner, 1995; W. L. Schmidt & Platt, 2022; Strating & Vissers, 1991; Van Den Beukel & Wortel, 1988). Brittle fractures, such as in peridotites, are explained by differential stresses above 200 MPa (Strating & Vissers, 1991). The occurrence of mylonites in serpentinites, on the other hand, is explained by a differential stress below 100 MPa (Strating & Vissers, 1991), in agreement with experiments on seismic and aseismic faulting (Hanks, 1977). Observed tensile fractures from regional metamorphism are explained by values below 60 MPa using a tensile strength below 20 MPa (Etheridge, 1983). Brittle failure of shales and high fluid pressures have also been explained by differential stresses $\leq$ 35 MPa (Condit, French, et al., 2022). This is consistent with the calculated stresses from a ridge model and gravity data, which give an upper limit of 30 to 60 MPa (Bird, 1978). The periodicity of slow slip events from geophysical observations also allow a differential stress of 55-80 MPa to be estimated when extensional shear failure occurs during subduction (Warren-Smith et al., 2019). Deformation-related microstructures have also been used to infer differential stress values of 30-80 MPa from paleo-subduction channels (Koyama et al., 2024). A differential stress value below 100 MPa is assumed here and the influence of this parameter on the model is further tested in the following.

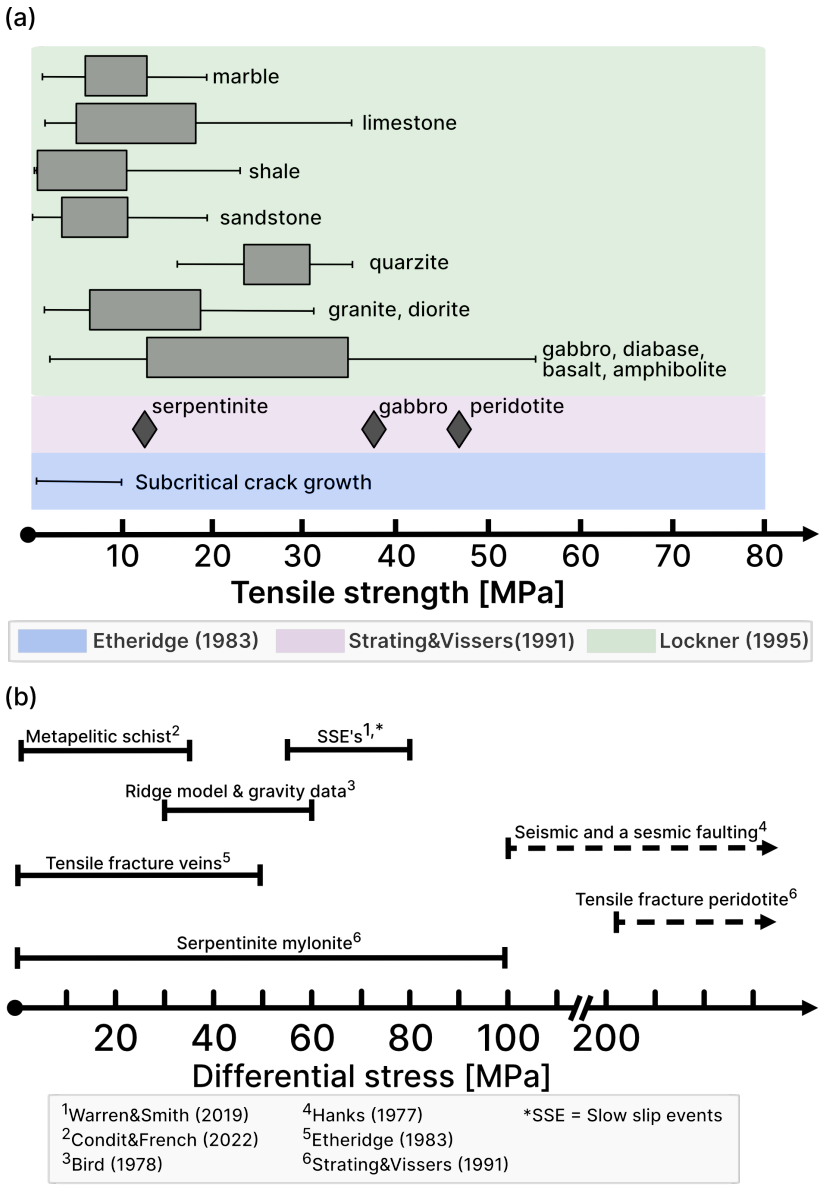

Figure 3.4: Overview of the values of tensile strength of different rock types and estimates of the differential stress in regional regimes summarized from the literature. (a) Compilation of values for the tensile strength of rocks showing their difference in competence modified after Lockner (1995). (b) Compilation of the differential stresses reported in the literature based on recorded pressure drops during earthquakes and outcrop observations from paleo-subduction zones.

3.4 Results

3.4.1 Comparative test of the integrated petrochemical model

The addition of the mechanical model can affect the petrochemical model because the fractionation of the fluid phase can influence both the amount of H_2O available for reaction and the $\delta^{18}O$ value of the system. A comparative test of ThorPT was performed using the same model settings as in Vho et al. (2020) with an unaltered basalt bulk rock composition from Gale et al. (2013) to simulate the evolution of a metabasalt. The Gibbs free energy minimisations were performed using the internally consistent dataset of Holland, Baker, and Powell (1998) with subsequent updates collected in the Theriak-Domino database tc55 (Table 3.1, Supplementary S1+S4 and Vho et al. (2020)). The P–T trajectory was set to an oceanic subduction geotherm using a convergence speed of 0.02 m/year and a dipping angle of 20° (Gerya et al., 2002, see Supplementary Material S2 Figure S2-2). Detailed information on the data used for input and the calculations used in the model can be found in Table 3.1 and Supplementary Material S1.

The main simulation results are summarised in Figure 3.5 using mode box diagrams showing the evolution of the predicted mineral modes and the cumulative volume of fluid extracted from the system (both expressed in vol%) along the P–T trajectory. The first model shown in Figure 3.5a assumes continuous fluid extraction as in Vho et al. (2020), and the second model shown in Figure 3.5b uses the integrated mechanical model to calculate whether the fluid should be extracted or retained in the system (see above). The full set of results, including the simulated oxygen isotope values for the bulk rock, the fluid and the mineral phases are given in the Supplementary Material S2. For both models, lawsonite, glaucophane, and actinolite make up ~80 vol% of the system at conditions below 450 °C and most of the fluid is released during garnet and omphacite growth associated with chlorite, amphibole and lawsonite breakdown. In both models, 12 vol% of fluid was produced and extracted at 700 °C, but the extent and timing of fluid extraction differs due to the mechanical model. The first model predicts continuous fluid extraction between 450 °C and 650 °C, whereas the second model predicts two discrete episodes of fluid extraction between 510 and 570 °C and at ~620 °C. In the absence of open system behaviour, the predicted mineral phases have similar oxygen isotope signatures in the two models, e.g., garnet starts at 4.8 ‰ (vs. VSMOW) at ~480 °C and ends at 4.6 ‰ (vs. VSMOW) at ~700 °C (see Supplementary Material S2).

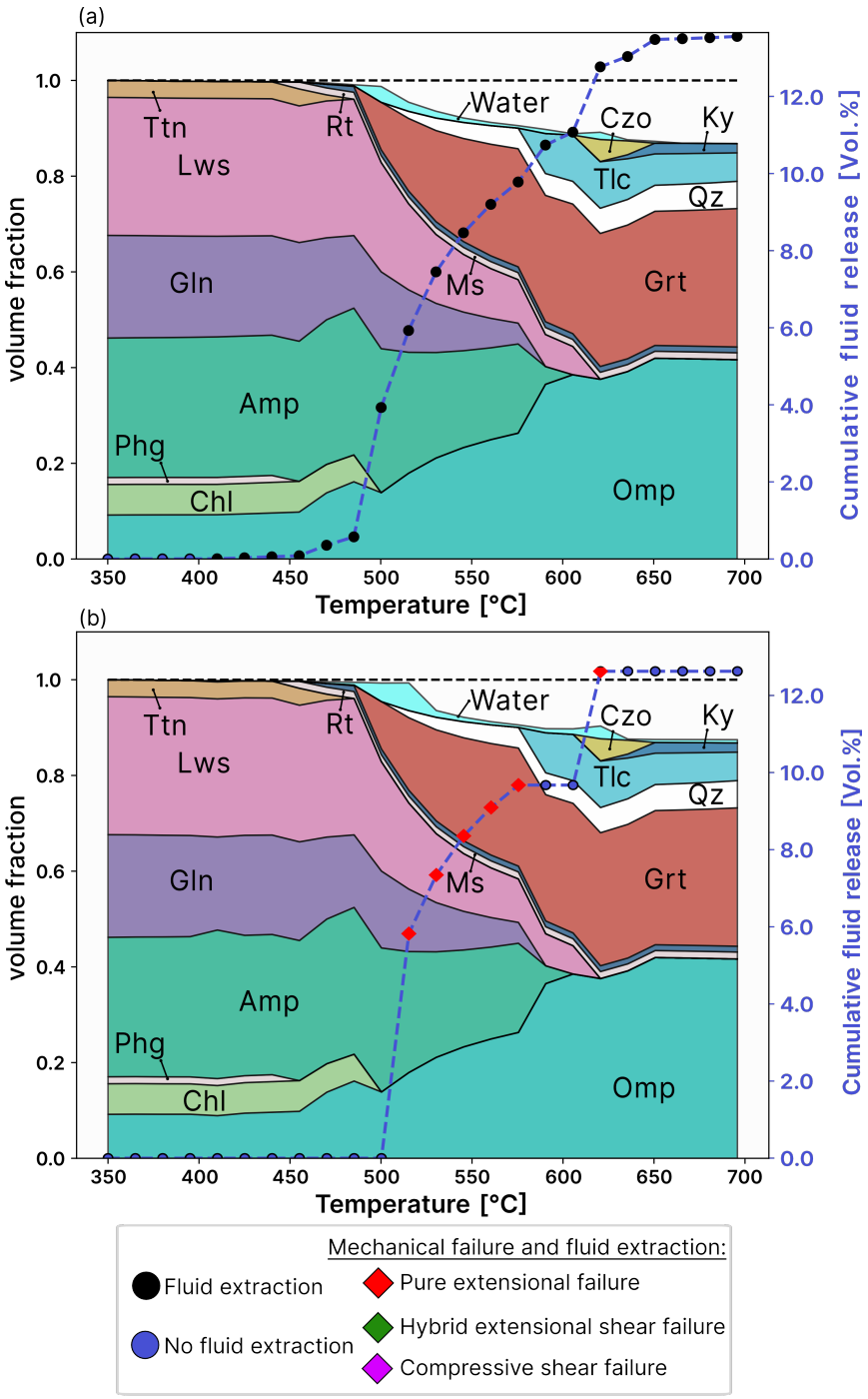

Figure 3.5: Box mode diagrams of an unaltered metabasalt with similar model parameters as Vho et al. (2020). Both plots show the relative volume fraction to the initial rock system on the y-axis, and temperature (also increasing pressure) steps on the x-axis. The cumulative volume of fluid extracted (in vol% of the total system) is shown as a dashed blue line on the right y-axis with each point representing a model step. (a) Continuous extraction: the free fluid phase is always fractionated when present in the system. Each blue point indicates the cumulative amount of fluid extracted (b) Fluid extraction associated with mechanical failure: the free fluid phase is fractionated only when failure is predicted by the mechanical model. The red diamonds indicate brittle failure and fluid extraction, while the blue dots indicate the cumulative amount of fluid extracted in the previous extraction step. Mineral abbreviations are after Warr (2021).

3.4.2 Fluid extraction behaviour in the integrated model

The fluid extraction episodes predicted by the mechanical model were examined using the P–T path representing the average rock record (Penniston-Dorland et al., 2015). These models evolve on a warmer geotherm than the previous model based on the P–T path of (see Supplementary Material S2, Figure S2-2, Gerya et al., 2002), as additional heat sources are considered, especially for depths below 70 km (Penniston-Dorland et al., 2015). The peak pressure and temperature of the two paths are identical. For these simulations, the P–T path was defined with a minimum step size of 500 MPa and 10 °C, a convergence rate of 0.015 m/year and a dip angle of 30°. Two rock types were studied, a metabasalt (unaltered basalt composition from Gale et al. (2013)) and a serpentinite (bulk composition from Ulrich et al. (2024)). The thermodynamic models used the internally consistent dataset of Holland, Baker, and Powell (1998) and the tc55 and tc55_Serp databases, similar to Vho et al. (2020) and Kempf et al. (2020) (see Supplementary Materials S4 for details). For the mechanical model, the serpentinite is assumed to have a low competence ($S = 3$ MPa), while the metabasalt is assumed to have a high competence ($S = 20$ MPa). The differential stress was initially set at 50 MPa for both rock types, which is an average value from the compilation in Figure 3.4b. Details of each model can be found in Supplementary Material S1. Figure 3.6a-b shows the mode box plots for both lithologies.

Three episodes of fluid extraction are predicted by the model for the metabasalt. All extractions are associated to pure extensional failure (red diamonds in Figure 3.6a). The first episode starts at ∼375°C and is maintained almost continuously till ∼500 °C. A very small amount of fluid (∼0.1 vol%) is continuously extracted due to the progressive consumption of chlorite. Above 500 °C chlorite breaks down rapidly but the fluid is predicted to remain in the system. The second episode of fluid extraction is continuous over an 80 °C interval starting at ∼550 °C during garnet growth and is associated with the breakdown of amphibole. It starts with a large pulse of fluid extraction, accounting for ∼4 vol% of fluid at one time. This is followed by a continuous extraction of fluid to reach a cumulative value of 5.5 vol% at ∼620 °C. The third and final episode begins with the extraction of ∼0.5 vol% of fluid at ∼650 °C after the retention of fluid due to the complete consumption of the amphibole. Thereafter, <0.1 vol% fluid is extracted continuously during the talc formation reaction. This last episode is also associated with garnet growth.

For the serpentinite simulation, no free fluid phases can be maintained in the system as compressive shear failure is predicted to occur once a fluid-filled porosity is generated by a metamorphic reaction. The first major release occurs during the brucite consumption, antigorite dehydration and olivine forming reaction starting ∼450°C and is responsible for the extraction of ∼26 vol% fluid. This is the largest fluid extraction episode waning at ∼510 °C. A second large fluid extraction starting at ∼670 °C is associated with antigorite

breakdown and olivine, chlorite, and orthopyroxene formation responsible for ∼10 vol% fluid. Chlorite dehydration above 670 °C contributes <1 vol% of fluid.

3.4.3 Sensitivity of the mechanical model

The sensitivity of the model to differential stress was tested for the metabasalt and the serpentinite. The results are shown in Figures 3.6c-d. The sensitivity to the tensile strength and the bulk rock composition is shown in Figure 3.7. Changes in tensile strength values were simulated using the same bulk rock composition of the metabasalt (see 3.4.2). Bulk rock composition sensitivity tests were performed using the same metabasalt composition, with the addition of the average metabasalt from Winter (2014), and the bulk rock compositions from Belgrano and Diamond (2019). A tensile strength value of 20 MPa was taken for the rocks at various differential stress values. Similarly, the P–T path of the average rock record was used (Penniston-Dorland et al., 2015, and see Supplementary Material S2, Figure S2-2 for the P–T path). All modelling details are summarized in Supplementary Material S1.

For the metabasalt, increasing the differential stress value increases the number of extraction steps (Figure 3.6c). A differential stress value below 37 MPa results in no fluid extraction, whereas values above 60 MPa predict up to 30 extraction steps of 34 model steps. The maximum number of extraction steps (30 steps) corresponds to a cumulative fluid extraction of ∼6 vol%. At the 20 MPa differential stress interval the model shows an increase in the number of extraction steps and the cumulative volume of fluid extracted, marking a choke point. This choke point is the transition for the start of extraction steps to the highest possible extraction over increasing differential stress. Differential stresses above $4S$ (≥80 MPa) simulate extensional shear failure, while even higher values above $5.66S$ (>113 MPa) simulate compressive shear failure. The maximum number of extraction steps and the higher amount of fluid extracted is first achieved in the pure extensional failure range.

The sensitivity test for the serpentinite simulation shows that for low differential stress values below $4S$ (<12 MPa), the mechanical model already predicts brittle extensional failure. This would mostly correlate with a cumulative fluid extraction between 15.5 and 31 vol% and a number of extraction steps between 2 and 25 (Figure 3.6d). The 31 vol% of fluid volume represent almost the maximum of the possible volume. In the case of only two extraction steps this represent the two major dehydration reaction events. The choke point of the serpentinites model starts already at a differential stress below 1 MPa. For differential stresses between $4S$ (12 MPa) and $5.66S$ (17 MPa), the mechanical model predicts extensional shear failure and above 17 MPa compressive shear failure. In this interval the maximum volume extracted reaches the possible maximum of ∼32 vol% and

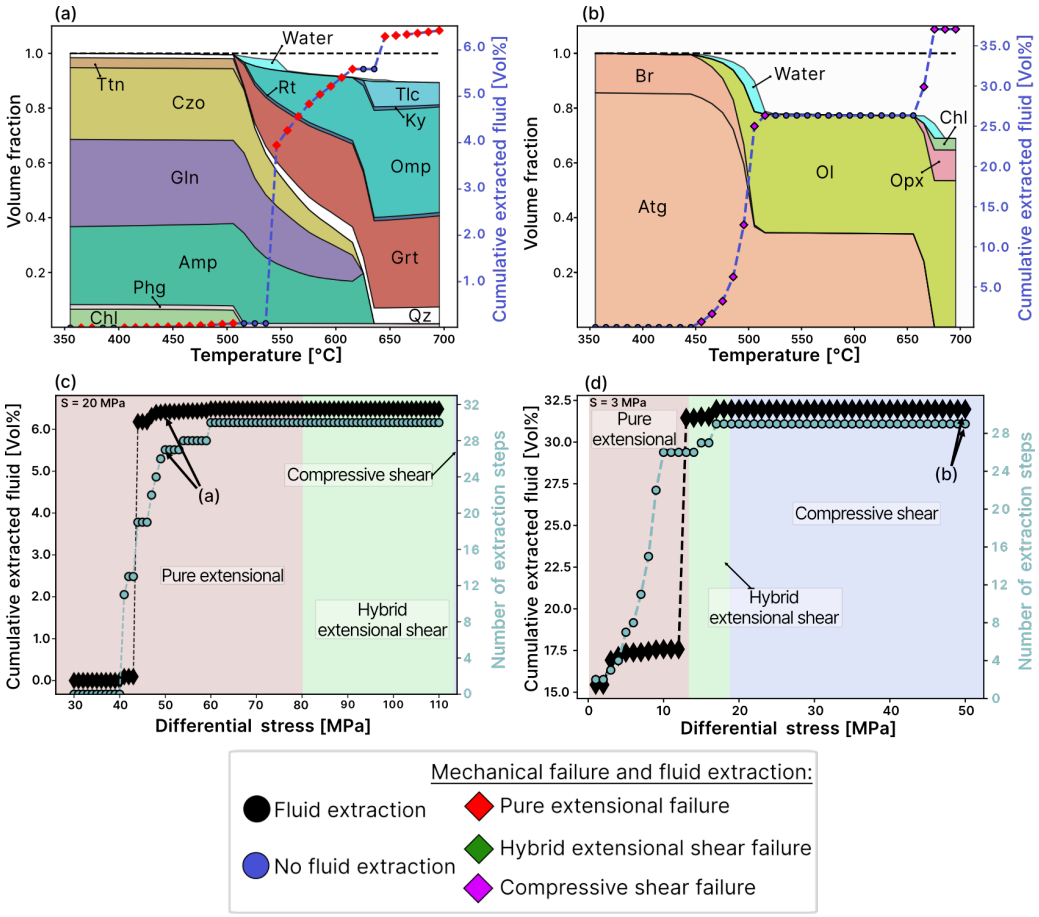

Figure 3.6: Modelling of a metabasalt und serpentinite on the average geoterm for a range of differential stress. (a-b) Mode box diagram of the metabasalt and serpentinite with the evolution of the cumulative extracted fluid volume (dashed blue line). Diamond marker show the type of mechanical failure and episodes of fluid extraction from the system (red diamonds = pure extensional failure, blue diamonds = compressive shear failure). (c-d) Cumulative fluid volume extracted from the system and number of fluid extraction steps vs. values of differential stress. Domains of failure mode are color coded for pure extensional failure (red), extensional shear failure (green), and compressive shear failure (blue). The used differential stress of 50 MPa in model of (a) and (b) are annotated in (c) and (d), respectively. See text for modelling details. Mineral abbreviations are after Warr (2021).

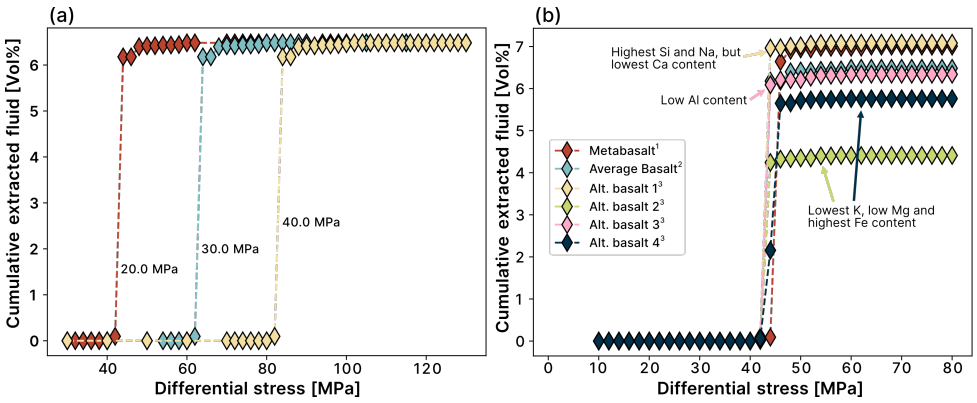

Figure 3.7: Modelling results for variation the tensile strength of the rock and the bulk chemistry. (a) Simulation showing the extracted fluid vs. increasing differential stress for increasing tensile strength using the metabasalt composition. Annotated values represent the used tensile strength. (b) Cumulative fluid extracted vs. differential stress plot showing the differences between the bulk rock compositions in the simulation. Annotations are qualitatively compared to the metabasalt. Metabasalt is again the unaltered basalt from [1]Gale et al. (2013), average basalt from [2]Winter (2014), and altered metabasalt compositions are taken from [3]Belgrano and Diamond (2019).

the maximum number of 30 extraction steps is reached for a total of 34 modelling steps.

Strengthening the metabasalt by increasing the tensile strength value from 20 MPa to 30 and 40 MPa makes brittle failure impossible; therefore, no fluid extraction is predicted by the model (Figure 3.7a). A similar result to the previous simulation shown in Figure 3.6a is obtained when the differential stress is increased by ∼20 MPa for the model with S = 30 MPa and by ∼40 MPa for the model with S = 40 MPa. Similar to the result shown in Figure 3.6c with S = 40 MPa, the choke point from low fluid extraction to high fluid extraction is shifted to a differential stress of ∼70 and ∼90 MPa when using S of 30 and 40 MPa respectively.

The choke point from lowest to highest cumulative fluid extraction shows that most basaltic bulk rock compositions respond similarly to the mechanical model as differential stress is increased (Figure 3.7b). All models predict rock failure between 40 and 50 MPa differential stress and the mean location of the choke point is 45 MPa. Rocks with lower Al, K, Mg and higher Fe content appear to result in less cumulative fluid between 0.1 and 2 vol% being able to be extracted from the system in total. Higher Si and Na contents in an altered basalt resulted in an almost negligible higher cumulative fluid extraction of ∼0.1 vol%.

3.5 Discussion

In our model the fluid extraction in restricted to brittle failure events. Migration of fluid in the crust nevertheless is only feasible if the porosity and permeability of the rock is large enough such as in reaction-induced nanopores (Plümper et al., 2017). Generally, experimental and analytical results showed that fracturing represent a rapid enhancement of the permeability in a rock by crack growth and surface enlargement (Nguyen et al., 2020; Sun & Liang, 2015). The formation of cracks and fractures serves as flow channels representing conduits of high permeability (Ague, 2011; Norton & Knapp, 1977). Regions of high fluid flow can in turn result in features such as crack-seil veins (Ramsay, 1980) or at least allow the drainage of the fluid from the rock system (Peacock, 2009). Changes in the porosity and permeability therefore can occur during cracking of the material which is eventually followed by earthquakes (Viete et al., 2018). Geophysical studies commonly suggest relatively high fluid-filled porosities of up to 4 vol% (Egbert et al., 2022; Peacock et al., 2011; Shiina et al., 2013), which is compatible with our model that builds up to 3-4 vol% of fluid when restricting the fluid extraction to the predicted brittle failure events (Figure 3.5 and 3.6).

The petrochemical model ThorPT is further evaluated below, starting with the calculation method for the volume changes. Key model parameters are then discussed, including the parameters of the mechanical model and the magnitude of pressure and temperature increments. Finally, the model is discussed in terms of its applicability to natural case studies by comparing the model results with natural observations from high-pressure rocks.

3.5.1 Reactivity of the system during increasing pressure and temperature

Gibbs free energy minimisation is performed at each P and T increment to simulate the instantaneous re-equilibration of the reactive part of the system towards an equilibrium state. This strategy does not take into account the transient small volume changes that may occur during the increase in P and T prior to the reaction, i.e. when the previous mineral assemblage and fluid are held metastable. The molar volume of a metastable phase is pressure and temperature dependent and changes can affect the transient fluid pressure prior to reaction. To test this effect, an unaltered basaltic rock composition was modelled with Theriak-Domino (de Capitani & Brown, 1987; de Capitani & Petrakakis, 2010). The rock system undergoes a continuous devolatilisation reaction during garnet growth from an arbitrary stage 1, at 500 °C and 2 GPa, and stage 2, at 550 °C and 2.15 GPa. The mineral assemblage predicted to be stable at stage 1 is omphacite, muscovite, tremolite, glaucophane, epidote, hematite, lawsonite, quartz and rutile. At stage 2, garnet

and fluid are predicted to be stable with epidote quartz omphacite, lawsonite and rutile. A much larger temperature increment is considered here to explore the effect of metastable persistence on the fluid pressure. The volumes of the phases predicted to be stable at stage 1 were calculated at 550 °C and 2.15 GPa using Theriak (de Capitani & Brown, 1987; de Capitani & Petrakakis, 2010). The volume and density of the system at each stage are summarised in Table 3.2 and shown in Figure 3.8a (see Supplementary Material S3 for modelling results). The calculated metastable system at stage 2.1 (Figure 3.8a) results in a negligible densification of the rock from 3.1608 g/cm^3 to 3.1612 g/cm^3 compared to stage 1 (Table 3.2). This densification is associated with a volume decrease of 0.01% (Table 3.2). The re-equilibration of the system at Stage 2.2 (Figure 3.8a) results in a decrease in rock density from 3.1608 g/cm^3 to 3.1514 g/cm^3 compared to Stage 1. This reaction is associated with a 0.3% increase in volume (Table 3.2) due to the fluid producing reaction and the presence of a free fluid phase in the system (Figure 3.8a). The production of fluid at stage 2.2 results in an increase of the fluid pressure as shown in Figure 3.8a using the valve mechanism. This increase in fluid pressure can lead to brittle failure and fluid extraction, which would correspond to a densification of 3.1674 g/cm^3 and an associated volume reduction of 0.5% (Table 3.2). A fluid pressure of 2161.4 MPa can be calculated using Equation 3.2.10 and a differential stress of 50 MPa (as in the model in 3.4.2) when the system goes from Stage 1 to 2.2, i.e. without considering the volume change caused by changing P and T for the metastable phases. If the metastable condition of stage 2.1 is considered, the fluid pressure value obtained is slightly higher at 2161.7 MPa. The difference of 0.3 MPa represents an increase of 0.01% when the metastable stage is considered. This small difference was obtained for an unrealistically large temperature step of 50°C, which is five times larger than the normal temperature step used in the model. The effect of this pressure difference on the failure model is shown in Figure 3.8b. The positions of the Mohr circle after displacement by fluid pressure are shown for the unmodified basalt model using an S of 20 MPa and a $\Delta\sigma$ of 50 MPa (see 3.4.2). The arrows show the shift of the Mohr circle due to increased pressure for (1) the large model step size of 50 °C and (2) the normal step size of 10 °C. The effect of the volume changes of the metastable phases is insignificant compared to the magnitudes of the circle displacements, even for the large temperature step of 50 °C considered here. Therefore, this effect is negligible in the calculations of the fluid pressure and has been ignored in the model.

System condition	Temperature [°C]	Pressure [GPa]	Volume [cm^3]	Density [g/cm^3]
Stage 1	500	2.00	240.9220	3.1608
Stage 2.1	550	2.15	240.8869	3.1612
Stage 2.2	550	2.15	241.6341	3.1514
Stage 2.3	550	2.15	239.6871	3.1674

Table 3.2: Modelling results using Theriak summarizing the modelled system volume and density for changing pressure and temperature.

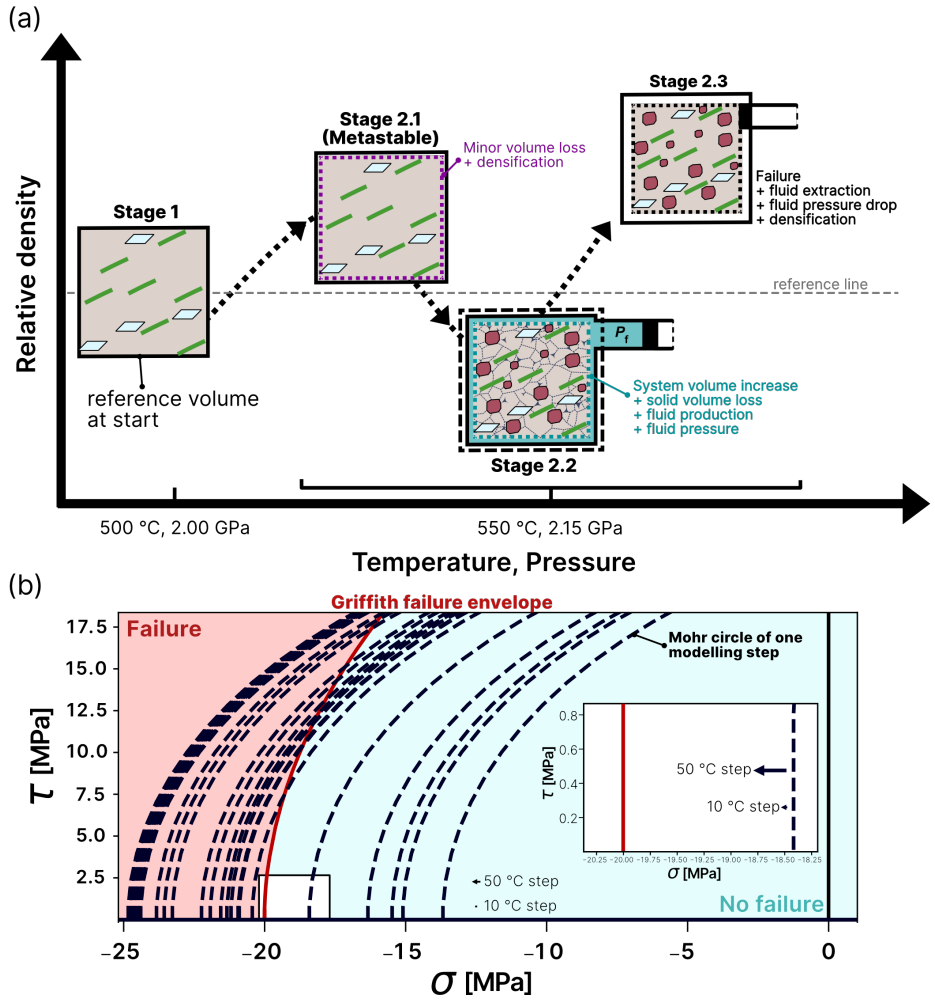

Figure 3.8: Conceptual model and results of the metastability test. (a) Density and volume changes for modelling stages 1 to 2.3. Stage 1 represents the initial conditions with the system at thermodynamic and mechanical equilibrium at 500 °C and 2.00 GPa. For stage 2, the system conditions are increased to 550 °C and 2.15 GPa. Stage 2.1, metastability, shows the densification of the metastable mineral assemblage associated to a decrease of the total volume of the system. Stage 2.2, represents the thermodynamically equilibrated system. Fluid and garnet are produced, and this reaction is associated with a decrease in density, an increase in total volume and an increase of the fluid pressure shown by the valve mechanism. Stage 2.3, the system reaches mechanical failure, fluid is extracted resulting in densification and a decrease in the total volume. The grey dashed line is the reference line for the density at stage 1. The black solid box always represents the same size with respect to the system volume at stage 1. (b) Example Mohr-Coulomb diagram from an unmodified basalt simulation with S of 20 MPa and $\Delta\sigma$ of 50 MPa. Coloured regions are the fractured (red) and intact (blue) regions. Dashed black lines show the Mohr circle of the system for each modelling step. The red line represents the failure envelope. Small black arrows indicate the calculated shift of the Mohr circle when the metastable feedback is included in the failure model. The white box is a zoom in to make the shift due to metastable feedback more visible.

3.5.2 Parameters of the mechanical model

The presented petrochemical model predicts brittle failure of the system as a function of volume and pressure changes. A simplification here is that fluid is always extracted during brittle failure regardless of the amount of fluid-filled porosity. It is assumed that the interconnectivity between pores is achieved during brittle failure and no fluid is retained in the system. Every time no failure is predicted the fluid will be maintained in the system, which is expressed as fluid-filled porosity, and can be possibly transported at depth (Figure 3.5b and Figure 3.6). Fluid-filled porosity estimates have been reported in several geophysical studies (Abers et al., 2009; Audet et al., 2009; Egbert et al., 2022; Gosselin et al., 2020; Kodaira et al., 2004; Peacock, 2009; Peacock et al., 2011; Shiina et al., 2013). The model results for the metabasalt as an example predict similar fluid-filled porosity of up to 4 vol% before brittle failure is predicted and fluid extraction is assumed (Figures 3.5b and 3.6a).

The results of the mechanical model indicate that a minimum stress should be applied as a function of the rheological strength to obtain a brittle failure of the system. This minimum stress is expressed as the onset of the choke point in a fluid extraction vs. differential stress diagram (see Figure 3.6c-d and Figure 3.7). This choke point is the transition from conditions resulting in no brittle failure (and zero fluid extraction) and reaching the maximum number of steps with brittle failure. The transition from zero to the maximum number of steps of brittle failure over an interval of 10 to 20 MPa is therefore always associated with fluid extraction (Figure 3.6 c-d and Figure 3.9). As shown in Figure 3.7, the transition interval is similar for one rock type, in this case the metabasalt, thus compositional variability. Deviation from the metabasalt composition only result in different amounts of fluid to be extracted, which is related to the stable abundance of hydrous phases. Increasing the tensile strength of the same rock type shifts the onset of the choke point to higher differential stress values (Figure 3.7a). The serpentinite model corresponding to a rheological weaker rock shows that the choke point is located at lower values of differential stress around 5 MPa (Figure 3.6d). The interval to the highest possible fluid extraction is also smaller at ∼10 MPa, represented by the number of brittle failures and therefore assumed extraction steps.

The simulation of brittle failure occurs in the typical range of differential stress values reported in the literature (Figure 3.4b). Several reports exist of natural occurring veining in eclogite, which is explained by pulsed internal fluid release by mineral breakdown reactions and coupled to shear or tensile failure (Angiboust et al., 2011; Angiboust & Raimondo, 2022; Philippot & Selverstone, 1991; Strating & Vissers, 1991; Taetz et al., 2018; Yamato et al., 2019). As the modelling results of the metabasalt demonstrate, a consecutive brittle failure for multiple distinct episodes can be achieved using a medium differential stress

value of 50 MPa and a tensile strength of 20 MPa (Figure 3.6a). Assuming that the fluid is extracted at each brittle failure event possibly explain the observed veining. Also, Warren-Smith et al. (2019) explain slow slip events (SSE's) in the subducting oceanic crust by demonstrating that episodic failure and fluid overpressure occurs for differential stresses of maximal 55-80 MPa. This aligns well with the stronger lithology model of the metabasalt, which showed the choke point for the onset of episodic brittle failure at ∼40 MPa (Figure 3.6a+c, Figure 3.7). Condit, French, et al. (2022) examined crack-seal veins in metasedimentary rocks and concluded in a differential stress of <35 MPa that facilitated elevated pore fluid pressures and resulted in slow slip and tremor. This would represent a lithology, which is rheological weaker than the metabasalt model. Strating and Vissers (1991) reported the localization of deformation in antigorite-rich serpentinites mylonites and the occurrence of olivine + Ti-clinohumite veins. Brittle failure of the rock was proposed to be linked to antigorite breakdown at a shear stress of 5 MPa below 40 km. Similar brittle failure at low differential stresses are shown in the model of the serpentinite representing a weak lithology (Figure 3.6b+d).

3.5.3 Pressure and temperature simulation increments

The incremental increase of P and T regulates the magnitude of the volume change as large increments can result in larger volume changes during a continuous reaction. The step size values in P and T can therefore have a drastic effect on the integrated model especially for the evaluation of brittle failure. In the models shown above, a step size of 500 MPa and 10 °C was used to add a small delay to the reactivity of the system, as an analogy to reaction overstepping. Reaction overstepping represents a delay in a reaction caused by kinetic barriers to nucleation and growth (e.g., Pattison et al., 2011; Yamato et al., 2022). A model with 100 MPa and 1 °C step size, representing a system with small kinetic barriers was used to assess the sensitivity of the model to smaller increments. Figure 3.9 shows the comparison between the standard simulation corresponding to medium kinetic barriers using the metabasalt with a tensile strength of 20 MPa and the high resolution step size model corresponding to low kinetic barriers along the same P–T trajectory.

Both models predict low fluid extraction during progressive chlorite breakdown up to ∼500 °C (Figure 3.9a) for S of 20 MPa and a $\Delta\sigma$ of 50 MPa (see 3.4.2). Chlorite dissolution then accelerates and the model with the smaller kinetic barriers has more steps associated with brittle failure between 500 and 525 °C. This results in more fluid extraction steps and less fluid-filled porosity that can form in the system, but in a similar cumulative amount up to 505 °C compared to the larger step size model (Figure 3.9). After this point, the larger step size simulation does not predict failure for the generated fluid pressure and volume changes because the next Gibbs free energy minimisation is performed at conditions when

chlorite is no longer stable. The small step size model instead simulates small volume changes first during chlorite dissolution and then during amphibole dissolution (Figure 3.9a, b). The consequence of these more frequent steps is that a fluid pressure is built up and maintained for each simulation step, leading to brittle failure of the system. Larger volume changes, on the other hand, result in a weakening effect, as the volume drop is greater and falls below the failure conditions at 515 °C (Figure 3.9c). The model therefore preserves the fluid while the fluid pressure starts to build up during amphibole breakdown, eventually reaching brittle failure at 545 °C.

The fluid extraction style resembles a longer continuous fluid extraction episode for the simulation with smaller step size. This behaviour can also be seen at the blueschist to eclogite transition between 525 and 620 °C (see Figure 3.6a and 9a). Both models predict the same cumulative amount of fluid extracted at the end of the blueschist to eclogite transition of ∼5.5 vol% but for different duration. A similar behaviour is observed for the reaction with talc up to a cumulative fluid extraction of ∼6 vol% (Figure 3.9a). Previous studies emphasized that a gradual and continuous fluid extraction is not expected for the transition from lawsonite blueschist to lawsonite eclogite (Tsujimori & Ernst, 2014). The model with low kinetic barriers is therefore less consistent with the natural record of fluid infiltration events during prograde metamorphism. The model with moderate kinetic barriers should be preferred when simulating prograde metamorphism for subduction settings. A similar behaviour is observed for the reaction with talc up to a cumulative fluid extraction of ∼6 vol% (Figure 3.9a).

The model with smaller kinetic barriers predicts the same fluid extraction behaviour for low (<40 MPa) and high (>55 MPa) differential stresses (Figure 3.9c). The number of extraction steps in comparison to the default model is almost ten-times larger reaching ∼290 steps. This behaviour is more like a continuous episode of fluid extraction from a continuously reacting system, but each extraction resembles a smaller volume of fluid. Both models show the onset of brittle failure for differential stress values above ∼40 MPa. The onset has a steeper increase in extractions step for the model with low kinetic barriers due to more but smaller fluid extractions caused by the model increment size. The choke point corresponding to the transition from no extraction to the maximum number of extractions is narrower in the low kinetic barrier model ($\Delta\sigma$ ∼55 MPa) compared to the standard model ($\Delta\sigma$ ∼60 MPa; see Figure 3.9c). This corresponds to the last fluid extractions of the talc reaction, which is attained earlier for the model with low kinetic barriers (Figure 3.9a).

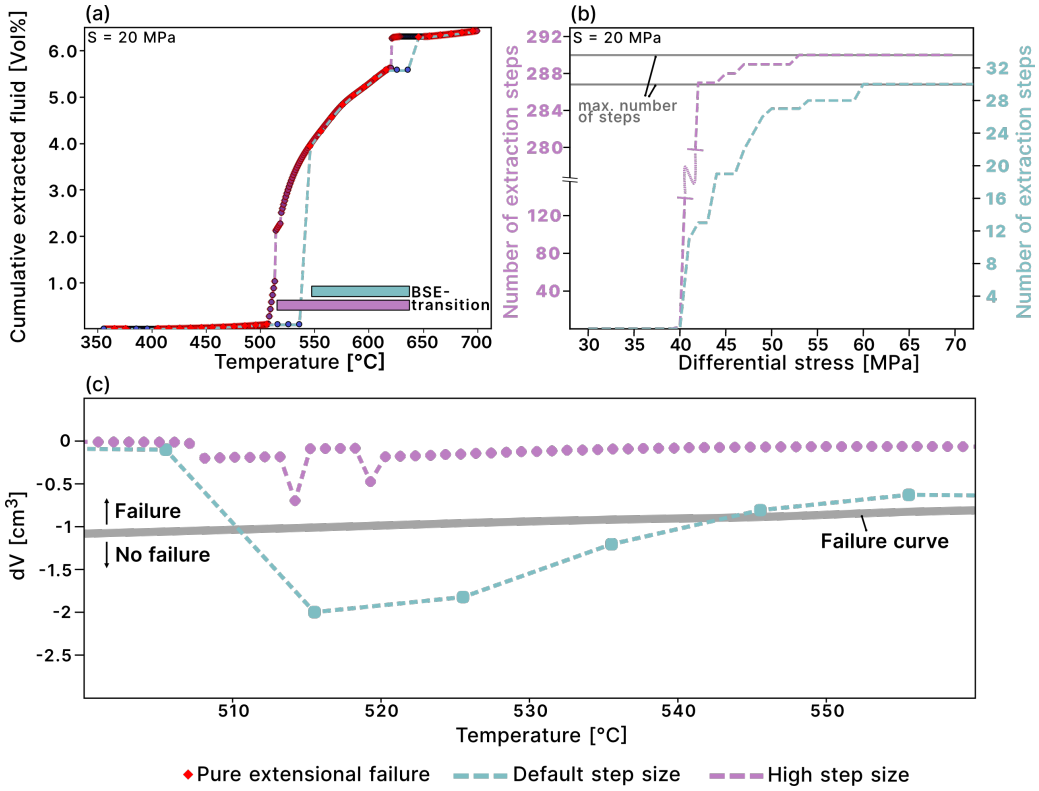

Figure 3.9: Simulation of two models with higher (default model) and lower kinetic barriers. (a) The cumulative extracted fluid comparing both models for the metabasalt composition using an S of 20 MPa and $\Delta\sigma$ of 50 MPa. Coloured bars show the duration of the blueschist to eclogite transition (BSE) with associated fluid extraction for both simulations. (b) Volume changes during the chlorite-out reaction (c) Total number of extraction events predicted for different values of differential stress. Left y-axis shows the smaller step size model whereas the right y-axis shows the larger step size model.

3.5.4 Fluid extraction in serpentinites and associated textures

Serpentinites play an important role in subduction zones due to their high fluid storage capacity and large amounts of fluid extracted during dehydration reactions (Kempf et al., 2020; Padrón-Navarta et al., 2010; M. W. Schmidt & Poli, 2014; Ulrich et al., 2024). The first formation of metamorphic olivine is associated with a dehydration reaction involving brucite and antigorite (450–500 °C in Figure 3.6b). In the Zermatt-Saas ophiolite located in the Western Alps, this reaction results in the formation of (i) cm sized patches of olivine in massive Ol-Atg-serpentinites, (ii) olivine in cm sized shear bands of serpentinites, (iii) olivine in cm wide shear zones in serpentinites, and (iv) olivine in cm sized veins (Ulrich et al., 2024). The second formation of metamorphic olivine is associated to antigorite dehydration (Jabaloy-Sánchez et al., 2022; Padrón-Navarta et al., 2010; Trommsdorff et al., 1998). In the Cerro del Almirez ultramafic massif, this reaction is associated with (v) olivine formation with spinifex-like textures, (vi) cm sized olivine crystals, and (vii) crosscutting bands on the cm size related to grain size reduction in chlorite-harzburgites (Padrón-Navarta et al., 2010, 2011; Trommsdorff et al., 1998). Those textures are thought to result from microcracking during brittle failure induced by hydrofracturing.

The serpentinite model presented in Figure 3.6 predicts a large fluid production at the onset of the brucite and antigorite breakdown reaction. Multiple brittle shear failure events are predicted by the model during the first dehydration reaction of brucite and antigorite as both the amount of fluid released and the amount of olivine increase. The associated formation of olivine during brittle shear failure is consistent with the natural occurrence of textures (i) to (iv) observed in the Western Alps (Ulrich et al., 2024).

Permeability values can be used to evaluate the possible passage of fluid through a rock and can be estimated from the model by the amount of fluid extracted over time calculated from the time-integrated fluid flux (Ague & Nicolescu, 2014; Bovay et al., 2021; Manning & Ingebritsen, 1999). Figure 3.10 shows the calculated permeability for the modelled fluid extraction episodes for the serpentinite (same settings as in Figure 3.6b). For the first episode of olivine formation and dehydration starting at ∼450 °C, centimetre-scale fractures and veins are assumed to have a surface area of 0.01 m^2 through which fluid passes when produced from 1 m^3 of serpentinite. The calculation results in permeability values of 10^{-19} to 10^{-18} m^2 (Figure 3.10). A smaller surface area of 0.001 m^2 would increase permeability by an order of magnitude. The lower limit of 10^{-19} m^2 is similar to the crustal permeability estimated by Manning and Ingebritsen (1999).

The second episode of olivine formation during the final antigorite breakdown at ∼670 °C is associated with a large fluid production of ∼10 vol% in total (Fig. 3.6b). The serpentinites model predicts brittle shear failure associated to the fluid production. This series of brittle failure events is associated with a second phase of olivine formation. Addition-

ally, orthopyroxene and chlorite are predicted to be stable by the model. These results are consistent with the textures (v) to (vii) described by (Padrón-Navarta et al., 2010) and (Trommsdorff et al., 1998). Calculated permeability results in high values, slightly above 10^{-19} m^2, assuming the discharge surface of 0.01 m^2 (Figure 3.10). After antigorite breakdown small volume changes are predicted, associated with minor chlorite dehydration in the model. This reaction results in a new series of brittle failure events following the brittle response during the final antigorite breakdown. For this stage, permeability values are $<10^{-20}$ m^2 for a discharge surface of 0.01 m^2 (Figure 3.10). Small fractures on the µm to mm scale and grain size reduction of olivine associated with brittle failure have been documented in samples from Cerro del Almirez (Jabaloy-Sánchez et al., 2022; Padrón-Navarta et al., 2010; Trommsdorff et al., 1998) and could be associated to the partial consumption of chlorite occurring after antigorite breakdown. Smaller fluid pathways described by a smaller discharge area of 0.001 m^2 result in permeability values above 10^{-20} m^2 (white diamonds in Figure 3.10). The simulation of a dehydrating serpentinite can potentially explain brittle failure and associated textures such as for the formation of olivine in veins, shear bands, and/or shear zones. The associated fluid production can therefore represent either large fluid extraction in structural conduits on the cm scale or possibly pervasive fluid flow (e.g., Bovay et al., 2021), whereas small amounts of fluid possibly occur smaller pathways such as fractures or veinlets on the mm or even µm scale.

3.5.5 Garnet as a proxy for fluid extractions

Garnet is one of the most used proxies to retrieve the amount of fluids produced during prograde metamorphism (Baxter & Caddick, 2013) and its major element zoning has been used as a recorder of seismic cycles (Viete et al., 2018). The integrated model can predict the brittle failure events associated to garnet growth. A possible correlation between major element zoning and brittle failure events is discussed using a compositionally zoned garnet from vugs observed in a Fe-Ti metgabbro of the Monviso area of the Western Alps (Angiboust & Raimondo, 2022). This high-pressure unit experienced peak conditions of 2.6–2.9 GPa and peak temperatures of 530–570 °C during alpine oceanic subduction (Angiboust & Raimondo, 2022). Oscillatory zoning in MnO has been reported for a garnet grain from a vug. The core of the grain contains larger zones of increasing and decreasing MnO within 300 µm, followed by an ∼500 µm mantle zone with a smooth decrease in MnO towards the outside of the grain (Figure 3.11a). Finally, a series of small overgrowths with an oscillatory MnO pattern form a ∼120 µm rim of the garnet.

The prograde history of this sample was simulated with ThorPT using the bulk rock composition, the P–T path from 445 °C and 17.0 GPa to 570 °C and 3.1 GPa and additional values for the subduction rate and angle from Angiboust and Raimondo (2022). The

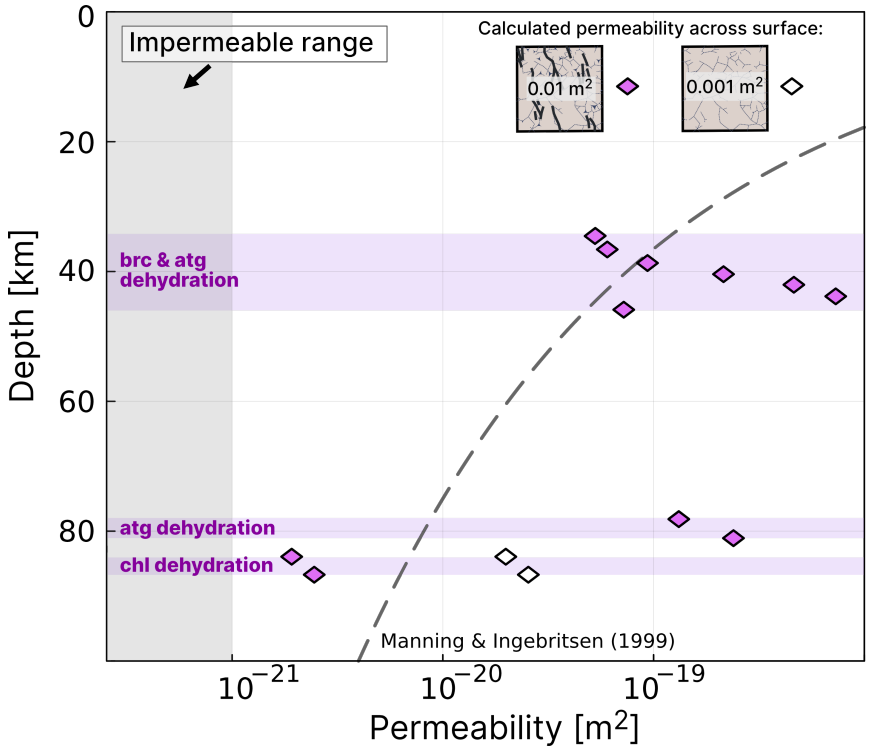

Figure 3.10: Calculated permeability of the serpentinites simulation (Figure 3.6b) from 1 m^3 of rock over a discharge surface of 0.01 m^2 or 0.001 m^2. Values represent the corresponding permeability when brittle failure occurs and associated fluid is assumed to be extracted. Purple areas highlight the duration of brucite, antigorite, and/or chlorite dehydration. The predicted permeability over depth estimated by Manning and Ingebritsen (1999) is shown as a gray dashed line for reference. Field of impermeability after Ganzhorn et al. (2019).

model was performed in the simplified Na_2O-CaO-K_2O-FeO-MnO-MgO-Al_2O_3-SiO_2-H_2O-O_2 (MnNCKFMASHO) system using the thermodynamic dataset of Holland, Baker, and Powell (1998) instead of Holland and Powell (2011) with similar solution models used by the authors (see Supplementary S1 and S4 for details). Note that Mn was included in the model compared to Angiboust and Raimondo (2022) as it allows garnet to be predicted to be stable at lower temperatures widening the T windows in which fluids are produced during eclogitisation. In addition, garnet fractionation was enabled to provide a more realistic model. Modelling increments were set to 10 °C steps assuming a system with moderate kinetic barriers (see 3.5.3) and pressure steps to 500 MPa. A tensile strength of 20 MPa and differential stress of 52 MPa were used. The simulation results are presented as a mode box diagram in Figure 3.11b. Several brittle failure episodes are predicted to occur during the crystallisation of this garnet related to compositional changes (Figure 3.11c). The predicted garnet compositions are shown using the spessartine fraction (Mn/(Mn+Fe+Mg+Ca)) as concentric growth shells using a circular shape. Each growth shell represent an instantaneous garnet growth episode at given P and T conditions. Multiple growth shells are predicted after the core growth and in the outer part of the grain before the rim. The predicted pattern resembles the observations made in the natural garnet, but the simulated garnet core has more Mn than the natural sample (Figure 3.11a). The increase of Mn observed in the sample, cannot be reproduced as the model assumes a closed system for Mn and does not consider possible garnet resorption along this P–T path. Mn can only decrease from core to rim due to Rayleigh fractionation with the mineral matrix. However, it is interesting to notice that the frequency of the Mn-zoning in the natural sample can be linked to the brittle failures events predicted by the model and caused by garnet growth. If linked to fluid extraction — as assumed in this work — these can explain variability in the diffusivity of Mn in the intergranular medium or an open system behaviour with an external Mn source.

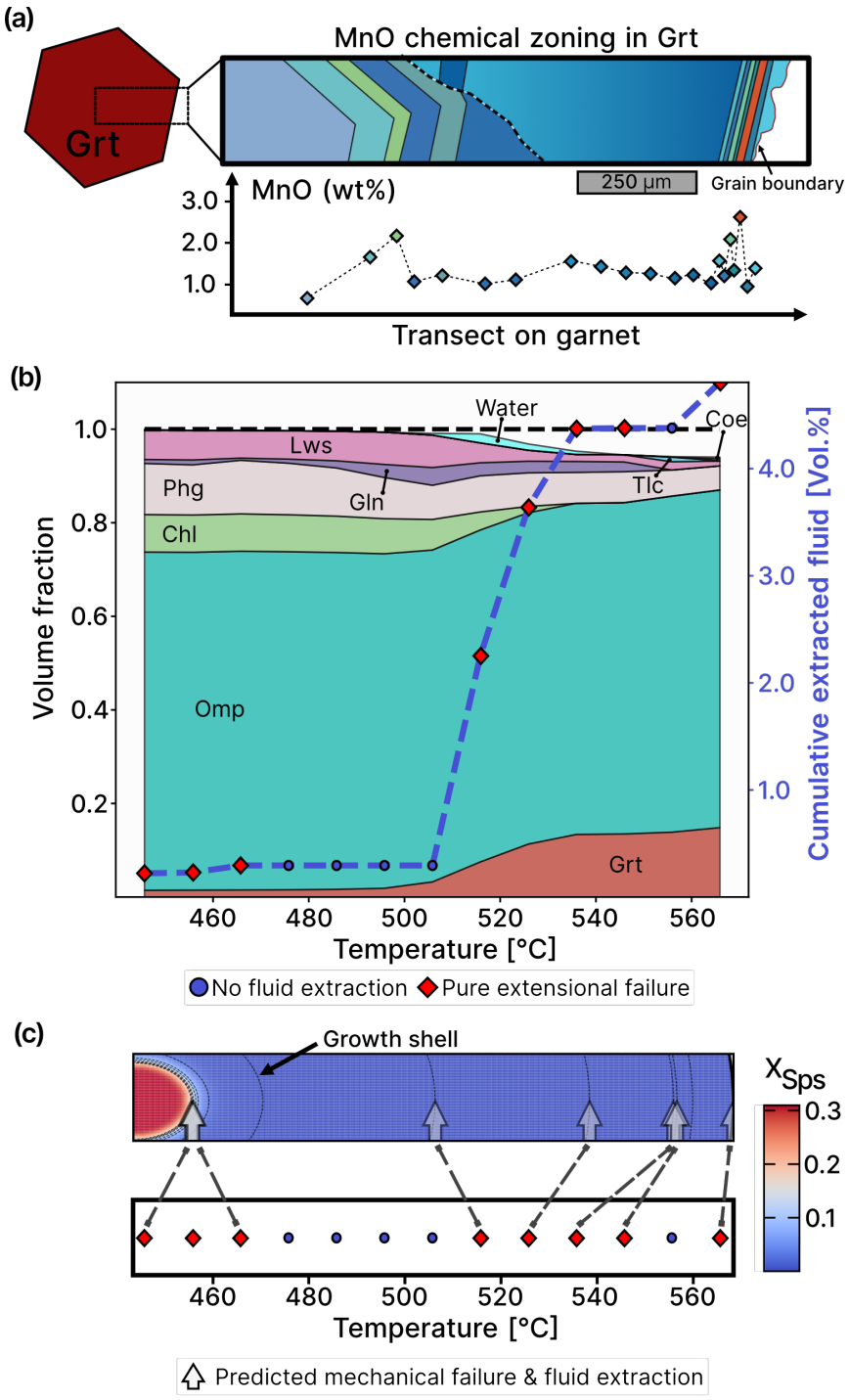

Figure 3.11: Summary of the natural occurring garnet from Monviso Lago Superiore Unit (Angiboust & Raimondo, 2022) and simulation results with ThorPT. (a) Sketch of the chemically zoned garnet as in (Angiboust & Raimondo, 2022) and the representative transect from core to rim. (b) Modelling results showing the box mode diagram, cumulative fluid extractions, and events of mechanical failure. (c) The simulated garnet presented as a sphere showing the spessartine fraction (X_{Sps} = Mn/(Mn+Fe+Mg+Ca)) as a colormap after diffusion. Arrows indicate the brittle failure events associated with the growth shell (dashed grey lines) when garnet fractionates during the simulation. Mineral abbreviations are after Warr (2021).

3.6 Conclusion

The development of a petrochemical model combined with a mechanical model is critical to understanding how metamorphic reactions can be coupled with brittle failure of the rock during major dehydration reactions. The software ThorPT allows the user to set up a simulation tailored to the geological problem of interest on a customised P–T path.

The results presented in this study show that the volume changes caused by metamorphic reaction and associated with fluid production are sufficient to initiate brittle failure at moderate differential stresses (40 - 50 MPa) for basaltic rocks assuming a competent rheology (20 MPa for tensile strength). Serpentinites with less competent rheology have a higher potential for brittle failure and are more sensitive to the mechanical stress. A higher mechanical resistance or low differential stress values can lead to episodic failure events.

It is known that brittle failure and crack formation increase the permeability of a rock and it is assumed here that fluid is extracted when brittle failure occurs. For episodically failing rocks this results in episodes of large fluid extraction rather than a small volume of fluid extracted continuously in the crust as assumed in other models. Distinct episodes of fluid extraction associated with brittle failure further support the link between metamorphic fluids and the occurrence of episodic tremor and slip events in subduction zones already suggested by many studies (Abers et al., 2009; Audet et al., 2009; Hacker, Abers, & Peacock, 2003; Kodaira et al., 2004; Oliver & Bons, 2001; Padrón-Navarta et al., 2013; Peacock, 2009; Peacock et al., 2011; Sippl et al., 2018; Taetz et al., 2018; Yardley, 1986).

Application of the model to subduction zone metamorphism shows that episodic and large fluid flows can be associated with brittle failure. These features are compatible with cm-sized veins and shear zones observed in serpentinites from the European Alps and Spain. Similar, failure events may be related to the geochemical zoning pattern recorded in a garnet grain of a metagabbro sample from the Western Alps. Consequently, a pulsed and localised fluid distribution in the crust may have implications for the fluid migration dynamics and mass transfer.

Bibliography

Abers, G. A., MacKenzie, L. S., Rondenay, S., Zhang, Z., Wech, A. G., & Creager, K. C. (2009). Imaging the source region of Cascadia tremor and intermediate-depth earthquakes. *Geology*, *37*(12), 1119–1122. https://doi.org/10.1130/G30143A.1

Ague, J. J. (2011). Extreme channelization of fluid and the problem of element mobility during Barrovian metamorphism. *American Mineralogist*, *96*(2-3), 333–352. https://doi.org/10.2138/am.2011.3582

Ague, J. J., & Nicolescu, S. (2014). Carbon dioxide released from subduction zones by fluid-mediated reactions. *Nature Geoscience*, *7*(5), 355–360. https://doi.org/10.1038/ngeo2143

Angiboust, S., Agard, P., Raimbourg, H., Yamato, P., & Huet, B. (2011). Subduction interface processes recorded by eclogite-facies shear zones (Monviso, W. Alps). *Lithos*, *127*(1-2), 222–238. https://doi.org/10.1016/j.lithos.2011.09.004

Angiboust, S., & Raimondo, T. (2022). Permeability of subducted oceanic crust revealed by eclogite-facies vugs. *Geology*, *50*(8), 964–968. https://doi.org/10.1130/G50066.1

Audet, P., Bostock, M. G., Christensen, N. I., & Peacock, S. M. (2009). Seismic evidence for overpressured subducted oceanic crust and megathrust fault sealing. *Nature*, *457*(7225), 76–78. https://doi.org/10.1038/nature07650

Baxter, E. F., & Caddick, M. J. (2013). Garnet growth as a proxy for progressive subduction zone dehydration. *Geology*, *41*(6), 643–646. https://doi.org/10.1130/G34004.1

Bebout, G. E., & Penniston-Dorland, S. C. (2016). Fluid and mass transfer at subduction interfaces-The field metamorphic record. *Lithos*, *240-243*, 228–258. https://doi.org/10.1016/j.lithos.2015.10.007

Beinlich, A., John, T., Vrijmoed, J. C., Tominaga, M., Magna, T., & Podladchikov, Y. Y. (2020). Instantaneous rock transformations in the deep crust driven by reactive fluid flow. *Nature Geoscience*, *13*(4), 307–311. https://doi.org/10.1038/s41561-020-0554-9

Belgrano, T. M., & Diamond, L. W. (2019). Subduction-zone contributions to axial volcanism in the Oman–U.A.E. ophiolite. *Lithosphere*, *11*(3), 399–411. https://doi.org/10.1130/L1045.1

Bird, P. (1978). Stress and temperature in subduction shear zones: Tonga and Mariana. *Geophysical Journal International*, *55*(2), 411–434. https://doi.org/10.1111/j.1365-246X.1978.tb04280.x

Bovay, T., Rubatto, D., & Lanari, P. (2021). Pervasive fluid-rock interaction in subducted oceanic crust revealed by oxygen isotope zoning in garnet. *Contributions to Mineralogy and Petrology*, *176*(7), 1–22. https://doi.org/10.1007/s00410-021-01806-4

Bras, E., Yamato, P., Schmalholz, S. M., Duretz, T., & Podladchikov, Y. Y. (2023). Eclogitisation of dry and impermeable granulite by fluid flow with reaction-induced porosity: Insights from hydro-chemical modelling. *Earth and Planetary Science Letters*, *617*, 118256. https://doi.org/10.1016/j.epsl.2023.118256

Bukała, M., Barnes, C. J., Jeanneret, P., Hidas, K., Mazur, S., Almqvist, B. S., Kośmińska, K., Klonowska, I., Šurka, J., & Majka, J. (2020). Brittle Deformation During Eclogitization of Early Paleozoic Blueschist. *Frontiers in Earth Science*, *8*(December), 1–17. https://doi.org/10.3389/feart.2020.594453

Byerlee, J. D. (1978). Friction of Rocks. *116*.

Condit, C. B., & French, M. E. (2022). Geologic Evidence of Lithostatic Pore Fluid Pressures at the Base of the Subduction Seismogenic Zone. *Geophysical Research Letters*, *49*(12). https://doi.org/10.1029/2022GL098862

Condit, C. B., French, M. E., Hayles, J. A., Yeung, L. Y., Chin, E. J., & Lee, C.-T. A. (2022). Rheology of Metasedimentary Rocks at the Base of the Subduction Seismogenic Zone. *Geochemistry, Geophysics, Geosystems*, *23*(2), 1–32. https://doi.org/10.1029/2021GC010194

Connolly, J. A. (1997). Devolatilization-generated fluid pressure and deformation-propagated fluid flow during prograde regional metamorphism. *Journal of Geophysical Research B: Solid Earth*, *102*(B8), 18149–18173. https://doi.org/10.1029/97jb00731

Connolly, J. A. (2005). Computation of phase equilibria by linear programming: A tool for geodynamic modeling and its application to subduction zone decarbonation. *Earth and Planetary Science Letters*, *236*(1-2), 524–541. https://doi.org/10.1016/j.epsl.2005.04.033

Connolly, J. A., & Podladchikov, Y. Y. (2004). Fluid flow in compressive tectonic settings: Implications for midcrustal seismic reflectors and downward fluid migration. *Journal of Geophysical Research: Solid Earth*, *109*(B4), 1–12. https://doi.org/10.1029/2003JB002822

Cox, S. F. (2010). The application of failure mode diagrams for exploring the roles of fluid pressure and stress states in controlling styles of fracture-controlled permeability enhancement in faults and shear zones. *Geofluids*, *10*(1-2), 217–233. https://doi.org/10.1111/j.1468-8123.2010.00281.x

Cox, S. F., Etheridge, M. A., & Wall, V. J. (1987). The role of fluids in syntectonic mass transport, and the localization of metamorphic vein-type ore deposists. *Ore Geology Reviews*, *2*(1-3), 65–86. https://doi.org/10.1016/0169-1368(87)90024-2

de Capitani, C., & Brown, T. H. (1987). The computation of chemical equilibrium in complex systems containing non-ideal solutions. *Geochimica et Cosmochimica Acta*, *51*(10), 2639–2652. https://doi.org/10.1016/0016-7037(87)90145-1

de Capitani, C., & Petrakakis, K. (2010). The computation of equilibrium assemblage diagrams with Theriak/Domino software. *American Mineralogist*, *95*(7), 1006–1016. https://doi.org/10.2138/am.2010.3354

Diener, J. F. A., Powell, R., White, R. W., & Holland, T. J. B. (2007). A new thermodynamic model for clino- and orthoamphiboles in the system Na 2 O–CaO–FeO–MgO–Al 2 O 3 –SiO 2 –H 2 O–O. *Journal of Metamorphic Geology*, *25*(6), 631–656. https://doi.org/10.1111/j.1525-1314.2007.00720.x

Dominguez, H. (2024). Iddingsite/DiffusionGarnet.jl: v0.1.7. https://doi.org/10.5281/zenodo.10783144

Duesterhoeft, E., Quinteros, J., Oberhänsli, R., Bousquet, R., & de Capitani, C. (2014). Relative impact of mantle densification and eclogitization of slabs on subduction dynamics: A numerical thermodynamic/thermokinematic investigation of metamorphic density evolution. *Tectonophysics*, *637*, 20–29. https://doi.org/10.1016/j.tecto.2014.09.009

Egbert, G. D., Yang, B., Bedrosian, P. A., Key, K., Livelybrooks, D. W., Schultz, A., Kelbert, A., & Parris, B. (2022). Fluid transport and storage in the Cascadia forearc influenced by overriding plate lithology. *Nature Geoscience*, *15*(8), 677–682. https://doi.org/10.1038/s41561-022-00981-8

Etheridge, M. A. (1983). Differential stress magnitudes during regional deformation and metamorphism: Upper bound imposed by tensile fracturing. *Geology*, *11*(4), 231. https://doi.org/10.1130/0091-7613(1983)11⟨231:DSMDRD⟩2.0.CO;2

Etheridge, M. A., Wall, V. J., & Vernon, R. H. (1983). The role of the fluid phase during regional metamorphism and deformation. *Journal of Metamorphic Geology*, *1*(3), 205–226. https://doi.org/10.1111/j.1525-1314.1983.tb00272.x

Etheridge, M. A., Daczko, N. R., Chapman, T., & Stuart, C. A. (2021). Mechanisms of melt extraction during lower crustal partial melting. *Journal of Metamorphic Geology*, *39*(1), 57–75. https://doi.org/10.1111/jmg.12561

Gale, A., Dalton, C. A., Langmuir, C. H., Su, Y., & Schilling, J.-G. (2013). The mean composition of ocean ridge basalts. *Geochemistry, Geophysics, Geosystems*, *14*(3), 489–518. https://doi.org/10.1029/2012GC004334

Ganzhorn, A. C., Pilorgé, H., & Reynard, B. (2019). Porosity of metamorphic rocks and fluid migration within subduction interfaces. *Earth and Planetary Science Letters*, *522*, 107–117. https://doi.org/10.1016/j.epsl.2019.06.030

Gerya, T. V., Stöckhert, B., & Perchuk, A. L. (2002). Exhumation of high-pressure metamorphic rocks in a subduction channel: A numerical simulation. *Tectonics*, *21*(6), 6–1. https://doi.org/10.1029/2002TC001406

Gies, N. B., Konrad-Schmolke, M., & Hermann, J. (2024). Modeling the Global Water Cycle—The Effect of Mg-Sursassite and Phase a on Deep Slab Dehydration and

the Global Subduction Zone Water Budget. *Geochemistry, Geophysics, Geosystems*, *25*(3). https://doi.org/10.1029/2024GC011507

Giuntoli, F., Menegon, L., Siron, G., Cognigni, F., Leroux, H., Compagnoni, R., Rossi, M., & Vitale Brovarone, A. (2024). Methane-hydrogen-rich fluid migration may trigger seismic failure in subduction zones at forearc depths. *Nature Communications*, *15*(1), 480. https://doi.org/10.1038/s41467-023-44641-w

Gold, T., & Soter, S. (1984). Fluid ascent through the solid lithosphere and its relation to earthquakes. *Pure and Applied Geophysics PAGEOPH*, *122*(2-4), 492–530. https://doi.org/10.1007/BF00874614

Gosselin, J. M., Audet, P., Estève, C., McLellan, M., Mosher, S. G., & Schaeffer, A. J. (2020). Seismic evidence for megathrust fault-valve behavior during episodic tremor and slip. *Science Advances*, *6*(4). https://doi.org/10.1126/sciadv.aay5174

Griffits, A. A. (1921). VI. The phenomena of rupture and flow in solids. *Philosophical Transactions of the Royal Society of London. Series A, Containing Papers of a Mathematical or Physical Character*, *221*(582-593), 163–198. https://doi.org/10.1098/rsta.1921.0006

Hacker, B. R., Abers, G. A., & Peacock, S. M. (2003). Subduction factory 1. Theoretical mineralogy, densities, seismic wave speeds, and H 2 O contents. *Journal of Geophysical Research: Solid Earth*, *108*(B1), 1–26. https://doi.org/10.1029/2001JB001127

Hacker, B. R., Peacock, S. M., Abers, G. A., & Holloway, S. D. (2003). Subduction factory 2. Are intermediate-depth earthquakes in subducting slabs linked to metamorphic dehydration reactions? *Journal of Geophysical Research: Solid Earth*, *108*(B1). https://doi.org/10.1029/2001JB001129

Hanks, T. C. (1977). Earthquake Stress Drops, Ambient Tectonic Stresses and Stresses That Drive Plate Motions BT - Stress in the Earth. In M. Wyss (Ed.). Birkhäuser Basel. https://doi.org/10.1007/978-3-0348-5745-1{_}28

Hernández-Uribe, D., & Palin, R. M. (2019). A revised petrological model for subducted oceanic crust: Insights from phase equilibrium modelling. *Journal of Metamorphic Geology*, *37*(6), 745–768. https://doi.org/10.1111/jmg.12483

Hobbs, B. E., & Ord, A. (2018). Coupling of fluid flow to permeability development in mid- to upper crustal environments: a tale of three pressures. *Geological Society, London, Special Publications*, *453*(1), 81–120. https://doi.org/10.1144/SP453.9

Holland, T. J. B., Baker, J., & Powell, R. (1998). Mixing properties and activity?composition relationships of chlorites in the system MgO?FeO?Al2O3?SiO2?H2O. *European Journal of Mineralogy*, *10*(3), 395–406. https://doi.org/10.1127/ejm/10/3/0395

Holland, T. J. B., & Powell, R. (1991). A Compensated-Redlich-Kwong (CORK) equation for volumes and fugacities of CO2 and H2O in the range 1 bar to 50 kbar and

100–1600°C. *Contributions to Mineralogy and Petrology*, *109*(2), 265–273. https://doi.org/10.1007/BF00306484

Holland, T. J. B., & Powell, R. (1996). Thermodynamics of order-disorder in minerals; II, Symmetric formalism applied to solid solutions. *American Mineralogist*, *81*(11-12), 1425–1437. https://doi.org/10.2138/am-1996-11-1215

Holland, T. J. B., & Powell, R. (1998). An internally consistent thermodynamic data set for phases of petrological interest. *Journal of Metamorphic Geology*, *16*(3), 309–343. https://doi.org/10.1111/j.1525-1314.1998.00140.x

Holland, T. J. B., & Powell, R. (2003). Activity–composition relations for phases in petrological calculations: an asymmetric multicomponent formulation. *Contributions to Mineralogy and Petrology*, *145*(4), 492–501. https://doi.org/10.1007/s00410-003-0464-z

Holland, T. J. B., & Powell, R. (2011). An improved and extended internally consistent thermodynamic dataset for phases of petrological interest, involving a new equation of state for solids. *Journal of Metamorphic Geology*, *29*(3), 333–383. https://doi.org/https://doi.org/10.1111/j.1525-1314.2010.00923.x

Hosokawa, T., & Hashimoto, Y. (2022). Geological constraints on dynamic changes of fluid pressure in seismic cycles. *Scientific Reports*, *12*(1), 14789. https://doi.org/10.1038/s41598-022-19083-x

Huber, K., Vrijmoed, J., & John, T. (2022). Formation of olivine veins by reactive fluid flow in a dehydrating serpentinite. *Geochemistry, Geophysics, Geosystems*. https://doi.org/10.1029/2021gc010267

Jabaloy-Sánchez, A., Sánchez-Vizcaíno, V. L., Padrón-Navarta, J. A., Hidas, K., Gómez-Pugnaire, M. T., & Garrido, C. J. (2022). Olivine-rich veins in high-pressure serpentinites: A far-field paleo-stress snapshot during subduction. *Journal of Structural Geology*, *163*(October 2021), 104721. https://doi.org/10.1016/j.jsg.2022.104721

Jaeger, C. (1979, June). *Rock Mechanics and Engineering* (4th editio, Vol. 9). Cambridge University Press. https://doi.org/10.1017/CBO9780511735349

Jung, H., Green II, H. W., & Dobrzhinetskaya, L. F. (2004). Intermediate-depth earthquake faulting by dehydration embrittlement with negative volume change. *Nature*, *428*(6982), 545–549. https://doi.org/10.1038/nature02412

Kato, A., Iidaka, T., Ikuta, R., Yoshida, Y., Katsumata, K., Iwasaki, T., Sakai, S., Thurber, C., Tsumura, N., Yamaoka, K., Watanabe, T., Kunitomo, T., Yamazaki, F., Okubo, M., Suzuki, S., & Hirata, N. (2010). Variations of fluid pressure within the subducting oceanic crust and slow earthquakes. *Geophysical Research Letters*, *37*(14), 1–5. https://doi.org/10.1029/2010GL043723

Kempf, E. D., Hermann, J., Reusser, E., Baumgartner, L. P., & Lanari, P. (2020). The role of the antigorite + brucite to olivine reaction in subducted serpentinites (Zermatt,

Switzerland). *Swiss Journal of Geosciences*, *113*(1). https://doi.org/10.1186/s00015-020-00368-0

Kerrick, D., & Connolly, J. A. (2001). Metamorphic devolatilization of subducted oceanic metabasalts: implications for seismicity, arc magmatism and volatile recycling. *Earth and Planetary Science Letters*, *189*(1-2), 19–29. https://doi.org/10.1016/S0012-821X(01)00347-8

Kirby, S. H., Stein, S., Okal, E. A., & Rubie, D. C. (1996). Metastable mantle phase transformations and deep earthquakes in subducting oceanic lithosphere. *Reviews of Geophysics*, *34*(2), 261–306. https://doi.org/10.1029/96RG01050

Kodaira, S., Iidaka, T., Kato, A., Park, J.-O., Iwasaki, T., & Kaneda, Y. (2004). High Pore Fluid Pressure May Cause Silent Slip in the Nankai Trough. *Science*, *304*(5675), 1295–1298. https://doi.org/10.1126/science.1096535

Konrad-Schmolke, M., Zack, T., O'Brien, P. J., & Barth, M. (2011). Fluid migration above a subducted slab - Thermodynamic and trace element modelling of fluid-rock interaction in partially overprinted eclogite-facies rocks (Sesia Zone, Western Alps). *Earth and Planetary Science Letters*, *311*(3-4), 287–298. https://doi.org/10.1016/j.epsl.2011.09.025

Koyama, Y., Wallis, S. R., & Nagaya, T. (2024). Subduction plate interface shear stress associated with rapid subduction at deep slow earthquake depths: example from the Sanbagawa belt, southwestern Japan. *Solid Earth*, *15*(2), 143–166. https://doi.org/10.5194/se-15-143-2024

Lanari, P., & Duesterhoeft, E. (2019). Modeling Metamorphic Rocks Using Equilibrium Thermodynamics and Internally Consistent Databases: Past Achievements, Problems and Perspectives. *Journal of Petrology*, *60*(1), 19–56. https://doi.org/10.1093/petrology/egy105

Lanari, P., Giuntoli, F., Loury, C., Burn, M., & Engi, M. (2017). An inverse modeling approach to obtain P–T conditions of metamorphic stages involving garnet growth and resorption. *European Journal of Mineralogy*, *29*(2), 181–199. https://doi.org/10.1127/ejm/2017/0029-2597

Lockner, D. A. (1995). Rock Failure. In *Rock physics & phase relations* (pp. 127–147). American Geophysical Union (AGU). https://doi.org/https://doi.org/10.1029/RF003p0127

Malvoisin, B., Podladchikov, Y. Y., & Vrijmoed, J. C. (2015). Coupling changes in densities and porosity to fluid pressure variations in reactive porous fluid flow: Local thermodynamic equilibrium. *Geochemistry, Geophysics, Geosystems*, *16*(12), 4362–4387. https://doi.org/10.1002/2015GC006019

Manning, C. E., & Ingebritsen, S. E. (1999). Permeability of the continental crust: Implications of geothermal data and metamorphic systems. *Reviews of Geophysics*, *37*(1), 127–150. https://doi.org/10.1029/1998RG900002

Mazzucchelli, M. L., Moulas, E., Kaus, B. J. P., & Speck, T. (2024). Fluid-mineral Equilibrium Under Nonhydrostatic Stress: Insight From Molecular Dynamics. *American Journal of Science*, *324*, 1–29. https://doi.org/10.2475/001c.92881

Mckenzie, D. (1984). The generation and compaction of partially molten rock. *Journal of Petrology*, *25*(3), 713–765. https://doi.org/10.1093/petrology/25.3.713

Morishige, M., & van Keken, P. E. (2018). Fluid Migration in a Subducting Viscoelastic Slab. *Geochemistry, Geophysics, Geosystems*, *19*(2), 337–355. https://doi.org/10.1002/2017GC007236

Moulas, E., Schmalholz, S. M., Podladchikov, Y., Tajčmanová, L., Kostopoulos, D., & Baumgartner, L. (2019). Relation between mean stress, thermodynamic, and lithostatic pressure. *Journal of Metamorphic Geology*, *37*(1), 1–14. https://doi.org/10.1111/jmg.12446

Nguyen, T. T., Vu, M. N., Tran, N. H., Dao, N. H., & Pham, D. T. (2020). Stress induced permeability changes in brittle fractured porous rock. *International Journal of Rock Mechanics and Mining Sciences*, *127*(January). https://doi.org/10.1016/j.ijrmms.2020.104224

Niu, F., Silver, P. G., Nadeau, R. M., & McEvilly, T. V. (2003). Migration of seismic scatterers associated with the 1993 Parkfield aseismic transient event. *Nature*, *426*(6966), 544–548. https://doi.org/10.1038/nature02151

Nordstrom, D. K., & Munoz, J. L. (1994). *Geochemical thermodynamics* (Second ed.). Blackwell Scientific Publ.

Norton, D., & Knapp, R. (1977). Transport phenomena in hydrothermal systems; the nature of porosity. https://doi.org/10.2475/ajs.277.8.913

Oliver, N. H. S., & Bons, P. D. (2001). Mechanisms of fluid flow and fluid-rock interaction in fossil metamorphic hydrothermal systems inferred from vein-wallrock patterns, geometry and microstructure. *Geofluids*, *1*(2), 137–162. https://doi.org/10.1046/j.1468-8123.2001.00013.x

Padrón-Navarta, J. A., Sánchez-Vizcaí, V. L., Garrido, C. J., & Gómez-Pugnaire, M. T. (2011). Metamorphic record of high-pressure dehydration of antigorite serpentinite to chlorite harzburgite in a subduction setting (Cerro del Almirez, Nevado-Filábride complex, Southern Spain). *Journal of Petrology*, *52*(10), 2047–2078. https://doi.org/10.1093/petrology/egr039

Padrón-Navarta, J. A., Sánchez-Vizcaíno, V. L., Hermann, J., Connolly, J. A., Garrido, C. J., Gómez-Pugnaire, M. T., & Marchesi, C. (2013). Tschermak's substitution in

antigorite and consequences for phase relations and water liberation in high-grade serpentinites. *Lithos*, *178*, 186–196. https://doi.org/10.1016/j.lithos.2013.02.001

Padrón-Navarta, J. A., Tommasi, A., Garrido, C. J., Sánchez-Vizcaíno, V. L., Gómez-Pugnaire, M. T., Jabaloy, A., & Vauchez, A. (2010). Fluid transfer into the wedge controlled by high-pressure hydrofracturing in the cold top-slab mantle. *Earth and Planetary Science Letters*, *297*(1-2), 271–286. https://doi.org/10.1016/j.epsl.2010.06.029

Pattison, D. R., de Capitani, C., & Gaidies, F. (2011). Petrological consequences of variations in metamorphic reaction affinity. *Journal of Metamorphic Geology*, *29*(9), 953–977. https://doi.org/10.1111/j.1525-1314.2011.00950.x

Peacock, S. M. (2009). Thermal and metamorphic environment of subduction zone episodic tremor and slip. *Journal of Geophysical Research*, *114*(8), B00A07. https://doi.org/10.1029/2008JB005978

Peacock, S. M., Christensen, N. I., Bostock, M. G., & Audet, P. (2011). High pore pressures and porosity at 35 km depth in the Cascadia subduction zone. *Geology*, *39*(5), 471–474. https://doi.org/10.1130/G31649.1

Penniston-Dorland, S. C., Kohn, M. J., & Manning, C. E. (2015). The global range of subduction zone thermal structures from exhumed blueschists and eclogites: Rocks are hotter than models. *Earth and Planetary Science Letters*, *428*, 243–254. https://doi.org/10.1016/j.epsl.2015.07.031

Philippot, P., & Selverstone, J. (1991). Trace-element-rich brines in eclogitic veins: implications for fluid composition and transport during subduction. *Contributions to Mineralogy and Petrology*, *106*(4), 417–430. https://doi.org/10.1007/BF00321985

Plümper, O., Botan, A., Los, C., Liu, Y., Malthe-Sørenssen, A., & Jamtveit, B. (2017). Fluid-driven metamorphism of the continental crust governed by nanoscale fluid flow. *Nature Geoscience*, *10*(9), 685–690. https://doi.org/10.1038/ngeo3009

Plümper, O., Røyne, A., Magrasó, A., & Jamtveit, B. (2012). The interface-scale mechanism of reaction-induced fracturing during serpentinization. *Geology*, *40*(12), 1103–1106. https://doi.org/10.1130/G33390.1

Ramsay, J. G. (1980). The crack–seal mechanism of rock deformation. *Nature*, *284*(5752), 135–139. https://doi.org/10.1038/284135a0

Saffer, D. M., & Tobin, H. J. (2011). Hydrogeology and Mechanics of Subduction Zone Forearcs: Fluid Flow and Pore Pressure. *Annual Review of Earth and Planetary Sciences*, *39*(1), 157–186. https://doi.org/10.1146/annurev-earth-040610-133408

Schmidt, M. W., & Poli, S. (2014). Devolatilization During Subduction. In *Treatise on geochemistry* (2nd ed., pp. 669–701, Vol. 4). Elsevier. https://doi.org/10.1016/B978-0-08-095975-7.00321-1

Schmidt, W. L., & Platt, J. P. (2022). Stress, microstructure, and deformation mechanisms during subduction underplating at the depth of tremor and slow slip, Franciscan Complex, northern California. *Journal of Structural Geology*, *154*(August 2021), 104469. https://doi.org/10.1016/j.jsg.2021.104469

Secor, D. T. (1965). Role of fluid pressure in jointing. *American Journal of Science*, *263*(8), 633–646. https://doi.org/10.2475/ajs.263.8.633

Shiina, T., Nakajima, J., & Matsuzawa, T. (2013). Seismic evidence for high pore pressures in the oceanic crust: Implications for fluid-related embrittlement. *Geophysical Research Letters*, *40*(10), 2006–2010. https://doi.org/10.1002/grl.50468

Sibson, R. H. (2000). A Brittle Failure Mode Plot Defining Conditions for High-Flux Flow. *Economic Geology*, *95*(1), 41–48. https://doi.org/10.2113/gsecongeo.95.1.41

Sibson, R. H. (2013). Stress switching in subduction forearcs: Implications for overpressure containment and strength cycling on megathrusts. *Tectonophysics*, *600*, 142–152. https://doi.org/10.1016/j.tecto.2013.02.035

Sibson, R. H. (2017). Tensile overpressure compartments on low-angle thrust faults. *Earth, Planets and Space*, *69*(1), 113. https://doi.org/10.1186/s40623-017-0699-y

Sippl, C., Schurr, B., Asch, G., & Kummerow, J. (2018). Seismicity Structure of the Northern Chile Forearc From >100,000 Double-Difference Relocated Hypocenters. *Journal of Geophysical Research: Solid Earth*, *123*(5), 4063–4087. https://doi.org/10.1002/2017JB015384

Stewart, E. M., & Ague, J. J. (2020). Pervasive subduction zone devolatilization recycles CO2 into the forearc. *Nature Communications*, *11*(1), 1–8. https://doi.org/10.1038/s41467-020-19993-2

Strating, E., & Vissers, R. (1991). Dehydration-induced fracturing of eclogite-facies peridotites: Implications for the mechanical behaviour of subducting oceanic lithosphere. *Tectonophysics*, *200*(1-3), 187–198. https://doi.org/10.1016/0040-1951(91)90014-J

Sun, C., & Liang, Y. (2015). A REE-in-garnet–clinopyroxene thermobarometer for eclogites, granulites and garnet peridotites. *Chemical Geology*, *393-394*, 79–92. https://doi.org/10.1016/j.chemgeo.2014.11.014

Taetz, S., John, T., Bröcker, M., Spandler, C., & Stracke, A. (2018). Fast intraslab fluid-flow events linked to pulses of high pore fluid pressure at the subducted plate interface. *Earth and Planetary Science Letters*, *482*, 33–43. https://doi.org/10.1016/j.epsl.2017.10.044

Trommsdorff, V., López Sánchez-Vizcaíno, V., Gómez-Pugnaire, M. T., & Müntener, O. (1998). High pressure breakdown of antigorite to spinifex-textured olivine and orthopyroxene, SE Spain. *Contributions to Mineralogy and Petrology*, *132*(2), 139–148. https://doi.org/10.1007/s004100050412

Tsujimori, T., & Ernst, W. (2014). Lawsonite blueschists and lawsonite eclogites as proxies for palaeo-subduction zone processes: a review. *Journal of Metamorphic Geology*, *32*(5), 437–454. https://doi.org/10.1111/jmg.12057

Ulrich, M., Rubatto, D., Hermann, J., Markmann, T. A., Bouvier, A.-s., & Deloule, E. (2024). Olivine formation processes and fluid pathways in subducted serpentinites revealed by in-situ oxygen isotope analysis (Zermatt-Saas, Switzerland). *Chemical Geology*, *649*(November 2023), 121978. https://doi.org/10.1016/j.chemgeo.2024.121978

Van Den Beukel, J., & Wortel, R. (1988). Thermo-mechanical modelling of arc-trench regions. *Tectonophysics*, *154*(3), 177–193. https://doi.org/https://doi.org/10.1016/0040-1951(88)90101-1

Van Keken, P. E., Kiefer, B., & Peacock, S. M. (2002). High-resolution models of subduction zones: Implications for mineral dehydration reactions and the transport of water into the deep mantle. *Geochemistry, Geophysics, Geosystems*, *3*(10). https://doi.org/10.1029/2001GC000256

Vho, A., Lanari, P., & Rubatto, D. (2019). An Internally-Consistent Database for Oxygen Isotope Fractionation Between Minerals. *Journal of Petrology*, *60*(11), 2101–2129. https://doi.org/10.1093/petrology/egaa001

Vho, A., Lanari, P., Rubatto, D., & Hermann, J. (2020). Tracing fluid transfers in subduction zones: an integrated thermodynamic and δ18O fractionation modelling approach. *Solid Earth*, *11*(2), 307–328. https://doi.org/10.5194/se-11-307-2020

Viete, D. R., Hacker, B. R., Allen, M. B., Seward, G. G. E., Tobin, M. J., Kelley, C. S., Cinque, G., & Duckworth, A. R. (2018). Metamorphic records of multiple seismic cycles during subduction. *Science Advances*, *4*(3), 1–13. https://doi.org/10.1126/sciadv.aaq0234

Wang, H., Huismans, R. S., & Rondenay, S. (2019). Water Migration in the Subduction Mantle Wedge: A Two-Phase Flow Approach. *Journal of Geophysical Research: Solid Earth*, *124*(8), 9208–9225. https://doi.org/10.1029/2018JB017097

Warr, L. N. (2021). IMA–CNMNC approved mineral symbols. *Mineralogical Magazine*, *85*(3), 291–320. https://doi.org/10.1180/mgm.2021.43

Warren-Smith, E., Fry, B., Wallace, L., Chon, E., Henrys, S., Sheehan, A., Mochizuki, K., Schwartz, S., Webb, S., & Lebedev, S. (2019). Episodic stress and fluid pressure cycling in subducting oceanic crust during slow slip. *Nature Geoscience*, *12*(6), 475–481. https://doi.org/10.1038/s41561-019-0367-x

Wilson, C. R., Spiegelman, M., van Keken, P. E., & Hacker, B. R. (2014). Fluid flow in subduction zones: The role of solid rheology and compaction pressure. *Earth and Planetary Science Letters*, *401*, 261–274. https://doi.org/10.1016/j.epsl.2014.05.052

Winter, J. D. (2014). *Principles of Igneous and Metamorphic Petrology*. Pearson Education. https://books.google.ch/books?id=0qmSAgAAQBAJ

Yamato, P., Duretz, T., & Angiboust, S. (2019). Brittle/Ductile Deformation of Eclogites: Insights From Numerical Models. *Geochemistry, Geophysics, Geosystems*, *20*(7), 3116–3133. https://doi.org/10.1029/2019GC008249

Yamato, P., Duretz, T., Baïsset, M., & Luisier, C. (2022). Reaction-induced volume change triggers brittle failure at eclogite facies conditions. *Earth and Planetary Science Letters*, *584*, 117520. https://doi.org/10.1016/j.epsl.2022.117520

Yardley, B. W. D. (1986). Fluid Migration and Veining in the Connemara Schists, Ireland. In *Fluid-rock interactions during metamorphism* (pp. 109–131). https://doi.org/10.1007/978-1-4612-4896-5{_}5

Zack, T., & John, T. (2007). An evaluation of reactive fluid flow and trace element mobility in subducting slabs. *239*, 199–216. https://doi.org/https://doi.org/10.1016/j.chemgeo.2006.10.020

Chapter 4

Isotope evidence of fluid-rock interaction processes from blueschists and eclogites on Syros (Cyclades, Greece)

Abstract

Dehydration during metamorphism in subduction zones plays a crucial role in the redistribution of fluids within the subducting oceanic crust, which can lead to significant fluid-rock interactions. If the fluids released from a particular rock type interact with other rock types, these interactions, and the associated chemical changes, can be traced using isotopic mineral compositions, specifically oxygen isotopes ($\delta^{18}O$). This study focuses on the quantification of small $\delta^{18}O$ variations to investigate fluid-rock interaction processes in three representative fragments of subducted oceanic crust outcropping at Achladi, Katergaki, and Ormos Lakkoi on Syros Island (Cyclades, Greece). The sampled sequences consist of metamorphosed mafic pillows, metasediments, and metagabbro, which all exhibit a hydrothermal overprint inherited from seafloor alteration under various temperature conditions. Garnet core $\delta^{18}O$ values reflect this interaction, with 11-13‰ at Achladi, 8-11‰ at Katergaki, and 4-5‰ in the metagabbro at Ormos Lakkoi. Notably, eclogites and blueschists at Achladi and Ormos Lakkoi show relatively homogeneous $\delta^{18}O$ values, suggesting an absence of interaction with an external fluid in isotopic disequilibrium during garnet growth, a contrast to the evidence of strong metasomatic processes reported on Syros.

The first stage of fluid interaction with an external fluid in isotopic disequilibrium is marked by $\delta^{18}O$ increases in the Katergaki sequence where garnet rims record higher values up to 12‰. This shift in the oxygen isotopic composition is interpreted as reflecting the interaction with isotopically heavier fluids during high-pressure metamorphism. Late recrystallization of phengite, with $\delta^{18}O$ values of 11-13‰, indicates rock-scale equilibration with this external fluid, likely sourced from dehydrating mafic lithologies. Petrochemical modeling of fluid transfer within a multi-rock sequence supports this interpretation, showing that hydrous phase stabilization contributed to fluid recycling and isotopic re-equilibration. These findings have implications for understanding pervasive fluid flow in subduction zones.

A second stage of fluid-rock interaction is marked by cross-cutting carbonate veins in both Achladi and Katergaki, which formed later, during greenschist metamorphism. These veins, are associated with a CO_2-rich fluid, exhibit $\delta^{18}O$ values of 14-16‰ and $\delta^{13}C$ values of 2‰ to -2‰, reflecting a distinct infiltration event and could have been sourced from the marbles on Syros.

4.1 Introduction

Subduction zones play a major role in the large-scale geochemical cycles where crustal material is recycled into the mantle. Subduction of crustal material is closely linked to arc magmatism, formation of continental crust and has driven the evolution of mantle geochemistry throughout Earth's history. High-pressure metamorphic rocks outcropping in the collision belts are relicts of fore-arc (depths of 40-80 km and $\leq$650 °C) and sub-arc (at $\geq$100 km and $\geq$700 °C) processes (Hermann et al., 2006). The destabilisation of hydrous phases during burial releases aqueous fluids which are important drivers of subduction zone processes, such as partial melting of the mantle wedge (Austrheim, 1987; Compagnoni et al., 1995; Schmidt & Poli, 2014).

The most abundant lithologies in the subducting crust are 1) mafic rocks such as mid-ocean-ridge basalts, ocean island basalts, or arc volcanic rocks, carrying up to 5-6 wt% of water to blueschist facies conditions (Schmidt & Poli, 1998), 2) sediments can carry 2-3 wt% mineral bound water and are the main reservoir for LILE, Th, U, Li, B, and Pb, and contribute these elements to transfer processes from the slab to the mantle wedge (Bebout & Penniston-Dorland, 2016; Plank & Langmuir, 1993; Schmidt & Poli, 2014), and 3) serpentinites, a major source of aqueous fluids carrying up to 13 wt% of fluid and are an important player for the redox budget (Piccoli et al., 2019; Ulmer & Trommsdorff, 1999; Vieira Duarte et al., 2021). A good understanding of the lithologies involved in the subduction zone and the associated fluid budget has been achieved, but it remains unclear how fluids are redistributed within and between the different units before finally reaching the mantle wedge (Bebout, 2014; Hermann et al., 2006; Plank & Langmuir, 1993; Poli & Schmidt, 1995).

Ocean-floor basalts can preserve their original oxygen isotope composition during subduction, which is then transferred to the deeper mantle (J. A. Miller et al., 2001; Putlitz et al., 2000). If these metabasalts interact with an external fluid in isotopic disequilibrium, their oxygen isotope composition will change by a magnitude depending on the degree of interaction and the difference in isotopic composition (Baumgartner & Valley, 2001; Martin et al., 2014; Putlitz et al., 2000; Rubatto & Angiboust, 2015; Vho, Lanari, Rubatto, & Hermann, 2020). The exhumed rocks and their isotopic composition can potential be used to identify fluid-rock interactions. Isotope studies have revealed that unaltered MORB and gabbros from ophiolitic sequences typically exhibit an average $\delta^{18}O$ value of 5.7$\pm$0.2 ‰ (Gregory & Taylor, 1981; Ito & Clayton, 1983; Ito et al., 1987). Rocks undergoing seafloor alteration before subduction can experience significant shifts in their $\delta^{18}O$ values (Alt et al., 1986; Gregory & Taylor, 1981; Muehlenbachs, 1986). Alteration during exchange with seawater at high temperatures will decrease $\delta^{18}O$ up to 13 ‰, and alteration at low temperatures will increase $\delta^{18}O$ by 3-4 ‰. The $\delta^{18}O$ value of a rock can change in

two primary ways: a homogeneous alteration caused by pervasive fluid infiltration along grain boundaries or through crack systems at a macroscopic scale, and a heterogeneous alteration resulting from channelized infiltration along veins, shear zones, or other textural conduits (Baumgartner & Valley, 2001). Fluid-rock interactions during metamorphism can leave distinct records in metamorphic minerals at the micrometer scale. Minerals such as garnet, phengite, lawsonite, calcite, zircon, titanite, and rutile have been effectively utilized to trace evidence of fluid-rock interaction in high-pressure rocks (e.g., Barr, 1989; Bovay et al., 2021, 2022; Kang et al., 2024; Martin et al., 2011; Page & Storey, 2023; Rubatto & Angiboust, 2015; Rubatto et al., 2023; Vho, Lanari, Rubatto, & Hermann, 2020).

The prediction of the oxygen isotope composition of minerals and fluids in a system is governed by the isotope fractionation of the coexisting mineral phases and the fluid phases (Kohn, 1993; Vho, Lanari, Rubatto, & Hermann, 2020; Vho et al., 2019). The fractionation model is valid for a closed system that does not experience any changes from external processes. Temperature is the main controlling variable for the isotope fractionation expressed as a second-order polynomial of $10^3/T$ for a phase assemblage in equilibrium (Vho et al. (2019) and references therein). The oxygen isotope composition of mineral phases at changing pressure (P) and temperature (T) conditions can be predicted by petrochemical models, which combine the thermodynamic modeling of phase equilibria with a model for oxygen isotope fractionation (e.g., Kohn, 1993; Vho, Lanari, Rubatto, & Hermann, 2020). The application of such petrochemical models allows a quantitative interpretation of intra-grain variation of $\delta^{18}O$ of key metamorphic mineral phases such as garnet. It has been shown with these models that the combined effect of isotope fractionation at temperatures above 350 °C, garnet fractionation, and the removal of excess fluid from the system is lower than 1‰ for phases such as garnet, phengite, or lawsonite and about 1‰ per 100 °C for quartz, calcite and rutile (Kang et al., 2024; Vho, Lanari, Rubatto, & Hermann, 2020; Vho et al., 2019). In addition, petrochemical models allow the simulation of fluid-rock interactions with externally-derived fluids, and to quantify the resulting intra-crystalline $\delta^{18}O$ variations of metamorphic minerals under specific open-system scenarios Vho, Lanari, Rubatto, and Hermann (2020). For a correct quantification of the fluid masses compared to the rock it is necessary to account the volumes of lithological units, for example based on outcrop observations.

The two main challenges in reconstructing detailed fluid-rock interaction histories are (i) distinguishing between open and closed system behavior, and (ii) to quantifying the degree of fluid-rock interaction. The second one can be done by calculating time-integrated fluid fluxes, which represents the volume of fluid infiltrating a specific rock volume over a defined surface area within a given timeframe (Ague & Nicolescu, 2014; Baumgartner & Valley, 2001). Because different minerals i.e., garnet and phengite can grow and/or be stable under different pressure-temperature conditions (e.g. prograde or retrograde),

an isotopic study combining more than one mineral provides a more complete fluid-rock history (see Kang et al., 2024; Page & Storey, 2023; Rubatto et al., 2023). For example, Rubatto et al. (2023) demonstrated for a single outcrop from Lago Di Cignana (Italy, European Alps) that the interaction with fluids from dehydrating mafic lithologies at peak metamorphic conditions can be retrieved by combining $\delta^{18}O$ in mica and garnet, whereas a later stage of fluid infiltration could be identified by strong changes in $\delta^{18}O$ ($\geq$ 10‰) in garnet result from external fluid influx. Precise estimates of when the fluid infiltration occured along the P–T trajectory were significantly improved by combining data from both garnet and phengite. Page and Storey (2023) used garnet, rutile and titanite $\delta^{18}O$ from the Franciscan complex combined with trace element compositions to reconstruct the fluid history of the mafic protolith and modification by polymetamorphic events. This approach required careful constraints from all three mineral phases, as the $\delta^{18}O$ values related to hydrothermal alteration in the protolith were altered in garnet rims and matrix rutile due to external fluid infiltration at the high-pressure peak of metamorphism.

Fluid production during progressive burial in subduction zones can be estimated through petrological models, which predict stable mineral phase assemblages and can be used to quantify the fluid production based on equilibrium thermodynamics (e.g., Baxter & Caddick, 2013). Such models can be further integrated with chemical models to calculate isotope or trace element compositions, offering a more comprehensive approach. Recent advancements, for instance, have demonstrated how trace element partitioning between fluid and rock can be modeled to explain the trace element patterns observed in high-pressure minerals (Konrad-Schmolke et al., 2011). Additionally, by coupling the calculations of oxygen isotope compositions of mineral phases and fluids, it is possible to simulate both closed and open system behaviors (Kohn, 1993; Vho, Lanari, Rubatto, & Hermann, 2020). Extending these models to account for fluid-rock interactions in multi-rock systems provides a valuable framework for tracking and quantifying these processes during prograde metamorphism.

This study focuses on the reconstruction of fluid-rock interaction history in three outcrops of a volcano-sedimentary suite located in the southeastern region and western region of Syros, Greece (Cyclades), through the application of stable isotope geochemistry and petrochemical modeling. Major element mapping is combined with stable isotope analysis across multiple mineral phases—using secondary ion mass spectrometry (SIMS) for silicates like garnet and phengite, and dual inlet mass spectrometry for carbonates—to investigate processes on both micro and macro scales. This integrated approach is essential, as the different mineral phases formed and/or recrystallized under different pressure-temperature (P-T) conditions, providing valuable insights into fluid interaction dynamics. Variations in oxygen isotope compositions from core to rim in chemically zoned garnet and phengite help trace fluid infiltration patterns, distinguishing between pervasive and channelized flow.

These observations are supported by outcrop and microscale textural data. Potential fluid sources are identified through oxygen isotope compositions recorded in garnet, phengite, and carbonate. The combination of natural data and petrochemical simulations based on outcrop observations allows for the quantification of fluid production, migration, and interaction processes at the outcrop scale.

4.2 Geological background

Syros is an island from the Cycladic Archipelago located in the centre of the Aegean domain (4.1a). The island resembles a part of the Cycladic Blueschist Unit (CBU), which is a piece of a fossilized subducted crust belonging to the Pidnos oceanic domain (Bonneau, 1984; Bonneau & Kienast, 1982). Today, it lies in the back-arc of the active Hellenic subduction zone (Ferriere et al., 2024; Jolivet et al., 2015; Laurent et al., 2016). In general, the CBU parts on Syros comprises a complex assemblage of schists, thick marbles, metabasites, and ultramafics that underwent HP–LT metamorphism typical of subduction zones. These lithologies represent remnants of a former oceanic-crust, including gabbros, cumulates, dikes, pillow lavas, and hydrothermal sediments, along with quartzites and banded tuffitic schists. Thes fragmented ophiolitic pieces are locally tectonically repeated and appears across the island as multiple smaller volcanic-sedimentary sequences (e.g., Keiter et al., 2011; Laurent et al., 2018; Marschall et al., 2006, 2009; Uunk et al., 2022). The whole CBU can be subdivided into three subunits by their extensional top-to-the east shear zones, lithology and metamorphic facies (Laurent et al. (2016); Figure 4.1b). From bottom to top this is (1) the Posidonia Subunit composed of the felsic gneiss of Komito below albitic micaschists and rare boudins of metabasite and thin marble layers, (2) the Chroussa Subunit as a sequence of alternating micaschists, thick marble layers and metabasites, and (3) the Kampos Subunit representing a tectonic mélange of metabasites wrapped into serpentinites with minor abundance of qz-phg schists. All of the subunits have undergone similar HP-LT metamorphism and peak P–T conditions (Laurent et al., 2018; Skelton et al., 2019; Trotet et al., 2001). The Chroussa and Kampos subunit records blueschist to eclogite metamorphism, while the Posidonia subunit mostly records a greenschist overprint. The peak P–T conditions in the CBU on Syros are estimated to be at 2.2 ± 0.2 GPa and 530 ± 30 °C (Gorce et al., 2021; Laurent et al., 2018; Skelton et al., 2019; Trotet et al., 2001; Tual et al., 2022).

This study focuses on two outcrops Achladi and Katergaki located along the south-eastern coast and one outcrop in the West occurring as an isolated block (Figure 4.1). A detailed map of the deformation features in the south-eastern part can be found in Gerogiannis et al. (2024). All outcrops belong to the Kampos Subunit and recorded HP–LT metamorphism with eclogite and blueschist facies assemblages, locally retrogressed into

greenschist (Figure 1). In these localities, slightly lower peak P–T conditions were proposed (Skelton et al., 2019) with a prograde lawsonite blueschist facies stage at 1.2 to 1.9 GPa and 410 to 530 °C and a peak stage at 2.1 GPa and 520 °C (see Figure 4.2). Greenschist facies overprint conditions were estimated at 0.34 ± 2.1 kbar and 456 ± 68 °C (Skelton et al., 2019). It was proposed by these authors that the rocks from Achladi and Katergaki did not record the isobaric heating stage during exhumation (Laurent et al., 2018), which was also proposed for high-pressure rocks from Tinos and Andros (Huet et al., 2015; Parra et al., 2002).

Garnet dating in the region provided constraints on the timing of garnet growth during burial, while later growth during exhumation is typically not preserved. Exhumation is recorded in garnet primarily through resorption and alteration, for example during the greenschist facies overprint. Bulk garnet Lu-Hf dating provided an age of 51.9 ± 1.4 Ma interpreted as reflecting garnet growth (Lagos et al., 2007). Gorce et al. (2021) dated zoned garnet crystals from a qz-rich metasediment sample from Katergaki using Sm-Nd and obtain ages of 45.3 ± 1.0 Ma for the core and 40.5 ± 1.9 Ma for the rim. This sample is from the same sequence analysed in our study. The obtained ages were combined with P–T estimates from quartz-in-garnet elastic geobarometry and thermodynamic modeling, indicating an initial exhumation after peak pressure starting at 2.0 to 2.2 GPa and 500 to 560 °C (Gorce et al., 2021, Figure 4.2). Garnet Lu-Hf dating of single growth zones cut using laser milling was applied to another qz-rich metasediment sample from Katergaki. This garnet grain recorded prograde growth between 51.8 ± 0.1 Ma and 51.3 ± 0.2 Ma at 2.3 GPa 500-550 °C (Tual et al., 2022). Additional age constrains were obtained on phengite from various localities on the island of Syros with a range from 52 to 30 Ma, interpreted as reflecting peak to retrograde growth or re-equilibration (Barnes et al., 2024; Bröcker & Enders, 2001; Cliff et al., 2017; Laurent et al., 2021; Maluski et al., 1987; Putlitz et al., 2005; Skelton et al., 2019).

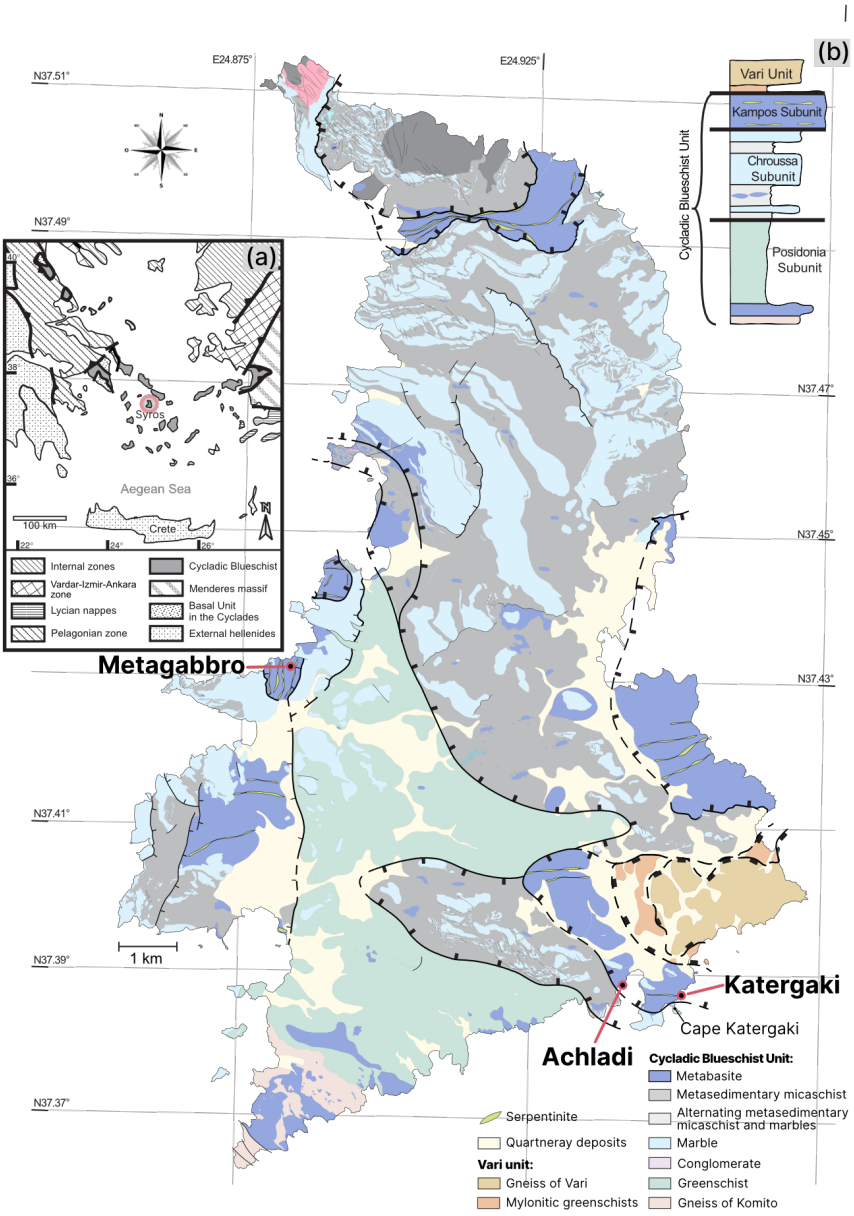

Figure 4.1: Geological maps of Greece and Syros. (a) Simplified geological map of Greece highlighting Syros (after Keiter et al., 2011). (b) Geological map of Syros modified after Laurent et al. (2016). Location of the two main outcrops Achladi and Katergaki are highlighted as well as the location of the sampled metagabbro.

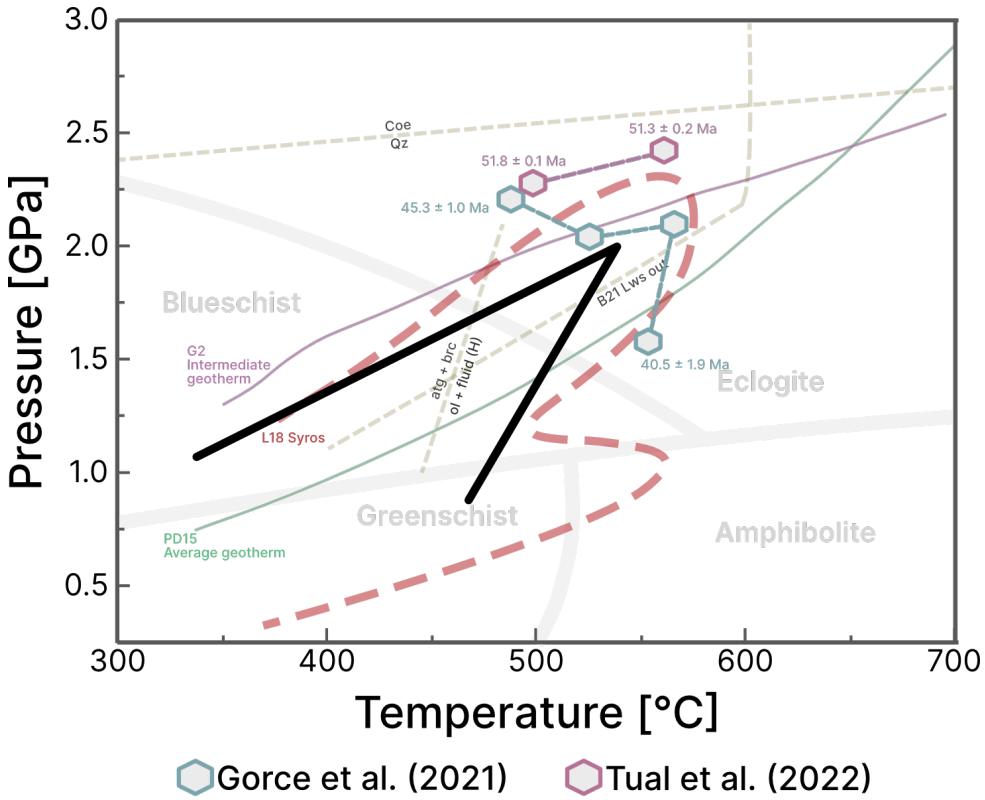

Figure 4.2: P–T diagram showing compiling different P–T paths, mineral reactions, and garnet growth ages. Black curve represents the path for rocks in the south of Syros from Skelton et al. (2019). The red path (L18) shows the P–T path representing multiple high-pressure subunits on Syros based on Laurent et al. (2018). For reference the average geotherm from Penniston-Dorland et al. (2015) (dashed green line PD15) as well as the intermediate geotherm from Gerya et al. (2002) (dashed purple line G2) are displayed. Blue polygons represent the garnet growth and ages from Gorce et al. (2021) and the reddish poylgons the garnet growth and ages from Tual et al. (2022). Lawsonite-out reaction is highlighted as dashed gray line Bovay et al. (2021) (B21) as well as the transition from quartz to coesite. Antigorite and brucite reaction to olivine and water visualized as grayish dashed line is from Hermann et al. (2000). Fields of the metamorphic facies are separated by gray lines.

4.3 Petrology and petrography

4.3.1 Field relationship, outcrops, and sample description

Three different outcrops have been studied Achladi and Katergaki in the SE of Syros and Ormos Lakkoi in the West of Syros near Galissas (Figure 4.1). Images and 3D reconstructions of the Achladi and Katergaki outcrops are shown in Figure 4.2, 4.3, and 4.5. Five different rock types were collected from the three localities and were classified as eclogite, blueschist (blueschist and epidote blueschist), greenschist, qz-phg schist, and metagabbro (Table 4.1, Figures 4.2, 4.3, and 4.5).

Field relationship

The sampled outcrops belong to the Kampos unit in the CBU and resemble different parts of an former oceanic-crust sequence, which are now distributed over the island of Syros probably due to the intensive thrusting and normal faulting (e.g., Ring et al., 2020). The specific sequences Achladi and Katergaki are located approximately 860 meters separated from each other in southeastern Syros, while Ormos Lakkoi is situated about 7 kilometers away on the west coast of the island (Figure 4.1). In between the scattered remnants of the oceanic crust the major geological formations on Syros are characterized by an alternating layers of schists and marbles (Keiter et al., 2011).

Achladi sequence

The first sequence Achladi consists of a single outcrop of 50 m wide and 12 m high, consisting of pile of stacked boudins varying in size from decimeter to meters (Figure 4.3a-c, Figure 4.2a). The main rock types observed in this sequence are (epidote-) blueschist and eclogite. The boudins at Achladi are a locus typicus where the boudins have an eclogitic core of 10 to 50 cm in diameter and blueschist rims of 5 to 10 cm thickness. The matrix between the boudins is composed mostly of blueschist varying between 10 cm to 1m thickness showing a sedimentary texture and a pale blue color. Furthermore, the boudins are wrapped and/or crosscut by several generations of carbonate veins. (Figure 4.4a-e). The veins contain calcite, siderite, dolomite and rarely quartz; cm-sized aragonite lenses were also found in nearby dislocated blocks that contain cm-sized eclogitic lenses in a carbonate-rich, sedimentary matrix (Figure 4.4f). The eclogite sample SY21-05 and blueschist samples SY21-04 and SY21-07 from this sequence were used for oxygen isotopes analysis of garnet and phengite.

Katergaki sequence

The second sequence, Katergaki, is located on the coastline between the village of Fabrikas in the east and the Katergaki cape in the west (see Figure 4.1). This locality is also referred to as Fabrikas in the literature (e.g., Gorce et al., 2021; Ring et al., 2020; Skelton et al., 2019; Tual et al., 2022) but is not used here to avoid confusion with the Fabrikas locality in the village itself. In Katergaki, deformed layers or lenses of eclogite, blueschist, greenschist, and quartz-phengite schists (qz-phg schist) with variable abundances and thickness on the size of several 10 to 50 meters are observed and the qz-phg schist resembles cm to m thick bands (see Figure 4.2b). In a 20 m thick layer of qz-phg schists, mafic boudin are observed as meter-sized blocks (4.5a). These boudins have blueschist cores and eclogite rims (4.5a-b). The blueschist sample SY21-01/2-1 and elcogite sample SY21-01/2-2 represent the transition from blueschist to eclogite sampled from the same boudin (SY21-01). Eclogite samples (SY21-01/2-2, SY21-02, SY21-33), blueschist samples (SY21-01/2-1) and qz-phg schist samples (SY21-01/3, SY21-03) from this sequence were used for a detailed study of the oxygen isotopes in garnet and phengite. Calcite veins were observed and sampled in eclogitic boudins (Figure 4.4g).

Ormos Lakkoi sequence

The metagabbro was sampled in the northwest near Ormos Lakkoi and represents an isolated block (knocker) with a predominantly coarse-grained texture (Figure 4.2c). The entire block is wrapped by talc-chlorite as commonly observed on Syros for such mafic blocks Gyomlai et al. (2021), Keiter et al. (2011), Marschall (2005), and Robson (2000).

4.3.2 Petrography

Eclogites from either locality show a fine grained omphacite matrix dark to pale green in color. Glaucophane varies in size from 100 µm to 1 mm. Epidote occurs as mm-sized crystals in the matrix. The garnet crystals are mm-sized and contain inclusions of quartz, zoisite-rich epidote, and/or phengite (Figure 4.3e, Figure 4.5e). Eclogite samples classified as retrogressed show euhedral epidote, a greater abundance of chlorite around strongly resorbed garnet. In addition the calcite abundance varies in the matrix increasing towards the rim of the boudins. Samples that show a sedimentary texture are banded in omphacite, glaucophane, and phengite and sometimes bear 100-500 µm calcite pods. Mineral abbreviations used in the text and figures are from Warr (2021).

The sample SY21-05 is a eclogite from Achladi showing little greenschist retrogression (Figure 4.3e). It contains garnet, omphacite, glaucophane, epidote, phengite, chlorite, titanite, calcite. Late chlorite is visible around the garnet and the chlorite abundance

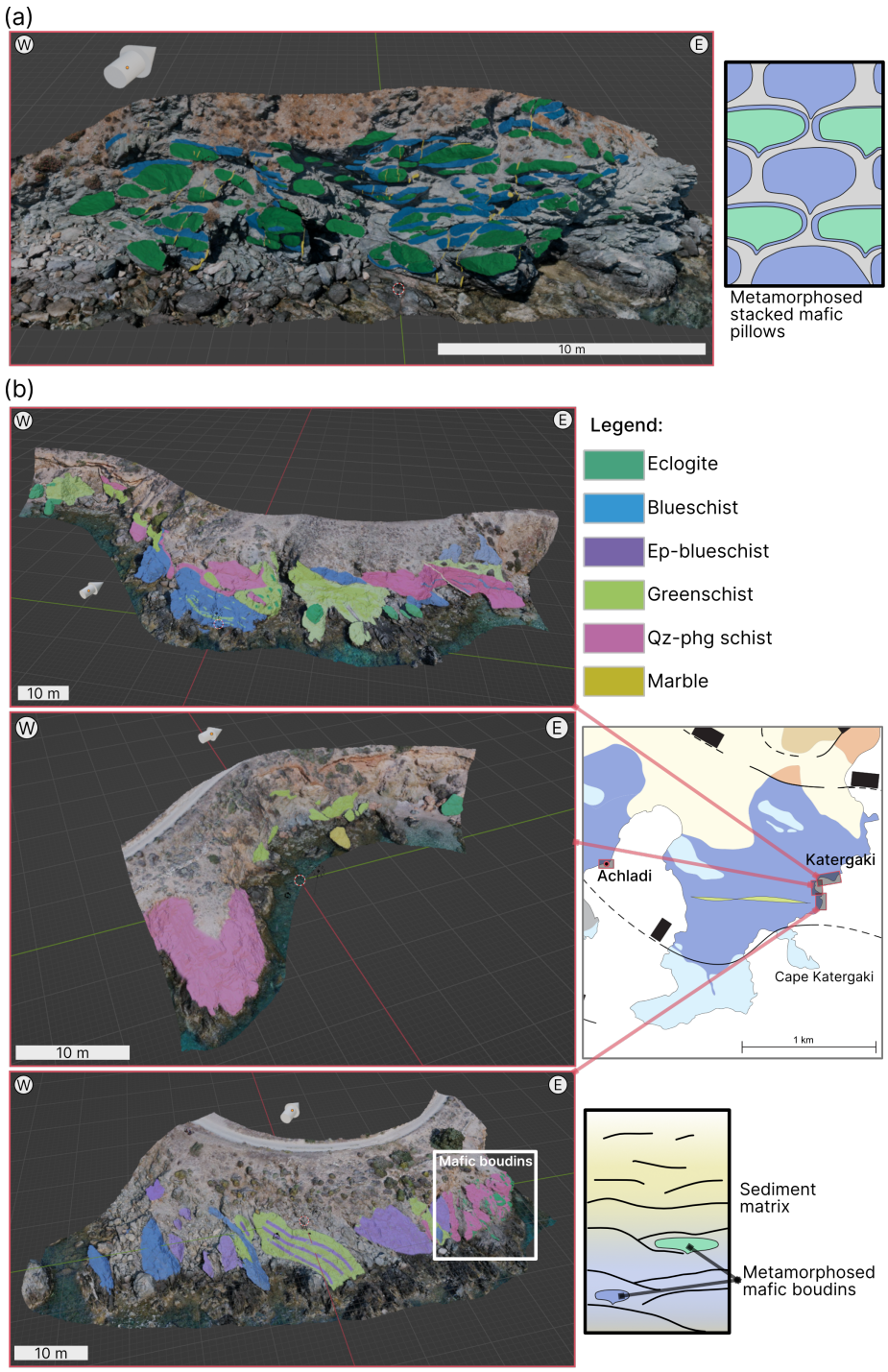
(a)
W
E
10 m
Metamorphosed stacked mafic pillows
(b)
W
E
10 m
Legend:
Eclogite
Blueschist
Ep-blueschist
Greenschist
Qz-phg schist
Marble
Achladi
Katergaki
Cape Katergaki
1 km
Mafic boudins
Sediment matrix
Metamorphosed mafic boudins

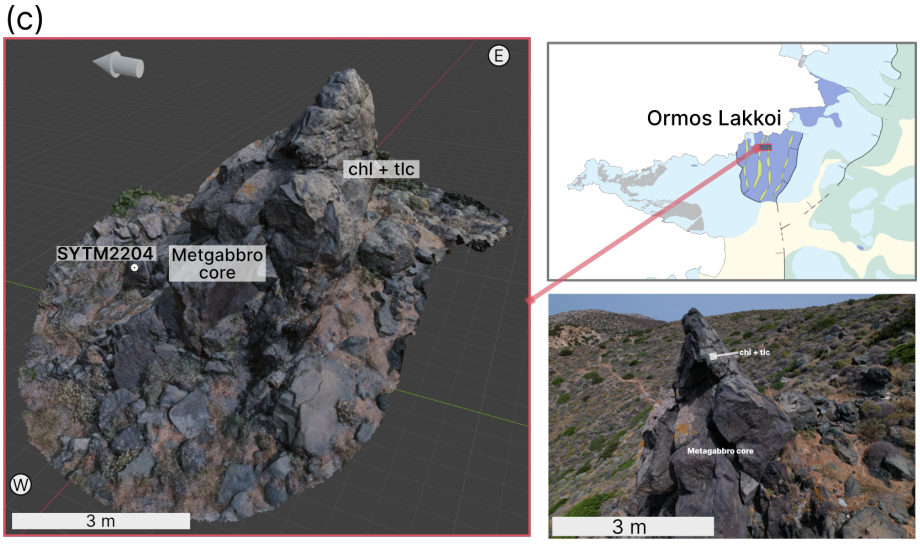

Figure 4.2 *(previous page)*: Three-dimensional reconstruction of the main outcrops. (a) Achladi sequence showing the stacked sequence of solidified pillow lavas, which experienced blueschist to elcogite metamorphism. (b) Parts of the Katergaki sequence showing the high variability of eclogites, blueschists, greenschist, and qz-phg schist on the outcrop scale. Highlighted is the main outcrop of the well-preserved blueschist and eclogitic mafic boudins in the qz-phg-schist shown in Figure 4.5. The miniature map highlights the visualized outcrop locations of Achladi and Katergaki as a zoom-in of Figure 4.1. The complete coastal sequence of Katergaki can be found in Supplementary Material S1. (c) Outcrop of Ormos Lakkoi showing the metagabbro and the field location. Geographic North is indicated by the white arrow in the 3D-models. Reconstruction of the outcrops from images was done using AgiSoft PhotoScan (Version 1.2.6).

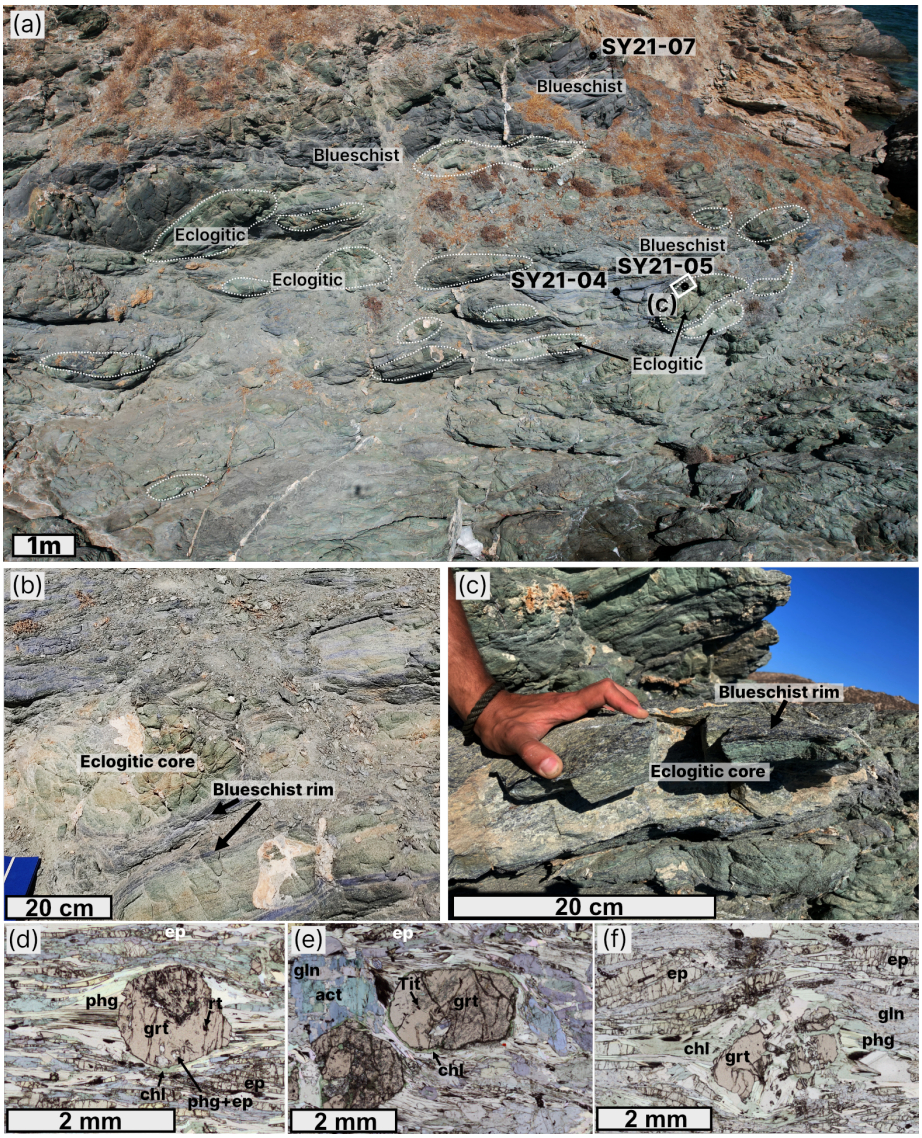

Figure 4.3: Field images and photomicrographs of the outcrop and samples from Achladi. (a) Overview drone image of the outcrop showing stacked mafic lenses interpreted as former volcanic pillows. (b) Close-up of the boudinaged mafic lenses. (c) Close-up of the mafic lense showing the eclogitic core and blueschist rim. (d) Photomicrograph of the blueschist of sample SY21-07. Garnet is wrapped in phengite in a matrix of glaucophane and epidote. (e) Photomicrograph of the eclogite sample SY21-05. The anhedral inclusion-rich garnet shows a slight redish color contrast and is surrounded by chlorite (green). The matrix consist of phengite, amphibole (glaucophane in blue wrapping actinolite in greenish) and some epidote. (f) Photomicrograph showing the blueschist sample SY21-04. Garnet occurs broken and is surrounded by chlorite inside a fine grained glaucophane-rich matrix and mm-sized epidote prisms. Mineral abbreviations are after Warr (2021).

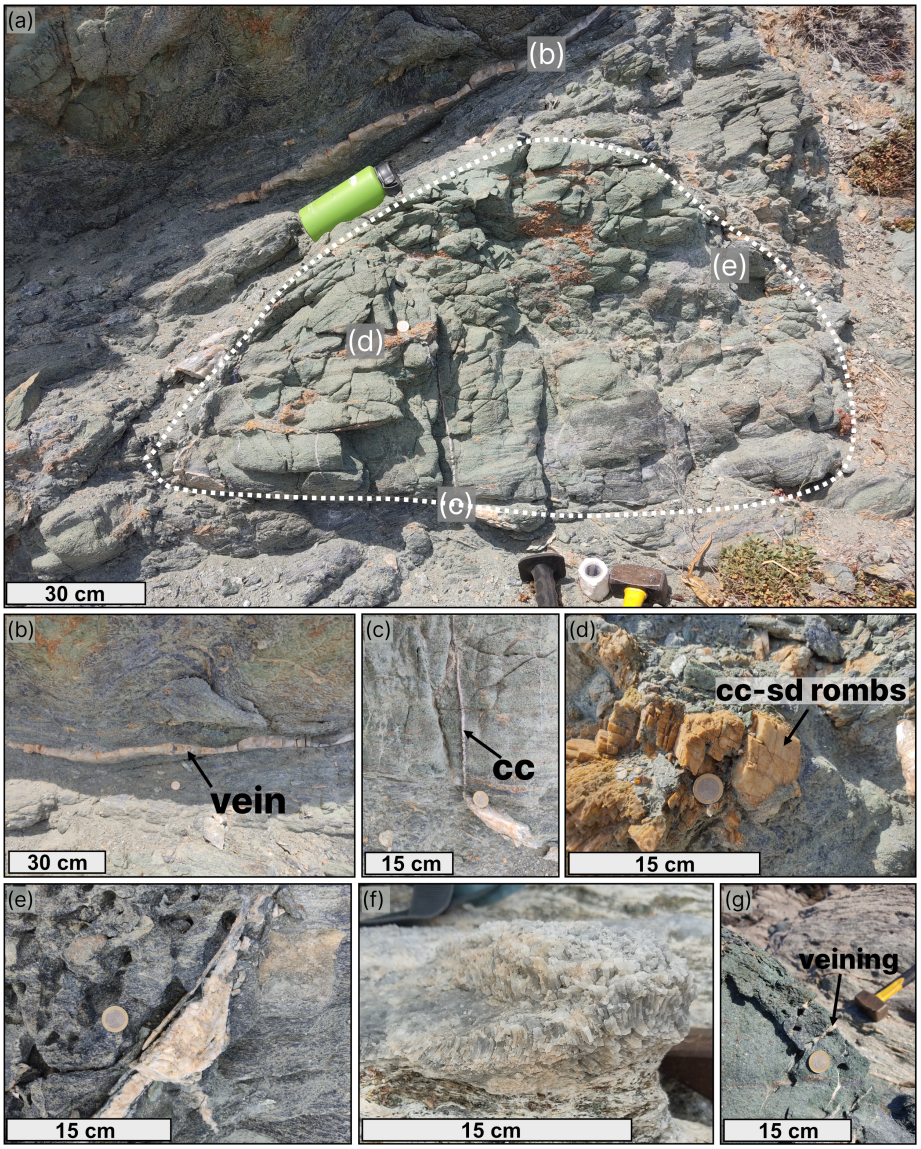

Figure 4.4: Carbonate occurence at Achladi and Katergaki. (a) Overview of a mafic pillow and the associated carbonate veins that wrap and crosscut the pillow. (b) Wrapping vein representing carbonate-quartz mix (sample SYTM2303). (c) Crosscutting calcite vein (sample SYTM2306). (d) Blocky carbonate-siderite rhombohedrons (sample SYTM2301). (e) massive crosscutting calcite-dolomite mix (sample SYTM2305). (f) Aragonite lense (sample SYTM2337). (g) Calcite veins in boudin at Katergaki (sample SYTM2311). Mineral abbreviations are after Warr (2021).

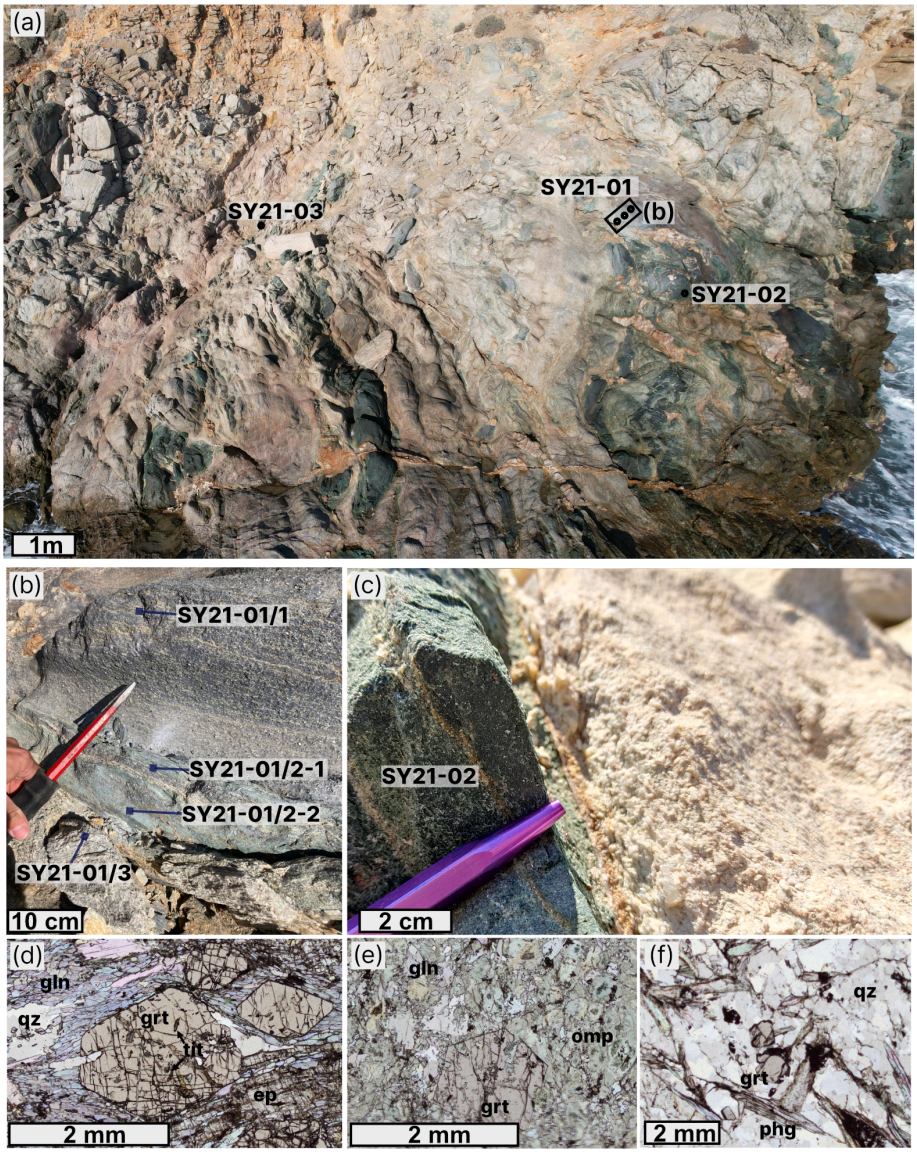

Figure 4.5: Field images and photomicrographs of the outcrop and samples from Katergaki. (a) Overview drone image of the outcrop where mafic boudins are wrapped into the qz-phg schist. (b) Contact zone of the mafic boudin contact and the qz-phg schist. The boudin shows a blueschist core and a blueschist to eclogite transition to the contact zone. (c) Close-up of the eclogite contact to the qz-phg schist. (d) Photomicrograph of the blueschist part of sample SY21-01/2. Fractured garnet is in a matrix of glaucophane with adjacent epidote. (e) Photomicrograph of the eclogite boudin SY21-33. Euhedral garnet in a matrix of omphacite with some glaucophane crystals. (f) Photomicrograph showing the qz-phg schist sample SY21-01/3 from the boudin contact in panel (b). The relatively small garnet sits in a matrix of quartz adjacent to packs of phengite. Mineral abbreviations are after Warr (2021).

increases toward the outside of the boudin at the thin section scale. Around 20% of the glaucophane shows 100-200 µm sized actinolite cores and 100-300 µm sized glaucophane rims. The outermost 1 cm of the boudin rim in sample SY21-05 has a high abundance of ~30 % calcite and the garnet is strongly resorbed and replaced by chlorite.

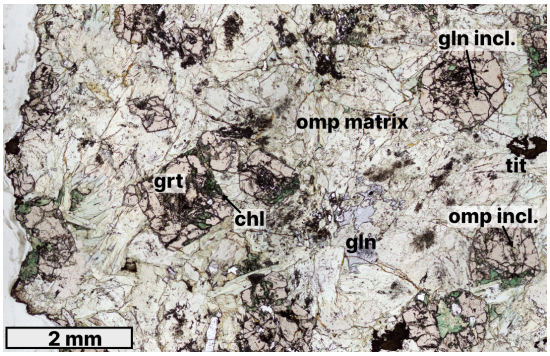

Figure 4.6: Photomicrograph showing the metagabbro sample SY2204 and the omphacite matrix with the partly resorbed garnet prophyrobalsts. Mineral abbreviations are after Warr (2021).

Blueschist samples show a medium to fine grained matrix of glaucophane (Figure 4.3d,f and 4.5d). Some samples show a high abundance of glaucophane (>80%), which would classify them as glaucophanites, but for simplicity these samples are also called blueschists in this study.

Blueschists samples SY21-04 and SY21-07 from Achladi have a foliation defined by phengite, epidote and glaucophane (Figure 4.3d). Garnet porphyroblasts (mm-sized) are wrapped by phengite in the pressure shadows and is associated with chlorite at the porphyroblast edges perpendicular to the foliation. Less chlorite is present in sample SY21-07 compared to sample SY21-04, which has more chlorite associated with strongly fractured and resorbed garnet. Garnet in SY21-07 also shows mm-sized inclusions composed of phengite and epidote having a rhomboidal shape, which could indicate pseudomorphs after lawsonite (see Supplementary Material S1). Sample SY21-01/2-1 from Katergaki has no clear foliation but patches of quartz, smaller phengite flakes, and mm-sized epidote. Euhedral garnet porphyroblasts (mm-sized) show fractures and 100 µm inclusions of epidote and titanite (Figure 4.5d), but no or only minor chlorite around the grain edges. Samples SY21-04, SYTM2326, SYTM2334, SYTM2333, SYTM2335, and SYTM2330 deviate the strongest from the typical blueschist. SY21-04, SY2333, SYTM2335, and SYTM2330 show the strongest resorption and fracturing of garnet grains, which are rounded and wrapped by chlorite (Figure 4.3f). These samples are also associated with a higher abundance of epidote in the matrix. Sample SYTM2334 consists mainly of 5 mm epidote crystals and sample SYTM2326 has no garnet but little patches chlorite visible in the matrix, which could represent a fully replaced garnet.

The greenschist sample SYTM2325 consists mainly of epidote, calcite, and quartz. Garnet is absent but chlorite aggregates are present in the matrix. These could represent areas of former garnet.

The qz-phg schists (samples SY21-01/3, SY21-03, SY2309, and SY2310) are foliated

rocks with garnet porphyroblasts (Figure 4.5f). Accessory minerals are titanite and rutile. Samples SY2309 and SY2310 show skeletal garnet ranging from 2 mm to 1 cm in size. Garnet inclusions are mainly quartz with minor phengite, epidote, rutile, and titanite. A calcite pod cuts a garnet in sample SY2310. SY2309 shows intense brownish weathering. Sample SY21-01/3 consists of glaucophane in its matrix associated with phengite and epidote.

The metagabbro sample (SYTM2204) is an omphacitite consisting mainly of mm grains of omphacite and subhedral fractured garnet (Figure 4.6). About 30% of the garnet grains are largely replaced by chlorite (30-70 vol% of garnet). Glaucophane is present in low abundance (∼1 vol%) and occurs as patches in the matrix. Titanite is relatively abundant at nearly 1 vol%. In a vein feature omphacite, chlorite, and also relicts of acthinolite needles can be found.

Lithology	Sample	Main assemblage	Detail
Achladi			
Eclogite	SY21-05 (-01 and -02)	Omp, Gln, Act, Phg, Ep, Grt, Chl, Cc, Qz	foliated matrix with patches of Cc increasing at the boudin rim
Blueschist	SY21-07	Gln, Phg, Grt, Pa, Chl, Ep, Rt, Tit	foliated sample with mm-sized Grt wrapped in Phg; Grt sometimes associated with Chl at the rim
	SY21-04	Gln, Grt, Ep, Phg, Chl, Cc, Rt, Tit	retrogression; fine grained and foliated Gln matrix with a band of Phg, remnant Grt associated with Chl
Katergaki embedded boudins			
Eclogite	SY21-01/2-2	Omp, Gln, Phg, Ep, Grt,Qz, Cc, Rt	fine grained Omp matrix with Gln and flakes of Phg
	SY21-02	Gln, Omp, Ep, Phg, Grt, Rt, Cc	foliated, fine grained Omp+ Gln matrix interbedded with Phg
	SY21-33	Gln, Omp, Ep, Phg, Grt, Rt, Cc	
Blueschist	SY21-01/2-1	Gln, Phg, Ep, Grt, Qz, Rt	subhedral to euhedral Grt
Qz-phg schist	SY21-01/3	Qz, Phg, Grt, Ep, Chl, Tit, Rt, Gln	mm-sized Grt with Qz inclusions
	SY21-03	Qz, Phg, Grt, Ep, Chl, Tit, Rt	200 um Grt without inclusions
Katergaki			
Eclogite	SYTM2323	Omp/jd, Grt, Ep, Phg, Gln Omp	fine grained omp matrix
	SYTM2307	Gln, Phg, Qz, Ep, Omp, Grt, Chl, Cc, Rt	sedimentary texture and Chl associated with Grt
	SYTM2308	Gln, Phg, Qz, Ep, Omp, Grt, Cc, Rt	sedimentary texture with aligned Gln, Phg and Ep
	SYTM2313	Gln, Phg, Qz, Ep, Omp, Grt, Cc, Rt	sedimentary texture with aligned Gln, Phg and Ep; patches of Qz in the amtrix
	SYTM2329	Gln, Phg, Qz, Omp, Grt	sedimentary texture with aligned Gln and Phg; mm-size Grt
	SYTM2332	Gln, Ep, Chl, Grt, Phg, Cc, Rt	retrogression; little Grt remnants with Chl around
	SYTM2331	Ep, Gln, Phg, Qz, Grt, Chl, Omp, Rt	retrogression; large Ep and Chl associated with remnant Grt
	SYTM2324	Ep, Gln, Phg, Qz, Cc, Omp, Rt/ox	retrogression; large Ep, Omp relict and no Grt
	SYTM2328	Omp, Gln, Qz, Phg, Chl, Ep, Rt, Cc	retrogression; much Ep and no Grt
	SYTM2327	Phg, Ep, Chl, Grt, Rt, Tit, Cc	retrogression; little garnet remnants
Blueschist	SYTM2326	Gln, Phg, Chl, Qz, Rt, Tit	large Phg patches, no Grt
	SYTM2334	Gln, Ep, Cc, Chl, Phg, Rt, Tit	epidotized; 5 mm sized Ep
	SYTM2333	Grt, Chl, Ep, Qz, Phg, Rt	retrogression; little garnet remnants associated with Chl which can pseudomorph mm-sized Grt shapes
	SYTM2330	Gln, Ep, Chl, Grt, Cc, Rt	retrogression; remnant Grt associated with Chl
	SYTM2335	Gln, Grt, Chl, Phg, Ep, Rt, Tit	fine grained Gln matrix, remnants Grt associated with Chl and bands of Phg
Greenschist	SYTM2325	Ep, Qz, Cc, Chl	Omp relicts
Qz-phg schist	SYTM2309	Qz, Phg, Grt, Ep, Chl, Cc, Tit, Rt	5 mm skeletal Grt associated with Qz and patches of Cc in the matrix
	SYTM2310	Qz, Phg, Grt, Ep, Chl, Cc, Tit, Rt	foliated, 2 mm skeletal Grt associated with Qz
	SYTM2314	Qz, Phg, Grt, Ep, Chl, Gln, Cc, Tit, Rt	¡1 mm Grt associated with chlorite and flakes of Gln in matrix
Ormos Lakkoi			
Metagabbro	SYTM2204	Omp, Grt, Chl, Gln, Tit, Qz, Act	sulphide included in garnet; chlorite associated with remnant grt and in the vein

Table 4.1: Investigated samples and their main mineral assemblage. Mineral abbreviations are after Warr (2021).

4.4 Methods

4.4.1 Bulk rock geochemistry

Bulk rock analyses were obtained at the Institute of Geological Sciences, University of Bern (Switzerland) using pressed powder pellets. Each rock sample was cleaned from weathered surfaces and then subsequently chipped by using stainless steel pliers with chisel heads, crushed in a stainless steel mortar and finally dry milled in an agate mill ring for 30 min. Each milling run of one sample was bracketed by milling using a sand quartz for 15 min to clean the milling beaker. The final pressed powder pellets were produced following the method of Peters and Pettke (2017) using cellulose as binding material. Bulk rock analyses were then performed by laser ablation inductively coupled plasma mass spectrometry using a GeoLas-Pro 193 nm ArF Excimer laser (Lambda Physik, Göttingen, Germany) attached to an ELAN DRC-e quadrupole mass spectrometer (Perkin Elmer, Waltham, MA, USA). The pellets were measured using single spot analysis mode at an on-sample fluence of 6 J cm^{-2} at a repetition rate of 10 Hz and a beam size of 90 µm. For each spot analysis, the sample surface was cleaned by pre-ablation using a larger spot size and each analysis used then the integration of a dwell time signal of 50-60 s. Sample calibration was done by using GSD-1G (Jochum et al., 2011) as primary reference material and BRP.1 (Cotta et al., 2007) was used as secondary external standard. Reproducibility was always better than 10%. The data reduction was performed using the software SILLS (Guillong et al., 2008) with the calculation method of the limit of detection from (Pettke et al., 2012). Internal standardization assumed a fixed total of 100 wt% for major and trace elements, minus the volatile contribution from loss on ignition. All Fe was assumed to be present as Fe_2O_3. The bulk rock measurements are summarized in Supplementary Material S2.

4.4.2 Major element mapping

Mapping of major elements was conducted on a JEOL-8200 instrument at the Institute of Geological Sciences, University of Bern (Switzerland) at an accelerating voltage of 15 keV and a 100–200 nA beam focused to a spot of approximately 1 µm diameter. Major elements were analyzed using wavelength-dispersive spectrometers (WDS; Si, Al, Ca, Fe, Mg), whereas other elements were analyzed using energy-dispersive spectrometer (EDS; K, Na, Mn, Ti, La, Ce, Zr, S, P). The X-ray maps were acquired using dwell times of 80–150 ms and step sizes of 1–3 µm. Element maps were processed and reduced in XMapTools 4.3 (Lanari et al., 2014, 2019). A total of more than 34 elemental maps were obtained, focusing primarily on detecting compositional variations within garnet and phengite. Summaries of the major element maps are provided in Supplementary Material S1 and S3. From these, 16 sections from 10 different rock samples were selected for further oxygen isotope analysis

using SIMS, as they represented the greatest compositional variability. Garnet samples, in particular, were chosen based on the presence of visible Mn-rich cores, where possible.

4.4.3 Oxygen isotopes of garnet and white mica using SIMS

All oxygen isotopes analyses on garnet and white mica were performed at the SwissSIMS facility at the University of Lausanne. Reference materials for garnet and white mica and samples as cuts from thin sections were mounted in the same indium mount. On the same sample thin section cuts compositional mapping with EPMA was performed beforehand. All mounts were checked for a topographical variation within 10 µm using a white light interferometer and coated with 35 nm of gold prior to analysis. For all measurements a 10 kV primary Cs+ beam was used with a current of ∼2 nA and a spot size of 10-15 µm. All values of $\delta^{18}O$ are reported against VSMOW.

In-situ oxygen isotope measurements by SIMS rely on a correction for instrumental mass fractionation (IMF) (Page et al., 2010). The fractionation during analysis is known as matrix effect as it usually dependents on the chemistry of the target mineral. For garnet the matrix effect is corrected for by using suitable reference materials which have a similar composition as the unknowns (Martin et al., 2014; Valley et al., 1995; Vho, Rubatto, Putlitz, & Bouvier, 2020). The garnet compositions in the analysed samples from Syros cover a range of 9-34 mol% for grossular, 1-49% in spessartine and have negligible andradite factions. In addition to the IMF, several garnet standards were analyzed to monitor and quantify the matrix effect of grossular and spessartine for correction. Garnet reference materials UWG-2 was used for sample standardization ($\delta^{18}O$ = 5.8‰ VSMOW; Valley et al. (1995)). The uncertainty on the mean value was ≤ 0.2‰ (± 2SE) for all measurement sessions. Further, CAP02 (X_{grs} (Ca/(Mn+Fe+Mg+Ca)) = 0.325; $\delta^{18}O$ = 4.6‰ VSMOW; Vho, Rubatto, Putlitz, and Bouvier, 2020) and ErrRED (X_{sps} (Mn/(Mn+Fe+Mg+Ca)) = 0.284; $\delta^{18}O$ = 9.3‰ VSMOW; Urosevic et al., 2018) were added to monitor and quantify possible matrix effects. Matrix bias was then corrected following the protocol from Vho, Rubatto, Putlitz, and Bouvier (2020), whereas the spessartine bias correction required an individual correction for each analytical session. Garnet chemical composition for each analysed intra-grain position was extracted from compositional maps acquired prior to SIMS analyses. The grossular matrix bias correction for the analyses range mostly between 0.3 and 1.5‰ and for the spessartine bias between 0.1 and 2.1‰. The uncertainties on individual analyses range between 0.10-0.27‰ (2σ), whereas the propagated uncertainty including the repeatability of the primary standard (0.10-0.20‰ for 2σ) and uncertainties form the matrix correction is 0.47-0.71‰ (2σ). Therefore spessartine bias correction is neglectable for garnet compositions yielding an end-member molar fractions of spessartine <0.1, because the calculated bias for most analyses would be smaller than

the internal standard uncertainty and could lead to over correction. The applied grossular bias correction and the spessartine bias correction for each measurement session are given in Supplementary Material S1 and S4. A summary of the measurement values, the corrected values and the garnet composition is given in Table 4.2. Corrected values and their position in the analyzed garnet grain are summarized in the major element maps compiled in Supplementary S3.

For white mica, the reference material UNIL WM-1 was used for standardisation (FeO of 1.13 wt% and XMg of 0.57; $\delta^{18}O$ = 10.4‰ VSMOW; Luisier et al. (2022)). There is no reported compositional matrix effect or orientation effect for O isotope analysis for white mica (Luisier et al., 2019, 2022). Therefore, the measurements of phengite were only corrected for the IMF of each individual measurement session known by analysing the reference material WM-1, which is similar in composition to the phengite of the analysed samples. The internal standard error on individual analyses range between 0.11-0.26‰ (2σ) and the propagated uncertainty including the repeatability of the primary standard (0.10-0.20‰ for 2σ) is 0.28-0.38‰ (2σ). A summary of the measurement values and the corrected values is given in Supplementary Material S4.

4.4.4 Oxygen and carbon isotopes on carbonate aliquots using dual inlet mass spectrometry

Aliquots of carbonate samples from veins were measured for $\delta^{18}O$ and $\delta^{13}C$ at the Institute of Earth Surface Dynamics (IDYST), University of Lausanne (Switzerland). About 200 μg carbonate powder were weighed into 2 ml glass vials and dried at 70 °C in a carousel within a NuCarb sample preparation device. The vials were subsequently evacuated and reacted with 100% orthophosphoric acid (ρ = 1.94-1.95 g/ml). The released CO_2 was passed through a water trap and frozen into a cold finger with liquid nitrogen for a further purification of the CO_2 before passing into a Nu Perspective isotope ratio mass spectrometer for stable carbon and oxygen isotope measurements in dual-inlet mode. The isotopic compositions were measured as six pulses against a calibrated reference gas. Carrara marble (CM) in-house standard, calibrated to NBS18 and NBS19, was analysed repeatedly within the same sequence and a final normalization of isotopic compositions was calculated against accepted values of the CM. The data are expressed as $\delta^{18}O$ values (in ‰ relative to VSMOW) and $\delta^{13}C$ values (in ‰ relative to VPDB, Vienna Pee Dee Belemnite international reference standard). The analytical precision was better than ±0.1‰ as standard deviation (1σ), determined from multiple analyses of the laboratory's in-house standards.

4.4.5 Petrochemical modeling of oxygen isotopes and fluid-rock interaction

Petrochemical models were generated based on bulk rock measurements and outcrop observations using the modeling package ThorPT (Markmann & Lanari, 2024). This open-source software combines chemical equilibrium calculations, isotope fractionation and a mechanical model for brittle failure on a predefined P–T path. Gibbs energy minimization were performed using Theriak (de Capitani & Brown, 1987; de Capitani & Petrakakis, 2010). The oxygen isotope composition for the predicted assemblage was modeled based on the oxygen isotope fractionation method of Kohn (1993) and Vho, Lanari, Rubatto, and Hermann (2020). In ThorPT, the fractionation of chemically zoned minerals such as garnet can be activated, as is known to significantly affect the volume fraction of the minerals in the model and can also influence the prediction of fluid production (Baxter & Caddick, 2013; Lanari & Engi, 2017). Here the produced garnet is fractionated at each step and a new reactive bulk composition is calculated. Similarly, fluid fractionation was activated and applied when brittle failure was predicted by the mechanical model (Markmann & Lanari, 2024). The P–T path of Skelton et al. (2019) was used because it was constrained based on samples fro the same location (Figure 4.2). The evolving mineral assemblages of the different bulk rock compositions were modeled over the predefined P–T path including Mn in the system, which widens the stability field of garnet (Mahar et al., 1997). This is expected to result in a larger $\delta^{18}O$ variability for the predicted garnet. In the case of fluid transfer, the fluid was allowed to be transferred in the model from bottom to top of the defined layers. In example, layer 1 represents rock type 1 of a given volume at the bottom and layer 2 the rock type 2 with a given volume. A fluid fractionated in layer 1 is transferred into layer 2 by transferring the corresponding mass of H and O to the infiltrated layer. Details on the modeling parameters are given in Supplementary Material S5.

4.5 Results

4.5.1 Bulk rock composition classification

The sampled rocks can be classified based on their major and trace element bulk rock composition (Figure 4.7, 4.8).

The bulk rock compositions of the blueschist, eclogite, and greenschist samples display significant variation in the Na_2O–CaO–MgO diagram. Compared to average MORB compositions, the sampled rocks follow trends associated with spilitization, chloritization, and epidotization (Figure 4.7). Specifically, the mafic boudins from Katergaki (SY21-01/2, SY21-02, SY21-33) exhibit elevated Na_2O values relative to MORB, aligning with the spili-

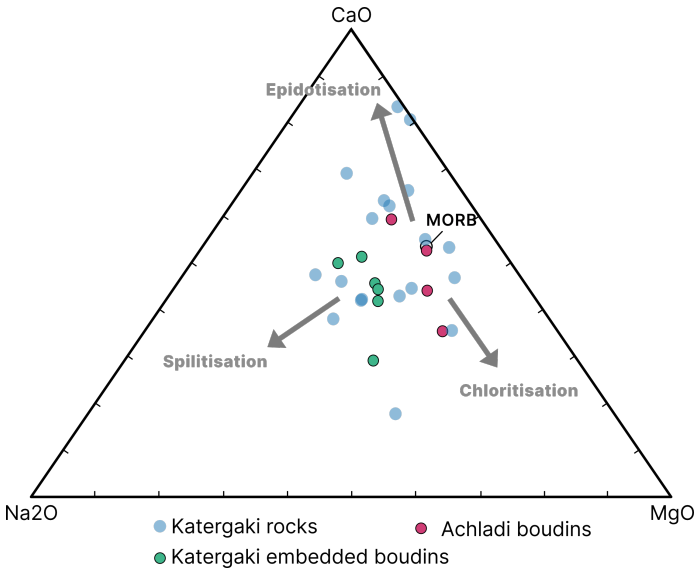

Figure 4.7: K_2O–SiO_2 diagram for volcanic rocks normalized to 100%. Samples from Achladi and Katergaki are highlighted and their sample names are annotated.

tization trend. In contrast, the samples from Achladi (SY21-04, SY21-05, SY21-07) define a vector extending between CaO and MgO enrichment, which partially overlaps with the MORB composition and encompasses the trends of epidotization and chloritization.

The sampled blueschist, eclogites, greenschist, and qz-phg schist cover a broad range in the REE composition, showing especially a large variation in LREE compared to HREE (Figure 4.8a). Two major pattern types are recognised in the eclogites, blueschists, and greenschists. The E-MORB type is relatively flat with small enrichment in LREE and the OIB type shows a continuous increase toward LREE (Figure 4.8b). The samples selected for oxygen isotope analysis from Achladi are similar to the OIB endmember and those from Katergaki are close to the E-MORB trend, but with a lower REE content compared to E-MORB. In contrast to these two major patterns, the qz-phg schist samples show a relatively flat pattern when normalized to chondritic composition. In addition, a typical anomaly in Eu is visible, the LREE is plotting between the OIB and E-MORB type, and the qz-phg schist also shows higher contents in HREE compared to the other bulk rock analyses.

Similar to the patterns in the REE-spider diagram, the analyzed bulk rocks show a large variation in their trace elements such as LILE, HFSE, or transition metals such as V (Figure 4.9a). A large variability is also visible in the negative Ta and Nb anomaly in the samples. Generally, the patterns with a lower Ta and Nb value show also a lower value in Cs, Rb, Ba, and Th. Two endmember patterns can be distinguished. One endmember shows the lowest Nb and Ta values, which are associated with a negative trend and the lowest values in Cs to Rb and Ba, and a negative anomaly in P (Figure 4.9b). This endmember pattern

is described by the mafic rocks at the Katergaki sequence. The second endmember shows the highest content of Nb and Ta, which is associated with an positive trend from Cs to Rb and Ba, and a higher content of K (Figure 4.9b). This pattern is represented by mafic rocks from the Achladi sequence. The analyzed qz-phg schist also show a negative anomaly in Nb and Ta plotting between the two described endmember patterns of the mafic rocks from Achladi and Katergaki. The qz-phg schist also show negative anomalies in Sr and P (Figure 4.9a). In addition, all rocks have a relatively similar Pb content, which appears as a negative anomaly in samples from Achladi and as a peak in the trace element pattern in samples from Katergaki.

The endmember patterns in (1) the REE distribution and (2) the variable Nb and Ta also show a distribution with increasing content within the Katergaki sequence from SW to NE (see Supplement Material S1 for details).

4.5.2 Garnet compositions and oxygen isotopes

Garnet from the different lithologies show intra-grain variability in their end-member molar fractions (expressed as X_{alm} for almandine defined as molar Fe/(Fe + Mg + Ca + Mn); X_{sps}; X_{prp} for pyrope as Mg/(Fe + Mg + Ca + Mn); and X_{grs}) with distinct zoning patterns (Figure 4.10, Supplementary Materials S3). Correction of the spessartine matrix effect required a correction for each analytical session visible by the monitored spessartine bias using the ErrRED reference material. In total 17 garnet grains were analyzed from eclogite, blueschists, and qz-phg schists samples from a total of more than 50 mapped grains (see supplementary material S1 and S3 for a summary). Number of spot analyses range between 3 to 20 on a single garnet grain and were placed systematically from core to rim, which was based on the compositional maps of spessartine and limited by suitable spot locations between inclusions and fractures (Figure 4.10). The $\delta^{18}O$ values shows a variability between the samples between the different localities, within one locality and within a few garnet grains. In Achladi, represented by blueschist and eclogite samples, the minimum value is 11.1±0.5‰ and the maximum value is 12.4±0.5‰. The $\delta^{18}O$ value do not clearly correlate with the garnet compositional zoning for these samples (Figure 4.11). For Katergaki, represented by blueschist, eclogite, and qz-ph schist samples, the minimum value is 8.3±0.7‰ and the maximum value is 12.2±0.5‰. The intra grain variation of $\delta^{18}O$ is the largest for blueschist and qz-phg schist samples showing a variation of up to 2.4±0.7‰. Samples with a larger variation show a correlation with the garnet composition and the position from core to rim (Figure 4.11), i.e. for samples SY21-02/1-1 (2.3±0.8‰), SY21-03 (2.4±0.7‰), SY21-01/3 (0.9±0.8‰). For Ormos Lakkoi the metagabbro sample shows a minimum value of 4.1±0.7‰ and a maximum value of 5.5±0.5‰. The propagated uncertainties on the single-spot analyses and the core-to-rim variations are reported at the

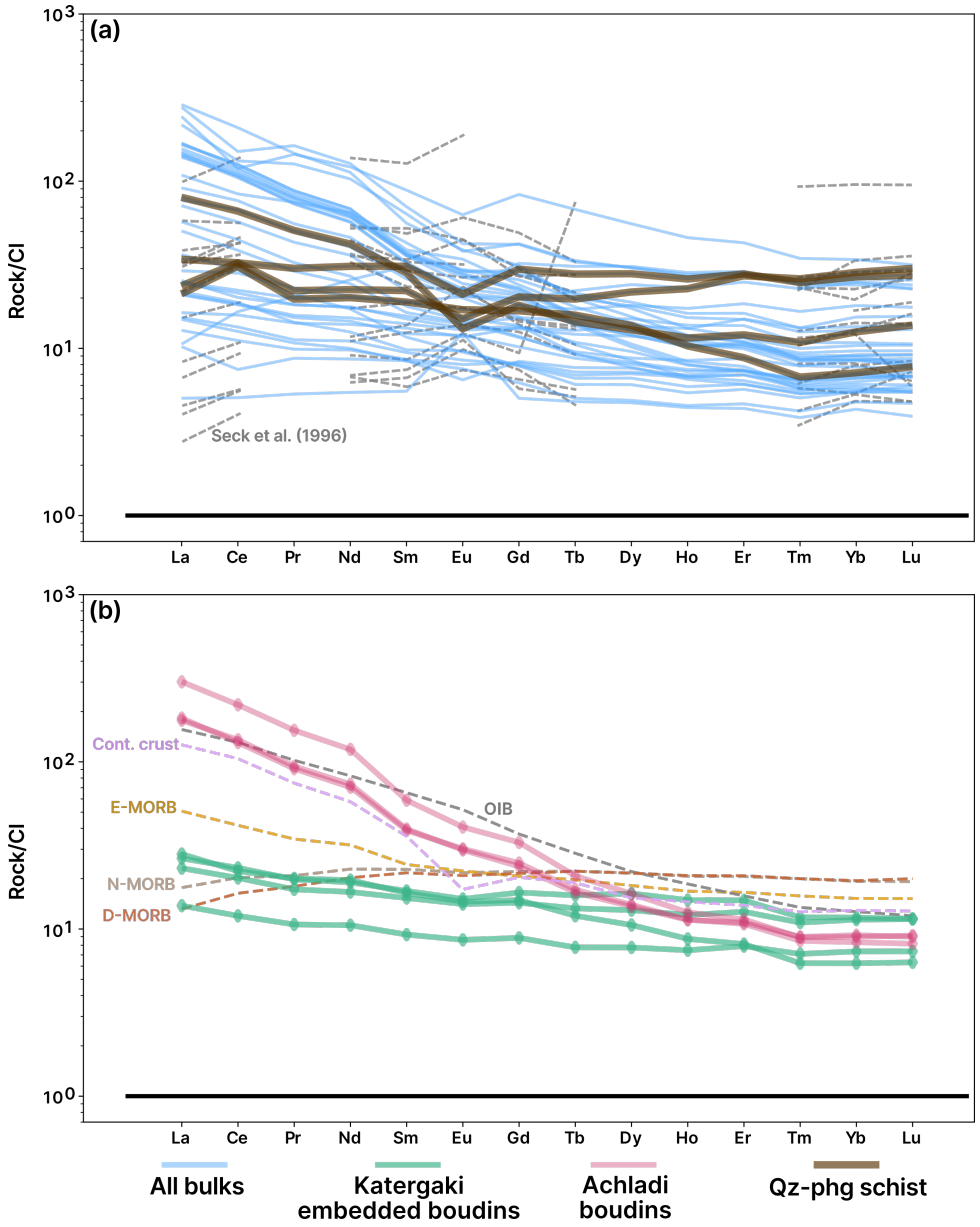

Figure 4.8: Chondrite-normalized rare earth element (REE) patterns for analyzed rock samples from the Katergaki and Achladi sequence. (a) REE pattern showing all bulk rock samples and highlights the qz-phg schist. (b) REE pattern showing the mafic pillows from Achladi and mafic boudins from Katergaki. Chondrite composition from Sun and McDonough (1989), N-MORB, E-MORB, and D-MORB from Gale et al. (2013), OIB from Sun and McDonough (1989), and continental crust from Taylor and McLennan (1985).

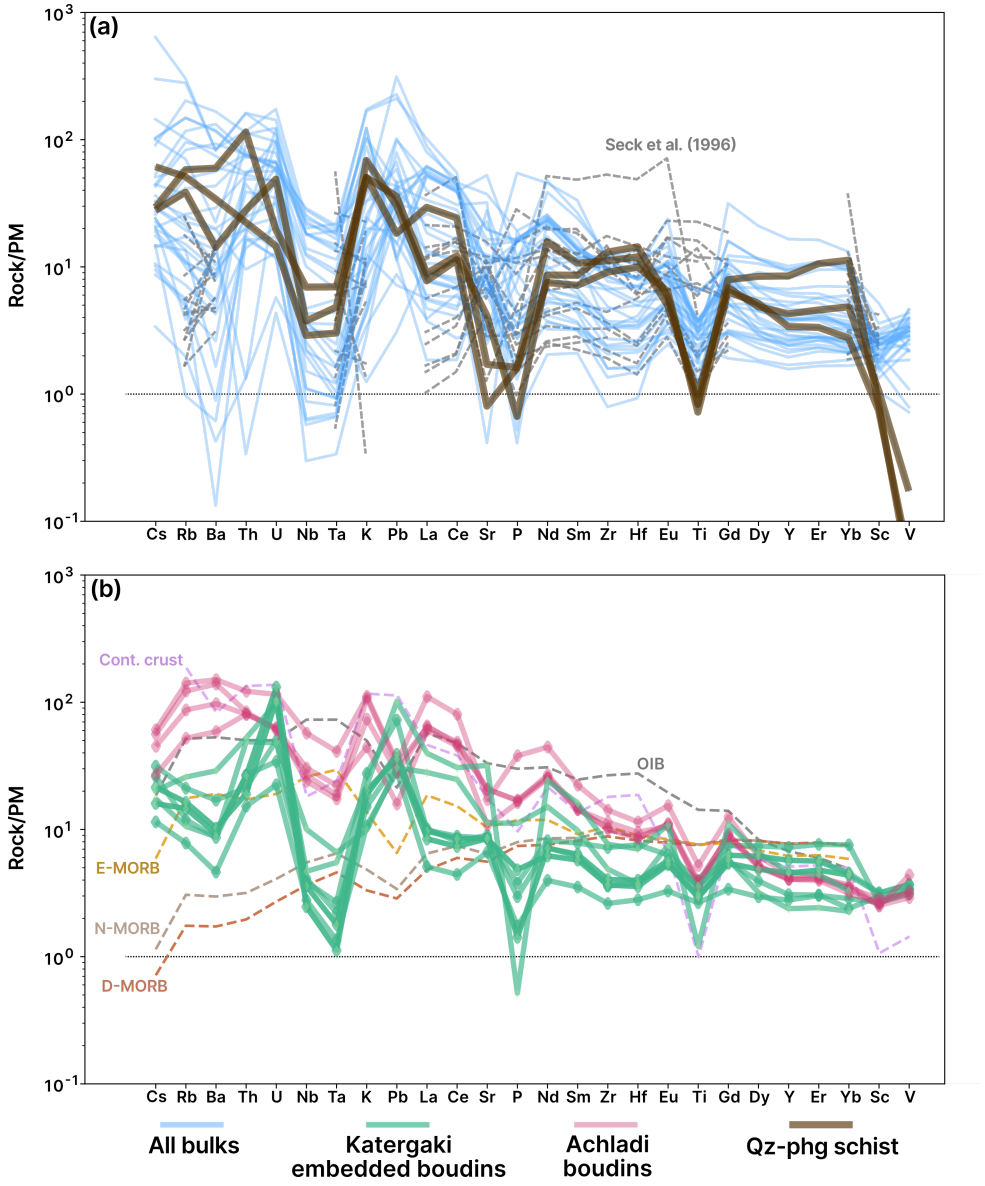

Figure 4.9: Primitive mantle-normalized (PM) trace element (TE) patterns for analyzed rock samples from the Katergaki and Achladi sequence. (a) TE elements normalized against primitive mantle (PM) showing all bulk rocks and highlights the qz-phg schist. (b) TE composition of mafic pillows from Achladi and mafic boudins from Katergaki normalized against PM. Primitive mantle composition is taken from Sun (1982), N-MORB, E-MORB, and D-MORB from Gale et al. (2013), OIB from Sun and McDonough (1989), and continental crust from Taylor and McLennan (1985).

95% confidence interval.

Eclogite and blueschist samples from Achladi. Garnet from these samples show a relatively weak zoning in almandine, spessartine, pyrope, and grossular from core to rim (Figures 4.10a,g and 4.11a). This weak zoning is associated with an almandine content of 53-65% as well as a grossular content of 22-33% (Figure 4.11a, d). Garnet analyses also show a moderate spread in spessartine content reaching up to 17% in the core of the grains (Figure 4.11b). The garnet compositions also show the highest pyrope contents of up to ∼15% in the rims of the grains (Figure 4.11c). Sample SY21-05 shows oscillatory zoning, which is best visible in the spessartine map (Figure 4.11g). Oscillatory zones are 30 μm wide and form an idiomorphic garnet shape. The complete oscillatory zoning is surrounded by a new garnet zone showing a distinct higher spessartine content and decrease in grossular and almandine. Inclusions and resorption textures cross-cut both, the oscillatory zoning and the surrounding rim. Garnet grains from Achladi show small or no variation in $\delta^{18}O$. The largest variation in $\delta^{18}O$ of 11.1±0.5‰ to 12.3±0.5‰ from core to rim is associated with a decrease in spessartine from 16 to 2 mol% and 11 to 2 mol% in samples SY21-07 and SY21-05, respectively (Figure 4.11b and Table 4.2).

Eclogite and blueschist samples from Katergaki. The garnet grains show gradual zoning from core to rim. They overlap in their almandine and grossular compositions with Achladi garnet, but have a larger range in grossular from 18 to 35% (Figure 4.11a, d). All eclogitic samples show a gradual change in composition from core to rim ranging from 67-54% in almandine, 10-1% in spessartine, 5-1% in pyrope, and 20-35% in grossular. Eclogite sample SY21-02 shows minor oscillatory zoning in spessartine content near the rim and is directly associated with resorption textures, also visible by patchy zones with higher grossular content (Figure 4.11 and 4.10e). The core and rim are similar in $\delta^{18}O$ showing 10.6±0.5‰ and 10.7±0.5‰, respectively. Sample SY21-33 shows a weak annulus in spessartine in the mantle region (<50 µm) correlating with an increase in grossular and a decrease in almandine, as well as an increase of spessartine toward the rim (∼100 µm) (Figure 4.10f). The core $\delta^{18}O$ is 10.9±0.5‰ and the rim is 11.3±0.5‰, showing no significant increase from core to rim. For eclogite sample SY21-01/2-2 $\delta^{18}O$ values in the core are 9.9±0.5‰ and in the rim 10.6±0.6‰, showing no clear change. Additionally, no spessartine rich core is visible (note, SY21-01/2-2 is the eclogite rim of the boudin SY21-01 and SY21-01/2-2 is the blueschist part of the same boudin).

Garnet from the blueschist sample SY21-01/2-1 show a change in almandine changes between core to mantle from 51 to 66%, whereas between mantle and rim it decreases to 60% (Figure 4.11a). They also show a larger range in grossular from 18% in the cores to 28% in the rim (Figure 4.11d). Similarly pyrope increases from 2% in the core to 13% in the rim. The grains have a spessartine rich core of 28% and a lower content of 1% in the

rim. Garnet from the blueschist sample also shows an annulus in the mantle (∼100 µm) visible in the map of spessartine (Figure 4.10b; Figure 4.11b; Supplementary Materials S1). Garnet from the blueschist sample records an intra-grain $\delta^{18}O$ increase from core to rim for four grains, showing a change from 8.3±0.6‰ to 10.4±0.6‰, 9.2±0.5‰ to 10.7±0.6‰, 9.0±0.5‰ to 10.7±0.5‰, and 9.1±0.6‰ to 10.7±0.6‰. This corresponds to a variation between 1.5±0.8‰ and 2.1±0.8‰ from core to rim. This systematic increase from core to rim was measured in different analytical sessions using slightly different matrix effect corrections (Supplementary Material S1 and S4).

Qz-phg schist samples from Katergaki. The garnet grains from qz-phg schists at Katergaki show a strong zoning in spessartine with rich cores (up to ∼50%) and a sharp drop from core to mantle (down to 2%) (Figure 4.10c; Figure 4.11b; Supplementary Materials S1). The largest variation is recorded by garnet from sample SY21-03, which represents the sedimentary matrix of the mafic boudins (e.g. samples SY21-01, SY21-02, SY21-33). The almandine component in garnet from sample SY21-03 increases from 37% in the core to 70% in the mantle and decreases to 63% in the rim. This trend is a similar to whas was observed in group 2 garnet from the blueschist samples (Figure 4.11a). The values of $\delta^{18}O$ increase from 8.3±0.6‰ in the core to 12.2±0.5‰ in the rim ($\Delta^{18}O_{grain}$ of 2.3-2.4±0.7‰). These variations are correlated with the compositional change in the garnet composition observed from core to rim. Sample SY21-01/3, at the contact with the mafic boudin, shows a flat distribution of spessartine from core to rim (2 to 4%) and no clear variability in $\delta^{18}O$ ranging from 10.2±0.6 to 11.1±0.6‰.

Group 4, metagabbro SYTM2204. Garnet grains from Ormos Lakkoi show a strong compositional zoning within each grain and a sharp increase of spessartine in the rim from 1 to 5% (Figure 4.10d and Supplementary Material S1). The garnet grains show minor increase of $\delta^{18}O$ from core to the mantle between 4.7±0.7 and 5.5±0.5‰ and no clear increase from mantle to the inner rim. In the outermost rim a $\delta^{18}O$ decrease to 4.1±0.7‰ is visible corresponding to a change of 1.2±0.8‰.

4.5.3 Phengite compositions and oxygen isotopes

Phengite in all samples shows minor to moderate chemical zoning for example in Si (expressed as atoms per formula unit, apfu). The zoning is mostly patchy and chemical maps are shown in Figure 4.10. Phengite from samples with oxygen isotope data, have Si between 3.25 and 3.49 apfu, XMg between 0.59 and 0.81 and Na between 0.03 and 0.16 apfu (Figure 4.12 and Table 4.3). Two groups can be separated based on the $\delta^{18}O$ values. Samples from Achladi show higher $\delta^{18}O$ values of 13.6±0.3‰ to 14.5±0.3‰. Samples from Katergaki show lower phengite $\delta^{18}O$ values between 10.9±0.3‰ and 13.2±0.3‰. No correlation was found between the major/minor element composition and the $\delta^{18}O$ of phengite in these

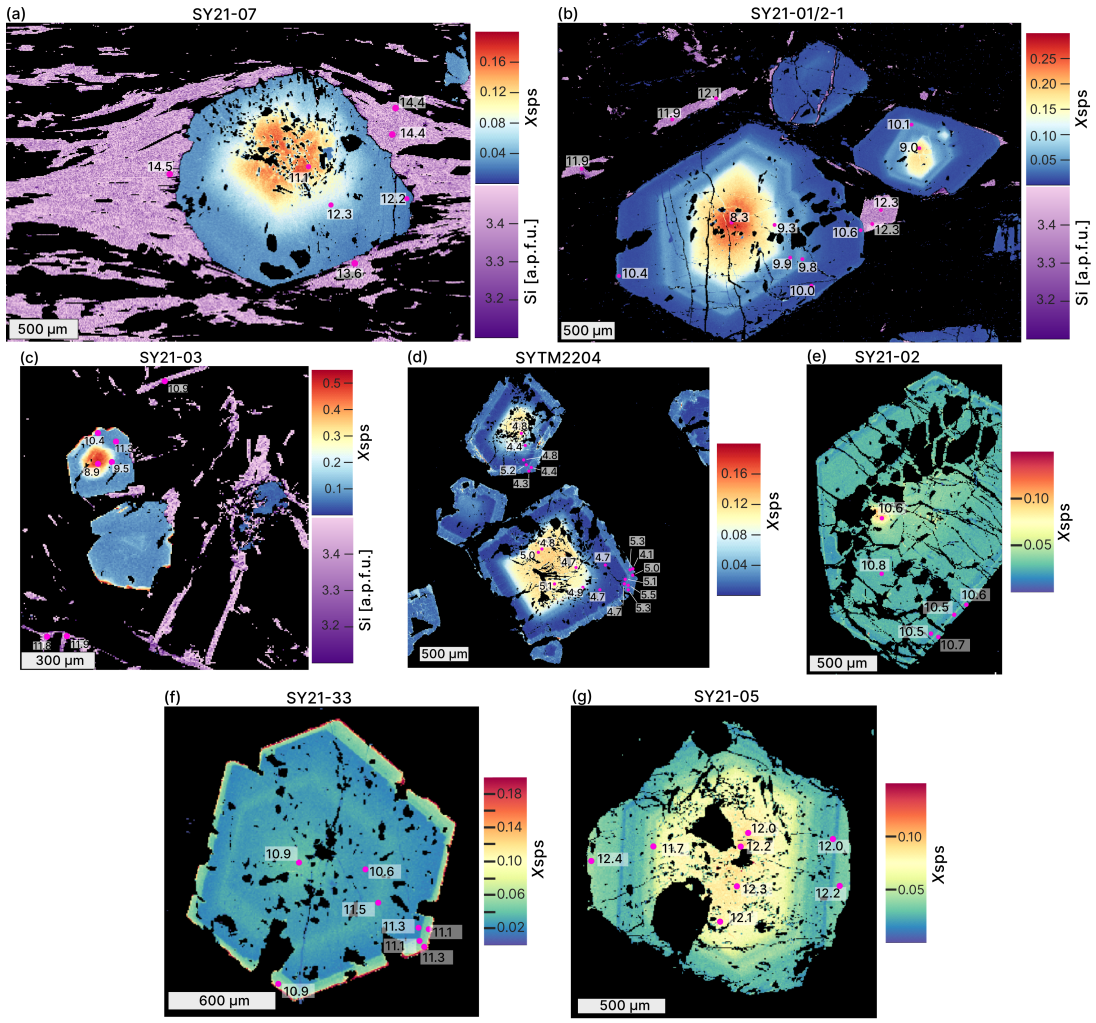

Figure 4.10: Combined major element maps of garnet and phengite including the in-situ $\delta^{18}O$ measurement values. (a) Representative oxygen isotope results for a blueschist (sample SY21-01/2) from Katergaki stacked on the X_{sps} X-ray map of garnet and Si (a.p.f.u.) X-ray map of phenigte. Watch out that the upper limit is cut at 20 % spessartine for improved comparable contrast and that the sample reaches up to 27 % spessartine. (b) Representative oxygen isotope results for a blueschist (sample SY21-7) from Achladi stacked on the X_{sps} X-ray map of garnet and Si (a.p.f.u.) X-ray map of phenigte. (c) Representative oxygen isotope results for a qz-phg schist sample (sample SY21-03) from Katergaki stacked on the X_{sps} X-ray map of garnet and Si (a.p.f.u.) X-ray map of phenigte. (d) Oxygen isotope results for the metagabbro (sample SYTM2204) stacked on the X_{sps} X-ray map of garnet and Si (a.p.f.u.) X-ray map of phenigte. (e) Oxygen isotope results for eclogite SY21-02. (f) Oxygen isotope results for eclogite SY21-33. (g) Oxygen isotope results for eclogite SY21-05. All maps were processed with XMapTools (Lanari et al., 2023).

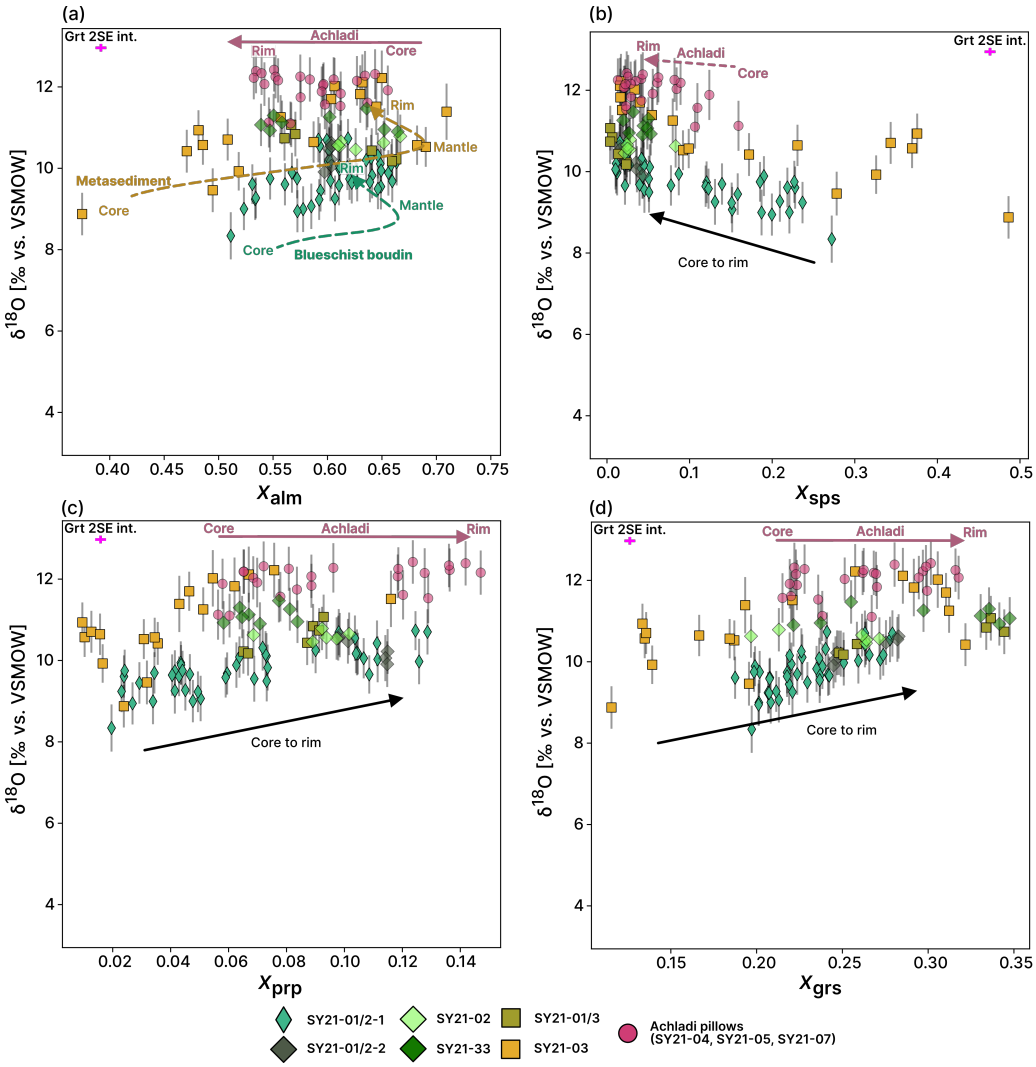

Figure 4.11: Garnet endmember composition against in-situ $\delta^{18}O$ measurement for samples from Achladi (SY21-04, SY21-05, SY21-07), Katergaki (SY21-01/2, SY21-02, SY21-03, SY21-33) and the metagabbro (SYTM2204). The $\delta^{18}O$ values are matrix corrected using the mount specific grossular bias and the spessartine bias for garnet compositions with relative high X_{sps}. Gray bars represent propagated uncertainty (95 % confidence interval). Pink bar represents the internal standard error (95 % confidence interval) of the measurements.

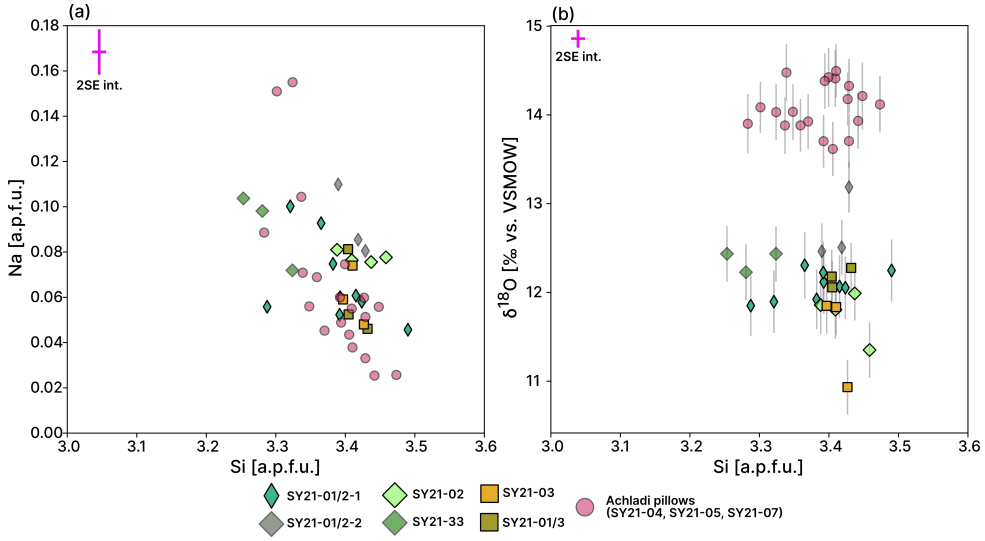

Figure 4.12: Phengite composition and in-situ $\delta^{18}O$ results. Gray bars represent propagated uncertainty (95% confidence interval). Pink bar represents the internal standard error (95% confidence interval) of the measurements.

samples.

4.5.4 Carbonate bulk oxygen and carbon isotope composition

The results of the oxygen and carbon isotope measurements for the carbonate aliquots from Achladi and Katergaki are shown in Table 4.4. The carbonates from different vein types show three distinct compositions.

Carbonate veins from Achladi are part of the first group with an average $\delta^{13}C$ value of 1.6±0.04‰ (±2σ unc.) and $\delta^{18}O$ of 16.0±0.04‰ (±2σ unc.). The vein sample containing quartz has a lower $\delta^{13}C$ value of -3.8±0.02‰ and an higher $\delta^{18}O$ value of 22.0±0.17‰.

Carbonate veins from Katergaki shows a different composition compared to Achladi samples which have a lower value of -2.0±0.17‰ in $\delta^{13}C$ and 13.9±0.54‰ in $\delta^{18}O$.

A third composition is associated with the marble sample showing the highest $\delta^{18}O$ of 28.9±0.69‰ and $\delta^{13}C$ of 3.2±0.22‰.

4.5.5 Modelling oxygen isotope variations of mineral phases in a semi-closed system

The evolution of the oxygen isotope composition of minerals and fluid was modeled on a prograde path between 355 °C, 1.10 GPa and 535 °C, 2.00 GPa for the blueschists, eclogites, and qz-phg schists of Achladi and Katergaki using their bulk rock composition and the petrochemical modeling software ThorPT. The P–T path is based on the proposed

path of Skelton et al. (2019) for rocks from the Katergaki outcrop. A representative model for each rock type is presented in Figure 4.13, in which the $\delta^{18}O$ values of minerals relative to the bulk composition are shown. The model was set as a water-saturated, semi-closed system where garnet and fluid fractionation is enabled (see the Methods section). The absolute values are controlled by the bulk rock $\delta^{18}O$. All modeling results can be found in Supplementary Material S1.

For the blueschist model, Grt, Qz, Phg, Gln, Law, Chl, Omp, Tit, and Ilm are predicted to be stable along the prograde trajectory. Chlorite-out is predicted at ~420 °C together with the production of a free aqueous fluid. Garnet is predicted to be stable from the beginning of the model at ~350 °C. For the garnet growing between 350 and 535 °C a maximum variation in $\delta^{18}O$ of 0.7‰ is predicted if the system is closed and only garnet and fluid fractionation is considered. Between 420 and 500 °C no garnet growth is predicted and therefore $\delta^{18}O$ in garnet is not modeled. Phengite is predicted to be stable throughout the prograde path, with a $\delta^{18}O$ variation of 0.4‰ due to T variation.

For the eclogite model, Grt, Phg, Gln, Tr, Law, Chl, Omp, Tit, Ilm, and Cc are predicted to be stable along the prograde trajectory. Garnet becomes stable at ~370 °C overlapping with the appearance of a free aqueous fluid. The variation of $\delta^{18}O$ in garnet from ~370 °C to ~535 °C is 0.7‰. Phengite is also predicted to be stable throughout the prograde path, with a $\delta^{18}O$ variation of 0.4‰.

For the qz-phg schist model, Grt, Phg, Pa, Gln, Tr, Qz, Law, Omp, Ep, Jd, Ilm, Cc, and Sd are predicted to be stable along the prograde path. Garnet is already stable at the starting conditions of 350 °C. The maximum predicted variation of $\delta^{18}O$ in garnet is 1.5‰ between 350 and 535 °C, although no garnet growth is predicted to occurr between 360 to 480 °C. Phengite is predicted to be stable throughout the model, with a $\delta^{18}O$ variation of 0.7‰.

For the metagabbro model, Grt, Omp, Px, Gln, Tr, Ky, Rt, and Ilm are predicted to be stable in the model. The maximum predicted variation of $\delta^{18}O$ is 0.7‰ for garnet (Figure 4.13d).

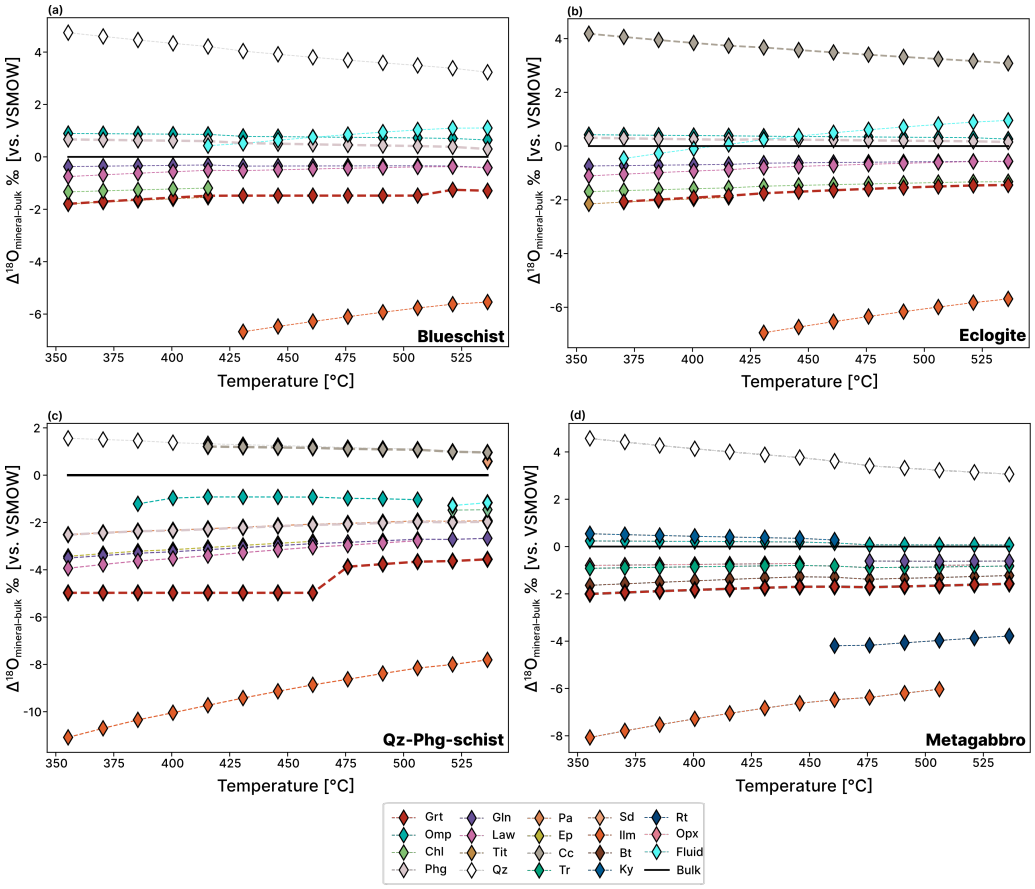

Figure 4.13: Oxygen isotope fractionation model results showing the difference between the bulk and the predicted mineral phase assemblage ($\Delta^{18}O_{mineral-bulk}$). Representative oxygen isotope model results for $\delta^{18}O$ between the bulk rock and the mineral phases the four rock types. (a) Representative model for a blueschist composition (SY21-01/2-1), (b) representative model for a eclogite composition (SY21-01/2-2), (c) representative model for a qz-phg schist composition (SY21-03), and (d) representative model for a metagabbro composition (Mg-gabbro sample 96-GB-6 from Barr, 1989). Mineral abbreviations are after Warr (2021).

Sample	Growth zone	Alm	Sps	Prp	Grs	Number of analyses	Matrix Corr. $\delta^{18}O$ [‰]	Range	± 2 SD
Achladi									
Eclogite									
SY21-05	Grain 1	0.53	0.02	0.07	0.25	8	12.2	11.7	0.4
		0.60	0.09	0.14	0.32			12.4	
	Grain 2	0.54	0.01	0.06	0.27	7	12.0	11.1	0.8
		0.61	0.11	0.15	0.32			12.3	
Blueschist									
SY21-07	Grain 1	0.55	0.02	0.06	0.22	7	11.9	11.1	1.3
		0.66	0.16	0.13	0.24			12.3	
	Grain 2	0.59	0.02	0.06	0.22	7	11.8	11.5	0.3
		0.66	0.12	0.13	0.24			12.3	
SY21-04		0.60	0.02	0.08	0.22	3	11.8	11.5	0.8
		0.63	0.11	0.13	0.24			12.3	
Katergaki									
Eclogites									
SY21-01/2 - 2 Eclogite		0.60	0.00	0.07	0.25	6	10.3	9.9	0.6
		0.60	0.02	0.09	0.34			10.6	
SY21-33 Eclogite		0.54	0.02	0.06	0.22	8	11.1	10.9	0.4
		0.66	0.05	0.08	0.35			11.5	
SY21-02 Eclogite		0.61	0.02	0.07	0.20	6	10.6	10.5	0.2
		0.67	0.08	0.10	0.27			10.8	
Blueschist									
SY21-01/2 - 1	Grain 1	0.51	0.01	0.02	0.20	9	9.7	8.3	1.4
		0.66	0.27	0.13	0.28			10.6	
	Grain 2	0.59	0.02	0.05	0.21	3	10.0	9.1	1.7
		0.64	0.15	0.13	0.26			10.7	
	Grain 3	0.53	0.01	0.02	0.19	20	9.8	8.9	0.8
		0.66	0.24	0.11	0.28			10.7	
	Grain 4	0.52	0.02	0.04	0.20	11	9.7	9.0	1.0
		0.65	0.22	0.12	0.27			10.7	
Qz-phg schist									
SY21-01/3		0.56	0.02	0.07	0.24	6	10.6	10.2	0.7
		0.66	0.04	0.09	0.28			11.1	
SY21-03	Grain 1	0.37	0.08	0.02	0.12	4	10.0	8.9	2.1
		0.56	0.49	0.05	0.32			11.3	
	Grain 2	0.48	0.02	0.01	0.13	14	11.2	9.9	1.5
		0.71	0.38	0.12	0.31			12.2	
Ormos Lakkoi									
Metagabbro									
SYTM2204	Garnet 1	0.54	0.01	0.01	0.13	14	4.9	4.1	0.7
		0.74	0.12	0.12	0.33			5.5	
	Garnet 2	0.56	0.01	0.02	0.12	6	4.7	4.3	0.6
		0.74	0.11	0.13	0.31			5.2	

Table 4.2: Ranges in the normative garnet composition and oxygen isotope composition of the sampled garnets.

Samples	Na (a.p.f.u.)	Si (a.p.f.u.)	X_{Mg}	Number of analyses	Average $\delta^{18}O$ [‰]	Range	± 2 SD
Achladi							
Eclogite							
SY21-05	0.03	3.34	0.69	3	13.8	13.7	0.2
	0.10	3.43	0.71			13.9	
	0.03	3.35	0.69	4	14.0	13.9	0.2
	0.06	3.47	0.72			14.1	
Blueschist							
SY21-04	0.06	3.30	0.65	4	14.3	14.0	0.5
	0.16	3.41	0.81			14.5	
SY21-07	0.05	3.28	0.61	5	14.1	13.9	0.4
	0.09	3.45	0.74			14.3	
	0.04	3.39	0.60	4	14.2	13.6	0.8
	0.07	3.41	0.70			14.5	
Katergaki							
Eclogite							
SY21-01/2 - 2	0.08	3.39	0.71	3	12.7	12.5	0.8
	0.11	3.43	0.73			13.2	
SY21-02	0.08	3.39	0.64	4	11.8	11.4	0.6
	0.08	3.46	0.67			12.0	
SY21-33	0.07	3.25	0.80	3	12.4	12.2	0.2
	0.10	3.32	0.81			12.4	
Blueschist							
SY21-01/2 - 1	0.05	3.29	0.59	5	12.1	11.9	0.4
	0.10	3.49	0.75			12.3	
	0.05	3.38	0.70	4	12.1	11.9	0.3
	0.07	3.42	0.74			12.2	
Qz-phg schist							
SY21-01/3	0.05	3.40	0.63	3	12.2	12.1	0.2
	0.08	3.43	0.74			12.3	
SY21-03	0.05	3.40	0.71	3	11.5	10.9	1.1
	0.07	3.43	0.72			11.9	

Table 4.3: Ranges in the normative phengite composition and oxygen isotope composition.

Samples	Outcrop	Material	$\delta^{18}O$ (vs. VSMOW)	2σ	$\delta^{13}C$ (vs. VPDB)	2σ
SYTM2301	Achladi	calcite w. siderite	16.22	0.09	1.57	0.08
SYTM2301	Achladi	calcite w. siderite	16.26	0.15	1.77	0.19
SYTM2301	Achladi	calcite w. siderite	15.93	0.17	1.52	0.03
SYTM2302	Achladi	calcite	16.31	0.15	1.56	0.10
SYTM2303	Achladi	quartz mix	no values because low yield			
SYTM2303	Achladi	quartz mix	22.02	0.17	-3.82	0.02
SYTM2304	Achladi	calcite	15.73	0.07	1.90	0.12
SYTM2305	Achladi	calcite + dolomite	15.67	0.06	1.60	0.07
SYTM2305	Achladi	calcite + dolomite	no values because low yield			
SYTM2306	Achladi	calcite	15.81	0.08	1.51	0.07
SYTM2337	Achladi	aragonite	17.52	0.06	0.56	1.59
SYTM2311	Katergaki	calcite	13.92	0.54	-2.02	0.17
SYTM2312	Katergaki	marble	28.93	0.69	3.19	0.22

Table 4.4: Carbonate analyse of $\delta^{13}C$ (vs. VPDB) and $\delta^{18}O$ (vs. VSMOW).

4.6 Discussion

4.6.1 Outcrop relationships

The three sampled outcrops—Achladi, Katergaki, and Ormos Lakkoi—are interpreted as part of the high-pressure, low-temperature (HP-LT) Kampos Unit, likely representing different fragments of former oceanic crust that have been tectonically dispersed across the island (Figure 4.1). Previous studies have identified on Syros several components of an ophiolitic sequence, highlighting the preservation of abyssal serpentinized mantle (Cooperdock et al., 2018), a diverse range of gabbros, and plagiogranites (Bloor, 1998; Bröcker & Keasling, 2006; Bröcker & Enders, 1999, 2001; Keiter et al., 2011; Putlitz et al., 2005; Robson, 2000; Seck et al., 1996; Tomaschek, 2003), as well as hydrothermally altered basalts (Mocek, 2001; Putlitz et al., 2000; Seck et al., 1996). The oceanic crust formation has been dated to the Cretaceous age (Bröcker & Keasling, 2006; Bröcker & Enders, 1999; Lagos et al., 2007; Tomaschek, 2003), and its association with adjacent lithologies — comprising Carboniferous gneisses and Triassic continental margin deposits, such as metasediments and marbles — may suggests a hyper-extended margin setting (e.g., Bonneau, 1984; Keiter et al., 2011; Seman, 2016; Tomaschek et al., 2008). In particular, the sampled outcrops at Achladi, Katergaki, and Ormos Lakkoi, along with the variety of magmatic rocks, may represent fragments of embryonic oceanic crust, similar to the vertical cross-section model described by Manatschal and Müntener (2009). A simplified cross-section in Figure 4.14 illustrates the main lithologies identified in the studied outcrops, including basalts, metasediments, gabbros, and serpentinites. Based on this succession, the reworked sediments of the Katergaki sequence may have originally been structurally located below the Achladi sequence. However, reworking and thrusting of these sequences, can result in an invertion of the lithological order. This has been proposed for Syros and interpreted as related to burial conditions corresponding to prograde metamorphism (Gerogiannis et al., 2024; Laurent et al., 2016; Ring et al., 2020; Schumacher et al., 2008). This is also supported by the oldest ages found in the HP ophiolithic sequence in the North of Syros (e.g., Lagos et al., 2007). Thus, it is possible that the Achladi sequence was positioned structurally above the Katergaky sequence during seafloor alteration and structurally below the Katergaki sequence during prograde metamorphism.

4.6.2 Interpretation of the bulk chemistry

Major and trace elements of blueschists and eclogites show a large geochemical diversity. The major element composition of the mafic boudins indicates substantial hydrothermal alteration when compared to typical MORB (Figure 4.7). At Achladi, alteration is dominated by epidotization and chloritization, while the boudins wrapped in the quartz-phengite schist

matrix at Katergaki are primarily altered through spilitization. Ocean-floor hydrothermal alteration has been observed in metabasites, metagabbros, and serpentinites on Syros and throughout the Cyclades (Cooperdock et al., 2018; Katzir et al., 1996; Mocek, 2001; Putlitz et al., 2000; Stouraiti et al., 2017). Alteration is further supported by the enrichment in mobile trace elements such as Cs, Rb, Sr, and Ba, but also K, compared to MORB (Figure 4.9). The trace element compositions of the mafic boudins show a range between E-MORB and OIB (Figure 4.8 & 4.9). The embedded boudins at Katergaki represent one endmember being similar to an E-MORB composition, while those from Achladi are enriched in LREE, LILE, and HFSE, similar to OIB. The qz-phg-schists plot plot within the geochemical variation defined by these mafic boudins. A similar geochemical diversity was reported by Seck et al. (1996) for rocks from Syros, where trace element and isotope composition (Sr and Nd) were used to infer a back-arc setting for the protoliths. Mafic rocks from Katergaki show a similar variation in LREE and MREE compared to their trace element pattern. Comparable trace element signatures in metabasalts and metagabbros from other Aegean islands, such as Tinos, Sifnos, Paros, and Samos, suggest that the protoliths of these sequences likely formed in fore-arc to back-arc settings (Katzir et al., 1996; Lagos et al., 2002; Mocek, 2001; Okrusch & Bröcker, 1990; Stouraiti et al., 2017). These Aegean islands, part of the Cycladic Blueschist Unit (CBU), show a similar enrichement in LILE and LREE compared to N-MORB, and similar patterns for Nb and Ta, as the rocks from Achladi and Katergaki. These geochemical signatures suggest that the protoliths of the blueschists and eclogites at Achladi and Katergaki were originally arc-related basalts and is also similar with models showing the enrichment in trace elements in a transitional geodynamic setting (e.g., rifting or breakup), which could also include a crustal contamination (François et al., 2018). Based on the lithological context and the geochemical data, the samples from Achladi, Katergaki, and Ormos Lakkoi likely represent fragments of an altered ophiolitic sequence, which experienced seafloor alteration prior to subduction (see Figure 4.14).

1. **Achladi:** the rounded and stacked boudins are interpreted as solidified pillow lavas that underwent blueschist to eclogite facies metamorphism.

2. **Katergaki:** the mafic boudins are interpreted as fragments of solidified pillow lavas intercalated into a sedimentary matrix, possibly emplaced during reworking prior subduction. These boudins experienced metamorphism alongside the enclosing quartz-phengite schist, reaching blueschist to eclogite facies conditions.

3. **Ormos Lakkoi:** The knocker block at Ormos Lakkoi is interpreted as a fragment of former gabbro from the oceanic crust. This gabbroic block has been reworked into ultramafic material represented by the talc-chlorite layer wrapping around it.

4.6.3 Protolith oxygen isotope composition

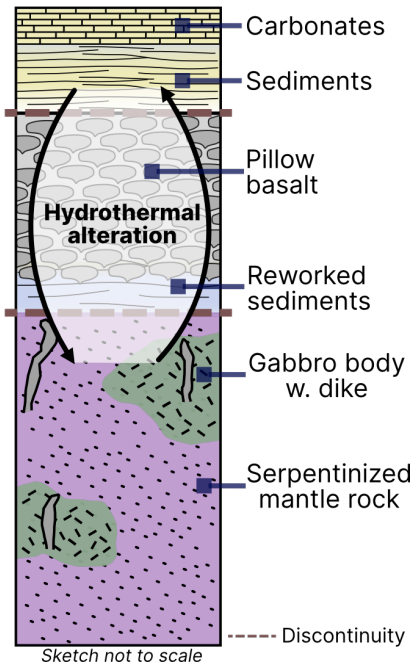

Figure 4.14: Possible vertical cross-section of the ophiolitic sequence after Manatschal and Müntener (2009) including the observations from basalts, metasediments, gabbros, and serpentinites on Syros. Hydrothermal alteration due to seawater infiltration into the different parts of the sequence at the seafloor. Sediments on top could resemble continental margin deposits.

Estimating the original $\delta^{18}O$ values of the protoliths prior to high-pressure metamorphism is essential for interpreting the isotopic composition of garnet, phengite, and carbonates in the rocks. Bulk rock $\delta^{18}O$ values for metabasalts from Syros, Sifnos, and Tinos typically range between 10‰ and 14‰, while metagabbros range between 4‰ and 7‰ on Syros and 7‰ to 9‰ on Tinos (Ganor et al., 1996; Katzir et al., 1996; Putlitz et al., 2000). Serpentinites from Syros range between 5 and 9‰, whereas those from Tinos can reach values as high as 14‰ (Cooperdock et al., 2018; Katzir et al., 1996; Pogge von Strandmann et al., 2015). A compilation of published values together with our data is shown in Figure 4.15. The recorded $\delta^{18}O$ values in the Cyclades reflect the typical isotopic trend of an ophiolitic sequence altered by hydrothermal processes at the seafloor (Alt et al., 1986; Gregory & Taylor, 1981; Muehlenbachs, 1986).

Previous studies have shown that garnet in similar rocks from Syros and Sifnos likely crystallized early during the prograde metamorphic path, at temperatures between 300 and 450°C (Dragovic et al., 2015; Gorce et al., 2021; Laurent et al., 2018; Skelton et al., 2019; Tual et al., 2022) and for which the original composition is kept unchanged due to limited diffusion at the conditions of 400-550 °C. Therefore the $\delta^{18}O$ composition of garnet cores from blueschists, eclogites, and metasediments is used to estimate post-seafloor alteration bulk rock values. The pre-subduction bulk rock values can be then used to evaluate whether the samples have the isotopic characteristics of altered rocks similar to those previously reported. The fractionation coefficient between garnet and bulk rock is approximately +2‰ at blueschist to eclogite facies conditions, and +4‰ for quartz-phengite schists (Figure 4.13; Vho, Lanari, Rubatto, and Hermann, 2020). Using the calculated bulk rock $\delta^{18}O$ values, the samples were positioned within a typical ophiolitic sequence (Figure 4.15). For comparison purposes, this idealized cross-section of altered, sediment-covered oceanic crust is used instead of the modified version shown in Figure 4.14.

Garnet cores from blueschist and eclogite in Achladi display $\delta^{18}O$ values of 11-12‰, corresponding to a bulk rock value of 13-14‰ at the time of garnet crystallization. These values are comparable to altered basalts from Syros, Sifnos, and Tinos (see Figure 4.15). This suggests that the stacked mafic pillows at Achladi underwent low-temperature seafloor alteration prior to subduction, likely near the sediment cover of the ophiolitic sequence. The uniform $\delta^{18}O$ values across the outcrop indicate that the entire locality experienced similar degrees of seafloor alteration at comparable depths.

Garnet in eclogite from Katergaki shows $\delta^{18}O$ values of 10-11‰, corresponding to a bulk rock $\delta^{18}O$ value of 12-13‰. In contrast, garnet cores from the blueschists have lower $\delta^{18}O$ values of 8-10‰, translating to a bulk $\delta^{18}O$ value of 10-11‰. These lower values, compared to previously reported data from Syros, Sifnos, and Tinos, suggest that the Katergaki rocks were situated deeper within the ophiolitic sequence and experienced seafloor alteration under higher temperature conditions and/or fluid-rock ratios than the samples from Achladi and those reported by Putlitz et al. (2000) (see Figure 4.15). A higher temperature is compatible with the position of the reworked sediments in the ophiolitic sequence of an hyper-extended margin.

Garnet cores from the qz-phg schist show $\delta^{18}O$ values of 8-9‰, which correspond to a bulk rock $\delta^{18}O$ value of 12-13‰ when the garnet crystallized. These values align with the typical $\delta^{18}O$ range for clastic or continental sediments (Eiler, 2001), but are lower than the values measured for similar rocks from Sifnos Ganor et al. (1996) (see Figure 4.15). The origin to clastic sediments is also supported by the relative high Ba (91.7 µg/g), U (1.0 µg/g), La (5.6 µg/g), and Th (2.2 µg/g) contents compared to recycled altered MORB, which could represent a mixture between with volcanic sediments (Eiler, 2000).

Garnet cores from the metagabbro sampled at Ormos Lakkoi yield a $\delta^{18}O$ value of approximately 5‰, indicating a bulk rock $\delta^{18}O$ value of about 7‰. This is similar to values documented by George et al. (2024). While this value is slightly above compared to unaltered MORB, which typically shows $\delta^{18}O$ values around 5.8±0.2‰, it aligns well with previously reported values from Syros Putlitz et al. (2000) (see Figure 4.15).

The $\delta^{18}O$ values of the protoliths prior to blueschist and eclogite metamorphism suggest that the rocks from Achladi, Katergaki, and Ormos Lakkoi underwent varying degrees and temperature conditions of seafloor alteration. Notably, the garnet cores from blueschists at Katergaki record one of the lowest $\delta^{18}O$ values measured on Syros.

Moreover, the lower $\delta^{18}O$ values observed in the mafic boudins from Katergaki, embedded within qz-phg schist of similar composition, compared to the rocks from Achladi, suggest that the lithologies at Katergaki may have been situated lower in the oceanic crust relative to the idealized cross-section and hydrothermal alteration profile, where $\delta^{18}O$ values tend to decrease from the top of the section toward the gabbros (Figure 4.15). Therefore,

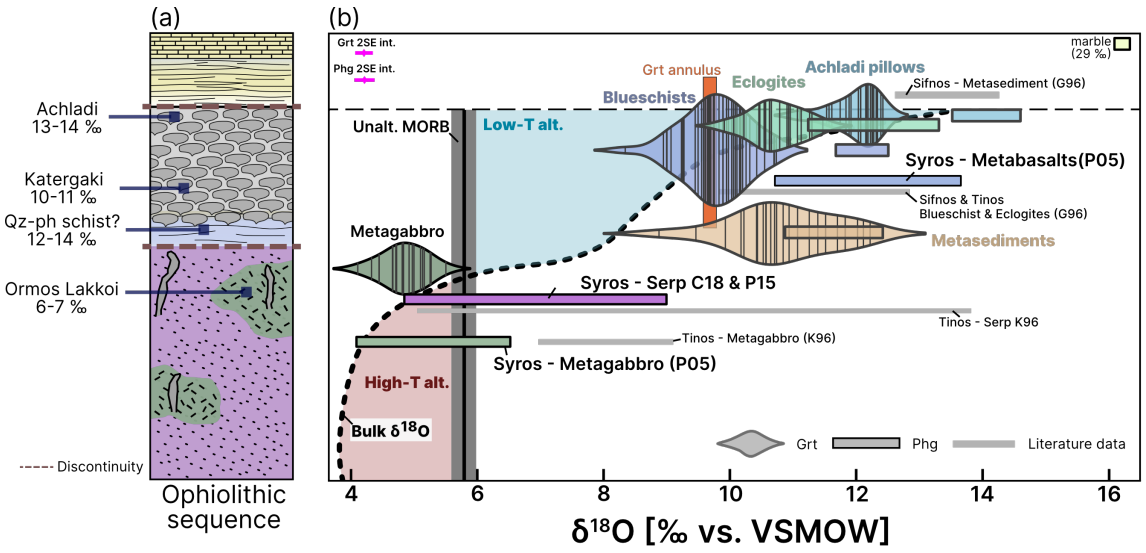

Figure 4.15: Ophiolithic sequence and oxygen isotope compositions. (a) Cross section modified after Manatschal and Müntener (2009) including the basalts, metasediments, gabbros, and serpentinites from Achladi, Katergaki, and Ormos Lakkoi with their calculated bulk rock $\delta^{18}O$ values (see text for details). (b) Oxygen isotope compositions of this study and literature values for different mineral phases from Syros, Sifnos, and Tinos. Garnet $\delta^{18}O$ values and their kernel density estimates are visualized by violins. Phengite $\delta^{18}O$ ranges are represented by bar plots. Oxygen isotope profile of an typical ophiolitic sequence modified after Gregory and Taylor (1981) and Muehlenbachs (1986) is given for reference of an expected alteration profile. Unaltered MORB composition of 5.8±0.2‰ from Gregory and Taylor (1981). K96 is Katzir et al. (1996), G96 is Ganor et al. (1996), P05 is Putlitz et al. (2000), P15 is Pogge von Strandmann et al. (2015), and C18 is Cooperdock et al. (2018).

the lower $\delta^{18}O$ values at Katergaki support a modified model of the oceanic crust, as depicted in Figure 4.14, where the rocks likely underwent hydrothermal alteration prior to subduction. This has been demonstrated, for example, in the case of serpentinites on Syros, where trace element composition and $\delta^{18}O$ values indicate an abyssal origin (Cooperdock et al., 2018).

4.6.4 Metamorphic evolution and garnet compositional zoning

The sequences Achladi, Katergaki, and Ormos Lakkoi represent distinct fragments of an altered oceanic crust that have experienced high-pressure metamorphism. Changes in garnet major element chemistry, particularly zoning patterns and sharp compositional changes, can be linked to shifts in the mineral assemblage, such as the breakdown of lawsonite, amphibole, or accessory minerals. Additionally, these changes may indicate the presence of solute-bearing fluid phases (e.g., Giuntoli et al., 2018; Konrad-Schmolke et al., 2006; Konrad-Schmolke et al., 2008). Quantitative compositional mapping of garnet reveals zoning features such as high Mn content in the cores that decreases towards the rims and an increase in pyrope content from core to rim. These features are indicative of prograde gar-

net growth under water-saturated conditions (e.g., Caddick et al., 2010; Konrad-Schmolke et al., 2006; Spear, 2014), as illustrated in Figure 4.10 and in Supplementary Materials S3&4. The potential for modification of garnet major element zoning due to volume diffusion is minimal, given the relatively low peak temperature conditions, which are below 550 °C (e.g., Caddick et al., 2010; Konrad-Schmolke et al., 2006; Page et al., 2014).

In total, 13 garnet grains from eclogites were mapped, with 5 of these analyzed for their oxygen isotope composition. In particular, spessartine-rich cores observed in mapped garnets from Achladi and Katergaki provide evidence for a typical prograde garnet growth with a bell shape zonning pattern. Early garnet growth (between 300 and 450°C) during prograde metamorphism has been modeled for several eclogites, blueschists, and metasediments in the southeastern region of Syros and Sifnos (Dragovic et al., 2015; Laurent et al., 2018; Skelton et al., 2019), where eclogites and blueschists generally display similar metamorphic histories and give ages in garnet cores are around 51 to 45 Ma (Gorce et al., 2021; Lagos et al., 2007; Tual et al., 2022).

However, most eclogitic garnets showed either lower spessartine content or lacked distinct high-Mn cores compared to garnets from blueschists (see Supplementary S4 for a compilation of spessartine maps). This difference is observed even among garnets from samples that are spatially related at meter- to centimeter-scales within the Achladi and Katergaki outcrop. Similarly, garnets from blueschists in Achladi also display lower spessartine content in their cores. Bulk rock data indicates that eclogites from Katergaki and Achladi contain slightly lower MnO concentrations (0.09–0.12 wt.%) compared to blueschists (0.14–0.15 wt.%). This could reflect varying degrees of MnO incorporation during alteration, as observed in altered basaltic crust compositions (Staudigel et al., 1996). Consequently, the difference in Mn availability may have resulted in garnet crystallization (Spear & Pattison, 2017), which might indicate a later garnet growth in rocks with lower MnO content compared to the blueschists. A similar or later garnet growth for eclogites above 400 °C is also demonstrated by multi-equilibrium calculations by (Laurent et al., 2018; Trotet et al., 2001).

Further evidence for early garnet growth is provided by the presence of titanite inclusions within the cores and mantles of garnet, as observed in blueschist sample SY21-01/2-1 from Katergaki (Figure 4.5d). Modeling suggests that titanite is stable with garnet at temperatures below 425 °C (Figure 4.13a) and overlap with prograde P–T estimates Skelton et al. (2019). Prograde garnet growth is further supported by rutile inclusions within the mantles and rims of garnet, such as in sample SY21-07. In addition glaucophane, phengite, and epidote are found as inclusions in eclogite and blueschist garnets.

In the eclogite sample SY21-05 from Achladi, oscillatory zoning is evident in the spessartine maps as idiomorphic shapes and chemically distinct garnet rims (Figure 4.10g). The

modification of Mn alone suggests that the availability of Mn changed under fluid-saturated conditions and during episodes of garnet growth (e.g., George et al., 2024; Giuntoli et al., 2018; Kohn, 2004). The homogeneous oxygen isotope composition within the oscillatory zone of garnet in SY21-05 indicates a relatively closed system during garnet growth.

In eclogite sample SY21-02 and garnet from SY21-33 at Katergaki, zoning is most likely associated with garnet dissolution and regrowth, potentially linked to external fluid infiltration (Figure 4.10e-f). The breakdown of Mn-bearing phases such as epidote or lawsonite could have supplied Mn and Ca to the system (Page et al., 2014). Additionally, the high grossular component in the garnet rim supports retrograde garnet growth during or after the lawsonite-out reaction, which could have occurred just after reaching the peak pressure forming chlorite, zoiste, and paragonite on the expense of lawsonite and glaucophane (Schumacher et al., 2008). The oxygen isotope composition in these samples is also relatively homogeneous, and consistent with these interpretations.

Blueschist sample SY21-01/2-1 from Katergaki exhibits an Mn-annulus, paired with a decrease in almandine content, which suggests a change in the Mn and Fe availability during garnet growth (Figure 4.10b). This annulus is present in several garnet grains and correlates with a gradual change in oxygen isotope composition from core to rim, by 1.5 to 2.1±0.8‰. Nevertheless, no resorption feature is associated with the annulus.

Garnet grains from the quartz-phengite schist SY21-03 at Katergaki show sharp zoning from core to rim, indicative of prograde growth, but with an abrupt compositional change at the rim, suggesting dissolution and reprecipitation (Figure 4.10c). The qz-phg schist encloses the mafic boudins at Katergaki, such as the blueschist sample SY21-01/2-1, and exhibits a similar gradual oxygen isotope changes from core to rim of up to 2.4±0.8‰, consistent with garnet composition changes.

Garnets from the metagabbro SYTM2204 deviate from these patterns, displaying sharp rim-mantle zoning across all garnet endmembers (Figure 4.10d). Radial veinlets suggest a dissolution-precipitation process (Giuntoli et al., 2018). While the oxygen isotope composition is mostly homogeneous throughout the grain, a decrease of 1.2±0.8‰ is observed at the rim, likely related to external fluid involvement during retrogression.

Phengite compositions from Achladi and Katergaki samples are consistent with those previously reported for Syros by Putlitz et al. (2005) and Trotet et al. (2001), with Na content ranging from 0.02 to 0.08 apfu and Si content between 3.35 and 3.45 apfu. As phengite is sensitive to fluid-induced recrystallization and pressure variations (e.g., Halama et al., 2018), these compositions likely represent peak and post-peak recrystallization under pressures below 2.0 GPa, indicated by the elevated Si content. Following garnet mantles to rims in samples from Achladi and Katergaki could have possibly formed in equilibrium and may be indicated by the ages of of 48.2 ± 3.1 Ma in phengite obtained in eclogites

by Rb-Sr dating (see for example the latest results of Barnes et al., 2024). Retrogression during exhumation is visible with the presence of late-stage chlorite and resorption textures in garnet, which suggest that garnet began breaking down and was replaced by chlorite as the rocks were exhumed to greenschist facies conditions. Carbonate veins that cross-cut and wrap around the boudins at Achladi and Katergaki likely formed after eclogitization, as previously discussed by Barr (1989). This veining is considered a late-stage feature, occurring during the exhumation process.

4.6.5 Interpretation of oxygen and carbon isotope compositions

In **Achladi** (blueschist and eclogite samples), garnet $\delta^{18}O$ values are relatively uniform with values of 11-13‰, with the largest variation of 1.2±0.8‰ within single grains (e.g., SY21-07 and SY21-05). This variation can be explained by isotope fractionation over a temperature increase of approximately 180 °C, accounting for fractionation effects in both garnet and any excess fluid present in the system (see Figure 4.13). The effect of temperature-dependent fractionation is consistent with previous studies, which suggest that combined fractionation effects are typically ≤1‰ for temperatures above 350 °C in closed systems (Kang et al., 2024; Kohn, 1993; Vho, Lanari, Rubatto, & Hermann, 2020). The same fractionation effect is also consistent with the range of phengite $\delta^{18}O$ values, which vary from 13.6±0.2‰ to 14.5±0.2‰. Therefore it is most likely that the sampled evolved as a closed system condition as indicated in the major element zoning of garnet. Nevertheless, from a purely isotopic perspective the system can also have been infiltrated by an external fluid of with an oxygen isotope composition in equilibrium with the rock. For instance, an infiltrating fluid could have re-equilibrated its isotopic composition through interaction with surrounding lithologies before entering the studied outcrop (Vho, Rubatto, Lanari, et al., 2020). The oscillatory zoning in garnet may also indicate the episodic growth of garnet when fluid was distributed in the system (Kohn, 2004; Konrad-Schmolke et al., 2023; Skora et al., 2006). However, it is most plausible that the garnet $\delta^{18}O$ values from Achladi reflect the isotopic signature of hydrothermally altered oceanic crust, which is supported by the relatively high $\delta^{18}O$ values in garnet and as seen in other areas of Syros (Putlitz et al., 2000). Additionally, the high $\delta^{18}O$ values in phengite (∼14‰) and its major element composition indicate recrystallization at or just after peak pressure conditions during metamorphism. This suggests that there was no significant modification of the bulk rock $\delta^{18}O$ during prograde metamorphism until phengite crystallization. Instead, the relatively high $\delta^{18}O$ values of ∼12‰ in garnet rims and ∼14‰ in phengite suggest that they grew in isotopic equilibrium, given a $\delta^{18}O$ difference of ∼2‰ at temperatures around 500°C (see Figure 4.13). Optionally, an internally-derived fluid in the mafic sequence could have triggered the recrystallization of phengite and the incremental growth of the garnet's outer shells, as lawsonite likely broke down near peak pressures, as demonstrated by Schumacher et al.

(2008). This could further explain the oscillatory zoning in some garnet grains, the increase in grossular content near the garnet rims, and the onset of garnet rim resorption, as seen in Figure 4.3.

The large number of wrapping and crosscutting carbonate veins in the outcrop indicate post kinematic infiltration of CO_2-rich fluids. The measured carbonate aliquots from these veins at Achladi do not appear to be in isotopic equilibrium with phengite and garnet. Specifically, the carbonates show a $\delta^{18}O$ value of 16.0±0.1‰, whereas fractionation calculations between garnet and calcite (using a 4‰ fractionation factor) would suggest an expected carbonate value of 17-18‰. This indicates that garnet and phengite likely did not crystallize or re-crystallize from the same fluid involved in the carbonate vein formation at Achladi. Instead, the $\delta^{18}O$ values of the carbonates point to a different fluid end-member, similar to marbles reported by Barr (1989), but with slightly lower $\delta^{18}O$ and a similar $\delta^{13}C$ of 1.6±0.1‰ (Figure 4.16). This is consistent with a late-stage CO_2-rich fluid infiltration and channelized flow at the outcrop scale, as also hypothesized by Barr (1989). Similary Gyomlai et al. (2023) has shown that heterogeneous fluid fluxes could have occurred during exhumation. Moreover, these late-stage fluids likely circulated through surrounding lithologies composed of metabasites and marbles, as the $\delta^{18}O$ and $\delta^{13}C$ values of the carbonates from Achladi overlap with those of marbles and carbonate samples from metabasites (Figure 4.16).

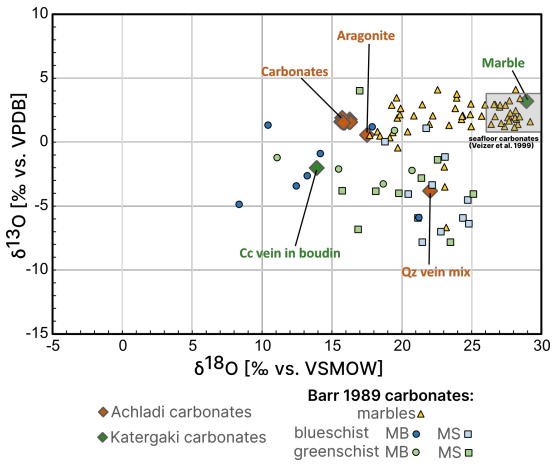

Figure 4.16: Isotope plot showing $\delta^{18}O$ vs. $\delta^{13}C$ of different carbonate samples. Gray field represents seafloor carbonates (Veizer et al., 1999). Carbonates samples from marbles, metabasalts (MB) and metasediments (MS) are from Barr (1989).

In **Katergaki** (blueschist, eclogite, and qz-phg schist samples), the relatively low $\delta^{18}O$ values of 8.3±0.6‰ in the blueschist represent the lowest recorded for metabasites on Syros. These values likely reflect the original $\delta^{18}O$ signature of seafloor-altered oceanic crust, as illustrated in Figure 4.15, and supported by other studies in the Cyclades (Ganor et al., 1996; George et al., 2024; Putlitz et al., 2000). This is further supported by the major and trace element signatures, which indicate seafloor alteration prior to subduction and subsequent garnet growth. Given that garnet inclusions (e.g., titanite) and thermodynamic modeling suggest early garnet growth in the blueschists, the modification of bulk rock $\delta^{18}O$ between seafloor alteration and garnet formation is likely to have been minimal. Interestingly, garnet rims in the same blueschist samples exhibit higher $\delta^{18}O$ values of

10.4±0.6‰ to 10.7±0.6‰, indicating a maximum increase of 2.1±0.8‰ from core to rim (corresponding to a minimum increase of 1.2‰). Petrochemical modeling predicts a 0.7‰ increase in blueschist $\delta^{18}O$ due to combined fractionation effects during a temperature rise, even accounting for early garnet growth below 400 °C, which is consistent with the commonly used value of ≤1‰ (Kohn, 1993; Vho, Lanari, Rubatto, & Hermann, 2020). Consequently, the measured increase from core to rim exceeds this simple closed-system fractionation effect, likely indicating that the bulk rock was modified in $\delta^{18}O$ during garnet growth. In contrast, eclogite samples from Katergaki show relatively homogeneous $\delta^{18}O$ values of 10-11‰. Despite the spatial proximity of blueschist, eclogite, and qz-phg schist rocks in Katergaki, which are linked on the meter-scale and expected to share a similar P-T metamorphic history, garnet in eclogites probably grew later during prograde metamorphism, at temperatures above 400 °C. This late growth was also previously outlined by Laurent et al. (2018). Interestingly, the major element composition and $\delta^{18}O$ values of garnet cores and mantles in the eclogites are similar to the $\delta^{18}O$ of blueschist garnet outer mantles confirming that the change should have occurred between 400 °C and garnet growth at 475 °C in the eclogite (Laurent et al., 2018). The geochemical similarity is marked by an annulus of spessartine increase and almandine decrease in the blueschist. Additionally, the increase in grossular content in eclogitic garnets is likely linked to the lawsonite-out reaction near peak pressure, which is also predicted by (Schumacher et al., 2008). The relatively high $\delta^{18}O$ values of 10-12‰ in garnet mantles and rims suggest that the bulk rock had already undergone $\delta^{18}O$ modification by this time.

In the qz-phg schist sample SY21-03, garnet cores display low $\delta^{18}O$ values of 8.9±0.5‰, similar to those found in the blueschist garnets, which likely formed from a protolith composed of mixed clastic and volcanic sediments (see protolith discussion). However, the significant increase of up to 2.4±0.7‰ from core to rim, reaching values of 11-13‰, likely reflects the modification of the bulk rock $\delta^{18}O$ during metamorphism and garnet growth. Petrochemical modeling suggests that the fractionation effects during temperature increase in a closed system cannot fully account for this variation, as only up to 1.4‰ can be modeled. Furthermore, phengite (re-)crystallization at Katergaki probably occurred close to or after peak pressure as indicated by the composition and thermodynamic modelling (e.g., Trotet et al., 2001), recording similarly high $\delta^{18}O$ values of 11-13‰.

In Ormos Lakkoi, the homogeneous $\delta^{18}O$ values of 4-6‰ in garnet from the metagabbro most likely reflect the protolith's original signature, which underwent hydrothermal seafloor alteration before subduction. The slight decrease in $\delta^{18}O$ at the garnet rim, reaching 4.1±0.7‰, correlates with resorption and recrystallization patterns in the garnet's major element composition. Nevertheless, this decrease does not clearly suggest any significant alteration of the bulk rock $\delta^{18}O$ by external processes. Neither any metasomatic alteration can be identified as it has been described around Kampos in the North of Syros (e.g.,

Bröcker & Enders, 2001; Cooperdock et al., 2018; Gyomlai et al., 2021; Marschall et al., 2006, 2008; D. P. Miller et al., 2009; Okrusch & Bröcker, 1990; Pogge von Strandmann et al., 2015; Ridley, 1984).

In summary, most of the $\delta^{18}O$ analyses in garnet, particularly in their cores, from Achladi, Katergaki, and Ormos Lakkoi suggest that the mafic rocks retained the $\delta^{18}O$ composition they acquired during hydrothermal seafloor alteration. This observation is consistent with the findings of Ganor et al. (1996) and Putlitz et al. (2000) for mafic rocks in the Cyclades. An exception to this pattern is observed in the blueschist and qz-phg schist samples from Katergaki, where geochemical zoning in garnet indicates a change in the bulk rock $\delta^{18}O$ composition during garnet growth. However, this modified composition remained stable after peak pressure, as indicated by the recrystallized phengite $\delta^{18}O$, which reflects the post-peak metamorphic history. For the Katergaki sequence, it is likely that an ^{18}O-enriched fluid in isotopic disequilibrium infiltrated the sequence, altering the bulk rock composition, as recorded in the garnet mantles and rims.

4.6.6 Fluid sources and flow in high-pressure metamorphic sequences

Lithologies on Syros that represent potential sources for a fluid with a $\delta^{18}O$ above 10‰ are the continental margin deposits (marbles and metasediments 10 to 30‰), serpentinites (5 to 9 ‰), and the altered mafic rocks (10 to 13‰) (see Figure 4.15). Continental margin deposits are not mapped in the vicinity to Katergaki and are represented by the Chroussa subunit that is thought to be tectonically separated from the studied Kampos subunit (Laurent et al., 2021). Therefore they are excluded as a possible fluid source for Katergaki but not for other localities.

Marbles are frequently occurring and typically exhibit relatively high $\delta^{18}O$ values, reaching up to 30‰, making them a potential source of fluids with elevated $\delta^{18}O$. Indeed it has been shown by glaucophane-marbles and the stability of lawsonite mineral assemblages that a water-rich fluid phase with a low CO_2 activity was present during metamorphism (Schumacher et al., 2008). Similar has been showed by the inclusion study in metamafic rocks of Barr (1989) on the outcrop of Achladi and surrounding lithologies, which suggest a water-rich and CO_2 poor fluid. Additionally, if a fluid derived from marbles had infiltrated Katergaki, it would be expected that calcite veins would exhibit $\delta^{18}O$ and $\delta^{13}C$ values similar to those of the marbles. However, this is not the case, as the $\delta^{13}C$ values of calcite in eclogites from Katergaki are approximately 5‰ lower than those of marbles from the Katergaki cape. Rather, the marbles exhibit units with a low permeability as described for Naxos (Etheridge et al., 1983), and might even have been fluid barriers, which helped to preserve blueschist rocks on Syros during metamorphism (Matthews & Schliestedt, 1984). Consequently, a fluid derived from marbles as the infiltrating agent at Katergaki is excluded,

although it is not necessarily eliminated as a candidate in other locations.

Serpentinites are an important fluid source during prograde metamorphism as they produce a significant amount of aqueous fluids when brucite and/or antigorite break down and olivine forms (e.g., Kempf et al., 2020; Ulmer & Trommsdorff, 1999; Ulrich et al., 2024). The measured bulk $\delta^{18}O$ values in serpentinites on Syros are up to 9‰ and could generate a fluid with maximum $\delta^{18}O$ values of 10‰ to 12‰. Commonly serpentinites are found surrounding metagabbros or in the close vicinity to metasediments within the Kampos unit such as in the North of Syros (e.g., Bröcker & Enders, 2001; Cooperdock et al., 2018; Gyomlai et al., 2021; Marschall et al., 2006, 2008; Okrusch & Bröcker, 1990; Pogge von Strandmann et al., 2015; Ridley, 1984). Metasomatic rinds are represented as meter-sized reaction zones at the contacts between metasedimentary blueschists and ultramafics indicating intensive fluid fluxing (e.g., Ague, 2007; Breeding et al., 2004; Gyomlai et al., 2021; D. P. Miller et al., 2009). The serpentinites on Syros show no indication of major dehydration at high pressure conditions, because antigorite still stable at these conditons (e.g., Kempf et al., 2020; D. P. Miller et al., 2009; Padrón-Navarta et al., 2013) and the major anhydrous reaction product olivine (e.g., Ulrich et al., 2024) was not reported. The same conclusion can be reached for metagabbro at Ormos Lakkoi as there is no $\delta^{18}O$ change during garnet growth that could support metasomatism as observed in the interiors of knockers in the North of Syros (Ague, 2007). Neither metasomatic alterations textures are observed at Achladi or Katergaki besides the greenschist overprint which is linked to exhumation and does not correlate with garnet growth. Consequently, the serpentinites are an unlikely fluid source even though they have been shown to be important in other localities such as in the Zermatt-Saas zone in the Alps (e.g., Bovay et al., 2021; Rubatto et al., 2023).

Mafic rocks, are in the closest relationship to the analyzed sequence at Katergaki. Blueschists, eclogites, and epidote blueschists representing the mafic rocks from the seafloor altered oceanic crust show a thickness of several 10 to 100 meters and are intercalated with several 10 meter thick layers of qz-phg schist (see Figure 4.2). Dehydrating mafics rocks have recently been identified to be responsible for changes in the oxygen isotope composition at the Lago di Cignana ultra HP unit in the Alps (Rubatto et al., 2023). Therefore the altered oceanic crust found at Achladi and Katergaki can be a viable source for fluids as a mafic $\delta^{18}O$ bulk rock composition of 10 to 13‰ could release a fluid of 11 to 14‰ (using a rock-fluid fractionation of +1‰, see Figure 4.13a,b). In addition, the associated qz-phg schist at Katergaki with a $\delta^{18}O$ of 12-13‰ could also contribute a fluid of 11-12‰ (using a rock-fluid fractionation of -1‰ , see Figure 4.13c).

To test the hypothesis that fluids from dehydrating mafic rocks could have modified the qz-phg schist, blueschist, and eclogite signatures at Katergaki, a multi-rock model

was designed based on the observed outcrop relationships. Calculations were performed using the ThorPT software (Markmann & Lanari, 2024, under review) and the modelling scenario is shown in Figure 4.17a based on Figure 4.14. As mafic rocks are surrounding the sampled sequence at Katergaki, in the model a stack of mafic rocks represented by an alternation of blueschists and eclogites is situated below the boudin in qz-phg schist sequence. Measurements and rocks from Achladi are taken to be representative for the mafic stack. Volumes and size dimensions are taken from the outcrop observations and description (see Petrology and petrography). Therefore, the full modelling sequence is consisting of (i) the top part, which is represented by the mafic boudin at Katergaki using the blueschist (SY21-01/2-1) as core and eclogite as rind (SY21-01/2-2). Each have a volume of 0.5 m^3 and are assumed to start with a bulk rock $\delta^{18}O$ of 10‰ (garnet will start at ∼8‰). This is followed by (ii) the qz-phg schist (SY21-03) with a layer thickness of 150 m^3 and a bulk rock $\delta^{18}O$ of 13‰ (garnet will also start at ∼8‰). The sequence corresponding to Katergako is on top of (iii) the stack of mafics alteranting between blueschist and eclogites corresponding to Achladi. The volume is estimated to 7200 m^3 based on the outcrop dimensions (12 m in height, 30 m in width, and 20 m in depth, see Figure 4.2). The eclogite is more abundant than the blueschist, and thus the model is simplified to five thinner layers of blueschist (0.5x35x20 m^3, SY21-07) and four thicker layers of eclogite (2.5x35x20 m^3, SY21-05-1). The initial bulk rock $\delta^{18}O$ value for these eclogites and blueschists was established at 12‰, which is between the lower values for metabasalts from Putlitz et al. (2000) and the slightly higher values measured at Achladi interfered from the garnet showing ∼11‰.

The multi-rock modeling results in Figure 4.17b-c show several major fluid infiltration events that infiltrate the Katergaki boudin sequence between 400 °C and peak conditions. The volume of fluid ranges between ∼25 m^3 and ∼180 m^3 with a $\delta^{18}O$ of ∼12‰ at the beginning and ∼13‰ at the end. The increase in the $\delta^{18}O$ of the fluid is due to the fractionation effect during increasing temperature but also buffered by the interaction with the qz-phg schist. The mafic boudin of Katergaki respond to the fluid infiltration and the bulk rock shows an increase from 10‰ at the beginning to ∼12‰ at the end. Similarly, garnet starts with a $\delta^{18}O$ of ∼8‰ in the blueschist, eclogite, and qz-phg schist and ends with a value of ∼10‰. This result is similar to the measured values in the garnet cores to rims in the analysed blueschists, eclogite, and qz-phg schist from Katergaki. The results in Figure 4.17c shows that the main dehydrating reactions in the mafic sequence at the bottom of the model are the chlorite and lawsonite dehydration indicated by the decreasing abundance of the two mineral phases in the model. Nevertheless, the blueschist layers stabilize glaucophane towards higher P–T conditions. Lawsonite was predicted to be stable in the qz-phg schist during fluid infiltration and is completely breaking down before peak P–T conditions, whereas glaucophane is still predicted to be stable in this lithology.

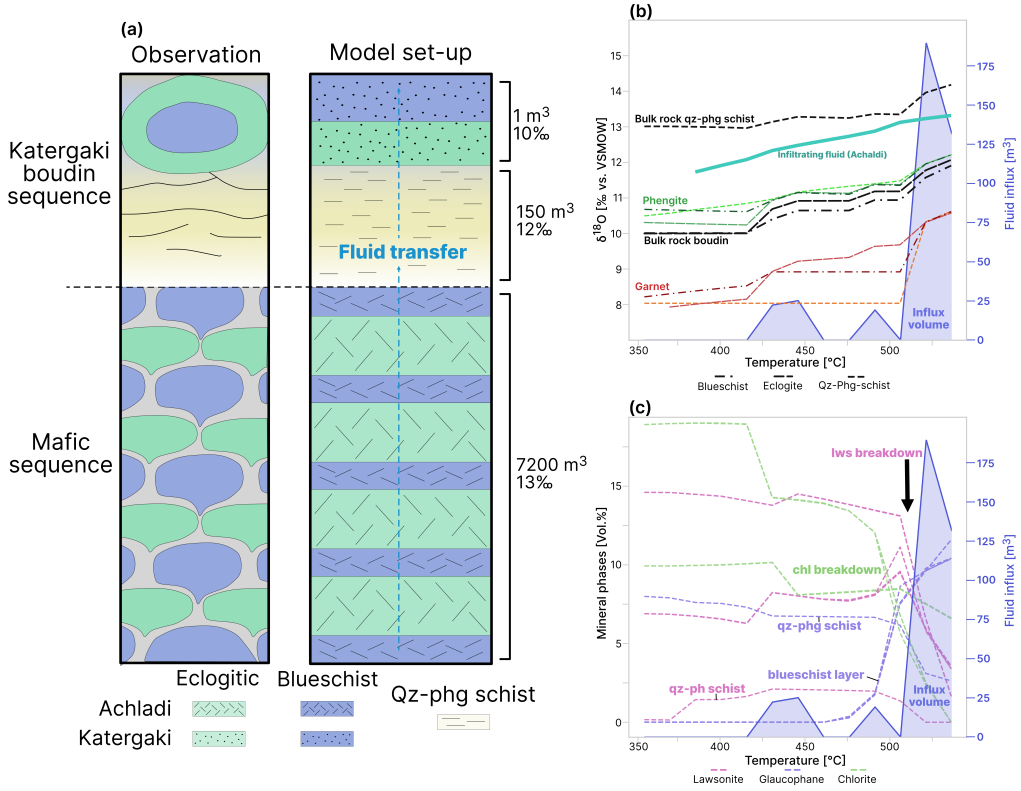

Figure 4.17: Modeling scenario and results of the fluid transfer model. (a) Depiction of the outcrop observations and modeling scenario. The upper part represents the sequence at Katergaki where boudins are wrapped in the qz-phg schist. The lower part represents the surrounding mafic sequence. Each rock layer represents one rock model in the multi-rock model scenario. Released free fluid migrates top-wards in the modeling column and will interact with each penetrated unit. (b) Oxygen isotope evolution of the bulk, garnet, and phengite for the Katergaki sequence (blueschist, eclogite, and qz-phg schist) on the left y-axis. The infiltrating volume of fluid is shown as a polygon with the scale one the right y-axis. The $\delta^{18}O$ value of the fluid infiltrating the Katergaki boudin sequence is shown in blue. (c) Abundance of hydrous phases in the mafic boudin sequence and the qz-phg schist. The infiltrating fluid volume is given as a reference.

4.7 Conclusion

The sampling of subducted oceanic crust on Syros, including metagabbro, pillow basalts, and intercalated mafic-siliciclastic sediments, has revealed distinct fluid-rock interaction histories across the outcrops of Achladi, Katergaki, and Ormos Lakkoi, as summarized in Figure 4.18. These rocks record multiple episodes of fluid-rock interaction, spanning from seafloor alteration to subsequent burial. This complex history has been reconstructed through in-situ oxygen isotope analyses of garnet and phengite, combined with major element mapping. Garnet cores in the metagabbro and metabasalts preserve oxygen isotope signatures inherited from hydrothermal seafloor alteration, resembling modern oceanic crust. These pre-subduction signatures align with similar findings from rocks on Tinos, Sifnos, and Syros, as shown in Figure 4.15.

The stack of metapillows at Achladi represents the upper part of the oceanic crust, characterized by low-temperature seafloor alteration, with $\delta^{18}O$ values of 11-13‰ in garnet (Figure 4.18, step I). Despite evidence of metasomatism on Syros (especially in the North of the island), the relatively homogeneous isotope values recorded during garnet growth suggest no significant fluid infiltration during prograde metamorphism in this sequence. Alternatively a fluid with a similar $\delta^{18}O$ could have infiltrated the sequence, but would not be possible to distinguish. A similar observation is also made in the metagabbro at Ormos Lakkoi, where $\delta^{18}O$ values of ∼5‰ in garnet reflect seafloor alteration, with no change during subsequent garnet growth. The presence of a chlorite-talc shell, along with garnet resorption and replacement by chlorite, indicates interaction with serpentinites (Figure 4.18, step III). The $\delta^{18}O$ values of serpentinites (5-9‰, Cooperdock et al., 2018) around Ormos Lakkoi indicate fluid interaction, though the absence of metamorphic olivine suggests limited dehydration, as documented in similar settings such as the Alps (Ulrich et al., 2024). However, talc and chlorite formation from antigorite, likely due to the introduction of SiO_2, may have triggered late-stage fluid production (D. P. Miller et al., 2009).

The Katergaki sequence, consisting of metapillows intercalated with quartz-phengite schists, also preserves seafloor alteration signatures, with lower $\delta^{18}O$ values (8-11‰) in garnet. This likely represents a deeper part of the oceanic crust, consistent with known profiles of altered oceanic crust (e.g., Eiler, 2001; Gregory et al., 1989; Muehlenbachs & Clayton, 1972). During subduction, garnet rims in blueschist and quartz-phengite schists at Katergaki show higher $\delta^{18}O$ values (10-12‰), indicating pervasive fluid infiltration not observed in other outcrops (Figure 4.18, step II and III). This isotopic increase is attributed to the influx of a heavier fluid (∼12-13‰), likely mafic-derived, as supported by a multi-rock fluid transfer model built from outcrop observations. Additionally, phengite recrystallization during or shortly after peak metamorphism is marked by $\delta^{18}O$ values of

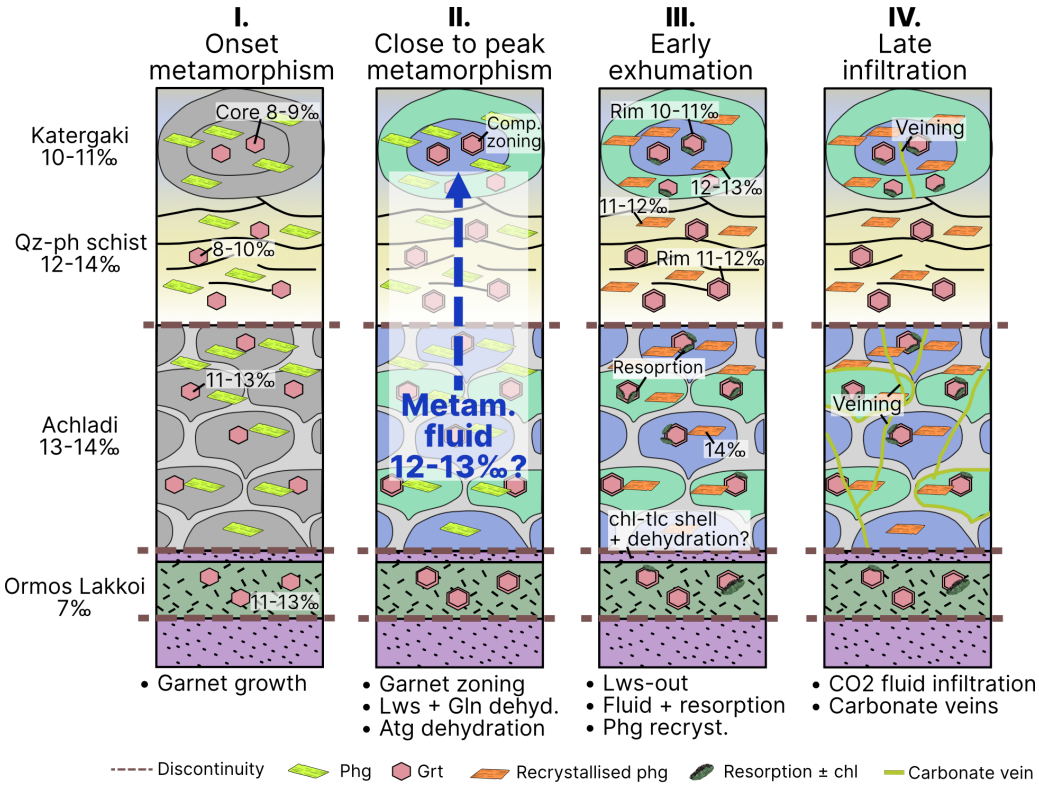

Figure 4.18: Summarizing sketch of the studied outcrops and their evolution during regional metamorphism. I.) Starting $\delta^{18}O$ values of the subducted pieces of the ophiolithe sequence and first values inherit in the garnet. II.) The potential metamorphic fluid production and transfer modifying the infiltrated units. III.) Changed $\delta^{18}O$ values of garnet and recrystallised phengite. This is followed by dehydration such as the lawsonite-out, which triggers resorption of garnet and chlorite production during exhumation. IV.) Infiltration of a late stage fluid responsible for the carbonate veining at Achladi and Katergaki.

11-13‰.

Veining and cross-cutting carbonates at Achladi and Katergaki, with $\delta^{18}O$ values of 16‰ and 14‰ and $\delta^{13}C$ values of 2‰ and -2‰, respectively, indicate a later fluid infiltration event involving CO_2-rich fluids, likely occurring during exhumation after blueschist-eclogite metamorphism (Figure 4.18, step IV).

Although not explored in detail, petrochemical modeling suggests that lithological sequences play a crucial role in recycling infiltrating fluids by stabilizing new hydrous phases, such as lawsonite, which is a key carrier of fluids in subducting crust. This process may significantly influence fluid redistribution during prograde metamorphism and the transport of fluids within subduction zones.

Bibliography

Ague, J. J. (2007). Models of permeability contrasts in subduction zone mélange: Implications for gradients in fluid fluxes, Syros and Tinos Islands, Greece. *Chemical Geology*, *239*(3-4), 217–227. https://doi.org/10.1016/j.chemgeo.2006.08.012

Ague, J. J., & Nicolescu, S. (2014). Carbon dioxide released from subduction zones by fluid-mediated reactions. *Nature Geoscience*, *7*(5), 355–360. https://doi.org/10.1038/ngeo2143

Alt, J. C., Muehlenbachs, K., Honnorez, J., Letters, P. S., Honnorez, J., Scwnces, P., Unwerstty, W., Louts, S., & Scwnce, A. (1986). An oxygen isotopic profile through the upper kilometer of the oceanic crust, DSDP Hole 504B. *Earth and Planetary Science Letters*, *80*(3), 217–229. https://doi.org/https://doi.org/10.1016/0012-821X(86)90106-8

Austrheim, H. (1987). Eclogitization of lower crustal granulites by fluid migration through shear zones. *Earth and Planetary Science Letters*, *81*(2-3), 221–232. https://doi.org/10.1016/0012-821X(87)90158-0

Barnes, C. J., Zack, T., Bukała, M., Rösel, D., Mark, C., & Schneider, D. A. (2024). Dating metamorphic processes and identifying 87Sr/86Sr inheritance using volume-coupled Rb/Sr geochronology and geochemistry of in situ white mica: A demonstration with HP/LT rocks from Syros, Greece. *Chemical Geology*, *660*(January), 122149. https://doi.org/10.1016/j.chemgeo.2024.122149

Barr. (1989). *Fluid-rock interactions during blueschist and greenschist metamorphism in the Aegean area of Greece Hazel Mary Barr Thesis submitted for the degree of Doctor of Philosophy Edinburgh University* [Doctoral dissertation, The University of Edinburgh].

Baumgartner, L. P., & Valley, J. W. (2001). Stable Isotope Transport and Contact Metamorphic Fluid Flow. *Reviews in Mineralogy and Geochemistry*, *43*(1), 415–467. https://doi.org/10.2138/gsrmg.43.1.415

Baxter, E. F., & Caddick, M. J. (2013). Garnet growth as a proxy for progressive subduction zone dehydration. *Geology*, *41*(6), 643–646. https://doi.org/10.1130/G34004.1

Bebout, G. E. (2014). Chemical and Isotopic Cycling in Subduction Zones. In *Treatise on geochemistry* (2nd ed., pp. 703–747, Vol. 15). Elsevier. https://doi.org/10.1016/B978-0-08-095975-7.00322-3

Bebout, G. E., & Penniston-Dorland, S. C. (2016). Fluid and mass transfer at subduction interfaces-The field metamorphic record. *Lithos*, *240-243*, 228–258. https://doi.org/10.1016/j.lithos.2015.10.007

Bloor, P. M. (1998). Genesis and distribution of Ca-Al Silicates in Aegean blueschists and implications for fluid flow in subduction zones. https://era.ed.ac.uk/handle/1842/10830

Bonneau, M. (1984). Correlation of the Hellenide nappes in the south-east Aegean and their tectonic reconstruction. *Geological Society, London, Special Publications*, *17*(1), 517–527. https://doi.org/10.1144/GSL.SP.1984.017.01.38

Bonneau, M., & Kienast, J. R. (1982). Subduction, collision et schistes bleus; l'exemple de l'Egee (Grece). *Bulletin de la Société Géologique de France*, *S7-XXIV*(4), 785–791. https://doi.org/10.2113/gssgfbull.S7-XXIV.4.785

Bovay, T., Lanari, P., Rubatto, D., Smit, M., & Piccoli, F. (2022). Pressure–temperature–time evolution of subducted crust revealed by complex garnet zoning (Theodul Glacier Unit, Switzerland). *Journal of Metamorphic Geology*, *40*(2), 175–206. https://doi.org/10.1111/jmg.12623

Bovay, T., Rubatto, D., & Lanari, P. (2021). Pervasive fluid-rock interaction in subducted oceanic crust revealed by oxygen isotope zoning in garnet. *Contributions to Mineralogy and Petrology*, *176*(7), 1–22. https://doi.org/10.1007/s00410-021-01806-4

Breeding, C. M., Ague, J. J., & Bröcker, M. (2004). Fluid-metasedimentary rock interactions in subduction-zone mé lange: Implications for the chemical composition of arc magmas. *Geology*, *32*(12), 1041–1044. https://doi.org/10.1130/G20877.1

Bröcker, M., & Keasling, A. (2006). Ionprobe U-Pb zircon ages from the high-pressure/low-temperature mélange of Syros, Greece: age diversity and the importance of pre-Eocene subduction. *Journal of Metamorphic Geology*, *24*(7), 615–631. https://doi.org/10.1111/j.1525-1314.2006.00658.x

Bröcker, M., & Enders, M. (1999). U-Pb zircon geochronology of unusual eclogite-facies rocks from Syros and Tinos (Cyclades, Greece). *Geological Magazine*, *136*(2), 111–118. https://doi.org/10.1017/S0016756899002320

Bröcker, M., & Enders, M. (2001). Unusual bulk-rock compositions in eclogite-facies rocks from Syros and Tinos (Cyclades, Greece): Implications for U-Pb zircon geochronology. *Chemical Geology*, *175*(3-4), 581–603. https://doi.org/10.1016/S0009-2541(00)00369-7

Caddick, M. J., Konopásek, J., & Thompson, A. B. (2010). Preservation of garnet growth zoning and the duration of prograde metamorphism. *Journal of Petrology*, *51*(11), 2327–2347. https://doi.org/10.1093/petrology/egq059

Cliff, R. A., Bond, C. E., Butler, R. W., & Dixon, J. E. (2017). Geochronological challenges posed by continuously developing tectonometamorphic systems: insights from Rb–Sr mica ages from the Cycladic Blueschist Belt, Syros (Greece). *Journal of Metamorphic Geology*, *35*(2), 197–211. https://doi.org/10.1111/jmg.12228

Compagnoni, R., Hirajima, T., & Chopin, C. (1995). Ultra-high-pressure metamorphic rocks in the Western Alps. In R. G. Coleman & X. Wang (Eds.), *Ultrahigh pressure metamorphism* (pp. 206–243). Cambridge University Press.

Cooperdock, E. H., Raia, N. H., Barnes, J. D., Stockli, D. F., & Schwarzenbach, E. M. (2018). Tectonic origin of serpentinites on Syros, Greece: Geochemical signatures of abyssal origin preserved in a HP/LT subduction complex. *Lithos*, *296-299*, 352–364. https://doi.org/10.1016/j.lithos.2017.10.020

Cotta, A. J. B., Enzweiler, J., Wilson, S. A., Pérez, C. A., Nardy, A. J. R., Larizzatti, J. H., Nard, A. J. R., & Larizzatti, J. H. (2007). Homogeneity of the Geochemical Reference Material BRP-1 (Paraná Basin Basalt) and Assessment of Minimum Mass. *Geostandards and Geoanalytical Research*, *31*(4), 379–393. https://doi.org/https://doi.org/10.1111/j.1751-908X.2007.00111.x

de Capitani, C., & Brown, T. H. (1987). The computation of chemical equilibrium in complex systems containing non-ideal solutions. *Geochimica et Cosmochimica Acta*, *51*(10), 2639–2652. https://doi.org/10.1016/0016-7037(87)90145-1

de Capitani, C., & Petrakakis, K. (2010). The computation of equilibrium assemblage diagrams with Theriak/Domino software. *American Mineralogist*, *95*(7), 1006–1016. https://doi.org/10.2138/am.2010.3354

Dragovic, B., Baxter, E. F., & Caddick, M. J. (2015). Pulsed dehydration and garnet growth during subduction revealed by zoned garnet geochronology and thermodynamic modeling, Sifnos, Greece. *Earth and Planetary Science Letters*, *413*, 111–122. https://doi.org/10.1016/j.epsl.2014.12.024

Eiler, J. M. (2000). Oxygen Isotope Geochemistry of Oceanic-Arc Lavas. *Journal of Petrology*, *41*(2), 229–256. https://doi.org/10.1093/petrology/41.2.229

Eiler, J. M. (2001, December). 5. Oxygen Isotope Variations of Basaltic Lavas and Upper Mantle Rocks. In *Stable isotope geochemistry* (pp. 319–364, Vol. 43). De Gruyter. https://doi.org/10.1515/9781501508745-008

Etheridge, M. A., Wall, V. J., & Vernon, R. H. (1983). The role of the fluid phase during regional metamorphism and deformation. *Journal of Metamorphic Geology*, *1*(3), 205–226. https://doi.org/10.1111/j.1525-1314.1983.tb00272.x

Ferriere, J., Jolivet, L., & Chanier, F. (2024). From subduction to collision and subduction again, the drivers of crustal-scale deformation in the Hellenides-Aegean region. *Comptes Rendus. Géoscience*, *356*(S2), 163–205. https://doi.org/10.5802/crgeos.238

François, C., Debaille, V., Paquette, J. L., Baudet, D., & Javaux, E. J. (2018). The earliest evidence for modern-style plate tectonics recorded by HP–LT metamorphism in the Paleoproterozoic of the Democratic Republic of the Congo. *Scientific Reports*, *8*(1), 1–10. https://doi.org/10.1038/s41598-018-33823-y

Gale, A., Dalton, C. A., Langmuir, C. H., Su, Y., & Schilling, J.-G. (2013). The mean composition of ocean ridge basalts. *Geochemistry, Geophysics, Geosystems*, *14*(3), 489–518. https://doi.org/10.1029/2012GC004334

Ganor, J., Matthews, A., Schliestedt, M., & Garfunkel, Z. (1996). Oxygen isotopic heterogeneities of metamorphic rocks: an original tectonostratigraphic signature, or an imprint of exotic fluids? A case study of Sifnos and Tinos islands (Greece). *European Journal of Mineralogy*, *8*(4), 719–732. https://doi.org/10.1127/ejm/8/4/0719

George, F. R., Viete, D. R., Ávila, J., Seward, G. G., Guice, G. L., Allen, M. B., & Harrower, M. J. (2024). Garnet zoning patterns record multiple processes of chemical transfer during subduction. *Earth and Planetary Science Letters*, *631*(March), 118634. https://doi.org/10.1016/j.epsl.2024.118634

Gerogiannis, N., Aravadinou, E., & Xypolias, P. (2024). Deformation Pattern of Well-Preserved High-Pressure Rocks (SE Syros, Cyclades). *Geosciences (Switzerland)*, *14*(1). https://doi.org/10.3390/geosciences14010011

Gerya, T. V., Stöckhert, B., & Perchuk, A. L. (2002). Exhumation of high-pressure metamorphic rocks in a subduction channel: A numerical simulation. *Tectonics*, *21*(6), 6–1. https://doi.org/10.1029/2002TC001406

Giuntoli, F., Lanari, P., & Engi, M. (2018). Deeply subducted continental fragments – Part 1: Fracturing, dissolution–precipitation, and diffusion processes recorded by garnet textures of the central Sesia Zone (western Italian Alps). *Solid Earth*, *9*(1), 167–189. https://doi.org/10.5194/se-9-167-2018

Gorce, J. S., Caddick, M. J., Baxter, E. F., Dragovic, B., Schumacher, J. C., Bodnar, R. J., & Kendall, J. F. (2021). Insight Into the Early Exhumation of the Cycladic Blueschist Unit, Syros, Greece: Combined Application of Zoned Garnet Geochronology, Thermodynamic Modeling, and Quartz Elastic Barometry. *Geochemistry, Geophysics, Geosystems*, *22*(8), 1–24. https://doi.org/10.1029/2021GC009716

Gregory, R. T., Criss, R. E., & Taylor, H. P. (1989). Oxygen isotope exchange kinetics of mineral pairs in closed and open systems: Applications to problems of hydrothermal alteration of igneous rocks and Precambrian iron formations. *Chemical Geology*, *75*(1-2), 1–42. https://doi.org/10.1016/0009-2541(89)90019-3

Gregory, R. T., & Taylor, H. P. (1981). An oxygen isotope profile in a section of Cretaceous oceanic crust, Samail Ophiolite, Oman: Evidence for δ 18 O buffering of the oceans by deep (¿5 km) seawater-hydrothermal circulation at mid-ocean ridges. *Journal of Geophysical Research: Solid Earth*, *86*(B4), 2737–2755. https://doi.org/10.1029/jb086ib04p02737

Guillong, M., Meier, D. L., Allan, M. M., Heinrich, C. A., & Yardley, B. W. D. (2008). SILLS: A Matlab-Based Program for the Reduction of Laser Ablation ICP–MS Data

of Homogeneous Materials and Inclusions. *Mineralogical Association of Canada Short Course*, *40*, 328–333.

Gyomlai, T., Agard, P., Marschall, H. R., & Jolivet, L. (2023). Hygrochronometry of punctuated metasomatic events during exhumation of the Cycladic blueschist unit (Syros, Greece). *Terra Nova*, *35*(2), 101–112. https://doi.org/10.1111/ter.12634

Gyomlai, T., Agard, P., Marschall, H. R., Jolivet, L., & Gerdes, A. (2021). Lithos Metasomatism and deformation of block-in-matrix structures in Syros : The role of inheritance and fl uid-rock interactions along the subduction interface. *LITHOS*, *386-387*, 105996. https://doi.org/10.1016/j.lithos.2021.105996

Halama, R., Glodny, J., Konrad-Schmolke, M., & Sudo, M. (2018). Rb-Sr and in situ 40Ar/39Ar dating of exhumation-related shearing and fluid-induced recrystallization in the Sesia zone (Western Alps, Italy). *Geosphere*, *14*(4), 1425–1450. https://doi.org/10.1130/GES01521.1

Hermann, J., Müntener, O., & Scambelluri, M. (2000). The importance of serpentinite mylonites for subduction and exhumation of oceanic crust. *Tectonophysics*, *327*(3-4), 225–238. https://doi.org/10.1016/S0040-1951(00)00171-2

Hermann, J., Spandler, C., Hack, A., & Korsakov, A. V. (2006). Aqueous fluids and hydrous melts in high-pressure and ultra-high pressure rocks: Implications for element transfer in subduction zones. *Lithos*, *92*(3-4), 399–417. https://doi.org/10.1016/j.lithos.2006.03.055

Huet, B., Labrousse, L., Monié, P., Malvoisin, B., & Jolivet, L. (2015). Coupled phengite 40Ar-39Ar geochronology and thermobarometry: P-T-t evolution of Andros Island (Cyclades, Greece). *Geological Magazine*, *152*(4), 711–727. https://doi.org/10.1017/S0016756814000661

Ito, E., & Clayton, R. N. (1983). Submarine metamorphism of gabbros from the Mid-Cayman rise: An oxygen isotopic study. *Geochimica et Cosmochimica Acta*, *47*(3), 535–546. https://doi.org/10.1016/0016-7037(83)90276-4

Ito, E., White, W. M., & Göpel, C. (1987). The O, Sr, Nd and Pb isotope geochemistry of MORB. *Chemical Geology*, *62*(3-4), 157–176. https://doi.org/10.1016/0009-2541(87)90083-0

Jochum, K. P., Weis, U., Stoll, B., Kuzmin, D., Yang, Q., Raczek, I., Jacob, D. E., Stracke, A., Birbaum, K., Frick, D. A., Günther, D., & Enzweiler, J. (2011). Determination of Reference Values for NIST SRM 610-617 Glasses Following ISO Guidelines. *Geostandards and Geoanalytical Research*, *35*(4), 397–429. https://doi.org/10.1111/j.1751-908X.2011.00120.x

Jolivet, L., Menant, A., Sternai, P., Rabillard, A., Arbaret, L., Augier, R., Laurent, V., Beaudoin, A., Grasemann, B., Huet, B., Labrousse, L., & Le Pourhiet, L. (2015).

The geological signature of a slab tear below the Aegean. *Tectonophysics*, *659*, 166–182. https://doi.org/10.1016/j.tecto.2015.08.004

Kang, P., Martin, L. A., Vitale Brovarone, A., & Whitney, D. L. (2024). Lawsonite and Garnet Oxygen Isotope Record of Fluid-Rock Interaction During Subduction. *Geochemistry, Geophysics, Geosystems*, *25*(4), 1–32. https://doi.org/10.1029/2023GC011389

Katzir, Y., Matthews, A., Garfunkel, Z., Schliestedt, M., & Avigad, D. (1996). The tectono-metamorphic evolution of a dismembered ophiolite (Tinos, Cyclades, Greece). *Geological Magazine*, *133*(3), 237–254. https://doi.org/10.1017/S0016756800008992

Keiter, M., Ballhaus, C., & Tomaschek, F. (2011). A new geological map of the Island of Syros (Aegean Sea, Greece): Implications for lithostratigraphy and structural history of the Cycladic Blueschist Unit. In *A new geological map of the island of syros (aegean sea, greece): Implications for lithostratigraphy and structural history of the cycladic blueschist unit* (pp. 1–43, Vol. 481). Geological Society of America. https://doi.org/10.1130/2011.2481

Kempf, E. D., Hermann, J., Reusser, E., Baumgartner, L. P., & Lanari, P. (2020). The role of the antigorite + brucite to olivine reaction in subducted serpentinites (Zermatt, Switzerland). *Swiss Journal of Geosciences*, *113*(1). https://doi.org/10.1186/s00015-020-00368-0

Kohn, M. J. (1993). Modeling of prograde mineral δ18O changes in metamorphic systems. *Contributions to Mineralogy and Petrology*, *113*(2), 249–261. https://doi.org/10.1007/BF00283232

Kohn, M. J. (2004). Oscillatory- and sector-zoned garnets record cyclic (?) rapid thrusting in central Nepal. *Geochemistry, Geophysics, Geosystems*, *5*(12), 1–9. https://doi.org/10.1029/2004GC000737

Konrad-Schmolke, M., Babtist, J., Handy, M. R., & O'Brien, P. J. (2006). The Physico-Chemical Properties of a Subducted Slab from Garnet Zonation Patterns (Sesia Zone, Western Alps). *Journal of Petrology*, *47*(11), 2123–2148. https://doi.org/10.1093/petrology/egl039

Konrad-Schmolke, M., Halama, R., Chew, D., Heuzé, C., De Hoog, J. C. M., & Ditterova, H. (2023). Discrimination of thermodynamic and kinetic contributions to the heavy rare earth element patterns in metamorphic garnet. *Journal of Metamorphic Geology*, *41*(4), 465–490. https://doi.org/10.1111/jmg.12703

Konrad-Schmolke, M., O'Brien, P. J., de Capitani, C., & Carswell, D. A. (2008). Garnet growth at high- and ultra-high pressure conditions and the effect of element fractionation on mineral modes and composition. *Lithos*, *103*(3-4), 309–332. https://doi.org/10.1016/j.lithos.2007.10.007

Konrad-Schmolke, M., Zack, T., O'Brien, P. J., & Barth, M. (2011). Fluid migration above a subducted slab - Thermodynamic and trace element modelling of fluid-rock in-

teraction in partially overprinted eclogite-facies rocks (Sesia Zone, Western Alps). *Earth and Planetary Science Letters*, *311*(3-4), 287–298. https://doi.org/10.1016/j.epsl.2011.09.025

Lagos, M., Münker, C., Tomaschek, F., & Ballhaus, C. (2002). Geochemistry and Lu—Hf-geochronology of the metavolcanic Grizzas sequence in northern Syros (Cyclades, Greece). *Beihefte zum European Journal of Mineralogy*, *14*(1), 97.

Lagos, M., Scherer, E. E., Tomaschek, F., Münker, C., Keiter, M., Berndt, J., & Ballhaus, C. (2007). High precision Lu–Hf geochronology of Eocene eclogite-facies rocks from Syros, Cyclades, Greece. *Chemical Geology*, *243*(1-2), 16–35. https://doi.org/10.1016/j.chemgeo.2007.04.008

Lanari, P., & Engi, M. (2017). Local Bulk Composition Effects on Metamorphic Mineral Assemblages. *Reviews in Mineralogy and Geochemistry*, *83*(1), 55–102. https://doi.org/10.2138/rmg.2017.83.3

Lanari, P., Markmann, T., Laughton, J., & Tedeschi, M. (2023). xmaptools/XMapTools_Public: XMapTools 4.2. https://doi.org/10.5281/zenodo.7656957

Lanari, P., Vho, A., Bovay, T., Airaghi, L., & Centrella, S. (2019). Quantitative compositional mapping of mineral phases by electron probe micro-analyser. *Geological Society, London, Special Publications*, *478*(1), 39–63. https://doi.org/10.1144/SP478.4

Lanari, P., Vidal, O., De Andrade, V., Dubacq, B., Lewin, E., Grosch, E. G., & Schwartz, S. (2014). XMapTools: A MATLAB©-based program for electron microprobe X-ray image processing and geothermobarometry. *Computers and Geosciences*, *62*, 227–240. https://doi.org/10.1016/j.cageo.2013.08.010

Laurent, V., Jolivet, L., Roche, V., Augier, R., Scaillet, S., & Cardello, G. L. (2016). Strain localization in a fossilized subduction channel: Insights from the Cycladic Blueschist Unit (Syros, Greece). *Tectonophysics*, *672-673*, 150–169. https://doi.org/10.1016/j.tecto.2016.01.036

Laurent, V., Lanari, P., Naïr, I., Augier, R., Lahfid, A., & Jolivet, L. (2018). Exhumation of eclogite and blueschist (Cyclades, Greece): Pressure-temperature evolution determined by thermobarometry and garnet equilibrium modelling. *Journal of Metamorphic Geology*, *36*(6), 769–798. https://doi.org/10.1111/jmg.12309

Laurent, V., Scaillet, S., Jolivet, L., Augier, R., & Roche, V. (2021). 40Ar behaviour and exhumation dynamics in a subduction channel from multi-scale 40Ar/39Ar systematics in phengite. *Geochimica et Cosmochimica Acta*, *311*, 141–173. https://doi.org/10.1016/j.gca.2021.06.001

Luisier, C., Baumgartner, L., Siron, G., Vennemann, T., & Robyr, M. (2019). H2O Content Measurement in Phengite by Secondary Ion Mass Spectrometry: A New Set of Reference Materials. *Geostandards and Geoanalytical Research*, *43*(4), 635–646. https://doi.org/10.1111/ggr.12287

Luisier, C., Baumgartner, L. P., Bouvier, A.-S., & Putlitz, B. (2022). Interplay between fluid circulation and Alpine metamorphism in the Monte Rosa whiteschist from white mica and quartz in situ oxygen isotope analysis by SIMS. *American Mineralogist*, *107*(5), 860–872. https://doi.org/10.2138/am-2020-7523

Mahar, E. M., Baker, J. M., Powell, R., Holland, T. J. B., & Howell, N. (1997). The effect of Mn on mineral stability in metapelites. *Journal of Metamorphic Geology*, *15*(2), 223–238. https://doi.org/10.1111/j.1525-1314.1997.00011.x

Maluski, H., Bonneau, M., & Kienast, J. R. (1987). Dating the metamorphic events in the Cycladic area; \\¡sup\\¿39\\¡/sup\\¿ Ar/ \\¡sup\\¿40\\¡/sup\\¿ Ar data from metamorphic rocks of the Island of Syros (Greece). *Bulletin de la Société Géologique de France*, *3*(5), 833–842. https://doi.org/10.2113/gssgfbull.III.5.833

Manatschal, G., & Müntener, O. (2009). A type sequence across an ancient magma-poor ocean–continent transition: the example of the western Alpine Tethys ophiolites. *Tectonophysics*, *473*(1-2), 4–19. https://doi.org/10.1016/j.tecto.2008.07.021

Markmann, T. A., & Lanari, P. (2024). Mechanical modelling in petrochemical models: implications for fluid extraction in subduction zones. *In review*.

Marschall, H. R. (2005). Lithium, Beryllium and Boron in High-Pressure Metamorphisc Rocks from Syros (Greece), 429.

Marschall, H. R., Altherr, R., Gméling, K., & Kasztovszky, Z. (2009). Lithium, boron and chlorine as tracers for metasomatism in high-pressure metamorphic rocks: a case study from Syros (Greece). *Mineralogy and Petrology*, *95*(3-4), 291–302. https://doi.org/10.1007/s00710-008-0032-3

Marschall, H. R., Altherr, R., Kalt, A., & Ludwig, T. (2008). Detrital, metamorphic and metasomatic tourmaline in high-pressure metasediments from Syros (Greece): Intragrain boron isotope patterns determined by secondary-ion mass spectrometry. *Contributions to Mineralogy and Petrology*, *155*(6), 703–717. https://doi.org/10.1007/s00410-007-0266-9

Marschall, H. R., Altherr, R., Ludwig, T., Kalt, A., Gméling, K., & Kasztovszky, Z. (2006). Partitioning and budget of Li, Be and B in high-pressure metamorphic rocks. *Geochimica et Cosmochimica Acta*, *70*(18), 4750–4769. https://doi.org/10.1016/j.gca.2006.07.006

Martin, L. A., Ballèvre, M., Boulvais, P., Halfpenny, A., Vanderhaeghe, O., Duchêne, S., & Deloule, E. (2011). Garnet re-equilibration by coupled dissolution-reprecipitation: Evidence from textural, major element and oxygen isotope zoning of 'cloudy' garnet. *Journal of Metamorphic Geology*, *29*(2), 213–231. https://doi.org/10.1111/j.1525-1314.2010.00912.x

Martin, L. A., Rubatto, D., Crépisson, C., Hermann, J., Putlitz, B., & Vitale-Brovarone, A. (2014). Garnet oxygen analysis by SHRIMP-SI: Matrix corrections and application

to high-pressure metasomatic rocks from Alpine Corsica. *Chemical Geology*, *374-375*, 25–36. https://doi.org/10.1016/j.chemgeo.2014.02.010

Matthews, A., & Schliestedt, M. (1984). Evolution of the blueschist and greenschist facies rocks of Sifnos, Cyclades, Greece. *Contributions to Mineralogy and Petrology*, *88*(1-2), 150–163. https://doi.org/10.1007/BF00371419

Miller, D. P., Marschall, H. R., & Schumacher, J. C. (2009). Metasomatic formation and petrology of blueschist-facies hybrid rocks from Syros (Greece): Implications for reactions at the slab-mantle interface. *Lithos*, *107*(1-2), 53–67. https://doi.org/10.1016/j.lithos.2008.07.015

Miller, J. A., Cartwright, I., Buick, I. S., & Barnicoat, A. C. (2001). An O-isotope profile through the HP-LT Corsican ophiolite, France and its implications for fluid flow during subduction. *Chemical Geology*, *178*(1-4), 43–69. https://doi.org/10.1016/S0009-2541(00)00428-9

Mocek, B. (2001). Geochemical evidence for arc-type volcanism in the Aegean Sea: The blueschist unit of Siphnos, Cyclades (Greece). *Lithos*, *57*(4), 263–289. https://doi.org/10.1016/S0024-4937(01)00043-3

Muehlenbachs, K. (1986). Chapter 12. ALTERATION of the OCEANIC CRUST and the 18O HISTORY of SEAWATER. In J. W. Valley, H. P. Taylor, & J. R. O'Neil (Eds.), *Stable isotopes in high temperature geological processes* (pp. 425–444). De Gruyter. https://doi.org/doi:10.1515/9781501508936-017

Muehlenbachs, K., & Clayton, R. N. (1972). Oxygen Isotope Studies of Fresh and Weathered Submarine Basalts. *Canadian Journal of Earth Sciences*, *9*(2), 172–184. https://doi.org/10.1139/e72-014

Okrusch, M., & Bröcker, M. (1990). Eclogites associated with high-grade blueschists in the Cyclades archipelago, Greece: A review. *European Journal of Mineralogy*, *2*(4), 451–478. https://doi.org/10.1127/ejm/2/4/0451

Padrón-Navarta, J. A., Sánchez-Vizcaíno, V. L., Hermann, J., Connolly, J. A., Garrido, C. J., Gómez-Pugnaire, M. T., & Marchesi, C. (2013). Tschermak's substitution in antigorite and consequences for phase relations and water liberation in high-grade serpentinites. *Lithos*, *178*, 186–196. https://doi.org/10.1016/j.lithos.2013.02.001

Page, F. Z., Essene, E. J., Mukasa, S. B., & Valley, J. W. (2014). A garnet-zircon oxygen isotope record of subduction and exhumation fluids from the Franciscan complex, California. *Journal of Petrology*, *55*(1), 103–131. https://doi.org/10.1093/petrology/egt062

Page, F. Z., Kita, N. T., & Valley, J. W. (2010). Ion microprobe analysis of oxygen isotopes in garnets of complex chemistry. *Chemical Geology*, *270*(1-4), 9–19. https://doi.org/10.1016/j.chemgeo.2009.11.001

Page, F. Z., & Storey, C. D. (2023). A rutile and titanite record of subduction fluids: Integrated oxygen isotope and trace element analyses in Franciscan high-pressure rocks. *Journal of Metamorphic Geology*, (February), 1–20. https://doi.org/10.1111/jmg.12717

Parra, T., Vidal, O., & Jolivet, L. (2002). Relation between the intensity of deformation and retrogression in blueschist metapelites of Tinos Island (Greece) evidenced by chlorite–mica local equilibria. *Lithos*, *63*(1), 41–66. https://doi.org/https://doi.org/10.1016/S0024-4937(02)00115-9

Penniston-Dorland, S. C., Kohn, M. J., & Manning, C. E. (2015). The global range of subduction zone thermal structures from exhumed blueschists and eclogites: Rocks are hotter than models. *Earth and Planetary Science Letters*, *428*, 243–254. https://doi.org/10.1016/j.epsl.2015.07.031

Peters, D., & Pettke, T. (2017). Evaluation of Major to Ultra Trace Element Bulk Rock Chemical Analysis of Nanoparticulate Pressed Powder Pellets by ¡scp¿LA¡/scp¿ - ¡scp¿ICP¡/scp¿ - ¡scp¿MS¡/scp¿. *Geostandards and Geoanalytical Research*, *41*(1), 5–28. https://doi.org/10.1111/ggr.12125

Pettke, T., Oberli, F., Audétat, A., Guillong, M., Simon, A. C., Hanley, J. J., & Klemm, L. M. (2012). Recent developments in element concentration and isotope ratio analysis of individual fluid inclusions by laser ablation single and multiple collector ICP-MS. *Ore Geology Reviews*, *44*, 10–38. https://doi.org/10.1016/j.oregeorev.2011.11.001

Piccoli, F., Hermann, J., Pettke, T., Connolly, J. A., Kempf, E. D., & Vieira Duarte, J. F. (2019). Subducting serpentinites release reduced, not oxidized, aqueous fluids. *Scientific Reports*, *9*(1), 1–7. https://doi.org/10.1038/s41598-019-55944-8

Plank, T., & Langmuir, C. H. (1993). Tracing trace elements from sediment input to volcanic output at subduction zones. *Nature*, *362*(6422), 739–743. https://doi.org/10.1038/362739a0

Pogge von Strandmann, P. A. E., Dohmen, R., Marschall, H. R., Schumacher, J. C., & Elliott, T. (2015). Extreme Magnesium Isotope Fractionation at Outcrop Scale Records the Mechanism and Rate at which Reaction Fronts Advance. *Journal of Petrology*, *56*(1), 33–58. https://doi.org/10.1093/petrology/egu070

Poli, S., & Schmidt, M. W. (1995). H 2 O transport and release in subduction zones: Experimental constraints on basaltic and andesitic systems. *Journal of Geophysical Research: Solid Earth*, *100*(B11), 22299–22314. https://doi.org/10.1029/95JB01570

Putlitz, B., Cosca, M. A., & Schumacher, J. C. (2005). Prograde mica 40Ar/39Ar growth ages recorded in high pressure rocks (Syros, Cyclades, Greece). *Chemical Geology*, *214*(1-2), 79–98. https://doi.org/10.1016/j.chemgeo.2004.08.056

Putlitz, B., Matthews, A., & Valley, J. W. (2000). Oxygen and hydrogen isotope study of high-pressure metagabbros and metabasalts (Cyclades, Greece): implications for the subduction of oceanic crust. *Contributions to Mineralogy and Petrology*, *138*(2), 114–126. https://doi.org/10.1007/s004100050012

Ridley, J. (1984). Evidence of a Temperature-dependent 'Blueschist' to 'Eclogite' Transformation in High-pressure Metamorphism of Metabasic Rocks. *Journal of Petrology*, *25*(4), 852–870. https://doi.org/10.1093/petrology/25.4.852

Ring, U., Pantazides, H., Glodny, J., & Skelton, A. (2020). Forced Return Flow Deep in the Subduction Channel, Syros, Greece. *Tectonics*, *39*(1), 1–27. https://doi.org/10.1029/2019TC005768

Robson, R. M. L. (2000). *High Grade Blueschist Metasomatism in a Serpentinite Melange , Syros , Greece* [Doctoral dissertation, The University of Edinburgh].

Rubatto, D., & Angiboust, S. (2015). Oxygen isotope record of oceanic and high-pressure metasomatism: a P–T–time–fluid path for the Monviso eclogites (Italy). *Contributions to Mineralogy and Petrology*, *170*(5-6), 44. https://doi.org/10.1007/s00410-015-1198-4

Rubatto, D., Williams, M., Markmann, T. A., Hermann, J., & Lanari, P. (2023). Tracing fluid infiltration into oceanic crust up to ultra-high-pressure conditions. *Contributions to Mineralogy and Petrology*, *178*(11), 79. https://doi.org/10.1007/s00410-023-02060-6

Schmidt, M. W., & Poli, S. (2014). Devolatilization During Subduction. In *Treatise on geochemistry* (2nd ed., pp. 669–701, Vol. 4). Elsevier. https://doi.org/10.1016/B978-0-08-095975-7.00321-1

Schmidt, M. W., & Poli, S. (1998). Experimentally based water budgets for dehydrating slabs and consequences for arc magma generation. *Earth and Planetary Science Letters*, *163*(1-4), 361–379. https://doi.org/10.1016/S0012-821X(98)00142-3

Schumacher, J. C., Brady, J. B., Cheney, J. T., & Tonnsen, R. R. (2008). Glaucophane-bearing Marbles on Syros, Greece. *Journal of Petrology*, *49*(9), 1667–1686. https://doi.org/10.1093/petrology/egn042

Seck, H. A., Kötz, J., Okrusch, M., Seidel, E., & Stosch, H.-G. (1996). Geochemistry of a meta-ophiolite suite: An association of metagabbros, eclogites and glaucophanites on the island of Syros, Greece. *European Journal of Mineralogy*, *8*(3), 607–624. https://doi.org/10.1127/ejm/8/3/0607

Seman, S. M. (2016). The tectonostratigraphy of the Cycladic Blueschist Unit and new garnet geo/thermochronology techniques, 275.

Skelton, A., Peillod, A., Glodny, J., Klonowska, I., Månbro, C., Lodin, K., & Ring, U. (2019). Preservation of high- P rocks coupled to rock composition and the absence

of metamorphic fluids. *Journal of Metamorphic Geology*, *37*(3), 359–381. https://doi.org/10.1111/jmg.12466

Skora, S., Baumgartner, L. P., Mahlen, N. J., Johnson, C. M., Pilet, S., & Hellebrand, E. (2006). Diffusion-limited REE uptake by eclogite garnets and its consequences for Lu-Hf and Sm-Nd geochronology. *Contributions to Mineralogy and Petrology*, *152*(6), 703–720. https://doi.org/10.1007/s00410-006-0128-x

Spear, F. S. (2014). The duration of near-peak metamorphism from diffusion modelling of garnet zoning. *Journal of Metamorphic Geology*, *32*(8), 903–914. https://doi.org/10.1111/jmg.12099

Spear, F. S., & Pattison, D. R. (2017). The implications of overstepping for metamorphic assemblage diagrams (MADs). *Chemical Geology*, *457*, 38–46. https://doi.org/10.1016/j.chemgeo.2017.03.011

Staudigel, H., Plank, T., White, B., & Schmincke, U. (1996). Fluxes During Seafloor Alteration of the Basaltic Crust ' DSDP Sites have pointed to the AND. *Geophysical Monograph*, *96*, 19–37.

Stouraiti, C., Pantziris, I., Vasilatos, C., Kanellopoulos, C., Mitropoulos, P., Pomonis, P., Moritz, R., & Chiaradia, M. (2017). Ophiolitic remnants from the upper and intermediate structural unit of the attic-cycladic crystalline belt (Aegean, Greece): Fingerprinting geochemical affinities of magmatic precursors. *Geosciences (Switzerland)*, *7*(1). https://doi.org/10.3390/geosciences7010014

Sun, S. S. (1982). Chemical composition and origin of the earth's primitive mantle. *Geochimica et Cosmochimica Acta*, *46*(2), 179–192. https://doi.org/10.1016/0016-7037(82)90245-9

Sun, S. S., & McDonough, W. F. (1989). Chemical and isotopic systematics of oceanic basalts: Implications for mantle composition and processes. *Geological Society Special Publication*, *42*(1), 313–345. https://doi.org/10.1144/GSL.SP.1989.042.01.19

Taylor, S. R., & McLennan, S. M. (1985). *The Continental Crust: Its Composition and Evolution*. Blackwell, Oxford.

Tomaschek, F. (2003). Zircons from Syros, Cyclades, Greece–Recrystallization and Mobilization of Zircon During High-Pressure Metamorphism. *Journal of Petrology*, *44*(11), 1977–2002. https://doi.org/10.1093/petrology/egg067

Tomaschek, F., Keiter, M., Kennedy, A. K., & Ballhaus, C. (2008). Pre-Alpine basement within the Northern Cycladic Blueschist Unit on Syros Island, Greece. *Zeitschrift der Deutschen Gesellschaft fur Geowissenschaften*, *159*(3), 521–532. https://doi.org/10.1127/1860-1804/2008/0159-0521

Trotet, F., Vidal, O., & Jolivet, L. (2001). Exhumation of Syros and Sifnos metamorphic rocks (Cyclades, Greece). New constraints on the P-T paths. *European Journal of Mineralogy*, *13*(5), 901–920. https://doi.org/10.1127/0935-1221/2001/0013/0901

Tual, L., Smit, M. A., Cutts, J., Kooijman, E., Kielman-Schmitt, M., Majka, J., & Foulds, I. (2022). Rapid, paced metamorphism of blueschists (Syros, Greece) from laser-based zoned Lu-Hf garnet chronology and LA-ICPMS trace element mapping. *Chemical Geology*, *607*(January), 121003. https://doi.org/10.1016/j.chemgeo.2022.121003

Ulmer, P., & Trommsdorff, V. (1999). Phase relations of hydrous mantle subducting to 300 km. *Mantle Petrology: Field Observations and High-Pressure Experimentation. Spec. Publ. Geochem. Soc. No. 6*, (6), 259–281.

Ulrich, M., Rubatto, D., Hermann, J., Markmann, T. A., Bouvier, A.-s., & Deloule, E. (2024). Olivine formation processes and fluid pathways in subducted serpentinites revealed by in-situ oxygen isotope analysis (Zermatt-Saas, Switzerland). *Chemical Geology*, *649*(November 2023), 121978. https://doi.org/10.1016/j.chemgeo.2024.121978

Urosevic, M., Nebel, O., Padro?n?Navarta, J. A., & Rubatto, D. (2018). Assessment of O and Fe isotope heterogeneity in garnet from Kakanui (New Zealand) and Erongo (Namibia). *European Journal of Mineralogy*, *30*(4), 695–710. https://doi.org/10.1127/ejm/2018/0030?2755

Uunk, B., Brouwer, F., de Paz-Álvarez, M., van Zuilen, K., Huybens, R., van 't Veer, R., & Wijbrans, J. (2022). Consistent detachment of supracrustal rocks from a fixed subduction depth in the Cyclades. *Earth and Planetary Science Letters*, *584*, 117479. https://doi.org/10.1016/j.epsl.2022.117479

Valley, J. W., Kitchen, N., Kohn, M. J., Niendorf, C. R., & Spicuzza, M. J. (1995). UWG-2, a garnet standard for oxygen isotope ratios: Strategies for high precision and accuracy with laser heating. *Geochimica et Cosmochimica Acta*, *59*(24), 5223–5231. https://doi.org/10.1016/0016-7037(95)00386-X

Veizer, J., Ala, D., Azmy, K., Bruckschen, P., Buhl, D., Bruhn, F., Carden, G. A., Diener, A., Ebneth, S., Godderis, Y., Jasper, T., Korte, C., Pawellek, F., Podlaha, O. G., & Strauss, H. (1999). 87Sr/86Sr, δ13C and δ18O evolution of Phanerozoic seawater. *Chemical Geology*, *161*(1-3), 59–88. https://doi.org/10.1016/S0009-2541(99)00081-9

Vho, A., Lanari, P., & Rubatto, D. (2019). An Internally-Consistent Database for Oxygen Isotope Fractionation Between Minerals. *Journal of Petrology*, *60*(11), 2101–2129. https://doi.org/10.1093/petrology/egaa001

Vho, A., Lanari, P., Rubatto, D., & Hermann, J. (2020). Tracing fluid transfers in subduction zones: an integrated thermodynamic and δ18O fractionation modelling approach. *Solid Earth*, *11*(2), 307–328. https://doi.org/10.5194/se-11-307-2020

Vho, A., Rubatto, D., Lanari, P., Giuntoli, F., Regis, D., & Hermann, J. (2020). Crustal reworking and hydration: insights from element zoning and oxygen isotopes of gar-

net in high-pressure rocks (Sesia Zone, Western Alps). *Contributions to Mineralogy and Petrology*, *175*(11), 109. https://doi.org/10.1007/s00410-020-01745-6

Vho, A., Rubatto, D., Putlitz, B., & Bouvier, A.-S. (2020). New Reference Materials and Assessment of Matrix Effects for SIMS Measurements of Oxygen Isotopes in Garnet. *Geostandards and Geoanalytical Research*, *44*(3), 459–471. https://doi.org/10.1111/ggr.12324

Vieira Duarte, J. F., Piccoli, F., Pettke, T., & Hermann, J. (2021). Textural and Geochemical Evidence for Magnetite Production upon Antigorite Breakdown during Subduction. *Journal of Petrology*, *62*(10), 1–29. https://doi.org/10.1093/petrology/egab053

Warr, L. N. (2021). IMA–CNMNC approved mineral symbols. *Mineralogical Magazine*, *85*(3), 291–320. https://doi.org/10.1180/mgm.2021.43

Chapter 5

Garnet porphyroblast analysis in 2D to 3D: Insights for major to trace element zoning in blueschists-facies rocks from Syros

Abstract

Mineral growth and stability during blueschist-eclogite facies play a critical role in mass transfer and element recycling on Earth. Garnet porphyroblasts, in particular, preserve in their chemical composition a record of prograde metamorphism. However, the mechanisms governing garnet growth are not yet fully understood. The major and trace element compositions of garnet are influenced by distinct growth mechanisms during the blueschist to eclogite transition, highlighting the release of important trace elements and metals from the subduction zone to the arc.

To investigate garnet porphyroblast growth during blueschist facies conditions, two blueschist samples from Syros — SY21-07 (Achladi) and SY21-01/2-1 (Katergaki) — were analyzed in 3D using micro-computed tomography (µCT) and in 2D for their chemical composition using laser ablation inductively-coupled-plasma mass-spectrometry (LA-ICP-MS). The results reveal differences in porphyroblast shapes, sizes, and elemental zoning, indicating varying degrees of fluid infiltration and trace element redistribution. The grain size distribution and elemental zoning analysis support the theory of interface-controlled growth for garnet porphyroblasts during prograde metamorphism. Variations in trace elements suggest episodic fluid pressure changes and mineral breakdown during metamorphism, which are reflected in major element zoning patterns.

Garnets from sample SY21-07 display smooth compositional zoning in their cores, indicating undisturbed growth, and fluctuations of trace elements in their mantles, suggesting changes in element availability during growth, likely due to fluid pressure variations. These variations are consistent with petrochemical modeling predictions of fluid pressures during dehydration reactions of chlorite and lawsonite.

In contrast, garnet from sample SY21-01/2-1 shows prograde elemental zoning in the core but reveals fluid-related disturbances in the mantle, including compositional oscillations and annuli formations in major and trace elements. Internal fluid pressure variations alone cannot fully account for these features, suggesting open-system conditions and infiltration of externally derived fluids. The compositional variations were likely governed by the breakdown of minerals such as titanite, chlorite, and lawsonite, which separately influenced major and trace element zoning.

5.1 Introduction

The transition from blueschist to eclogite facies has been studied because it is a primary indicator for oceanic subduction in Earth's evolution (Tsujimori & Ernst, 2014; Tsujimori et al., 2006). The blueschist-eclogite transition is crucial in subduction zones because it releases aqueous fluids and results in a density change of the subducting slab, an important driver of plate tectonics and subduction (e.g., Hacker et al., 2003; Vitale Brovarone et al., 2011). Hydrous fluids released from the dehydrating subducting crust are also responsible for melting in the mantle wedge and generation of arc magmas (e.g., Peacock, 1996; Schmidt & Poli, 1998). In terms of fluid release capacity, the metamorphic subfacies lawsonite blueschist and lawsonite eclogite metamorphic rocks are of special interest because of the large amount of water incorporated in the crystal lattice of lawsonite (11.5 wt.% H_2O, $CaAl_2Si_2O_7(OH)_2{\cdot}H_2O$) (Hernández-Uribe & Tsujimori, 2023; Tsujimori & Ernst, 2014; Vitale Brovarone et al., 2014; Whitney et al., 2020). The transition from lawsonite-blueschist to epidote-eclogite and associated dehydration reactions redistribute aqueous fluids and fluid mobile elements within the subducting crust and to the mantle wedge (Bebout et al., 2007; Hermann et al., 2006; Manning, 2004; Poli & Schmidt, 2002; Schmidt & Poli, 2014; Spandler et al., 2003). Important (trace-) element liberating phases besides lawsonite (rare earth elements (REE), Pb, Sr, Th, U) are phengite (large-ion lithophile elements (LILE), Ba, B, transition metals), glaucophane (LILE, Ba, REE), epidote/zoisite/allanite (Light-REE (LREE), Sr, Th, U, Pb), titanite (REE, Nb, Ta) (Kunz et al., 2022; Spandler et al., 2003; Tsujimori et al., 2006). Nevertheless, the release of elements from the rock up to eclogite facies conditions appear to be minimal (Spandler et al., 2003) thus mineral phases in blueschists can show strong compositional zoning in trace elements (i.e. Y+REE in garnet). Interpreting the zoning patterns and determining if internal process e.g., the breakdown of other mineral phases, is responsible for their creation or if externally-derived fluid are involved, often requires additional analytical tools e.g., in-situ oxygen isotope analyses (e.g., Rubatto & Angiboust, 2015; Rubatto et al., 2023, and Chapter 4) or modelling (e.g., Konrad-Schmolke et al., 2011; Konrad-Schmolke et al., 2023).

Garnet is a major mineral in various metamorphic rocks and can record compositional and/or isotopic changes as it grows under a wide range of temperature (T) and pressure (P) conditions (e.g., Caddick et al., 2010; Hermann & Rubatto, 2003; Konrad-Schmolke et al., 2006; Konrad-Schmolke et al., 2008; Rubatto & Angiboust, 2015; Skora et al., 2006; Yang & Rivers, 2001). Garnet is especially useful in monitoring REE variations as it is a major REE-carrying mineral. The diffusivity of REEs in garnet and the host rock is orders of magnitudes slower then major elements (Carlson, 2012; Chernoff & Carlson, 1999; George et al., 2018; Kohn, 2004; Konrad-Schmolke et al., 2023; Tirone et al., 2005).

Recent improvements in the visualization of trace element distribution in two-dimensions via mapping using LA-ICP-MS have provided a more comprehensive picture of mineral growth (Bovay et al., 2022; Gaidies et al., 2021; George et al., 2018; Konrad-Schmolke et al., 2023; Markmann et al., 2024; Rubatto et al., 2020). Compositional profiles of trace elements can be extracted from such maps and used for diffusion chronometry allowing the calculation of diffusion coefficients in garnet (e.g., Carlson, 2012; Rubatto et al., 2023; Smit et al., 2024) or calculating the garnet growth duration (e.g., Gaidies et al., 2021, Liu et al., under review).

Nucleation, growth, and dissolution of minerals, in particular of porphyroblasts such as garnet, are fundamental processes that rely on reaction kinetics, fluid-interaction and element transport in the rock system (Carlson, 2011; Cygan & Lasaga, 1982; Fisher, 1978; Kile & Eberl, 2003; Kirkpatrick, 1981; Lasaga, 1986, 1998). The availability of elements during garnet growth can be (i) limited by transport mechanisms (diffusion) in the intergranular medium (chemical potential gradients in the matrix) or by interface processes (the growth rate of the interface is slower than supply by diffusion) (Gaidies et al., 2017; Lanari et al., 2017). The associated growth mechanism are referred to as i) diffusion-controlled or ii) interface-controlled growth (Carlson, 2011). Porphyroblast growth is probably limited to the slower diffusion-controlled processes (Carlson & Denison, 1992; Carlson et al., 1995; George & Gaidies, 2017) and may be catalysed by pulses of fluids (Cruz-Uribe et al., 2021; Tual et al., 2022). The processes of porhpyroblast growth is also captured by the crystal size distribution (CSD), which is directly governed by the rate of growth of the minerals (Kretz, 1974).

A CSD can be determined quantitatively by three-dimensional (3D) analysis using micro-computed tomography (µCT) (Carlson & Denison, 1992; Ketcham & Carlson, 2001) and applied to automatically segmented prophyroblasts (Hartmeier et al., 2024). This 3D analysis together with the information of major and trace element zoning in garnet can unravel the nucleation and growth during metamorphic rock forming processes (George et al., 2018). Two contrasting compositional zoning features in garnet appear to document different growth conditions, smooth zoning and compositional fluctuation such as oscillatory zoning or annuli. George et al., 2018 described a case where smooth zoning in garnet was linked to equilibrium partitioning between garnet and the rock matrix, whereas annuli were dependent on the spatial disposition and reflected varying growth rates and the incorporation of heterogeneities due to slow matrix diffusion of trace elements. So far, the number of studies combining micro-tomography and major, minor and trace element zoning in porphyroblasts is limited in the literature.

This study examines two blueschist samples from Syros (Greece) to analyze the crystal size distribution (CSD) of garnet porphyroblasts, their major, minor and trace element

zoning patterns, and the distribution of trace elements across multiple minerals in these samples. Each sample was investigated using a combination of micro-computed tomography (uCT) and Laser-Ablation Inductively Coupled Plasma Mass Spectrometry (LA-ICP-MS). The samples come from two outcrops, Achladi and Katergaki corresponding to different parts of a subducted oceanic crust (see Chapter 4). Garnet porphyroblasts from a blueschist in Achladi display varying degrees of resorption, gradual zoning of major elements, and consistent oxygen isotope composition, suggesting relatively undisturbed growth with minimal external fluid infiltration. In contrast, the Katergaki garnets are larger with euhedral grain shapes and show evidence of fluid-related disturbance during growth, as indicated by changes in oxygen isotope composition and the formation of an annulus in the mantle. The study begins by investigating porphyroblast shapes and crystal size distributions (CSD), which are consistent with observations of interface-controlled growth mechanisms (Gaidies et al., 2021; George & Gaidies, 2017). This 3D analysis forms the basis for interpreting element zoning patterns and associated growth mechanisms, as it often translates into distinct chemical zonation for both major and trace elements (e.g., George et al., 2018; Konrad-Schmolke et al., 2023; Skora et al., 2006). Finally, the study concludes by presenting a scenario for the distribution of trace elements within the garnet porphyroblasts of these two blueschist samples.

5.2 Samples and Methods

5.2.1 µCT-scanning of drill cores

The three-dimensional imaging of the samples at high resolution (6-9 µm) was performed using cylindrical sample cores and a BRUKER SKYSCAN 1273 3D X-ray microscope at the Institute of Geological Sciences, University of Bern. Detailed measurement conditions are available in the Supplementary Material S1. Garnet segmentation was carried out using Dragonfly 2024.1 software (Dragonfly, Dragonfly 2024.1 [Computer software]. Comet Technologies Canada Inc., Montreal, Canada; available at https://dragonfly.comet.tech/). The garnet grains were selected and isolated based on the X-ray absorption histogram, morphological kernel operations, and connected component analysis (CCA). Each individual grain was examined to identify and eliminate possible artefacts, such as inclusions or other minerals or mineral mixture with similar X-ray absorption values as garnet. Grain measurements, including geometric center position, volume, and orientation angles (phi and theta), were obtained using the built-in functions of CCA (Silversmith, 2021). The spherical equivalent radius of each segmented garnet volume was calculated using a convex hull fitted around each garnet, which minimizes the influence of resorption textures in porphyroblasts (Hartmeier et al., 2024), but has a minor effect on broken garnet pieces,

fragments, and deformed samples. This spherical equivalent radius was then applied for crystal size distribution (CSD) analysis. Additionally, a thickness mesh (a type of density mesh) was generated in Dragonfly, where the thickness represents the diameter of a hypothetical sphere that can fit at each boundary point. This thickness mesh helps to identify voxels from other mineral phases that may be included in the segmented garnet in the 3D model.

5.2.2 Multi phase element mapping by LA-ICP-MS

Mapping of major, minor and trace elements with LA-ICP-MS followed the protocol described in Markmann et al. (2024). In each sample an area of ∼2x2 mm was selected covering a best-preserved garnet grain and its surrounding matrix. Each sample area previously mapped with EPMA and selected among >25 mapped garnets. Garnet and phengite have been analysed for $\delta^{18}O$ composition by SIMS (see chapter 4). LA-ICPMS mapping experiments were conducted at the Institute of Geological Sciences, University of Bern, using an ASI Resonetics RESOlution-SE 193 nm excimer laser system with the S155 dual volume sample cell coupled to an Agilent 7900 quadrupole mass spectrometer. The ablated material was transported in an atmosphere of He at a flux of 0.7 L/min mixed with Ar (0.86–0.87 L/min) from the ablation cell to the plasma and N2 (0.003 L/min) at the exit of the ablation cell. Before each session the instrument was optimized to reduce the oxide production using the ThO/Th intensity ratio that was maintained at values below 0.3%, and for robust plasma conditions monitored by a U/Th sensitivity ratio of >0.97 (Günther and Hattendorf, 2005). The samples were loaded as thin section pieces (30 µm thick) into a spring holder of the S155 sample cell. The map areas were defined by a rectangular shape of evenly spaced line scans using the GeoStar© software (Norris Scientific). The used spot size was 12 µm using a on-sample fluence of 5 J/cm^2 and a repetition rate of 5 Hz. Detailed conditions for the mapping experiment can be found in the Supplementary material S2.

Two maps have been measured. Map 1 on sample SY21-07 from Achladi and map 2 on sample SY21-01/2-1 from Katergaki. Multi mineral phases have been calibrated in each map including garnet, phengite, epidote, glaucophane, titanite, apatite, and rutile. For the calibration with an internal standard element the composition were taken from the beforehand acquired major element maps from EPMA.

In Map 1 garnet was calibrated using a constant composition for Ca as the internal standard element (57,180 µg/g corresponding to 8 wt.% of CaO), phengite using a constant composition of Al (141,300 µg/g corresponding to 26.7 wt.% of Al_2O_3), epidote using a constant composition of Si (176,700 µg/g corresponding to 37.8 wt.% SiO_2), glaucophane using a constant composition of Al (254,800 µg/g corresponding to 48.1 wt.% of Al_2O_3), titanite using a constant composition of Ca (214,400 µg/g corresponding to 30.0 wt.%

CaO), apatite using a constant composition of Ca (400,200 µg/g corresponding to 56.0 wt.% CaO), and rutile using a constant composition of Ti (593,500 µg/g corresponding to 99 wt.% TiO_2).

In Map 2 garnet was calibrated using a variable composition for Ca as the internal standard element (50,744 µg/g corresponding to 7.1 wt.% of CaO in the core and 70,041 µg/g corresponding to 7.1 wt.% of CaO in the rim), phengite using a constant composition of Si (238,374 µg/g corresponding to 51.0 wt.% SiO_2), epidote using a constant composition of Si (182,286 µg/g corresponding to 39.0 wt.% SiO_2), glaucophane using a constant composition of Si (272,027 µg/g corresponding to 58.2 wt.% SiO_2), titanite using a constant composition of Ca (214,400 µg/g corresponding to 30.0 wt.% CaO), and apatite using a constant composition of Ca (371,644 µg/g corresponding to 52.0 wt.% CaO).

5.3 Results

5.3.1 Garnet grain shape

Garnet porphyroblasts in the blueschist samples SY21-07 and SY21-01/2 exhibit distinct differences in shape, size, and inclusion characteristics. Each sample contains two main classes of garnets: whole garnets and fragmented garnets (Figure 5.0).

Sample SY21-07 is a strong foliated blueschist. Whole garnet porphyroblasts have a rounded shapes referred to as shape 1.1, are mm-sized and contain inclusions of phengite, quartz, epidote, and occasionally chlorite, ranging in size from 50 to 300 µm (Figure 5.0a,b). These porphyroblasts are commonly wrapped by phengite, which is present in the pressure shadows (Figure 5.0a). Glaucophane and epidote are oriented parallel to the foliation around the garnet-phengite assemblage. In addition, chlorite is present at the garnet tips located perpendicular to the foliation. Porphyroblast shape 1.1 show lower values in the thickness mesh (darker color) indicating a lower voxel density compared to the fragmented garnet porphyroblasts designated shapes 1.2, 1.3, and 1.4 (Figure 5.0b). Shapes 1.2 to 1.4 are usually smaller (sub-mm sized; 50 to 10 vol% of the porphyroblasts with a shape 1.1), phengite is less abundant in the pressure shadows, and the abundance of chlorite around the porphyroblast increases compared to the shape 1.1. The association with chlorite accounts for up to approximately 50 vol% of the original garnet and the remnant porphyroblast retains some of the inclusions described for shape 1.1.

In the blueschist section of sample SY21-01/2, whole garnet porphyroblasts have a euhedral shape with prominent crosscutting cracks (shape 2.1 in Figure 5.0b,d). These shape 2.1 porphyroblasts contain fewer and smaller inclusions compared to shape 1.1 porphyroblasts from sample SY21-07, primarily epidote and quartz, with occasional titanite, and

inclusion sizes ranging between 10 and 50 µm. Fragmented garnets in the blueschist section appear either as halves of whole garnet, with chlorite filling the cracks, or as rounded fragments that constitute 5 to 20 vol% of the original garnet (shape 2.2 in Figure 5.0b,d). None of these garnets are surrounded by abundant chlorite.

In the eclogitic part of sample SY21-01/2, whole garnets (shape 2.3) are less euhedral and show extensive cracking throughout the grain (Figure 5.0b,d). These garnets contain inclusions of quartz and titanite, approximately 50 µm in size. Fragmented garnets (shape 2.4) in the eclogitic section are also rounded, but their fragments are closely aligned and exhibit a stretched, ellipsoidal appearance. These garnets show a minor association with chlorite at their edges.

The size and distribution of garnet grains in samples SY21-07 and SY21-01/2-1 differs significantly, as shown in Figure 5.1.

Sample SY21-07 shows a strong foliation, the garnet grains are predominantly concentrated in three distinct bands (Figure 5.1a), and garnets are typically smaller than 0.8 mm^3 (Figure 5.1b). The lowermost band shows the largest grain density in the drill-core and decreases towards the top. Further, three distinct groups of grain sizes can be identified by plotting the CSD using the spherical equivalent radius (SER). The CSD can be approximated by a log-normal distribution (Figure 5.2a). Group 1.1 comprises grains larger than 0.1 mm^3, are the least abundant and are accumulated in the lowest layer. Group 1.2 includes medium-sized grains ranging from 0.004 to 0.1 mm^3, and Group 1.3 represents the smallest grains with volumes less than 0.004 mm^3 (see Figure 5.2a).

Group 1.1 grains are the least abundant and accumulate in the lowest layer showing the largest grain density in the drill-core. **Group 1.2**, the medium-sized grains, decrease in their abundance within the three layers from bottom to top. **Group 1.3**, the smallest grains, are distributed relative equally in the three layers.

In sample SY21-01/2-1, garnets are most abundant in the upper part of the drill core, which represents the blueschist section of the sample. This part shows a preferred distribution of garnet grains in two distinct bands and can be approximated by a log-normal distribution (Figure 5.1b). The CSD based on the SER reveals two main grain size groups (Figure 5.2b): Group 2.1, which includes grains with a volume larger than 1.4 mm^3, and Group 2.2, which encompasses grains with a volume smaller than 1.4 mm^3.

Group 2.1, the largest grains, are predominantly found in the uppermost band of the blueschist section, where garnet grain density is highest. The relative proportion of Group 2.1 is the highest in the eclogite part. **Group 2.2**, the smaller grains are distributed more evenly throughout the drill core, following the two bands in the blueschist section.

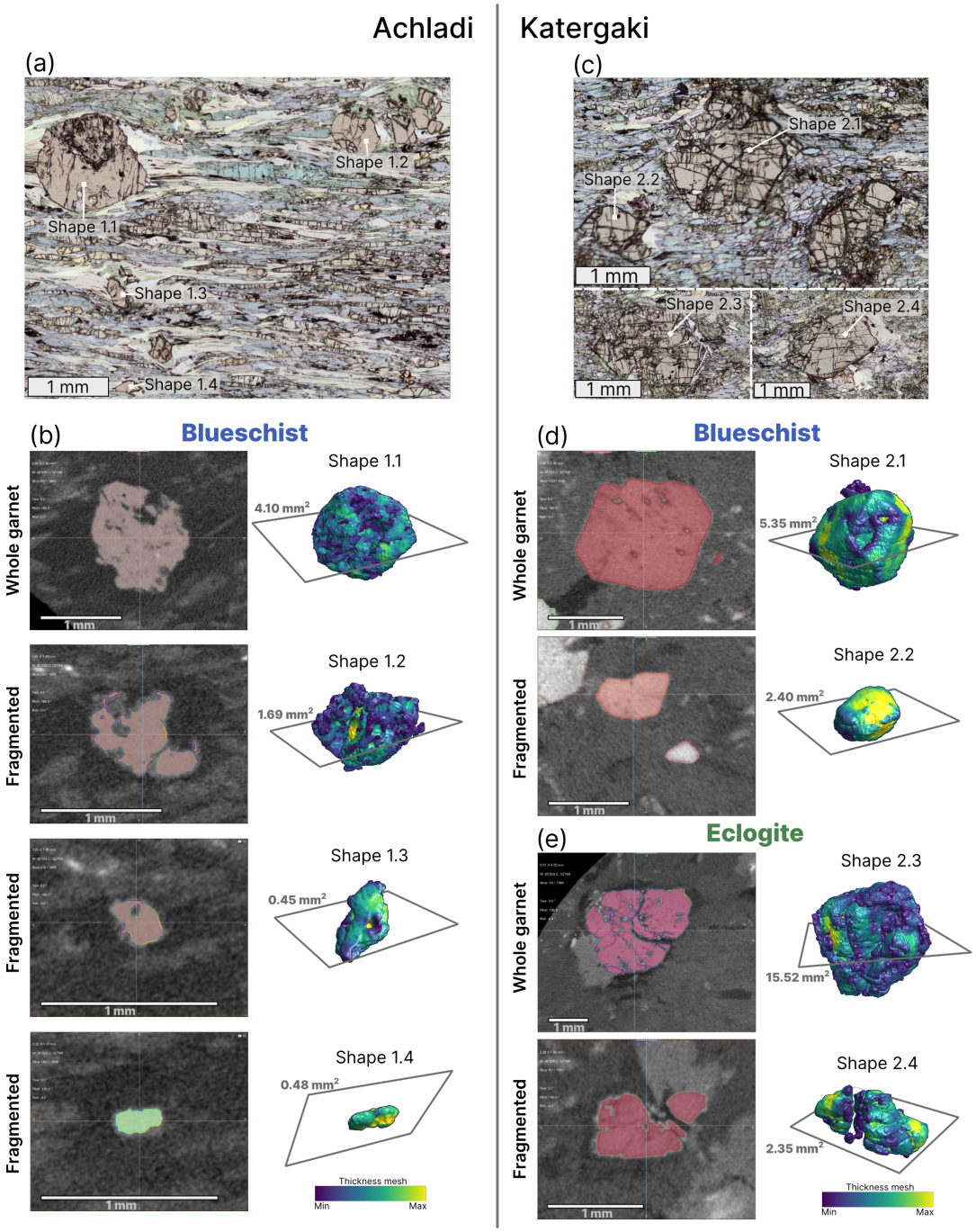
Achladi
Katergaki
(a)
Shape 1.1
Shape 1.2
Shape 1.3
Shape 1.4
1 mm
(c)
Shape 2.1
Shape 2.2
Shape 2.3
Shape 2.4
1 mm
(b)
Blueschist
Whole garnet
Fragmented
Fragmented
Fragmented
Shape 1.1
4.10 mm²
Shape 1.2
1.69 mm²
Shape 1.3
0.45 mm²
Shape 1.4
0.48 mm²
Thickness mesh
Min
Max
(d)
Blueschist
Whole garnet
Fragmented
Shape 2.1
5.35 mm²
Shape 2.2
2.40 mm²
(e)
Eclogite
Whole garnet
Fragmented
Shape 2.3
15.52 mm²
Shape 2.4
2.35 mm²
Thickness mesh
Min
Max

Figure 5.0 *(previous page)*: Overview of garnet porphyroblast shapes in blueschist samples from Achladi (SY21-07) and Katergaki (SY21-01/2-1). (a) Photomicrograph of the blueschist sample SY21-07 from Achladi, illustrating garnet shapes 1.1 to 1.4. These range from euhedral, millimeter-sized garnets (1.1) to garnet fragments in the matrix measuring 50–100 µm (1.4). (b) Reconstructed gray-scale CT scan images of SY21-07. The left side highlights classified garnets in color, while the right presents a selected grain visualized in 3D using a thickness-mesh-based color scale. (c) Photomicrograph of the blueschist and eclogite portions of sample SY21-01/2-1 from Katergaki. Garnet shapes 2.1 and 2.2 (top) show euhedral, millimeter-sized garnets with cracks (2.1) and sub-millimeter garnet fragments with cracks (2.2). Garnet shapes 2.3 and 2.4 (bottom) from the eclogite section display millimeter-sized garnets with cracks, often associated with chlorite. (d) Reconstructed gray-scale CT scan images of SY21-01/2-1, focusing on garnet shapes 2.1 and 2.2 in the blueschist section. Classified garnets are highlighted in color on the left, and the selected grain is rendered in 3D on the right using a thickness-mesh-based color scale. (3) Reconstructed CT scan images of garnet shapes 2.3 and 2.4 from the eclogite section. As in previous panels, classified garnets are shown in color (left), and a selected grain is visualized in 3D (right) with the thickness-mesh-based color scale. The color scale reflects the thickness mesh, a density-based representation of segmented voxels (3D pixels) within each grain (see text for details).

5.3.2 Major element zoning

Major element maps were generated in Chapter 4, prior to LA-ICP-MS mapping, to identify garnet porphyroblasts with central cross-sections, characterized by high spessartine content. Figure 5.4 presents the major element maps for two selected garnet grains from samples SY21-07 and SY21-01/2-1, showing their respective end-member molar fractions: spessartine (X_{sps} as Mn/(Fe+Mg+Ca+Mn)), almandine (X_{alm}, Fe/(Fe+Mg+Ca+Mn)), pyrope (X_{prp}, Mg/(Fe+Mg+Ca+Mn)), and grossular (X_{grs}, Ca/(Fe+Mg+Ca+Mn)). The oxygen isotope analysis spot measurements discussed in Chapter 4 are displayed along with their values in Figures 5.4b and f. Figure 5.3 illustrates the spessartine molar fraction maps of multiple garnet grains from sample SY21-07 and a mapped domain of the thin section from sample SY21-01/2-1, highlighting the diversity of garnets in the sample. The cross-cut through the center of each garnet is indicated by the spessartine content.

The two grains also analused for trace elements by LA-ICP-MS exhibit gradual zoning from core to rim in major elements (Figure 5.4). In both samples, spessartine decreases from the core to the rim, while almandine and pyrope increase. In sample SY21-07, grossular exhibits patchy, non-concentric zoning. In contrast, sample SY21-01/2-1 shows patchy fluctuations in grossular content within the core, indicated by a Ca-rich zone (outlined by the purple dashed line), followed by an increase from the mantle to the rim. The map of spessartine shows a slight increase at the rim in sample SY21-07 , while in sample SY21-01/2-1, there is a noticeable increase in the mantle, forming an annulus (highlighted by a brownish dashed line). This annulus is also evident in the depletion of almandine. For further details see Chapter 4.

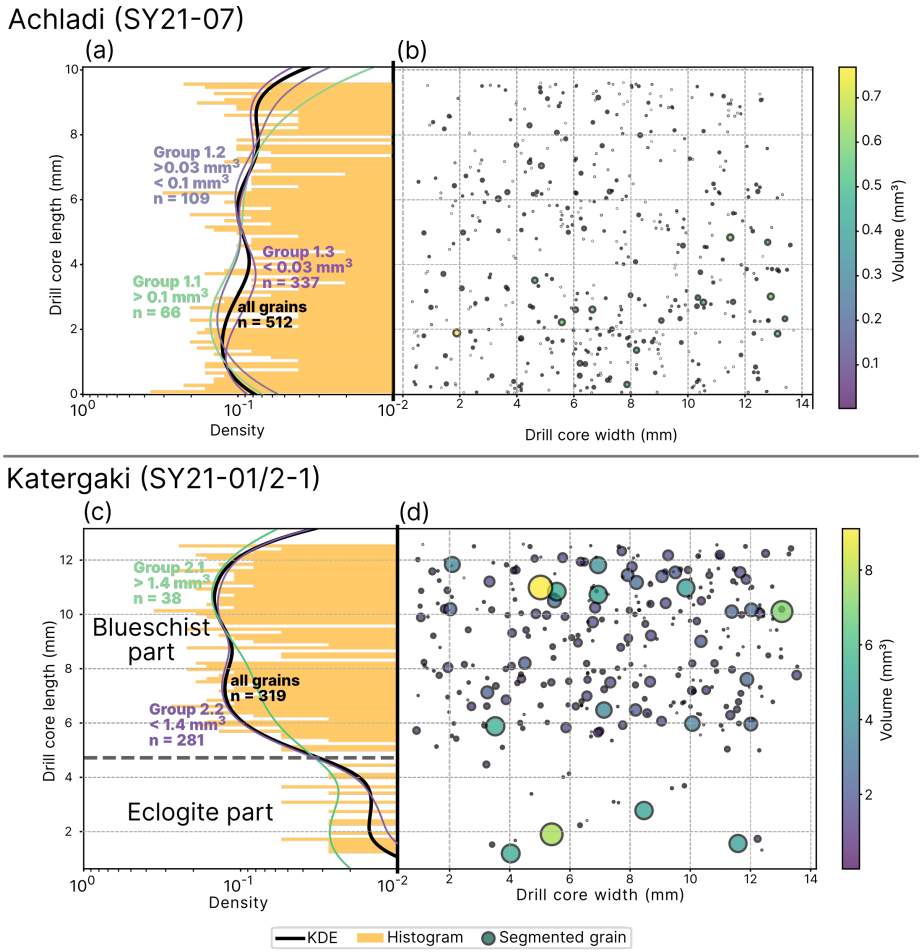

Figure 5.1: Distribution of garnet grains in CT-scanned drill cores from blueschist samples collected at Achladi (SY21-07) and Katergaki (SY21-01/2-1). (a) Histogram (yellow bars) and kernel density distribution (KDE, blue curve) depicting the distribution of garnet grain volumes in the drill core of sample SY21-07. Colored curves show grain volume filtered KDEs. (b) Visualization of classified garnet grains in sample SY21-07, showing their spatial distribution in the x and y positions within the drill core. Grain volumes are represented by a color scale*. (c) Histogram (yellow bars) and kernel density distribution (blue curve) showing the garnet grain volume distribution in the drill core of sample SY21-01/2-1. Colored curves show grain volume filtered KDEs. (d) Visualization of classified garnet grains in sample SY21-01/2-1, displaying their x and y positions within the drill core, with grain volumes indicated by a color scale*.
*Note: Grain volumes are scaled by a factor of 100 to enhance visibility in the illustrations.

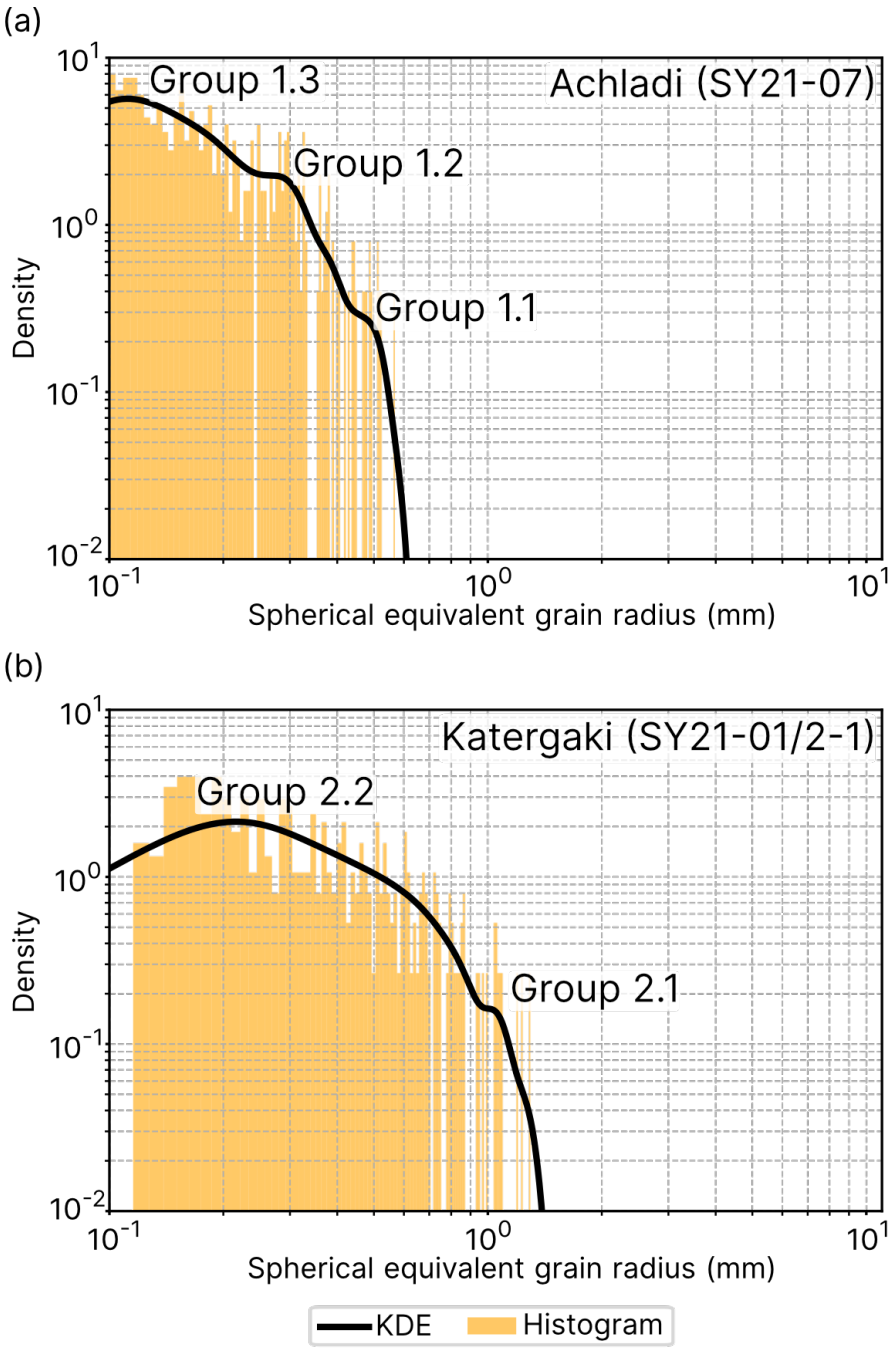

Figure 5.2: Grain size distribution (CSD) of garnet grains in drill cores from samples SY21-07 and SY21-01/2-1. (a) Density plot of the garnet population in sample SY21-07, where grain size is represented as the spherical equivalent radius, calculated from the grain volume. (b) Density plot of the garnet population in sample SY21-01/2-1, with grain size expressed as the spherical equivalent radius, derived from the grain volume.

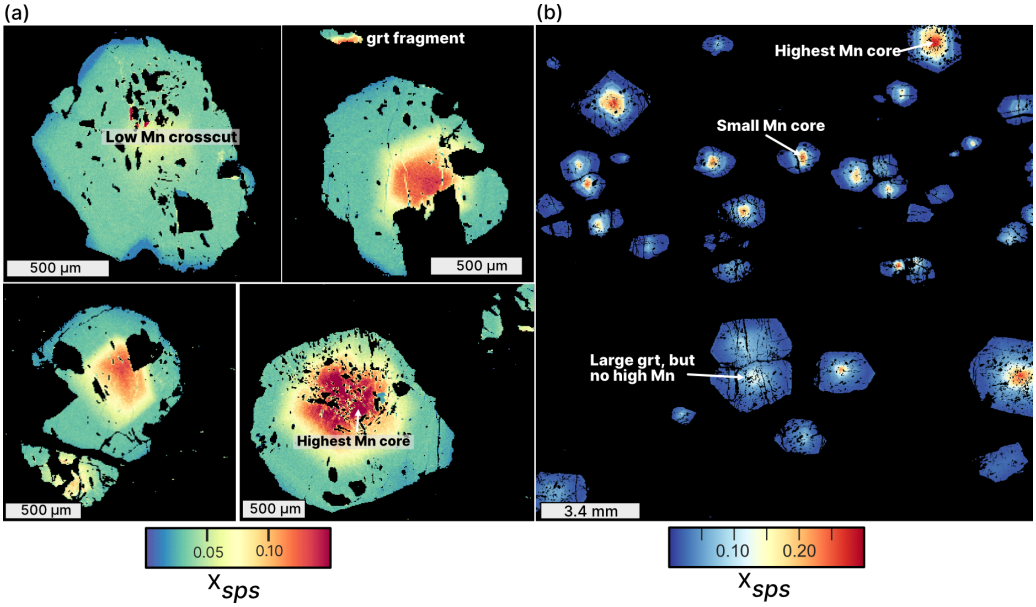

Figure 5.3: Compositional map of spessartine molar fraction acquired by EPMA. (a) Four randomly selected garnets with shape type 1.1 from sample SY21-07, displaying varying cross-sections of garnet cores, highlighted by the higher spessartine content concentrated towards the core. (b) Spessartine map of a region containing garnets from sample SY21-01/2-1, illustrating different cross-sections of garnets within the thin section. Garnet cores are distinguished by their elevated spessartine content.

In sample SY21-07, all garnets exhibit core-to-rim zoning in spessartine content, provided a core can be identified (Figure 5.3a). Among the largest visually selected garnets from SY21-07, only one mapped grain captures the highest spessartine concentration at its core. Garnets of similar size, however, display comparable compositional gradients from core to rim. Fragmented garnets do not consistently preserve high-spessartine regions but demonstrate similar zoning patterns to the larger garnets, with spessartine levels akin to those in the core and mantle of the larger grains. The spatial decrease in spessartine content is more abrupt in these fragments compared to the more gradual core-to-rim transition seen in larger grains.

In sample SY21-01/2-1, the thin section map represents a random 2D slice through various garnet grains of differing shapes and sizes. No clear correlation between garnet size and spessartine content at the slice center is observed (Figure 5.3b). The highest spessartine concentrations occur in some larger and resorbed garnets. Each garnet exhibits a spessartine decrease from center to rim, with most showing a Mn-rich annulus in the mantle of similar intensity. The cores of smaller garnets, which also exhibit high spessartine content, are proportionally smaller compared to those of larger grains. Similarly, the distance between the core and the annulus is narrower in smaller garnets compared to the larger ones.

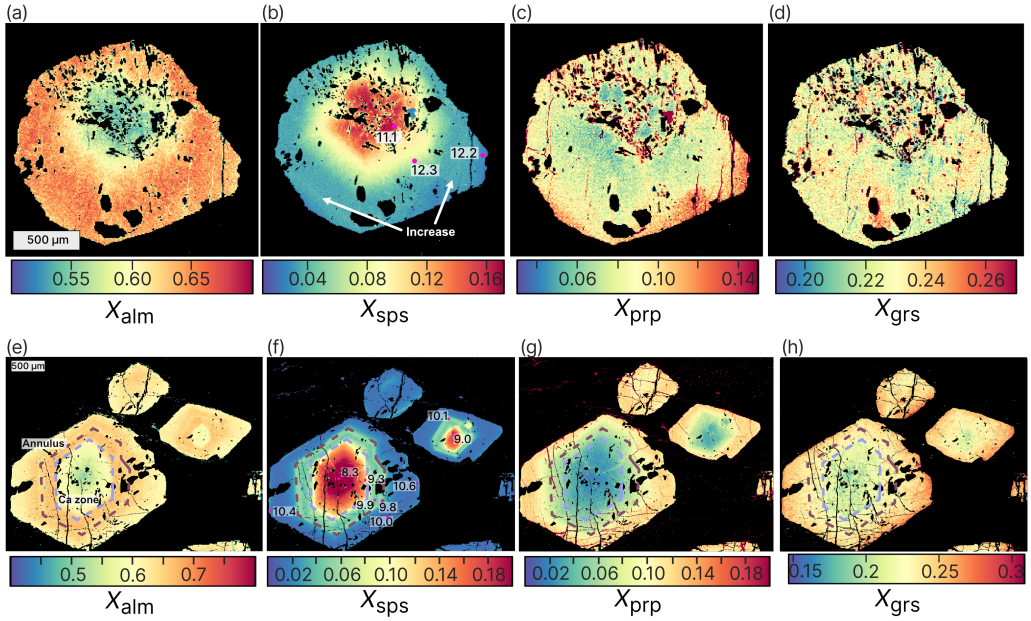

Figure 5.4: Calculated end-member maps of almandine (X_{alm}), spessartine (X_{sps}), pyrope (X_{prp}), and grossular (X_{grs}). (a-d) End-member maps for garnet from sample SY21-07. (b) Includes $\delta^{18}O$ values in garnet from Chapter 4, with the increase in spessartine content in the mantle highlighted. (e-h) End-member maps for garnet from sample SY21-01/2-1. Dashed lines indicate the position of the Ca-rich zone (purple) and the Mn-annulus (brownish). (f) Includes $\delta^{18}O$ values in garnet from Chapter 4.

5.3.3 Trace element zoning and distribution

A total of 48 elements, including major, minor, and trace elements, were measured using LA-ICP-MS mapping. Selected trace element maps highlight key compositional differences and distribution patterns, as shown in Figure 5.5. These maps, covering the multi-mineral phase assemblage, reveal significant variations in composition and zoning within garnet, phengite, glaucophane, epidote, and accessory phases in the two blueschist samples from Achladi (Figure 5.5a-d) and Katergaki (Figure 5.5e-h). The full set of trace element maps is available in the supplementary material S3. Detailed trace element maps of Co, Y, Er, and Lu in garnet are displayed in Figure 5.6 including the in-situ measurements for oxygen isotope composition from Chapter4. Compositional data for garnet, epidote, glaucophane, phengite, apatite, rutile, and titanite were extracted from these maps after phase-specific calibration using XMapTools 4.3 (Lanari et al., 2023). This approach enabled precise targeting of compositionally distinct mineral grains and zones within the maps. The extracted data are presented in spider diagrams in Figures 5.7 and Figure 5.8.

Garnet from Achladi, representing shape 1.1, exhibits a notable increase in Co concentration from core to rim, ranging from 10 to 30 µg/g (Figure 5.6a). The mapped garnet shows a gradual decrease in Y, Er, and Lu from core to mantle (Figure 5.6b-d). The garnet shows a high Y content of ∼1000 µg/g in the core with a diameter of ∼300 µm, while the

mantle is depleted, containing ∼75 µg/g. Within the mantle, there is a slight increase to around 88 µg/g, followed by a drop to approximately 50 µg/g, and a subsequent rise to about 67 µg/g at the rim. This corresponds to a change of ∼43% in Y within the mantle to rim zone. A similar zoning pattern is observed in the heavy rare earth elements (HREEs) (Figure 5.6c-d) and is also reflected in the REE spider diagram (Figure 5.7a).

Garnet from Katergaki, representing shape 2.1, shows an increase in Co concentration from core to rim, ranging from 10 to 40 µg/g (Figure 5.6e). The mapped garnet exhibits more complex zoning patterns in Y, Er, and Lu from core to rim (Figure 5.6f-h). For Yttrium, the core contains ∼700 µg/g and has a diameter of ∼300 µm. Around the core, Y content fluctuates between 200 and 500 µg/g, forming oscillatory zoning that only partially follows the euhedral garnet shape and overlaps with similar zoning found in the grossular content (Figure 5.4h). This initial mantle zone is followed by a sharp increase in Y content to around 600 µg/g, forming an annulus feature that mirrors the garnet's euhedral structure and is closely related to the Mn annulus (highlighted as bronwish dashed line). Beyond this annulus, Y concentrations drop sharply to approximately 100 µg/g at the rim, with a slight rise to about 200 µg/g at the garnet grain boundary. A similar zoning pattern is observed for heavy rare earth elements (HREEs) such as Er and Lu (Figure 5.6g-h), as well as Yb (see Supplementary Material S3). This is also reflected in the REE spider diagram (Figure 5.7d). The annulus feature is also marked by a sharp decrease in the V content (see Supplementary Material S3).

Epidote also incorporates up to 300 µg/g Y alongside garnet (Figure 5.5b,f) and serves as the primary phase incorporating Sr (up to ∼8000 µg/g) in both blueschist samples (Figure 5.5c,g). In sample SY21-07, epidote within the matrix shows Sr zoning from core to rim. The cores of matrix epidote, as well as epidote inclusions within garnet, are relatively enriched in Sr (¿1000 µg/g) compared to the rims of matrix epidote (¡1000 µg/g). In sample SY21-01/2-1, three distinct types of epidote can be identified based on trace element composition and textural association. Epidote 1, included within garnet has the lowest Sr content ∼1000 µg/g. Epidote 2, characterized by diamond-shaped flakes, is relatively enriched in Sr compared to Epidote 1. Epidote 3 in the pressure shadows of garnet has slightly higher Sr content compared to epidote 1, but is lower than epidote 3. Besides Sr, epidote in both samples incorporates Pb and Eu, and also contains trace amounts of Zr (¡12 µg/g) (Supplementary Material S3).

Epidote in sample SY21-07 and epidote 2 in sample SY21-01/2-1 exhibit enrichment in LREEs, similar to their bulk rock composition patterns (Figure 5.7a,d, 5.8a,d). These two epidote groups also show notable enrichment in Th and U, which is not observed in Epidote 1 from SY21-01/2-1.

Phengite is the second most prominent mineral phase for incorporating Sr in the

order of 10 to 100 µg/g (Figure 5.5c,g). The Sr content in phengite is nearly an order of magnitude lower in SY21-07 compared to SY21-01/2-1 although phengite is more abundant in SY21-07. The lithium content ranges from 20 to 40 µg/g in sample SY21-07 and from 0 to 20 µg/g in SY21-01/2-1 (Figure 5.5d,h). Additionally, phengite is the main mineral incorporating B (Supplementary Material S3).

Phengite generally shows low concentrations of LREE with similar patterns in both SY21-07 and SY21-01/2-1 (Figure 5.7b,e). It is also enriched in LILEs such as Rb and Ba in both blueschist samples (Figure 5.8b,e). Notably, in SY21-07, phengite exhibits an anomalously high Nb content, approximately an order of magnitude higher than in SY21-01/2-1.

Glaucophane exhibits the highest lithium (Li) content of up to ∼80 µg/g, in both SY21-07 and SY21-01/2-1 (Figure 5.5d,h). The 200 µm sized glaucophane flakes display slight zoning with a decrease to ∼40 µg/g Li from core to rim in sample SY21-07, whereas glaucophane in SY21-01/2-1 shows and increase from the center to the rim of the grains. Glaucophane is the primary mineral phase incorporating Co, showing slight compositional zoning decreasing from 70 to 50 µg/g from core to rim (Figure 5.6a,e). Additionally, glaucophane incorporates Zn (see Supplementary Material S3). Glaucophane has generally low concentration of REEs in the blueschist samples. Glaucophane from sample SY21-07 is slightly more enriched in REEs compared to SY21-01/2-1 (Figure 5.7b,e).

Apatite in sample SY21-07 exhibits a REE pattern similar to the bulk rock composition but shows slightly higher enrichment in medium REEs (MREEs) (Figure 5.7c). This apatite is also more enriched in LREEs compared to the apatite in sample SY21-01/2-1 (Figure 5.7c,f). Conversely, apatite in SY21-01/2-1 is relatively depleted in LREEs compared to the bulk rock composition (Figure 5.7f). Apatite from SY21-07 is enriched in U and Th (Figure 5.8c), a feature not observed in the apatite from SY21-01/2-1.

Titanite in both samples SY21-07 and SY21-01/2-1 exhibits a pattern of decreasing REE from HREE to LREE (Figure 5.7c,f). In SY21-01/2-1, titanite is relatively enriched in MREEs and HREEs compared to the bulk rock composition and compared to titanite in sample SY21-07. Additionally, titanite in SY21-01/2-1 from the matrix shows a decrease in Eu compared to the titanite included in the garnet grain. Titanite in SY21-01/2-1 also displays higher U content and a positive anomaly for Nb and Ta (Figure 5.7f). The U content in titanite from SY21-07 is nearly one order of magnitude lower compared to titanite in SY21-01/2-1 but also exhibits a positive Nb and Ta anomaly (Figure 5.7c).

Rutile in sample SY21-07 exhibits a REE composition similar to that of titanite in the sample, with enrichment in HREEs relative to LREEs (Figure 5.7c). Additionally, rutile displays a positive anomaly for Nb and Ta in the spider diagram.

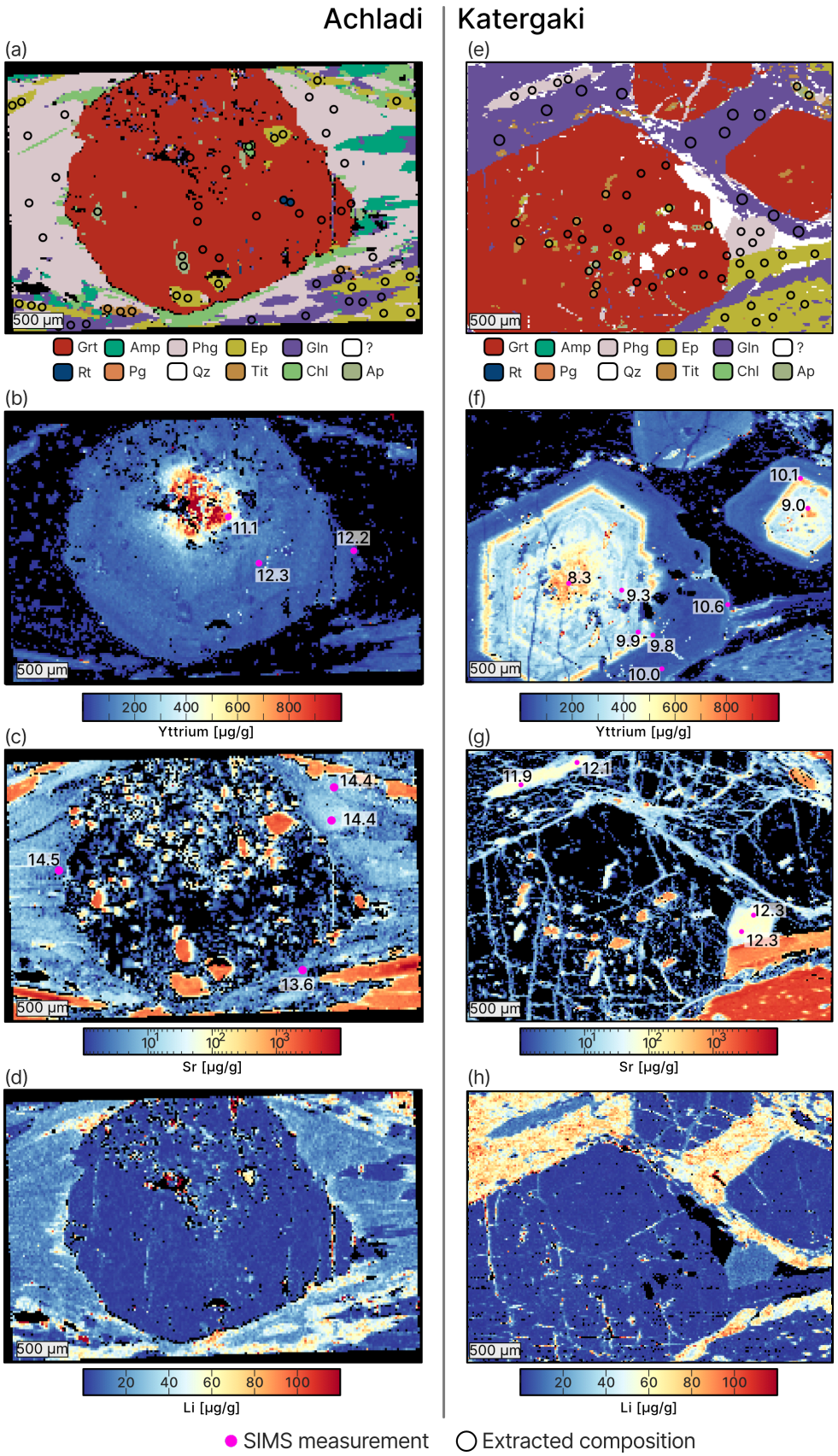

Figure 5.5: Compilation of (a,e) the mineral assemblage, (b,f) calibrated quantitative map of Y, (c,g) calibrated quantitative map of Sr, (d,h) calibrated quantitative map of Li for the two blueschist samples SY21-07 (a-d) and SY21-01/2-1 (e-h). Values of oxygen isotope composition in garnet from Chapter 4 are presented as pink spots in panel b and f. Values of oxygen isotope composition in phengite from Chapter 4 are presented as pink spots in panel c and g. Mineral abbreviations are from Warr (2021).

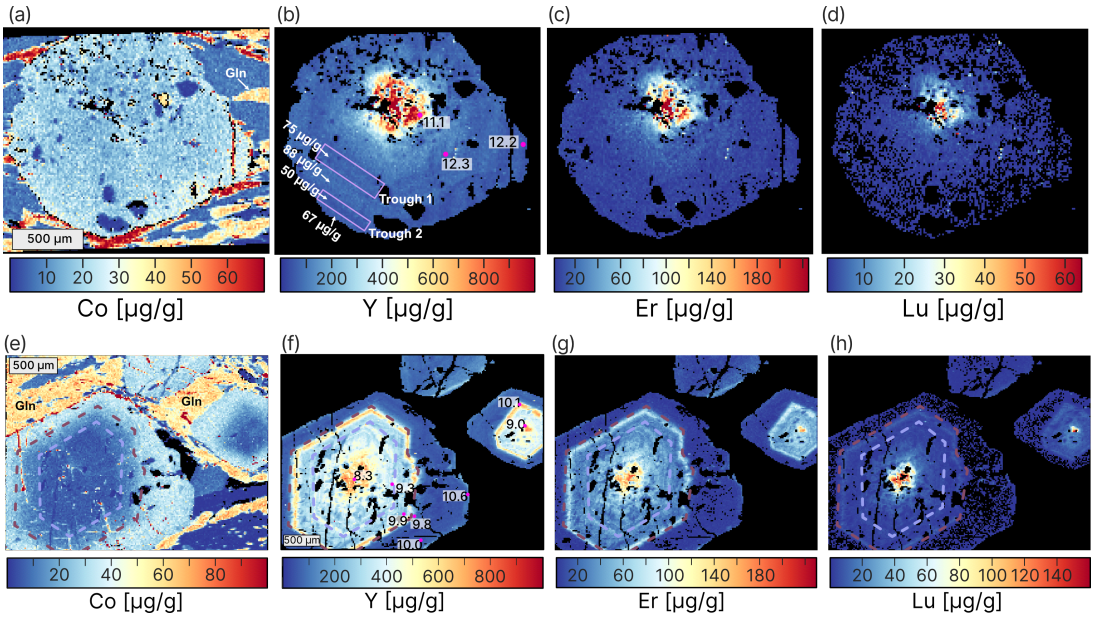

Figure 5.6: LA-ICP-MS element maps for selected trace elements for sample SY21-07 (a-d) and SY21-01/2-1 (e-h). LA-ICP-MS element maps for selected trace elements in samples SY21-07 (a-d) and SY21-01/2-1 (e-h). (a, e) Co content in garnet, glaucophane, and other mineral phases. (b, f) Y content in garnet, with higher concentrations in the core of sample SY21-07, along with associated $\delta^{18}O$ values from Chapter 4. (b) Increases and decreases in Y content, representing peaks and troughs, are highlighted with squares and the average value. (c, g) Er content in garnet, showing higher concentrations in the core of sample SY21-07. (d, h) Lu content in garnet, with higher concentrations in the core of sample SY21-01/2-1. (e-h) Dashed lines indicate the position of the Ca-rich zone (purple) and the Mn-annulus (brownish) visible in the major element maps (Figure 5.4e-h).

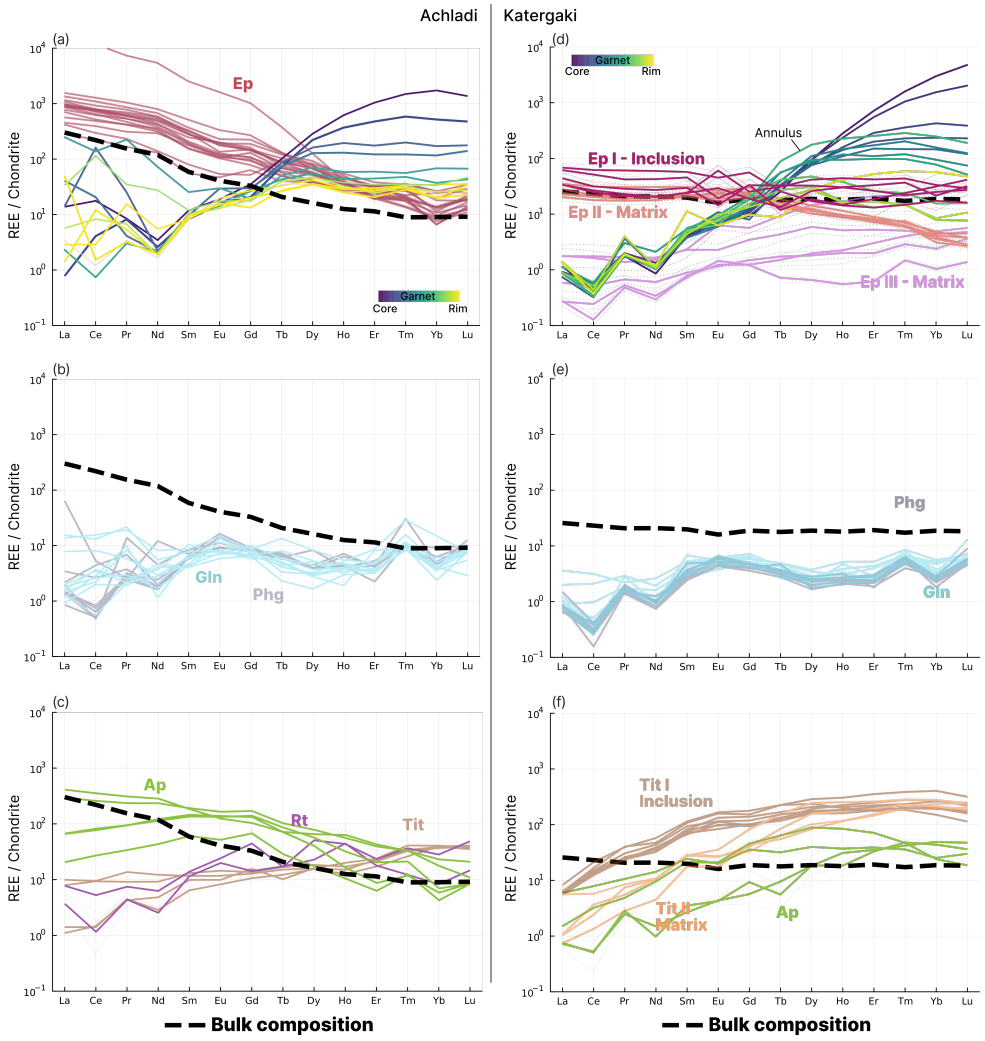

Figure 5.7: REE patterns normalized to chondrite of different mineral phases extracted from circular ROIs (see Figure 5.5a,d) from the calibrated maps (values from Taylor & McLennan, 1985). (a) Garnet pattern from core to rim and epidote pattern in sample SY21-07. (b) Glaucophane and phengite pattern in sample SY21-07. (c) Apatite, rutile, and titanite pattern in sample SY21-07. (d) Garnet pattern from core to rim and epidote pattern in sample SY21-01/2-1. (e) Phengite and glaucophane pattern in sample SY21-01/2-1. (f) Apatite and titanite pattern in sample SY21-01/2-1. Bulk rock REE pattern of the rock samples SY21-07 and SY21-01/2-1 are represented by the dashed black line.

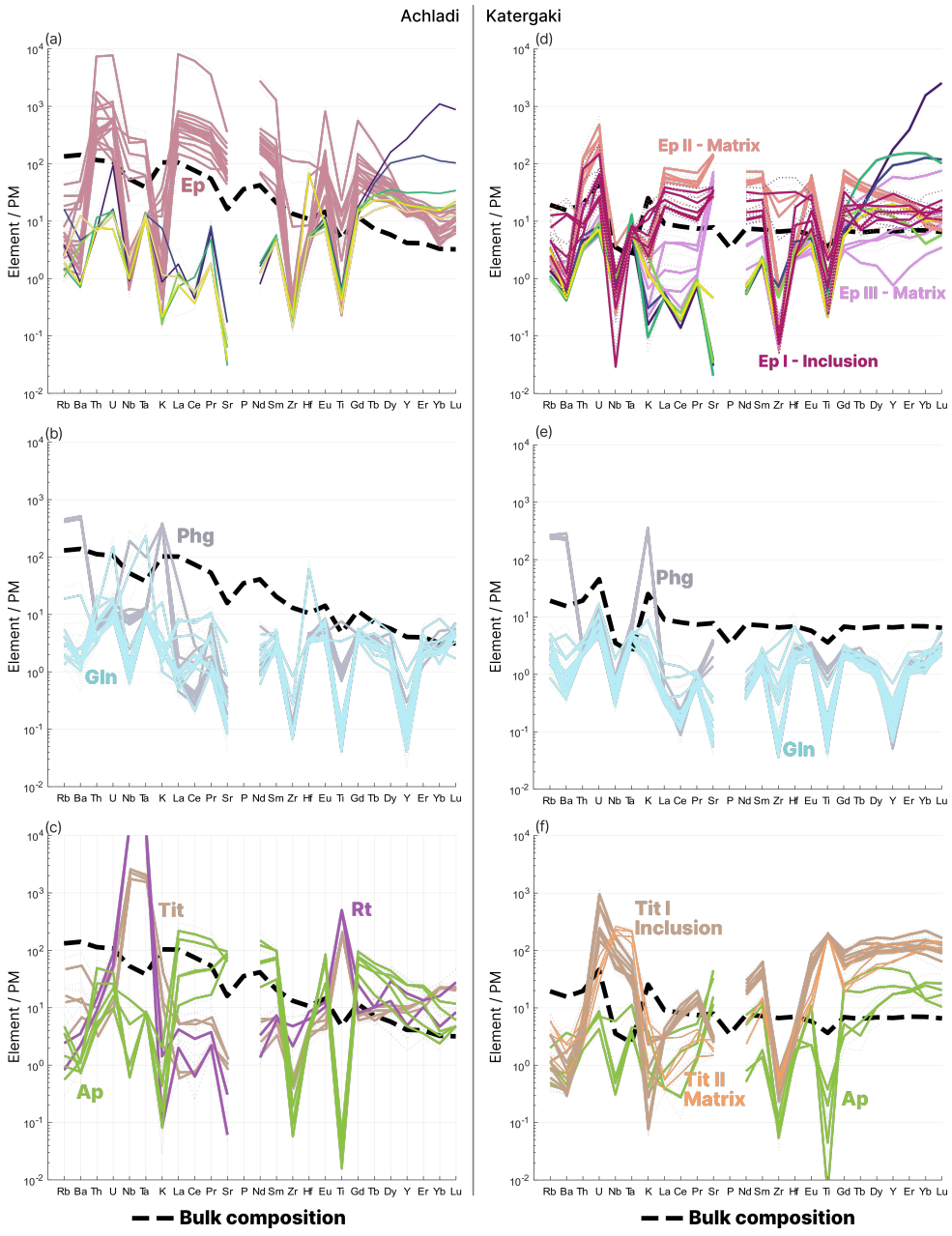

Figure 5.8: Spider diagram showing trace element patterns normalized to primitive mantle of different mineral phases extracted from circular ROIs (see Figure 5.5a,d) from the calibrated maps (values from Sun & McDonough, 1989). (a) Garnet pattern from core to rim and epidote pattern in sample SY21-07. (b) Glaucophane and phengite pattern in sample SY21-07. (c) Apatite, rutile, and titanite pattern in sample SY21-07. (d) Garnet pattern from core to rim and epidote pattern in sample SY21-01/2-1. (e) Phengite and glaucophane pattern in sample SY21-01/2-1. (f) Apatite and titanite pattern in sample SY21-01/2-1. Bulk rock REE pattern of the rock samples SY21-07 and SY21-01/2-1 are represented by the dashed black line.

5.3.4 Phase assemblage modelling, garnet growth and fluid pressure

Petrochemical modelling for samples SY21-07 and SY21-01/2-1 was performed in Chapter 4 on the prograde path from Skelton et al. (2019) ranging between 355 °C, 1.10 GPa and 535 °C, 2.00 GPa using the modelling software ThorPT developed in Chapter 3. Modelling results visible in Figure 5.9 show the predicted evolution of the i) stable mineral phase assemblage, ii) fluid extraction, iii) garnet growth, and iv) fluid pressure changes, relative to the fluid pressure before volume changes. All extractions are associated to pure extensional failure (red diamonds in Figure 5.9a,c; see Chapter 3 for detailed explanation). The relative fluid pressure change indicates a deviation of the fluid pressure from the calculated pressure at the beginning caused by volume changes of the system (solids and fluid volumes).

For sample SY21-07, garnet growth and fluid production are predicted to occur between 375 °C and ∼1.20 GPa, continuing until the end of the model at 535 °C and 2.00 GPa (Figure 5.9a). During garnet growth, fluid pressure exhibits three notable deviations from the initial conditions, ranging from 1.0 to 4.0 MPa (Figure 5.9b). Despite these fluctuations, the fluid pressure remains relatively stable throughout the growth process. The first significant phase of fluid production and extraction is linked to the consumption of chlorite, which occurs until ∼430 °C and ∼1.50 GPa. This phase is associated with a predicted fluid release of 1 vol% and a decrease in the volume of the mineral assemblage (Figure 5.9a). This release correlates with a fluid pressure deviation of ∼4 MPa during garnet growth (Figure 5.9b). A second major fluid release, amounting to 4 vol%, is predicted to occur between ∼480 °C and ∼1.70 GPa, towards the end of the model. This event is associated with the dehydration of both chlorite and lawsonite, as well as the increased formation of glaucophane and garnet. The resulting fluid release is coupled with two fluid pressure deviations between 2.0 and 4.0 MPa, coinciding with an increased garnet growth representing 5-10 vol% of the mineral assemblage.

For sample SY21-01/2-1, fluid production is predicted to begin at ∼420 °C and ∼1.40 GPa, continuing until the end of the model (Figure 5.9c). Garnet nucleation occurs early, starting at 375 °C and 1.10 GPa, with growth predicted along the entire prograde path (Figure 5.9c-d). The first phase of fluid production and extraction is linked to chlorite consumption between 420-430 °C and 1.40-1.50 GPa, corresponding to a release of ∼0.5 vol%. This is associated with a fluid pressure deviation of ∼1.7 MPa, and no new garnet forms during this stage (Figure 5.9d). Subsequent fluid production, driven by lawsonite dehydration, is minor, with fluid pressure remaining relatively constant, deviating by less than 0.5 MPa. An increased fluid production of 0.8 vol% is predicted after ∼510 °C and ∼1.80 GPa, associated with the dehydration of lawsonite and glaucophane. This phase coincides with increased garnet stabilization, and the fluid pressure deviates by less than 0.5 MPa from the starting conditions.

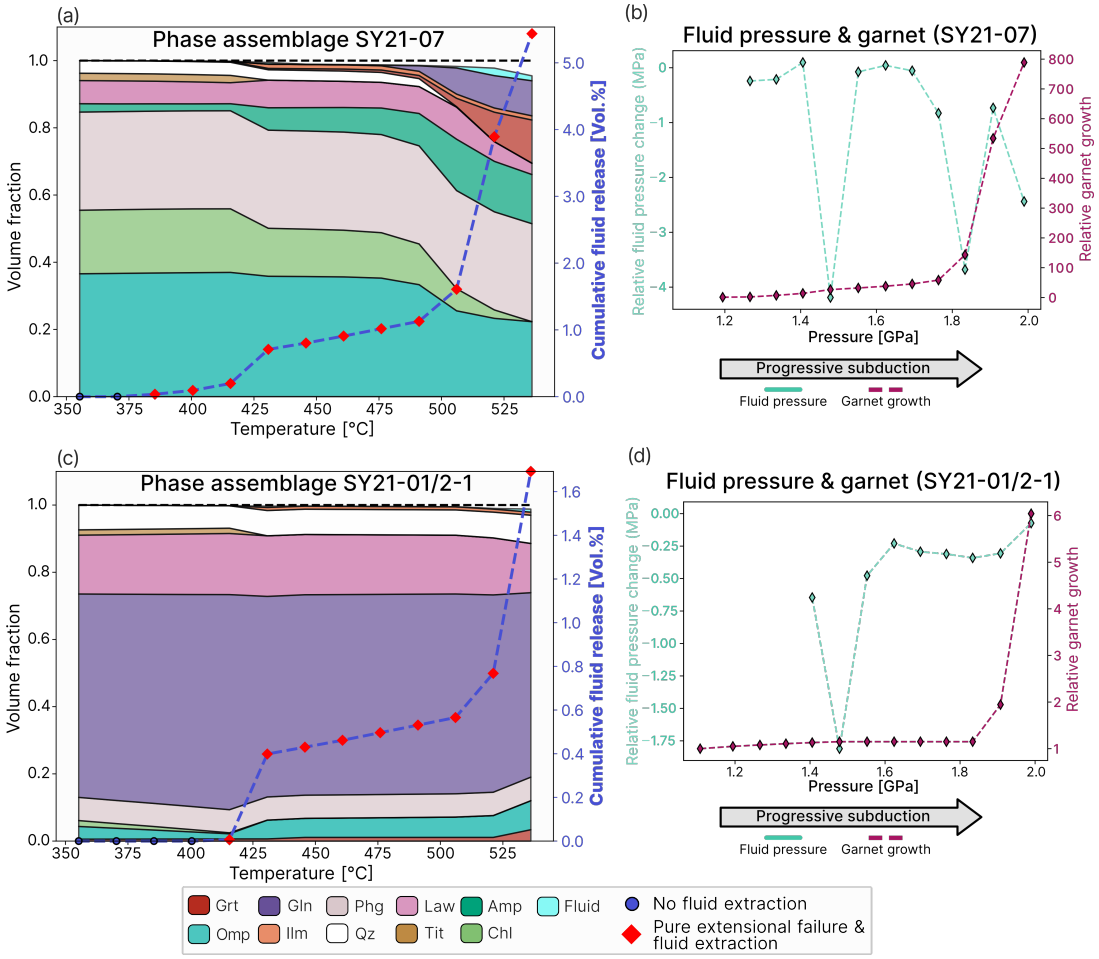

Figure 5.9: Phase assemblage and mechanical modelling results. (a,c) Box mode diagrams showing the phase assemblage of sample SY21-07 (a) and SY21-01/2-1 (c). The red diamonds indicate brittle failure and fluid extraction evaluated by the mechanical model (see Chapter 3 for details). (b,d) Relative fluid pressure change in blue and relative garnet growth in red for sample SY21-07 (b) and SY21-01/2-1 (d). Relative fluid pressure change is due to volume changes in the system before failure (see text for details). Relative garnet growth is expressed as the increase of garnet abundance compared to the first garnet formation. Mineral abbreviations are after Warr, 2021.

5.4 Discussion

5.4.1 Porphyroblast growth, distribution and shape

The distribution of porphyroblasts in both blueschist samples generally follows a log-normal pattern (Figure 5.2), which is typically associated with progressive nucleation and crystallization as the reactive bulk rock composition evolves over time (Carlson, 1989; Carlson et al., 1995; Denison & Carlson, 1997; George & Gaidies, 2017; Kretz, 1974). However, the distribution, visualized by the KDE curve, also reveals distinct humps — an unusual feature for a crystal size distribution (CSD) that is solely growth-controlled.

The overall log-normal trend can be attributed to the production of a limited number of nucleation sites during early stages of garnet stability, on which there is considerable growth to form large garnet porphyroblasts. The number of nucleation sites increases over time, with relatively lower growth rates on these grains forming smaller garnet porphyroblasts. In both samples, SY21-07 and SY21-01/2-1, porphyroblast density is notably higher in specific bands, suggesting preferential garnet nucleation in these areas (Figure 5.1). An extreme example of this preferred growth is observed in the drill core of sample SY21-01/2-1, where the eclogite volume shows a significantly lower porphyroblast density compared to the blueschist section at the top (Figure 5.1c), indicating compositionally dependent growth.

The humps in the CSD suggest a deviation from the typical log-normal distribution, likely due to a combination of factors. These include resorbed and chloritized garnet grains (e.g., shapes 1.2, and 2.3 in Figure 5.0), fragmented garnet pieces (shapes 1.3, 1.4, and 2.2), and deformation features such as cracked and resorbed garnets (e.g., shapes 1.2, 2.3, and 2.4), which may artificially elongate the segmented garnet volumes.

The classified and segmented voxels of garnet provide a detailed visualization of garnet grains in both 2D and 3D (see Figure 5.0b,d,e). When examining the thin section microphotographs (Figure 5.0a,c) and corresponding segmented 2D images (Figure 5.0b,d,e), it is evident that the garnet porphyroblasts in sample SY21-07 (Achladi sequence) and SY21-01/2-1 (Katergaki sequence) contain mineral inclusions, particularly in the larger grains. Notably, sample SY21-07 appears to have more inclusions than sample SY21-01/2-1. This observation is further supported by the 3D thickness-mesh, which represents the density of segmented voxels for each porphyroblast. Lower density mesh values, shown in blue, indicate areas with fewer voxels to the grain boundaries (thinner regions), whereas higher values, shown in yellow, correspond to regions with more voxels to the grain boundaries (thicker regions).

A comparison of the 2D and 3D images confirms that garnet in sample SY21-07 contains

more inclusions, which correlates with lower thickness-mesh values (e.g., porphyroblast shape 1.1 in Figure 5.0b). Conversely, more intact garnets, such as shape 2.1, or smaller fragments show fewer inclusions and correspond to higher thickness-mesh values (Figure 5.0d). Garnet with significant cracking, like shape 2.3, exhibits lower thickness-mesh values overall, but maintain higher values in more coherent grain regions.

In both samples, porphyroblast growth seems to have favored surface growth over equilibration with the surrounding matrix phases, as indicated by the abundance of inclusions in the garnets (Konrad-Schmolke et al., 2023). The modelled garnet abundance in the phase assemblage shows a consistent increase in garnet volume with increasing pressure (P) and temperature (T) for both samples (Figure 5.9). However, garnet abundance relative to the start of nucleation increases much more steeply in sample SY21-07 (Figure 5.9b), representing an increased stability if garnet with rising temperatures. Increased garnet stability potentially indicates also a faster growth rate, as the increased stabilization in the model imitates increases from simulations of porphyroblast crystallization e.g., by Carlson (1989). An increased growth rate in turn would explain the higher number of inclusions, in SY21-07 (apatite, epidote, galucophane, rutile), as faster-growing crystals tend to trap more inclusions (Konrad-Schmolke et al., 2023). The rutile inclusion emphasizes the growth of garnet during prograde metamorphism and at higher P–T conditions close to peak metamorphic conditions of 2 GPa. In contrast, sample SY21-01/2-1 shows a more gradual increase in garnet abundance, about two orders of magnitude smaller than in SY21-07, indicating slower growth. This slower growth is consistent with the observed lower number of inclusions in the garnet (Figure 5.9d). Furthermore, inclusions of titanite from core to mantle are probably linked to early garnet growth during prograde metamorphism at temperatures below 425 °C as indicated by the stability of garnet an titanite in Figure 5.9c and would be in accordance with titanite growth in metabasites (Frost et al., 2001).

The garnets in the two blueschist samples show clear evidence of excavation around earlier inclusion sites, with dissolved and fractured garnets closely associated with chlorite (Figure 5.0). Previous studies have demonstrated that dissolution reactions in retrogressed mafic eclogites preferentially affect larger garnet grains, are associated with atoll garnet textures and can be triggered by water release during lawsonite breakdown along the retrograde path (Hartmeier et al., 2024). Given that lawsonite is a common mineral in the blueschists of Syros, and lawsonite pseudomorphs, composed of white mica and epidote, are frequently observed in the matrix but also as garnet inclusions (see Hamelin et al., 2018, Figure 5.0 and Chapter 4), it is likely that the dissolution and fracturing of garnet porphyroblasts in both SY21-07 and SY21-01/2-1 are linked to a similar process of lawsonite breakdown-induced garnet resorption. This consequently influences the CSD and is probably represented by the hump in the KDE e.g., for group 1.1 and 1.2 in Figure 5.2a.

In sample SY21-07, most garnets appear as porphyroblasts with pressure shadows of phengite (Figure 5.0a). The presence of phengite in these pressure shadows suggests syntectonic growth, while matrix phases such as glaucophane and epidote, which align with the foliation, indicate growth prior to deformation. The smallest garnet fraction (grain types 1.3 and 1.4) appears homogeneously distributed across the porphyroblast bands (Figure 5.1a,b). These smaller grains are less associated with phengite and more frequently accompanied by chlorite. One possible explanation for this distribution and mineral association is that these smaller grains may represent a mixture of strongly resorbed garnets and broken-off fragments of larger garnets. These fragments were likely mechanically redistributed within the porphyroblast bands during deformation, as indicated by the foliation direction and pressure shadows.

In summary, the log-normal distribution observed in the samples suggests progressive nucleation and growth of porphyroblasts in the two blueschist samples. This pattern indicates that diffusion was not the primary limiting factor for garnet nucleation and growth. In a scenario of diffusion-controlled growth, garnet would be expected to deplete nutrients from the surrounding rock volume, thereby suppressing further nucleation and growth (Carlson et al., 1995; Denison & Carlson, 1997). However, this is not observed, as similarly sized garnet grains are found in contact with one another (see Figure 5.0 and 5.4). While this does not entirely rule out diffusion-controlled growth, it suggests that garnet growth was slower than nutrient transport within the rock, especially for the relatively fast diffusing major elements. This could be emphasized by the expected water-saturated conditions during garnet growth, evidenced by typical prograde garnet zoning patterns (e.g., Konrad-Schmolke et al., 2006, see Figure 5.4). Therefore, compositional zoning of major and trace elements in garnet could offer further insights into the growth processes (e.g., Daniel & Spear, 1999; Denison & Carlson, 1997; Gaidies et al., 2017; George & Gaidies, 2017; George et al., 2018). In the next section, we will analyze the major and trace element zoning of garnets from the blueschist samples collected at Achladi and Katergaki.

5.4.2 Zoning patterns in porphyroblasts

The compositional zoning pattern of a prograde metamorphic garnet porphyroblast growing during subduction is expected to be influenced by disequilibrium and/or fractionation processes, driven by changes in the reactive bulk rock composition (Carlson, 1989; Chernoff & Carlson, 1997; Chernoff & Carlson, 1999; Daniel & Spear, 1999; Gaidies et al., 2017; George et al., 2018; Hickmott & Spear, 1992; Konrad-Schmolke et al., 2005; Konrad-Schmolke et al., 2006; Lanari et al., 2017). In addition, intra-grain diffusion can modify this compositional zoning for relatively high temperatures above 550 °C (e.g., Caddick et al., 2010; Konrad-Schmolke et al., 2006; Page et al., 2014). For samples from Syros

it has been shown that they experienced lower temperatures (Gorce et al., 2021; Laurent et al., 2018; Skelton et al., 2019; Tual et al., 2022) and therefore significant modification by diffusion can be disregarded in the two studied blueschist samples.

In the analyzed blueschist samples SY21-07 and SY21-01/2-1, the largest garnets — representing shapes 1.1 and 2.1, respectively — exhibit a classic prograde growth zoning pattern in major elements similar to other high-pressure rocks on Syros (e.g., Gorce et al., 2021; Laurent et al., 2018; Skelton et al., 2019; Tual et al., 2022, see Figure 5.4). This pattern suggests that garnet formed during dehydration, under water-saturated conditions, as indicated by the increase in pyrope content from core to rim and the bell-shaped distribution of spessartine (e.g., Konrad-Schmolke et al., 2006, 2023, see Chapter 4 for further comparison). Such zoning is consistent with garnet that grew with an evolving reactive bulk rock composition to the fractionation of elements in garnet during growth (e.g., Evans, 2004; George & Gaidies, 2017; Hollister, 1966; Konrad-Schmolke et al., 2023; Lanari et al., 2017; Tracy, 1982; Trzcienski, 1977). Additionally, in both blueschist samples, similarly sized garnets exhibit comparable compositional gradients, evident in the consistent distribution of spessartine content from core to mantle to rim (Figure 5.3). In contrast, smaller garnets display a similar spessartine content in the core and record the same garnet growth history, including the Mn annulus in sample SY21-01/2-1. However, the distances between the core and annulus, as well as between the core and mantle, are smaller in comparison to larger grains (Figure 5.3b). In a diffusion-controlled growth model, it is typically expected that the compositional gradient decreases with increasing porphyroblast size - this is not observed. In comparison, interface-controlled growth has been shown to lead to size-dependent garnet growth, favoring larger crystals (e.g., Gaidies et al., 2017; George & Gaidies, 2017). As a result, smaller porphyroblasts exhibit steeper compositional gradients, as they grow more slowly while the surrounding rock composition continues to evolve. This theory corroborates the observed compositional zoning patterns in the two blueschist samples.

In addition to Mn, the garnet cores in both blueschist samples show enrichment in Y and REEs, although these elements form a smaller core with about 60% of the diameter relative to the high-Mn zone, with a more pronounced and rapid decrease towards the mantle and rim. This trend is particularly evident in the Achladi sample (Figure 5.4b and 5.6b). The smaller core diameter and steeper decrease in Y and REEs are expected in garnets growing under diffusion-controlled conditions, as REEs typically diffuse slowly compared to major cations such as Fe, Mn, and Mg (Carlson, 2012; Chernoff & Carlson, 1999; George et al., 2018; Kohn, 2004; Konrad-Schmolke et al., 2023).

In porphyroblast populations, smaller garnets tend to show smaller enriched cores, sharper gradients towards the rim, and lower overall trace element concentrations (e.g., Y

and REEs). This may result from later nucleation and increased competition for nutrients during growth (e.g., George et al., 2018). Such behavior can be observed in sample SY21-01/2-1, where a smaller adjacent garnet grain, which cuts through or near the grain geometric center, displays a smaller core diameter and slightly lower trace element contents (Figure 5.3b, 5.4e-h, 5.6e-h). These observations align with a model where competition for nutrients within a diffusion-limited rock volume influences the compositional zoning of garnets.

Achladi

The zoning from mantle to rim in garnet sample SY21-07 shows significant fluctuations in trace elements such as Y and REEs, with Y varying by up to 40% (Figure 5.6b). These fluctuations may arise from changes in pressure and temperature during garnet growth (Kohn, 2004; Skora et al., 2006; Viete et al., 2018), although significant variations in these factors are unlikely along the prograde P–T path. According to Hickmott and Spear, 1992, pressure drops of <100 MPa can reduce the amount of Mn, Y, and REEs incorporated in garnet. In sample SY21-07, two troughs of low Mn and Y+REE content are observed, that could indicate episodic fluctuations in fluid pressure during garnet growth (Figure 5.4b, 5.6b). One plausible explanation for these episodic changes in fluid pressure can be found in the occurrence of devolatilization reactions during prograde metamorphism. Previous studies have shown that devolatilization can cause fluctuations in fluid pressure (e.g., Connolly, 1997; Oliver & Bons, 2001). As shown in Figure 5.9a, brittle failure is predicted during chlorite and lawsonite dehydration. These dehydration reactions lead to episodic changes in fluid pressure and three major deviation of up to 4 MPa are predicted during garnet growth (Figure 5.9b). The first fluid pressure deviation occurs near 1.5 GPa, shortly after garnet nucleation. Assuming that at this point the garnet core has formed as predicted by the model, this coincides with the first trough observed in the Y content of the garnet mantle (Figure 5.6b). Following this, garnet growth continues as fluid pressure stabilizes, which may correspond to the observed increase in Y content in the newly formed garnet. Two additional pulses of fluid pressure change are predicted after 1.8 GPa, aligning with the second trough in Y content seen in the natural garnet. In the model, these two pulses are also associated with an drastic increase in the predicted amount of garnet, which could indicate an acceleration in the growth rate similar to descriptions by Kretz (1993). After this trough, Y content increases once more, before the garnet ultimately undergoes resorption.

Alternatively, variations in zoning could be driven by changes in growth rates (George & Gaidies, 2017; Skora et al., 2006), potentially coupled with shifts in element availability. In sample SY21-07, garnet growth seems to accelerate with increasing temperature (Figure

5.9b), suggesting that more garnet forms under higher temperature conditions. This accelerated growth, combined with diffusion limitations, may account for the observed zoning patterns of REEs in the garnet rims. However, a constantly increase in garnet growth does not fully account for the episodic troughs and peaks observed in the garnet rims.

In conclusion, the petrological model of fluid pressure fluctuations, driven by fluid production and extraction, may provide a plausible explanation for the observed variations in REE content in garnet from sample SY21-07. The episodic pressure changes during prograde metamorphism likely contributed to the troughs and peaks in trace element concentrations, particularly in Y and REEs. While this model aligns well with the current observations, further investigation across additional samples is necessary to fully confirm and refine this interpretation in future research.

Katergaki

In sample SY21-01/2-1, similar fluctuations in Y+REE contents but also Ca are observed around the core. In addition an annulus with increased Y, REE, and Mn content is visible. Profiles of Y, Ca, and Mn highlight their positional overlap and differences in the mantle and annulus (Figure 5.10). Typically, Ca and Y+REE are expected to diffuse similarly during garnet growth (e.g., Chernoff & Carlson, 1997; Chernoff & Carlson, 1999; Kohn, 2004), which would indicate a process linked to transport limitations of these elements.

Yttrium varies in the fluctuation zone by approximately 100 µg/g corresponding to 30% absolute variation (Figure 5.10b). However, this variation is not mirrored in the Mn content. Similarly to SY21-07, modelling results for SY21-01/2-1 predict a fluid pressure change during garnet growth associated with glaucophane breakdown (Figure 5.9c-d). Considering the system on its own, the fluid pressure deviation events show a magnitude of 0.4 to 1.8 MPa and are smaller compared to the sample from Achladi. Further, the pressure deviation would indicate a limited transport of Y+REE, which should correspond to lower contents. Nevertheless, this does not correlate with the increases observed for Y+REE in the annulus or the fluctuations in the mantle (Figure 5.10 and 5.6f-h). Additionally, the element fluctuations are also observed in the grossular content, which overlaps with Y (see Figure 5.10b). This behaviour was not observed in sample SY21-07. This suggests that factors other than fluid pressure drops in a closed system may have influenced the chemical variations in sample SY21-01/2-1. Following, trace element variations cannot be determined with this model without considering the breakdown of Y+REE bearing phases and/or open system behaviour.

The annuli of Y and REEs (rare earth elements) exhibit no shift in position toward the rim, which suggests that the transport of these elements is not limited by diffusion in the matrix. In diffusion-limited uptake scenarios, one would expect the annulus to

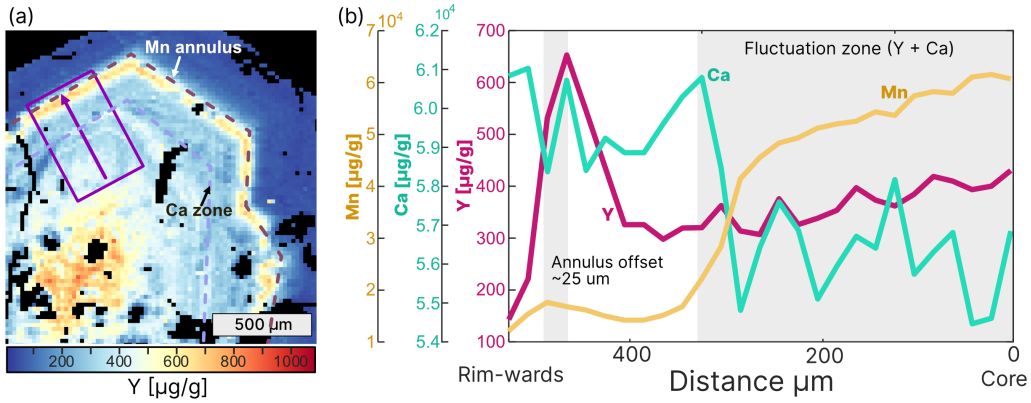

Figure 5.10: Compositional zoning of major and trace elements in garnet from blueschist sample SY21-01/2-1. (a) Zoom-in of the Y element map in garnet, with the extracted transect marked in purple. The Ca zoning is indicated by the purple dashed line, and the position of the Mn annulus is marked by the brown dashed line. (b) Profiles of Mn, Ca, and Y along the extracted transect. The region of element fluctuations in Y and Ca, along with the ~25 µm offset between the Mn and Y annuli, is shaded in gray.

migrate toward the rim for elements with increasing ionic radii (e.g., the increase between Lu to Sm) as demonstrated by Skora et al. (2006). The possibility of an influence on the annulus position and zoning due to the spatial resolution used (12 µm) is ruled out, since no positional shift is observed at any point along the annulus, even though the scanning direction (from left to right in Figure 5.6) crosses the annulus at varying angles (Markmann et al., 2024).

Conversely, there is a noticeable offset of approximately 25 µm between the positions of Y (or REEs) and Mn (and similarly Fe) following the Y+REE annulus (Figure 5.6f-h and 5.10b). If the Mn or Y+REE annuli were controlled by garnet dissolution and reprecipitation, one would expect a steeper gradient on the inner side of the annulus. However, the transects reveal an even gradient for Y and an inverted gradient for Mn, contrary to expectations (Yang & Rivers, 2002).

Optionally, the change in Mn and Y+REE in the garnet could be associated with the breakdown of minerals such as titanite, epidote, or lawsonite.

- The breakdown of titanite is expected to release Y and heavy rare earth elements (HREE) (Garber et al., 2017; Kohn, 2017; Konrad-Schmolke et al., 2023). The enrichment of these elements in titanite inclusions is visible in Figure 5.7f. Notably, titanite inclusions are predominantly located within the inner mantle of the garnet, and there is no spatial overlap between these inclusions and the Y (or REE) or Mn (or Fe) annulus. Additionally, the breakdown of titanite is predicted to occur simultaneously with garnet growth, as indicated in Figure 5.9c.

- Lawsonite breakdown is also predicted in the model (Figure 5.9c). Lawsonite can

contain up to 17 wt% Ca, as well as significant quantities of REE, Sr, and Pb. The matrix epidote shows enrichment in LREE and Sr (Figure 5.5g, Figure 5.7d), and a similar enrichment is visible in Pb (see Supplementary Material S3), suggesting a formation after lawsonite. This may have occurred similar to a reaction such as 52 Lws + 5 Gln = 26 Czo + 10 Pg + 3 Chl + 27 Qz + 74 H2O (Hamelin et al., 2018). However, lawsonite breakdown typically results in an annulus forming at the same position for Mn and Y+REE (**Yang2002**), which is not the case for sample SY21-01/2-1. This discrepancy might suggest an external contribution to the element budget of the blueschist at Katergaki during garnet growth.

Furthermore, the oxygen isotope composition in the garnet from sample SY21-01/2-1 shows an increase from core to rim of more than 2‰, which was interpreted as evidence of modification of the bulk rock $\delta^{18}O$ during garnet growth (Chapter 4). This increase was attributed to the infiltration of an externally-derived mafic fluid, as it could not be explained by a simple, semi-closed evolving mineral assemblage fractionating garnet and fluid at increasing temperatures. The presence of this externally-derived fluid offers another explanation for the distinct changes observed in the garnet composition in both major and trace elements, as released elements are distributed by the fluid, which elevates pore fluid pressures (e.g., Connolly, 1997; Oliver & Bons, 2001).

Figure 5.11 shows the modelled fluid fluxes into the mafic boudin at Katergaki (sample SY21-01/2-1), after it had been expelled from a dehydrating mafic sequence and interacted with a quartz-phengite schist sequence before infiltration into the mafic boudin. The model predicts three pulses of fluid influx, driven by dehydration in the external mafic rock: the first pulse corresponds to chlorite dehydration, the second to chlorite plus lawsonite breakdown, and the final pulse to lawsonite decomposition. These fluid infiltrations occurred during garnet growth, after the formation of the garnet core. Similar pulse-like fluid fluxes have been shown to affect the interconnectivity within the transport matrix (Cruz-Uribe et al., 2021; Kohn, 2004; Konrad-Schmolke et al., 2023). Such a mechanism could explain the infiltration of external fluids into the sampled outcrop at Katergaki.

By comparing garnet zoning with the modelling results, the first two fluid fluxes, associated with chlorite breakdown, could have influenced the availability of Ca and REEs at Katergaki. Chlorite does not release significant amounts of Mn, which might explain the absence of a Mn annulus alongside the Y+REE annulus. In addition, the breakdown of chlorite can also liberate Co (**2018**) and a increase of Co is visible before the annulus in Y+REE (Figure 5.6e). Nevertheless also glaucophane is a major Co-bearing phase and shows a decrease in the rims, which could indicate a release of Co. However, the infiltrating fluid could have scavenged Mn by interacting with the surrounding lithologies, such as the quartz-phengite schist at Katergaki. Moreover, the predicted breakdown of lawsonite,

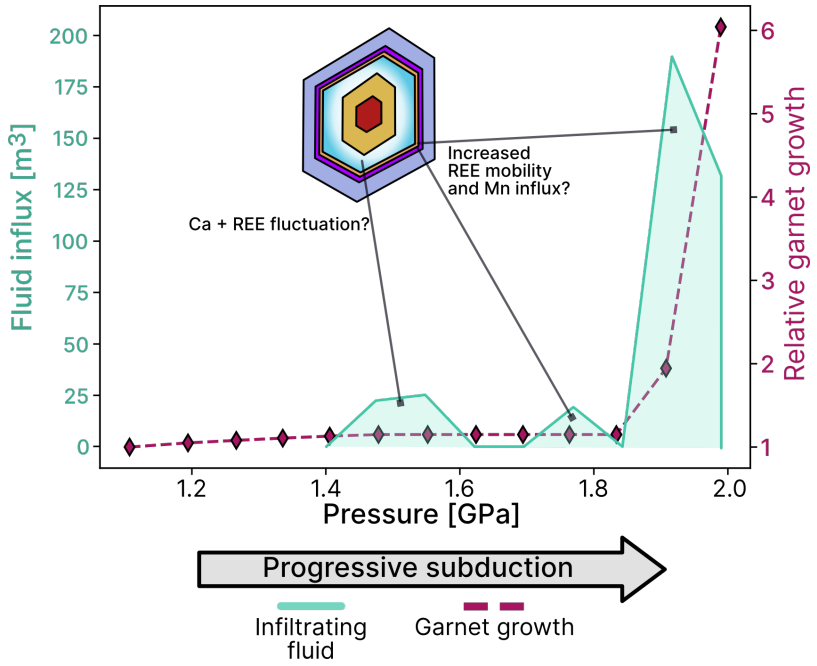

Figure 5.11: Modelling results from Chapter 4 showing the calculated fluid volume influx into the mafic boudin of Katergaki, which is represented by the sample SY21-01/-2-1. The infiltrating fluid was expelled from a mafic sequence and interacted with a sequence of qz-phg schist before infiltrating the mafic boudin at Katergaki.

which releases significant REE and some Mn, could account for the annuli visible in the garnet mantle.

Based on the available data from sample SY21-01/2-1, it is not clear how the annulus in the major elements and the trace elements evolved, but it is likely related to the breakdown reactions of chlorite, titanite, and/or lawsonite which occurred during garnet growth, altering the interconnectivity within the transport matrix. This process influenced the availability of elements during garnet crystallization, with the breakdown of titanite and/or lawsonite releasing REEs, which were subsequently incorporated into the garnet. Additionally, these breakdown reactions may be responsible for fluid influx from an external source, as suggested by the isotopic data and modelling in Chapter 4. This externally-derived fluid could have interacted with the surrounding quartz-phengite schist at Katergaki. This interaction could lead to an increase of fluid mobile elements scavenged in the schist such as Li, Co, Zn, or LILE, which could be incorporated into phengite or glaucophane of the fluid-infiltrated rock.

5.4.3 Trace element distribution in the blueschist mineral assemblages

The bulk rock compositions from Achladi and Katergaki show distinct differences in trace element content. Achladi has higher contents of LREE, is enriched in fluid-mobile ele-

ments (e.g., LILE), and exhibits elevated levels of Th, Nb and Ta compared to the sample from Katergaki (Figure 5.7 and 5.8). These bulk compositional differences are reflected in the trace element composition of e.g., garnet, epidote and titanite in the two samples. For instance, garnet in sample SY21-01/2-1 shows higher contents of HREE in the core compared to sample SY21-07. Epidote in sample SY21-07 from Achladi is enriched in LREE and Th compared to epidotes in SY21-01/2-1 (Figure 5.8a,d). Similarly, titanite in SY21-07 contains higher concentrations of Nb and Ta than in SY21-01/2-1 (Figure 5.8c,f).

The dominant matrix phases, glaucophane and phengite, exhibit similar trace element contents (e.g., LILE). The similar content of such matrix phases supports the findings from Spandler et al. (2003), arguing that no significant quantities of trace elements are liberated during prograde metamorphism whereas the oxygen isotope composition points to significant fluid-rock interaction (see Chapter 4).

Nevertheless, the opposing zoning of Li between glaucophane in the two samples may challenge this missing transport. In SY21-07, Li decreases from core to rim, while in SY21-01/2-1, Li increases towards the rim (Figure 5.5d,h). This Li enrichment in SY21-01/2-1 may be linked to the breakdown of lawsonite, which can release Li, or to Li-bearing fluids that interacted with the surrounding quartz-phengite schists.

5.5 Conclusion

The nucleation and growth process of garnet porphyroblasts in the two blueschist samples generally shows strong similarities. Both samples have log-normal CSDs, similar major element zoning in the inner part of garnet, and typical prograde garnet compositions from core to mantle i.e., spessartine cores found in different porphyroblast sizes. Furthermore, the steeper compositional gradients for smaller garnet grains found in sample SY21-01/2-1 strongly suggest that garnet porphyroblast growth was interface-controlled similar to samples from Gaidies et al. (2017) and George and Gaidies (2017). In addition, the annulus of REE at the same position within the garnet grain emphasizes that diffusion was not the growth limiting factor.

However, despite the probably similar growth mechanism during nucleation, garnet developed different compositional zoning during its metamorphic evolution. The distinct evolution is summarized in the following and visualized in a conceptual sketch (see Figure 5.12).

In blueschist sample SY21-07 from Achladi, garnet growth proceeds through several stages. Initially, nucleation begins, and the porphyroblast core contains the highest concentrations of Y and heavy rare earth elements (HREE), which are largely determined by the starting bulk composition of the rock (Stage I in Fig. 5.12a). As garnet continues to

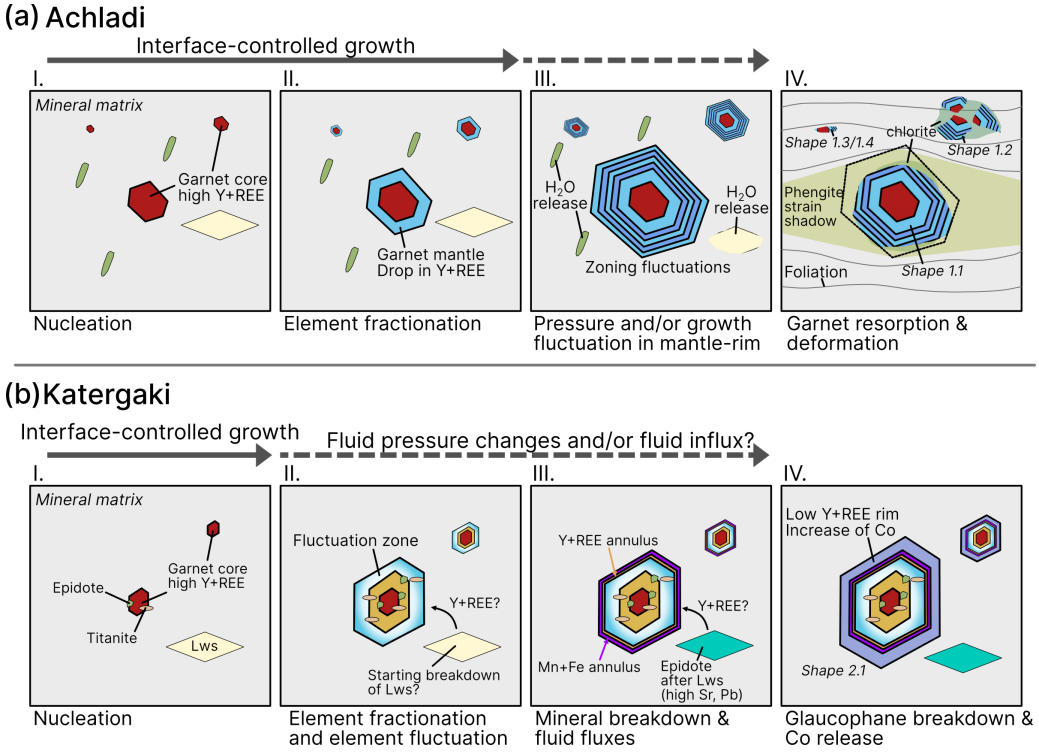

Figure 5.12: Illustration of porphyroblast growth and trace element distribution in the two blueschists from Achladi and Katergaki.

grow, HREE are fractionated from the rock volume, leading to a decrease in their concentration within the growing garnet mantle relative to the core (Stage II). With further increases in temperature and pressure, chlorite and lawsonite dehydrate, causing changes in volume and fluid pressure, which influence the availability of trace elements like Y and REE, resulting in fluctuating zoning patterns (Stage III). During lawsonite breakdown which likely occurred near peak pressure conditions (Schumacher et al., 2008), garnet resorption can take place, with chlorite replacing garnet during early exhumation. The rock then undergoes deformation, leading to the development of pressure shadows around the porphyroblasts and the formation of garnet shape 1.1 (see Figure 5.0a-b). This stage is also associated with phengite recrystallization, which commonly occurs during exhumation (Putlitz et al., 2005; Trotet et al., 2001).

In blueschist sample SY21-01/2-1 from Katergaki, the initial nucleation and growth follow a similar pattern to that observed at Achladi, with garnet initially incorporating the highest amounts of Y and REE, which decrease due to fractionation from the rock volume (Stage I in Figure 5.12b). Epidote and titanite inclusions are incorporated into the garnet, further fractionating trace elements from the rock. In Stage II, trace elements availability has decreased, resulting in lower HREE and Y content garnet but also in the matrix epidote (Figure 5.7d). During Stages II and III, lawsonite and chlorite breakdown occurs

within the system and external mafic sequences, as indicated by modelling in Chapter 4. These breakdowns release fluids, elevating pore fluid pressures and leading to compositional fluctuations and the formation of annuli in the garnet due to the liberated major and trace elements. After this fluid transfer event, no new elements are available, leading to decreased concentrations of Y and REE in the garnet rim, resulting in the final garnet grain shape 2.1 (see Figure 5.0c-d).

Bibliography

Bebout, G. E., Bebout, A. E., & Graham, C. M. (2007). Cycling of B, Li, and LILE (K, Cs, Rb, Ba, Sr) into subduction zones: SIMS evidence from micas in high-P/T metasedimentary rocks. *Chemical Geology*, *239*(3-4), 284–304. https://doi.org/10.1016/j.chemgeo.2006.10.016

Bovay, T., Lanari, P., Rubatto, D., Smit, M., & Piccoli, F. (2022). Pressure–temperature–time evolution of subducted crust revealed by complex garnet zoning (Theodul Glacier Unit, Switzerland). *Journal of Metamorphic Geology*, *40*(2), 175–206. https://doi.org/10.1111/jmg.12623

Caddick, M. J., Konopásek, J., & Thompson, A. B. (2010). Preservation of garnet growth zoning and the duration of prograde metamorphism. *Journal of Petrology*, *51*(11), 2327–2347. https://doi.org/10.1093/petrology/egq059

Carlson, W. D. (2012). Rates and mechanism of Y, REE, and Cr diffusion in garnet. *American Mineralogist*, *97*(10), 1598–1618. https://doi.org/10.2138/am.2012.4108

Carlson, W. D. (1989). The significance of intergranular diffusion to the mechanisms and kinetics of porphyroblast crystallization. *Contributions to Mineralogy and Petrology*, *103*(1), 1–24. https://doi.org/10.1007/BF00371361

Carlson, W. D. (2011). Porphyroblast crystallization: linking processes, kinetics, and microstructures. *International Geology Review*, *53*(3-4), 406–445. https://doi.org/10.1080/00206814.2010.496184

Carlson, W. D., & Denison, C. (1992). Mechanisms of Porphyroblast Crystallization: Results from High-Resolution Computed X-ray Tomography. *Science*, *257*(5074), 1236–1239. https://doi.org/10.1126/science.257.5074.1236

Carlson, W. D., Denison, C., & Ketcham, R. A. (1995). Controls on the nucleation and growth of porphyroblasts: Kinetics from natural textures and numerical models. *Geological Journal*, *30*(3-4), 207–225. https://doi.org/10.1002/gj.3350300303

Chernoff, C. B., & Carlson, W. D. (1997). Disequilibrium for Ca during growth of pelitic garnet. *Journal of Metamorphic Geology*, *15*(4), 421–438. https://doi.org/10.1111/j.1525-1314.1997.00026.x

Chernoff, C. B., & Carlson, W. D. (1999). Trace element zoning as a record of chemical disequilibrium during garnet growth. *Geology*, *27*(6), 555. https://doi.org/10.1130/0091-7613(1999)027⟨0555:TEZAAR⟩2.3.CO;2

Connolly, J. A. (1997). Devolatilization-generated fluid pressure and deformation-propagated fluid flow during prograde regional metamorphism. *Journal of Geophysical Research B: Solid Earth*, *102*(B8), 18149–18173. https://doi.org/10.1029/97jb00731

Cruz-Uribe, A. M., Page, F. Z., Lozier, E., Feineman, M. D., Zack, T., Mertz-Kraus, R., Jacob, D. E., & Kitajima, K. (2021). Trace element and isotopic zoning of garnetite

veins in amphibolitized eclogite, Franciscan Complex, California, USA. *Contributions to Mineralogy and Petrology*, *176*(5), 1–19. https://doi.org/10.1007/s00410-021-01795-4

Cygan, R. T., & Lasaga, A. C. (1982). Crystal growth and the formation of chemical zoning in garnets. *Contributions to Mineralogy and Petrology*, *79*(2), 187–200. https://doi.org/10.1007/BF01132887

Daniel, C. G., & Spear, F. S. (1999). The clustered nucleation and growth processes of garnet in regional metamorphic rocks from north-west Connecticut, USA. *Journal of Metamorphic Geology*, *17*(5), 503–520. https://doi.org/10.1046/j.1525-1314.1999.00200.x

Denison, C., & Carlson, W. D. (1997). Three-dimensional quantitative textural analysis of metamorphic rocks using high-resolution computed X-ray tomography: Part II. Application to natural samples. *Journal of Metamorphic Geology*, *15*(1), 45–57. https://doi.org/10.1111/j.1525-1314.1997.00007.x

Evans, T. P. (2004). A method for calculating effective bulk composition modification due to crystal fractionation in garnet-bearing schist: Implications for isopleth thermobarometry. *Journal of Metamorphic Geology*, *22*(6), 547–557. https://doi.org/10.1111/j.1525-1314.2004.00532.x

Fisher, G. W. (1978). Rate laws in metamorphism. *Geochimica et Cosmochimica Acta*, *42*(7). https://doi.org/10.1016/0016-7037(78)90292-2

Frost, B. R., Chamberlain, K. R., & Schumacher, J. C. (2001). Sphene (titanite): Phase relations and role as a geochronometer. *Chemical Geology*, *172*(1-2), 131–148. https://doi.org/10.1016/S0009-2541(00)00240-0

Gaidies, F., Milke, R., Heinrich, W., & Abart, R. (2017, March). Metamorphic mineral reactions: Porphyroblast, corona and symplectite growth. In *Mineral reaction kinetics: Microstructures, textures, chemical and isotopic signatures* (pp. 469–540, Vol. 16). Mineralogical Society of Great Britain & Ireland. https://doi.org/10.1180/EMU-notes.16.14

Gaidies, F., Morneau, Y. E., Petts, D. C., Jackson, S. E., Zagorevski, A., & Ryan, J. J. (2021). Major and trace element mapping of garnet: Unravelling the conditions, timing and rates of metamorphism of the Snowcap assemblage, west-central Yukon. *Journal of Metamorphic Geology*, *39*(2), 133–164. https://doi.org/10.1111/jmg.12562

Garber, J. M., Hacker, B. R., Kylander-Clark, A. R., Stearns, M., & Seward, G. (2017). Controls on trace element uptake in metamorphic titanite: Implications for petrochronology. *Journal of Petrology*, *58*(6), 1031–1057. https://doi.org/https://doi.org/10.1093/petrology/egx046

George, F. R., & Gaidies, F. (2017). Characterisation of a garnet population from the Sikkim Himalaya: insights into the rates and mechanisms of porphyroblast crystallisation. *Contributions to Mineralogy and Petrology*, *172*(7). https://doi.org/10.1007/s00410-017-1372-y

George, F. R., Gaidies, F., & Boucher, B. (2018). Population-wide garnet growth zoning revealed by LA-ICP-MS mapping: implications for trace element equilibration and syn-kinematic deformation during crystallisation. *Contributions to Mineralogy and Petrology*, *173*(9), 1–22. https://doi.org/10.1007/s00410-018-1503-0

Gorce, J. S., Caddick, M. J., Baxter, E. F., Dragovic, B., Schumacher, J. C., Bodnar, R. J., & Kendall, J. F. (2021). Insight Into the Early Exhumation of the Cycladic Blueschist Unit, Syros, Greece: Combined Application of Zoned Garnet Geochronology, Thermodynamic Modeling, and Quartz Elastic Barometry. *Geochemistry, Geophysics, Geosystems*, *22*(8), 1–24. https://doi.org/10.1029/2021GC009716

Hacker, B. R., Abers, G. A., & Peacock, S. M. (2003). Subduction factory 1. Theoretical mineralogy, densities, seismic wave speeds, and H 2 O contents. *Journal of Geophysical Research: Solid Earth*, *108*(B1), 1–26. https://doi.org/10.1029/2001JB001127

Hamelin, C., Brady, J. B., Cheney, J. T., Schumacher, J. C., Able, L. M., & Sperry, A. J. (2018). Pseudomorphs after Lawsonite from Syros, Greece. *Journal of Petrology*, *59*(12), 2353–2384. https://doi.org/10.1093/petrology/egy099

Hartmeier, P., Lanari, P., Forshaw, J. B., & Markmann, T. A. (2024). Tracking Garnet Dissolution Kinetics in 3D Using Deep Learning Grain Shape Classification. *Journal of Petrology*, *65*(3), 1–9. https://doi.org/10.1093/petrology/egae005

Hermann, J., & Rubatto, D. (2003). Relating zircon and monazite domains to garnet growth zones: Age and duration of granulite facies metamorphism in the Val Malenco lower crust. *Journal of Metamorphic Geology*, *21*(9), 833–852. https://doi.org/10.1046/j.1525-1314.2003.00484.x

Hermann, J., Spandler, C., Hack, A., & Korsakov, A. V. (2006). Aqueous fluids and hydrous melts in high-pressure and ultra-high pressure rocks: Implications for element transfer in subduction zones. *Lithos*, *92*(3-4), 399–417. https://doi.org/10.1016/j.lithos.2006.03.055

Hernández-Uribe, D., & Tsujimori, T. (2023). Progressive lawsonite eclogitization of the oceanic crust: Implications for deep mass transfer in subduction zones. *Geology*, *51*(7), 678–682. https://doi.org/10.1130/G51052.1

Hickmott, D., & Spear, F. S. (1992). Major-and trace-element zoning in garnets from calcareous pelites in the NW shelburne falls Quadrangle, Massachusetts: Garnet growth histories in retrograded rocks. *Journal of Petrology*, *33*(5), 965–1005. https://doi.org/10.1093/petrology/33.5.965

Hollister, L. S. (1966). Garnet Zoning: An Interpretation Based on the Rayleigh Fractionation Model. *Science*, *154*(3757), 1647–1651. https://doi.org/10.1126/science.154.3757.1647

Ketcham, R. A., & Carlson, W. D. (2001). Acquisition, optimization and interpretation of X-ray computed tomographic imagery: applications to the geosciences. *Computers & Geosciences*, *27*(4), 381–400. https://doi.org/10.1016/S0098-3004(00)00116-3

Kile, D. E., & Eberl, D. (2003). On the origin of size-dependent and size-independent crystal growth: Influence of advection and diffusion. *American Mineralogist*, *88*(10), 1514–1521. https://doi.org/10.2138/am-2003-1014

Kirkpatrick, R. J. (1981, December). CHAPTER 8. KINETICS OF CRYSTALLIZATION OF IGNEOUS ROCKS. In *Kinetics of geochemical processes* (pp. 321–398). De Gruyter. https://doi.org/10.1515/9781501508233-012

Kohn, M. J. (2004). Oscillatory- and sector-zoned garnets record cyclic (?) rapid thrusting in central Nepal. *Geochemistry, Geophysics, Geosystems*, *5*(12), 1–9. https://doi.org/10.1029/2004GC000737

Kohn, M. J. (2017). Titanite Petrochronology. *Reviews in Mineralogy and Geochemistry*, *83*(1), 419–441. https://doi.org/10.2138/rmg.2017.83.13

Konrad-Schmolke, M., Babtist, J., Handy, M. R., & O'Brien, P. J. (2006). The Physico-Chemical Properties of a Subducted Slab from Garnet Zonation Patterns (Sesia Zone, Western Alps). *Journal of Petrology*, *47*(11), 2123–2148. https://doi.org/10.1093/petrology/egl039

Konrad-Schmolke, M., Halama, R., Chew, D., Heuzé, C., De Hoog, J. C. M., & Ditterova, H. (2023). Discrimination of thermodynamic and kinetic contributions to the heavy rare earth element patterns in metamorphic garnet. *Journal of Metamorphic Geology*, *41*(4), 465–490. https://doi.org/10.1111/jmg.12703

Konrad-Schmolke, M., Handy, M. R., Babist, J., & O'Brien, P. J. (2005). Thermodynamic modelling of diffusion-controlled garnet growth. *Contributions to Mineralogy and Petrology*, *149*(2), 181–195. https://doi.org/10.1007/s00410-004-0643-6

Konrad-Schmolke, M., O'Brien, P. J., de Capitani, C., & Carswell, D. A. (2008). Garnet growth at high- and ultra-high pressure conditions and the effect of element fractionation on mineral modes and composition. *Lithos*, *103*(3-4), 309–332. https://doi.org/10.1016/j.lithos.2007.10.007

Konrad-Schmolke, M., Zack, T., O'Brien, P. J., & Barth, M. (2011). Fluid migration above a subducted slab - Thermodynamic and trace element modelling of fluid-rock interaction in partially overprinted eclogite-facies rocks (Sesia Zone, Western Alps). *Earth and Planetary Science Letters*, *311*(3-4), 287–298. https://doi.org/10.1016/j.epsl.2011.09.025

Kretz, R. (1974). Some models for the rate of crystallization of garnet in metamorphic rocks. *Lithos*, *7*(3), 123–131. https://doi.org/10.1016/0024-4937(74)90025-5

Kretz, R. (1993). A garnet population in Yellowknife schist, Canada. *Journal of Metamorphic Geology*, *11*(1), 101–120. https://doi.org/10.1111/j.1525-1314.1993.tb00134.x

Kunz, B. E., Warren, C. J., Jenner, F. E., Harris, N. B., & Argles, T. W. (2022). Critical metal enrichment in crustal melts: The role of metamorphic mica. *Geology*, *50*(11), 1219–1223. https://doi.org/10.1130/G50284.1

Lanari, P., Giuntoli, F., Loury, C., Burn, M., & Engi, M. (2017). An inverse modeling approach to obtain P–T conditions of metamorphic stages involving garnet growth and resorption. *European Journal of Mineralogy*, *29*(2), 181–199. https://doi.org/10.1127/ejm/2017/0029-2597

Lanari, P., Markmann, T., Laughton, J., & Tedeschi, M. (2023). xmaptools/XMapTools_Public: XMapTools 4.2. https://doi.org/10.5281/zenodo.7656957

Lasaga, A. C. (1986). Metamorphic reaction rate laws and development of isograds. *Mineralogical Magazine*, *50*(357), 359–373. https://doi.org/10.1180/minmag.1986.050.357.02

Lasaga, A. C. (1998, December). *Kinetic Theory in the Earth Sciences*. Princeton University Press. https://doi.org/10.1515/9781400864874

Laurent, V., Lanari, P., Naïr, I., Augier, R., Lahfid, A., & Jolivet, L. (2018). Exhumation of eclogite and blueschist (Cyclades, Greece): Pressure-temperature evolution determined by thermobarometry and garnet equilibrium modelling. *Journal of Metamorphic Geology*, *36*(6), 769–798. https://doi.org/10.1111/jmg.12309

Manning, C. E. (2004). The chemistry of subduction-zone fluids. *Earth and Planetary Science Letters*, *223*(1-2), 1–16. https://doi.org/10.1016/j.epsl.2004.04.030

Markmann, T. A., Lanari, P., Piccoli, F., Pettke, T., Tamblyn, R., Tedeschi, M., Lueder, M., Kunz, B. E., Riel, N., & Laughton, J. (2024). Multi-phase quantitative compositional mapping by LA-ICP-MS: Analytical approach and data reduction protocol implemented in XMapTools. *Chemical Geology*, *646*(December 2023), 121895. https://doi.org/10.1016/j.chemgeo.2023.121895

Oliver, N. H. S., & Bons, P. D. (2001). Mechanisms of fluid flow and fluid-rock interaction in fossil metamorphic hydrothermal systems inferred from vein-wallrock patterns, geometry and microstructure. *Geofluids*, *1*(2), 137–162. https://doi.org/10.1046/j.1468-8123.2001.00013.x

Page, F. Z., Essene, E. J., Mukasa, S. B., & Valley, J. W. (2014). A garnet-zircon oxygen isotope record of subduction and exhumation fluids from the Franciscan complex, California. *Journal of Petrology*, *55*(1), 103–131. https://doi.org/10.1093/petrology/egt062

Peacock, S. M. (1996, March). Thermal and Petrologic Structure of Subduction Zones. In *Geophysical monograph series* (pp. 119–133, Vol. 96). https://doi.org/10.1029/GM096p0119

Poli, S., & Schmidt, M. W. (2002). Petrology of Subducted Slabs. *Annual Review of Earth and Planetary Sciences*, *30*(1), 207–235. https://doi.org/10.1146/annurev.earth.30.091201.140550

Putlitz, B., Cosca, M. A., & Schumacher, J. C. (2005). Prograde mica 40Ar/39Ar growth ages recorded in high pressure rocks (Syros, Cyclades, Greece). *Chemical Geology*, *214*(1-2), 79–98. https://doi.org/10.1016/j.chemgeo.2004.08.056

Rubatto, D., & Angiboust, S. (2015). Oxygen isotope record of oceanic and high-pressure metasomatism: a P–T–time–fluid path for the Monviso eclogites (Italy). *Contributions to Mineralogy and Petrology*, *170*(5-6), 44. https://doi.org/10.1007/s00410-015-1198-4

Rubatto, D., Burger, M., Lanari, P., Hattendorf, B., Schwarz, G., Neff, C., Keresztes Schmidt, P., Hermann, J., Vho, A., & Günther, D. (2020). Identification of growth mechanisms in metamorphic garnet by high-resolution trace element mapping with LA-ICP-TOFMS. *Contributions to Mineralogy and Petrology*, *175*(7), 61. https://doi.org/10.1007/s00410-020-01700-5

Rubatto, D., Williams, M., Markmann, T. A., Hermann, J., & Lanari, P. (2023). Tracing fluid infiltration into oceanic crust up to ultra-high-pressure conditions. *Contributions to Mineralogy and Petrology*, *178*(11), 79. https://doi.org/10.1007/s00410-023-02060-6

Schmidt, M. W., & Poli, S. (2014). Devolatilization During Subduction. In *Treatise on geochemistry* (2nd ed., pp. 669–701, Vol. 4). Elsevier. https://doi.org/10.1016/B978-0-08-095975-7.00321-1

Schmidt, M. W., & Poli, S. (1998). Experimentally based water budgets for dehydrating slabs and consequences for arc magma generation. *Earth and Planetary Science Letters*, *163*(1-4), 361–379. https://doi.org/10.1016/S0012-821X(98)00142-3

Schumacher, J. C., Brady, J. B., Cheney, J. T., & Tonnsen, R. R. (2008). Glaucophane-bearing Marbles on Syros, Greece. *Journal of Petrology*, *49*(9), 1667–1686. https://doi.org/10.1093/petrology/egn042

Skelton, A., Peillod, A., Glodny, J., Klonowska, I., Månbro, C., Lodin, K., & Ring, U. (2019). Preservation of high- P rocks coupled to rock composition and the absence of metamorphic fluids. *Journal of Metamorphic Geology*, *37*(3), 359–381. https://doi.org/10.1111/jmg.12466

Skora, S., Baumgartner, L. P., Mahlen, N. J., Johnson, C. M., Pilet, S., & Hellebrand, E. (2006). Diffusion-limited REE uptake by eclogite garnets and its consequences

for Lu-Hf and Sm-Nd geochronology. *Contributions to Mineralogy and Petrology*, *152*(6), 703–720. https://doi.org/10.1007/s00410-006-0128-x

Smit, M. A., Vrijmoed, J. C., Scherer, E. E., Mezger, K., Kooijman, E., Schmitt-Kielman, M., Tual, L., Guilmette, C., & Ratschbacher, L. (2024). Retentiveness of rare earth elements in garnet with implications for garnet Lu-Hf chronology. *Journal of Metamorphic Geology*, *42*(5), 703–727. https://doi.org/10.1111/jmg.12769

Spandler, C., Hermann, J., Arculus, R., & Mavrogenes, J. (2003). Redistribution of trace elements during prograde metamorphism from lawsonite blueschist to eclogite facies; implications for deep subduction-zone processes. *Contributions to Mineralogy and Petrology*, *146*(2), 205–222. https://doi.org/10.1007/s00410-003-0495-5

Sun, S. S., & McDonough, W. F. (1989). Chemical and isotopic systematics of oceanic basalts: Implications for mantle composition and processes. *Geological Society Special Publication*, *42*(1), 313–345. https://doi.org/10.1144/GSL.SP.1989.042.01.19

Taylor, S. R., & McLennan, S. M. (1985). *The Continental Crust: Its Composition and Evolution*. Blackwell, Oxford.

Tirone, M., Ganguly, J., Dohmen, R., Langenhorst, F., Hervig, R., & Becker, H. W. (2005). Rare earth diffusion kinetics in garnet: Experimental studies and applications. *Geochimica et Cosmochimica Acta*, *69*(9), 2385–2398. https://doi.org/10.1016/j.gca.2004.09.025

Tracy, R. J. (1982, December). Chapter 9. COMPOSITIONAL ZONING and INCLUSIONS in METAMORPHIC MINERALS. In *Characterization of metamorphism through mineral equilibria* (pp. 354–398, Vol. 501). De Gruyter. https://doi.org/10.1515/9781501508172-013

Trotet, F., Vidal, O., & Jolivet, L. (2001). Exhumation of Syros and Sifnos metamorphic rocks (Cyclades, Greece). New constraints on the P-T paths. *European Journal of Mineralogy*, *13*(5), 901–920. https://doi.org/10.1127/0935-1221/2001/0013/0901

Trzcienski, W. E. (1977). Garnet zoning; product of a continuous reaction. *The Canadian Mineralogist*, *15*(2), 250–256.

Tsujimori, T., & Ernst, W. (2014). Lawsonite blueschists and lawsonite eclogites as proxies for palaeo-subduction zone processes: a review. *Journal of Metamorphic Geology*, *32*(5), 437–454. https://doi.org/10.1111/jmg.12057

Tsujimori, T., Sisson, V. B., Liou, J. G., Harlow, G. E., & Sorensen, S. S. (2006). Very-low-temperature record of the subduction process: A review of worldwide lawsonite eclogites. *Lithos*, *92*(3-4), 609–624. https://doi.org/10.1016/j.lithos.2006.03.054

Tual, L., Smit, M. A., Cutts, J., Kooijman, E., Kielman-Schmitt, M., Majka, J., & Foulds, I. (2022). Rapid, paced metamorphism of blueschists (Syros, Greece) from laser-based zoned Lu-Hf garnet chronology and LA-ICPMS trace element mapping. *Chemical Geology*, *607*(January), 121003. https://doi.org/10.1016/j.chemgeo.2022.121003

Viete, D. R., Hacker, B. R., Allen, M. B., Seward, G. G. E., Tobin, M. J., Kelley, C. S., Cinque, G., & Duckworth, A. R. (2018). Metamorphic records of multiple seismic cycles during subduction. *Science Advances*, *4*(3), 1–13. https://doi.org/10.1126/sciadv.aaq0234

Vitale Brovarone, A., Alard, O., Beyssac, O., Martin, L., & Picatto, M. (2014). Lawsonite metasomatism and trace element recycling in subduction zones. *Journal of Metamorphic Geology*, *32*(5), 489–514. https://doi.org/10.1111/jmg.12074

Vitale Brovarone, A., Groppo, C., Hetenyi, G., Compagnoni, R., & Malavieille, J. (2011). Coexistence of lawsonite-bearing eclogite and blueschist: phase equilibria modelling of Alpine Corsica metabasalts and petrological evolution of subducting slabs. *Journal of Metamorphic Geology*, *29*(5), 583–600. https://doi.org/10.1111/j.1525-1314.2011.00931.x

Warr, L. N. (2021). IMA–CNMNC approved mineral symbols. *Mineralogical Magazine*, *85*(3), 291–320. https://doi.org/10.1180/mgm.2021.43

Whitney, D. L., Fornash, K. F., Kang, P., Ghent, E. D., Martin, L., Okay, A. I., & Vitale Brovarone, A. (2020). Lawsonite composition and zoning as tracers of subduction processes: A global review. *Lithos*, *370-371*, 105636. https://doi.org/10.1016/j.lithos.2020.105636

Yang, P., & Rivers, T. (2001). Chromium and manganese zoning in pelitic garnet and kyanite: Spiral, overprint, and oscillatory (?) zoning patterns and the role of growth rate. *Journal of Metamorphic Geology*, *19*(4), 455–474. https://doi.org/10.1046/j.0263-4929.2001.00323.x

Yang, P., & Rivers, T. (2002). The origin of Mn and Y annuli in garnet and the thermal dependence of P in garnet and Y in apatite in calc-pelite and pelite, Gagnon terrane, western Labrador. *American Mineralogist*, *88*(8-9), 1398.

Chapter 6

General conclusion

This thesis investigated the processes of fluid-rock interaction in subduction zones during prograde metamorphism. The research focused on mechanisms of fluid release and transport, which are fundamental to understanding element redistribution within subduction environments and are preserved in the compositional zoning of minerals, particularly in porphyroblasts such as garnet.

The research pursued two main objectives. First, significant methodological advancements were developed, including refined techniques for compositional mapping (Chapter 2) and petrochemical modelling (Chapter 3). Second, these techniques were applied to natural samples from preserved subduction zone relics, focusing on specimens from Syros (Cyclades, Greece), where diverse metamorphic lithologies—including metagabbros, pillow basalts, and mafic-siliciclastic sediments—provide an exceptional record of subducted oceanic crust. The integration of petrological and geochemical analyses in 2D and 3D, combined with in-situ oxygen isotope measurements and petrochemical simulations, enabled a comprehensive reconstruction of fluid-rock interaction processes in high-pressure terranes.

The integration of a mechanical model into the petrochemical modelling framework within ThorPT revealed crucial insights into the coupling of metamorphic reactions with brittle failure during dehydration. This demonstrated that episodic fluid release contributes to permeability increases in the rock, consistent with natural observations of veins and shear zones in serpentinites. Significantly, this episodic release correlates with seismic phenomena, establishing a direct link between fluid movement and tremor and slip events in subduction zones.

Compositional mapping at the microscale emerged as a powerful analytical method for characterizing mineral phases and determining geochemical variations across multi-mineral assemblages. The newly developed LA-ICP-MS mapping routine addresses a critical gap in major-to-trace element mapping, enabling the calibration of chemically diverse minerals and making extensive datasets accessible through integration with open-source software, XMapTools. The broad applicability of this technique was demonstrated through successful applications to diverse rock types, including glaucophane-bearing eclogite from Latto Hills (Togo), migmatites from the El Oro Complex (Ecuador), and rutile in metapelite from Val Malenco (Italian Alps).

The application of compositional mapping with EPMA and LA-ICP-MS proved particularly valuable for the Syros case study. The calibrated element maps for garnet, phengite, and associated phases were essential for correlating SIMS-based in-situ oxygen isotope analyses on garnet and phengite, enabling precise matrix correction of spot analyses and establishing clear links between isotope compositions and growth zones. This coupled application of in-situ oxygen isotope analysis on garnet and phengite, previously validated through the Lago di Cignana case study, revealed multiple stages of external fluid infiltra-

tion in the Unit (Chapter 7).

Oxygen isotope compositions in garnet and phengite determined by in-situ SIMS analysis, combined with carbonate isotopes from IRMS, revealed distinct stages of fluid-rock interaction during both seafloor alteration, burial, and exhumation. Significant oxygen isotope shifts (8 to 12‰) in the Katergaki samples provide evidence for pervasive fluid infiltration, contrasting markedly with other Syros outcrops such as Achladi and Ormos Lakkoi, where prograde metamorphism occurred without significant or isotopic indistinguishable fluid infiltration. The advanced petrochemical modelling software ThorPT successfully simulated multi-rock fluid-rock interaction processes based on field observations and modelled the expected evolution of oxygen isotope compositions in stable mineral phases. These simulations demonstrate that a mafic-derived fluid with elevated oxygen isotope signatures could account for the observed shifts at Katergaki.

Trace element mapping of garnet and associated minerals from two blueschist samples from Syros enabled a reconstruction of metamorphic history and trace element distribution among mineral phases. This approach allowed for evaluation of trace element budgets across coexisting minerals without requiring intensive single-spot analysis, representing a significant advancement in analytical efficiency. The observations indicate that garnet in these samples preserves a record of mineral phase changes, particularly involving the breakdown of titanite, epidote, and lawsonite. Furthermore, modelled fluid pressure variations appear responsible for subtle zoning patterns in garnet. Notably, the garnet from Katergaki exhibits distinctive zoning characterized by Mn and Y+REE annuli in the mantle, which correlates with the documented changes in oxygen isotope composition. Additionally, the integration of compositional zoning in garnet porphyroblasts with 2D and 3D petrographic analysis reveals random crystallization and interface-controlled growth during prograde metamorphism. The distribution of fractured and resorbed garnet grains is most likely linked to post-peak metamorphism. While the trace element mapping focused primarily on two blueschist samples, broader application to additional blueschist and eclogite samples would further enhance our understanding of garnet growth mechanisms and trace element distribution patterns during metamorphism.

The successful integration of in-situ oxygen isotope analysis, compositional mapping, and petrochemical modelling has proven to be a powerful methodology for deciphering fluid-rock interaction processes in subduction zones under complex outcrop conditions. This comprehensive approach shows considerable promise for broader applications, particularly because the petrochemical and brittle failure model can be adapted for specific case studies and is not limited to subduction zone settings. Finally, the modelling results suggest that infiltrating fluids play a crucial role in stabilizing hydrous phases within the subducting slab, significantly influencing fluid redistribution and recycling. This mechanism potentially

delays mantle wedge melting, thereby affecting both element cycling and the timing of magmatic activity in subduction zones. These findings warrant further investigation and can be enhanced by incorporating trace element partitioning into the model, which would enable quantitative assessment of trace element fluxes.

Chapter 7

Supplementary Material - Contribution to published articles

Content:

1. Tracing fluid infiltration into oceanic crust up to ultra-high-pressure conditions
2. Tracking garnet dissolution kinetics in 3D using deep learning grain shape classification
3. Olivine formation processes and fluid pathways in subducted serpentinites revealed by in-situ oxygen isotope analysis (Zermatt-Saas, Switzerland)

7.1 Contribution to published articles

The following Appendix is summarizing the published articles in which I scientifically contributed.

1. In the study "Tracing fluid infiltration into oceanic crust up to ultra-high-pressure conditions" by Rubatto et al., 2023, I contributed the d18O analyses on phengite and the associated major element maps.

2. In the study "Tracking garnet dissolution kinetics in 3D using deep learning grain shape classification" by Hartmeier et al., 2024, which is the result of a Bachelors thesis I co-supervised, I was involved in the 3D data acquisition and processing from micro-CT and helped in the segmentation protocol of this study.

3. In the study "Olivine formation processes and fluid pathways in subducted serpentinites revealed by in-situ oxygen isotope analysis (Zermatt-Saas, Switzerland)" by Ulrich et al., 2024, I contributed with my developed petrochemical modeling software represented in Chapter 2. The modeling was applied to understand the evolution of the mineral phase assemblage and to quantify the oxygen isotope composition of the stable mineral phase assemblages to decipher their fluid-rock interaction.

Bibliography

Hartmeier, P., Lanari, P., Forshaw, J. B., & Markmann, T. A. (2024). Tracking Garnet Dissolution Kinetics in 3D Using Deep Learning Grain Shape Classification. *Journal of Petrology*, *65*(3), 1–9. https://doi.org/10.1093/petrology/egae005

Rubatto, D., Williams, M., Markmann, T. A., Hermann, J., & Lanari, P. (2023). Tracing fluid infiltration into oceanic crust up to ultra-high-pressure conditions. *Contributions to Mineralogy and Petrology*, *178*(11), 79. https://doi.org/10.1007/s00410-023-02060-6

Ulrich, M., Rubatto, D., Hermann, J., Markmann, T. A., Bouvier, A.-s., & Deloule, E. (2024). Olivine formation processes and fluid pathways in subducted serpentinites revealed by in-situ oxygen isotope analysis (Zermatt-Saas, Switzerland). *Chemical Geology*, *649*(November 2023), 121978. https://doi.org/10.1016/j.chemgeo.2024.121978

Tracing fluid infiltration into oceanic crust up to ultra-high-pressure conditions

Rubatto, D.[1, 2, 3], Williams, M.[3, 4], **Markmann, T. A.**[1], Hermann, J.[1], Lanari, P.[1]

[1]Institute of Geological Sciences, University of Bern, 3012 Bern, Switzerland

[2]Institut des Sciences de la Terre, University of Lausanne, 1015 Lausanne, Switzerland

[3]The Australian National University, Research School of Earth Sciences, Canberra, ACT 2601, Australia

[4]CSIRO, Mineral Resources, Kensington, WA 6151, Australia

Abstract

Fluid–rock interaction within the altered oceanic crust and across the slab-mantle boundary during subduction facilitates element transfer, but the dynamics of fluid transport and fluid–rock exchange during upward fluid migration are still unclear. A study of metamorphic fluid–rock interaction within a section of subducted oceanic crust was carried out on eclogites and metasediments of the ultra-high-pressure Lago di Cignana Unit (NW Italian Alps). The P–T modeling of a quartzschist shows that garnet grew during the prograde and sporadically during the retrograde path and that phengite mainly records the peak to retrograde conditions. Microscale geochemical analysis of garnets has revealed a systematic evolution of oxygen isotopic composition with garnet major element zonation, with extreme within-sample core–rim variations in $\delta^{18}O$ between 18 and 4‰ providing evidence for external fluid influx. Garnet in eclogites and calcschists, as well as garnet cores in quartz-rich lithologies, shows normal compositional zoning, as expected for prograde garnet growth, and a relatively constant oxygen isotopic composition. The outer garnet growth zones within a few metasediments show reverse or discontinuous zoning and progressively lower $\delta^{18}O$. Despite major element zoning, the isotopic composition of mica is homogeneous across chemical zoning in one eclogite and one quartzschist, but shows 6‰ variability in another quartzschist. In the underlying Zermatt–Saas serpentinites, antigorite from nine serpentinite samples shows some variation in $\delta^{18}O$, with average $\delta^{18}O$ values for individual samples ranging from 1 to 6‰. These results provide evidence for two main stages of external fluid infiltration: (i) fluids from the dehydration of mafic lithologies entered the sequence at peak conditions around 3 GPa, as indicated by the oxygen composition of intermediate zones of mica and garnet, and (ii) low $\delta^{18}O$ fluids from serpentinites infiltrated parts of the sedimentary package during exhumation prior to 1.5 GPa, as recorded by the 4‰ garnet outer rims. Samples recording external fluid infiltration are concentrated in the lower part of the sequence, indicating channelized fluid flow, suggesting focused fluid infiltration due to permeability contrasts between metasedimentary and eclogitic lithologies. Channelized fluid flow in the ultra-high-pressure metasediments of Lago di Cignana has not resulted in systematic decarbonation of the metasediments.

DOI: https://doi.org/10.1007/s00410-023-02060-6

Tracking Garnet Dissolution Kinetics in 3D Using Deep Learning Grain Shape Classification

Hartmeier, P.[1], Lanari, P.[1], Forshaw, J. B.[1], **Markmann, T. A.**[1]

[1]Institute of Geological Sciences, University of Bern, Baltzerstrasse 3, 3012 Bern, Switzerland

Abstract

The kinetics of fluid-driven metamorphic reactions are challenging to study in nature because of the tendency of metamorphic systems to converge towards chemical equilibrium. However, in cases where mineral textures that reflect incomplete reactions are preserved, kinetic processes may be investigated. Atoll garnet, a texture formed by the dissolution of a garnet's core, has been described in 2D from thin sections of rocks worldwide. Quantifying the extent of this dissolution reaction requires a sample-wide examination of hundreds of individual grains in 3D. In this study, we quantified the distribution of atoll garnet using micro-computed tomography and grain shape analysis. A convolutional neural network was trained on human-labeled garnet grains for automated garnet classification. This approach was applied to a retrogressed mafic eclogite from the Zermatt–Saas Zone (Western Alps). Pervasive atoll-like resorption preferentially affected the larger porphyroblasts,suggesting that compositional zoning patterns exert a first-order control on dissolution rates. A kinetic model shows that the reactivity of metastable garnet to form atolls is favored at pressure–temperature conditions of 560±30∘C and 1.6±0.2 GPa. These conditions coincide with the release of water when lawsonite breaks down during the exhumation of mafic eclogites. The model predicts dissolution rates that are three to five times faster for the garnet core than for the rim. This study shows that deep learning algorithms can perform automated textural analysis of crystal shapes in 3D and that these datasets have the potential to elucidate petrological processes, such as the kinetics of fluid-driven metamorphic reactions.

DOI: https://doi.org/10.1093/petrology/egae005

Olivine formation processes and fluid pathways in subducted serpentinites revealed by in-situ oxygen isotope analysis (Zermatt-Saas, Switzerland)

Ulrich, M.[1], Rubatto, R.[1,2], Hermann, J.[1], **Markmann, T. A.**[1], Bouvier, A.[2], Deloule, E.[3]

[1]Institute of Geological Sciences, University of Bern, Bern CH-3012, Switzerland

[2]Institute des Sciences de la Terre, University of Lausanne, Lausanne CH-1015, Switzerland

[3]Universit´e de Lorraine, CNRS, CRPG, 54500 Vandœuvre-l'es-Nancy, France

Abstract

Dehydration of serpentinites plays a crucial role in mass transfer into the Earth's interior by releasing aqueous fluids and forming new minerals. These minerals, such as metamorphic olivine, can serve as tracers of fluid- related processes. High-pressure (HP) antigorite, metamorphic olivine, and coexisting magnetite in serpentinites from a continuous, km-scale outcrop within the Zermatt-Saas HP ophiolite were analyzed in situ for trace elements and oxygen isotopes to identify differences in the initial serpentinization conditions and to investigate fluid pathways during subduction-related metamorphism. The oxygen isotopic composition, and As and Sb concentrations in antigorite reveal two distinct serpentinization conditions within the studied region: i) high As and Sb (1–25 µg/g and 0.5–5 µg/g, respectively), coupled with $\delta^{18}O$ of +6 to +7 ‰, suggesting serpentinization at relatively low temperatures near the seafloor, and ii) low As and Sb (0.03–5 µg/g and *leq* 0.1 µg/g, respectively), coupled with mostly lower $\delta^{18}O$ of +4 to +6 ‰, suggesting serpentinization at higher temperatures by interaction with fluids deeper below the seafloor. Olivine produced in situ by the brucite + antigorite dehydration reaction during subduction shows isotopic equilibrium with antigorite, and coexisting magnetite with $\Delta^{18}O_{Atg\text{-}Ol}$ of +1.5–2.5 ‰ and $\Delta^{18}O_{Ol\text{-}Mt}$ of ∼+3 ‰ at reaction temperature conditions of 550–600 ∘C. The obtained isotopic signatures of metamorphic olivine with $\delta^{18}O$ values of +1 to +2 ‰ and + 4 to +5 ‰ correspond to two different isotopic compositions of the released fluid of +5 to +6 ‰ and + 8 to +9 ‰ at these temperature conditions. This suggests that fluids released from subducted serpentinites may have variable $\delta^{18}O$ under forearc conditions. The presence of fluids with variable $\delta^{18}O$ can cause olivine in structures associated with fluid flow (e.g., shear bands, shear zones and veins) to be in isotopic equilibrium with magnetite, but in either isotopic equilibrium or disequilibrium with antigorite. Isotopic equilibrium with antigorite is achieved when the fluid responsible for olivine crystallization is internally derived. Isotopic disequilibrium is due to an externally derived fluid released by dehydration of serpentinite with a different isotopic composition than the serpentinite with which the fluid interacts. The restricted occurrence of non-equilibrated olivine only in shear bands and nearly pure Ol-veins indicates channelized fluid flow in sub- duction zone settings and demonstrates that isotopic disequilibrium can be used as a tracer for fluid infiltration.

DOI: https://doi.org/10.1016/j.chemgeo.2024.121978

Chapter 8

Supplementary material of the Chapters

8.1 List of supplementary material

The supplementary material is available on request or via the Bern Open Repository and Information System (BORIS) portal under https://boris-portal.unibe.ch/handle/20.500.12422/137471.

8.1.1 Chapter 2

- Measurement conditions LA-ICP-MS mapping
- Compilation of multi-phase trace element maps

8.1.2 Chapter 3

- Petrochemical modelling parameters and modelling results
- P–T path compilation
- Metastable phase assemblage modelling
- Compilation of multi-phase trace element maps

8.1.3 Chapter 4

- Photomicropgraphy
- SIMS matrix bias plots
- 2D and 3D outcrops
- Isotope fractionation models
- Trace elements pattern over the outcrop
- Bulk rock compositions
- Compilation EPMA maps
- Compilation garnet and phengite oxygen isotope data and carbonates oxygen and carbon isotope data
- Petrochemical modelling parameters

8.1.4 Chapter 5

- Measurement conditions µCT
- Measurement conditions LA-ICP-MS mapping
- Compilation of multi-phase trace element maps

Declaration of consent

on the basis of Article 18 of the PromR Phil.-nat. 19

Name/First Name: Markmann / Thorsten

Registration Number: 20-131-306

Study program: Earth Sciences

Bachelor ☐ Master ☐ Dissertation ☑

Title of the thesis: The geochemical record of metamorphic fluid-rock interaction in subducted terranes

Supervisor: Prof. Dr. Pierre Lanari

I declare herewith that this thesis is my own work and that I have not used any sources other than those stated. I have indicated the adoption of quotations as well as thoughts taken from other authors as such in the thesis. I am aware that the Senate pursuant to Article 36 paragraph 1 litera r of the University Act of September 5th, 1996 and Article 69 of the University Statute of June 7th, 2011 is authorized to revoke the doctoral degree awarded on the basis of this thesis.
For the purposes of evaluation and verification of compliance with the declaration of originality and the regulations governing plagiarism, I hereby grant the University of Bern the right to process my personal data and to perform the acts of use this requires, in particular, to reproduce the written thesis and to store it permanently in a database, and to use said database, or to make said database available, to enable comparison with theses submitted by others.

Bern, 22.10.24

Place/Date

Signature